AD 742146

12289-TR2 March 1972

EXCAVATION SEISMOLOGY
First Annual Technical Report

Duane E. Soland, Project Engineer 612/331-4141
Dr. Harold M. Mooney, Subcontract Principal Investigator 612/331-3137
Sudarshan Singh 612/331-3137
Dr. Duane Tack 612/331-4141
Richard Bell 612/331-4141

Honeywell Inc.
Systems and Research Center
Research Department
2345 Walnut Street
St. Paul, Minnesota 55113

DOCUMENT CONTROL DATA - R & D

Security classification of title, body of abstract and indexing annotation must be entered when the overall report is classified)

1. ORIGINATING ACTIVITY *(Corporate author)*	2a. REPORT SECURITY CLASSIFICATION
Honeywell Inc. Systems and Research Center, Research Dept. St. Paul, Minnesota 55113	Unclassified
	2b. GROUP NA

3. REPORT TITLE

EXCAVATION SEISMOLOGY

4. DESCRIPTIVE NOTES *(Type of report and inclusive dates)*

First Annual Technical Report   19 February 1971 - 19 February 1972

5. AUTHOR(S) *(First name, middle initial, last name)*

Duane E. Soland, Harold M. Mooney, Dr. Duane Tack, Richard Bell

6. REPORT DATE	7a. TOTAL NO. OF PAGES	7b. NO. OF REFS
March 1972	227	21
8a. CONTRACT OR GRANT NO H0210025	9a. ORIGINATOR'S REPORT NUMBER(S) 12289-TR2	
b. PROJECT NO ARPA Order No. 1579, Amend. 2	9b. OTHER REPORT NO(S) *(Any other numbers that may be assigned this report)*	
c. Program Code No. 1F10 d.		

10. DISTRIBUTION STATEMENT

11. SUPPLEMENTARY NOTES	12. SPONSORING MILITARY ACTIVITY Advanced Research Projects Agency Department of Defense Washington, D.C.

13. ABSTRACT

The objective of the program is to develop seismic techniques and equipment which can be used in a hard-rock rapid-excavation system to provide indication of potentially hazardous or changing geologic conditions ahead of the working face. The seismic reflection method is considered the most suitable one for the application. The principal technical problem is identification of reflections superimposed on other source-produced coherent interference. Signal processing techniques such as cross-correlation and velocity filtering or beamforming using an array of receiving sensors are being investigated for enhancement of reflections. The initial part of the program emphasized the development of a seismic source/receiver combination which produces a simple, repeatable transmitted seismic pulse. A field recording system was assembled and seismic signals recorded and digitized for reflections from free surfaces on granite blocks and in situ using a single receiver at various locations to simulate an array of receivers. The digitized signals were subsequently processed by digital computer to simulate and assess signal processing techniques. Those experimentally evaluated included delay-and-sum beamforming, Dolph-Tchebyscheff weighted beamforming, fixed and adaptive milling, adaptive weighted beamforming, and time-averaged product arrays.

14 KEY WORDS	LINK A		LINK B		LINK C	
	ROLE	WT	ROLE	WT	ROLE	WT
Rapid excavation system						
Seismic waves						
Seismic reflection method						
Seismic array processing						
Cross-correlation						
Piezoelectric transducer						
Seismic-source radiation characteristics						
Signal averaging						
Field experiments						
Instrumentation						
Seismic model						
Travel-time curves						
Transmission measurements						
Beamforming						
DIMUS						
Time-averaged, product arrays						
Delay-and-sum						
Adaptive weighting						
Dolph-Tchebyscheff weighting						

EXCAVATION SEISMOLOGY

First Annual Technical Report

Duane E. Soland, Project Engineer 612/331-4141
Dr. Harold M. Mooney, Subcontract Principal Investigator 612/331-3137
Sudarshan Singh 612/331-3137
Dr. Duane Tack 612/331-4141
Richard Bell 612/331-4141

Honeywell Inc.
Systems and Research Center
Research Department
2345 Walnut Street
St. Paul, Minnesota 55113

TECHNICAL REPORT SUMMARY

This is the first annual technical report of the Excavation Seismology study, sponsored by the Advanced Research Projects Agency under the Military Geophysics Program.

The objective of the excavation seismology program is to develop reflection seismic/acoustic techniques and equipment for use in underground hard-rock excavation. The principal recognized need is to provide early warning of hazardous or geologically changing conditions ahead of the excavation working face or in the roof of the opening. Such conditions include fractures or faults, presence of water, and changes in rock type.

The feasibility of implementing an on-line, real-time seismic reflection system for geologic prediction in advance of a tunnel-boring machine in hard rock has been determined. The proposed system utilizes a general-purpose minicomputer to provide the functions of (1) coherent summation of repetitive signals, (2) beamforming , and (3) display generation. The requirements established for the minicomputer CPU include 12,000 words of random access memory and a 1-μsec cycle time. These requirements are compatible with present commercially available machines of moderate cost. The remainder of the system consists of a repetitive seismic source, a receiver array, and an oscilloscope display.

An L-shaped array was judged to be the configuration most suitable for the underground excavation problem. Individual beams at the desired look angles are formed on each of the two line arrays making up the legs of the L, and the time-averaged product (TAP) of the beams produces a narrow output beam.

The recommended beamforming algorithm for each line array consists of summation of the polarities of the output signals of the individual receivers, known as DIMUS beamforming in sonar applications, or a modified version developed in this program. The modified version, called DIMUS/AN, adaptively produces a null in the DIMUS beam pattern to reject a coherent interference arriving simultaneously with the desired reflection but with a different apparent velocity across the array. The adaptive-null version of DIMUS should be of value in reducing shear-wave and reflected surface-wave interference in an operational system.

In addition to substantially reducing computer memory requirements and simplifying the analog-to-digital interface, the DIMUS and DIMUS/AN consistently outperformed, by 10 to 12 db, conventional delay-and-sum beamforming in comparison tests on a limited sample of seismic reflection data recorded during the study program.

The recommended DIMUS array consists of two perpendicular line arrays of six to nine elements each with element spacing equal to one-third the compressional P wavelength. A total of 25 TAP beams, or five beams on each line, will provide coverage over a 40-degree solid angle with individual 3-db beam widths of about 20 degrees. The computation time required to form each beam is estimated to be six seconds. Allowing for data acquisition and display generation, each beam output would require an estimated 30 seconds, exclusive of setup time.

The optimum frequency for the transmitted seismic pulse is about 5 KHz which corresponds to a wavelength of 2 to 4 feet in hard rock. This choice is a compromise between shorter wavelengths for better resolution and smaller array size, and longer wavelengths for minimum propagation loss. The best attainable resolution at 5 KHz will be about 3 feet, which is adequate for detecting and resolving geological anomalies of comparable dimensions. The array element spacing will be one-third wavelength or about 1 foot at 5 KHz. Each line of six to nine elements would then be 5 to 8 feet long.

A longitudinal piezoelectric transducer is a convenient seismic source, except for the necessity to prepare a smooth surface for transducer-rock coupling. Its advantages include excellent repeatability of waveform, low power requirements, moderate size and cost, and the capability of being triggered at a precise time. However, its characteristic exponentially damped sinusoidal waveform substantially reduces resolution, particularly with DIMUS beam-forming.

Theoretically, a simple one-cycle pulse can be produced by impedance matching at either end of the transducer. However, this appears prohibitively difficult to achieve in practice. An alternative approach is to cancel the exponential tail by pulsing the transducer twice, the second pulse delayed by one cycle of the transducer resonant frequency. This approach was used successfully, but not consistently, in field experiments during the study.

Use of the DIMUS beamformers on selected data recorded in small-scale field experiments in hard rock produced mixed results. The P wave reflected from a free surface on a homogeneous granite block was easily detected, but the reflection from a natural fracture in granite in situ was not; surface waves reflected randomly from cracks in the rock surface was the primary source of interference.

A recommended approach to the problem of reflected surface-wave interference is to place the receiver array in boreholes in the tunnel wall. Two perpendicular, small-diameter holes about 10 feet in length would be required. The smooth hole would also provide mechanically simple and positive transducer-rock coupling.

The proposed operator CRT display consists of the correlator output signal versus time (or depth). A positive peak in the output waveform at a particular time indicates a reflection at the corresponding depth in the direction of the beam being displayed. The simultaneous display of three or four similar beams pointed in the same direction were found indispensable for positive identification of a reflection. Overlapping groups of receivers are used to form the redundant beams. Thus, for example, the nine-element array provides four subarrays of six elements each. A good reflection indication will appear on each displayed beam in vertical registration. The display for each of the 25 pointing directions is repeated in sequence.

A unique alternative display concept was recently described for applications in oil exploration (Ref. 1). An experimental evaluation of the concept was not possible with the L-array configuration data used for this study. However, the possibilities for underground use are attractive, and an evaluation is recommended for inclusion in further development of a seismic system for rapid excavation. Interpretations are made directly from variable-intensity, two-dimensional displays of the received signals.

CONTENTS

ILLUSTRATIONS

ix

x

TABLES

xiv

SECTION I

INTRODUCTION

The objective of the Excavation Seismology program is to develop techniques and equipment, using sound waves, with which to "see" ahead of a tunnel excavation in hard rock.

The anticipated development of continuous tunnel-boring machines, capable of advancing up to 200 feet per day in hard rock at depths of several thousand feet, will require significant advancement in techniques for geologic prediction. A timely forewarning of changing and possible hazardous ground conditions will allow appropriate action to avert loss of time and assure safety.

Typically, an excavation would encounter a complex geologic situation which might consist of many different materials of varying physical properties. For example, there may be faulted zones where the rock had been fractured and crushed, water-filled fissures, or gas pockets, all of which present potential hazards. In principle, these geologic anomalies can be detected and located by echoes of sound waves artificially produced in the rock mass by a suitable seismic source.

The seismic reflection method has been highly developed and widely used, particularly in oil exploration, for gross mapping of subsurface geology from the earth's surface. The resolving power of this method is limited by the practical difficulties of generating sufficient high-frequency, short-wavelength seismic energy to penetrate through highly attenuating near-surface materials to depths of interest. For rapid underground excavation, a feasible alternative is to adapt the reflection seismic method for concurrent operation underground with the excavation system.

Because of the shorter penetration distances involved and the absence of excessively high-attenuation materials, it is not difficult as demonstrated by previous investigators, to achieve sufficient resolution with low-energy seismic sources. However, significant differences between the seismic underground reflection problem and the surface problem require the development of new techniques for generating the transmitted seismic signal, the sensing and processing of the received echoes, and the display and interpretation of the processed data. These differences include:

- The inherent three-dimensional nature of the underground problem, requiring the use of two-dimensional sensor arrays

- The limited available working space, which limits the size of an array and the rock volume available for probing

- The necessity of providing final results in essentially real time

1-1

The critical problem is to develop techniques to minimize interference so that any reflections can easily be recognized. The principal cause of interfering noise is the seismic source itself. The interference includes Rayleigh surface waves, reflected surface waves, possibly other reflected and refracted waves and locally scattered waves. The principal technique under investigation consists of multiple-sensor-array signal processing, which utilizes differences in the time-coherency characteristics of reflection signal and interfering noise to discriminate against the interference.

The technical approach consists of the following steps:

- Devise a technique, using actual field-recorded data representative of the problem, which is capable of achieving the desired results.

- Develop prototype equipment which will validate the technique under realistic but controlled conditions.

- Adapt the equipment for use under production conditions by semiskilled personnel.

The present program has been primarily concerned with the first two of these steps.

In summary, the present reseach program seeks to extend previous underground seismic reflection work by employing array signal-processing techniques to achieve sufficient, controllable depths of penetration in hard rock with low-power seismic sources and to enhance reflection signals of interest for easier detection and recognition. The goals of the initial phase of the program were to:

- Bring the transmitted seismic waveform under control

- Determine the characteristics of the interference

- Devise techniques to minimize the interferences

- Establish the feasibility of implementing these techniques in practical hardware compatible with a rapid excavation system

This report summarizes the effort and progress toward these goals. Section II consists of a discussion of the system concept and of general principles; Section III describes the laboratory and field experiments performed; Section IV details the results of array processing investigation using the recorded experimental data; and Section V describes a digital implementation of the recommended approach, based on the results of the array processing study.

SECTION II
SYSTEM CONCEPT AND ANALYSIS

2.1 DISCUSSION OF THE PROBLEM

2.1.1 Operational Requirements

The performance of a high-speed excavation system based on continuous tunneling machines is likely to be adversely affected by an unexpected encounter with an unknown major fault zone or a fissure filled with water under pressure. The need for the capability to predict the presence of such geologic features is well recognized.

Such predictions, to be useful, must be reliable and timely, and the methods used must not interfere with the tunneling operation itself. The depth to which the geologic medium must be probed in advance of the tunneling operation is directly related to the tunneling rate of advance, the frequency of probing, and the delay incurred in the processing and analysis of results.

Allowing for some major advances in rock fragmentation technology, tunneling machines of the future are expected to have a capability for tunneling 200 feet per day in a hard-rock environment. A prediction of geologic conditions at least one day in advance of the tunnel appears desirable to provide time for any necessary corrective measures.

2.1.2 Application of the Seismic Reflection Method

Of the geophysical techniques, the seismic reflection method is potentially capable of meeting the operational requirements. Acoustic energy produced by mechanical impact or an electromechanical transducer is reflected from anomalies in the surrounding rock. The reflected echoes are converted to electrical signals by other transducers and the signals further processed to provide the data which forms the basis for a geologic interpretation. The time elapsed from transmission to echo reception is related to the distance to the reflector. Differences in time of arrival at different receiver positions determine direction to the reflector. The geologic features of major interest to this program, such as transitions from hard rock to air, water, gouge or clay, are excellent acoustic reflectors.

In some respects, seismic data can complement drillhole data. A single drillhole can detect and precisely characterize the nature of an anomaly which is intersected by the hole, but multiple drillholes are required to determine its spatial orientation and extent. The addition of the seismic data can provide this information without the need for multiple drillholes. Alternatively, the seismic method can be used without drill data for detecting and locating an anomaly, but with less certainty as to its nature.

2.1.3   Seismic Reflection Problem

Use of the seismic reflection method is not simply a matter of transmitting an acoustic pulse into the rock and measuring the time of arrival of the echo. A number of problems exist which must be overcome if the method is to be useful in rapid underground excavation.

The seismic reflection problem can be modeled as a linear communication system as shown in Figure 2-1. Ideally, the source produces a force impulse with which we wish to measure the subsurface impulse response. The subsurface impulse response, $S(t)$, is a sequence of impulses, or

$$S(t) = a_1 \, \delta(t-T_1) + a_2 \, \delta(t-T_2) + \ldots$$

where

a_i = amplitude of ith reflection

T_i = two-way travel time of the ith reflection

$\delta(t)$ = delta function

Each term in the expression for $S(t)$ represents a reflection of the source impulse from an acoustic impedance contrast within the rock. Large contrasts will produce larger a_i than small ones.
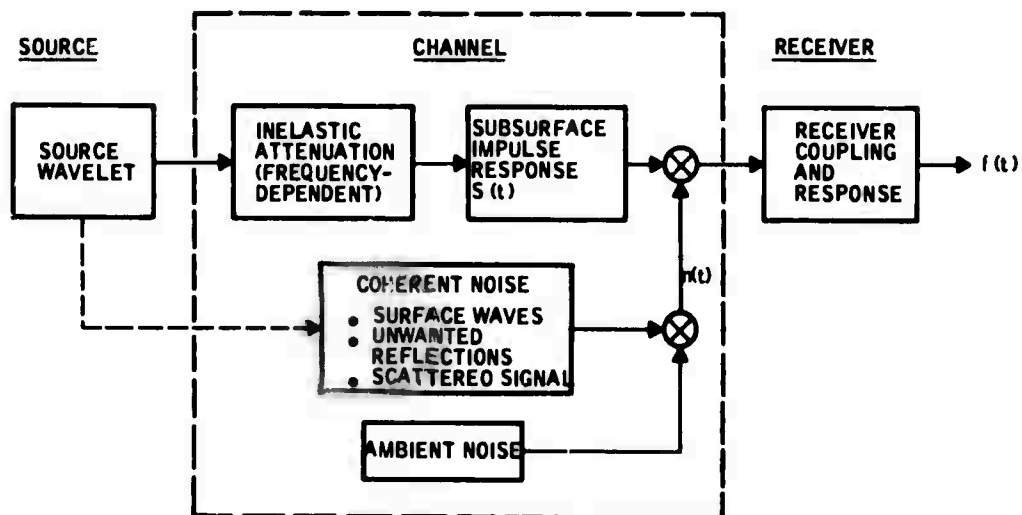
Figure 2-1.   Model of Seismic Reflection Problem

2-2

The goal of the seismic reflection method is to determine S(t). However, as indicated in Figure 2-1, the receiver output is not S(t) but instead a distorted version. The principal causes of distortion include:

- The source waveform is not a simple impulse.

- Propagation through the rock attenuates the signal; higher-frequency components are attenuated more rapidly than lows.

- Source-produced coherent and incoherent ambient noise is super-imposed on the desired signal.

2.1.3.1 <u>Types of Noise</u> — The noise obscuring the desired signal may be categorized as:

- Direct Rayleigh waves from the source
- Reflected Rayleigh surface waves
- Ambient non-source-generated seismic noise
- Side reflections other than scattering
- Scattering
- Instrument and cable pick-up noise

These are discussed in the following paragraphs.

<u>Direct Rayleigh Waves from the Source</u> — The direction of propagation is known, namely from the source to the receiver along the surface except for possible small deflections from local inhomogeneities. The apparent velocity across an array of receivers equals the true velocity of surface waves for the medium, roughly 9 to 12 ft/msec. The character of the waveform and its spectral characteristics depend strongly upon the source waveform and source-rock coupling, but often the surface wave looks like a few cycles of a damped sinusoid. The amplitude of the signal dies out with distance as roughly 1/R. The waveform changes only moderately with distance from the source.

In earthquake and exploration seismology, analysis leans heavily on frequency-wavenumber representations of the signal and noise. Using frequency-wavenumber analysis and filtering, the compressional wave may be separated from the surface waves of both source-generated and non-source-generated types. The presumption is that the two waves differ in both direction of arrival and waveform spectrum; hence, the most power-ful method for separating them will take both factors into account.

The frequency-wavenumber representation appears to have limited value in the excavation seismology problem. The reason lies in the probable

similarity of waveform spectra for the reflection and the surface wave. In earthquake and exploration seismology, the waveform of the surface wave is determined largely by propagation effects along the path, whereas in this problem it (like the reflected waveform) will be determined largely by the source waveform. Thus we cannot hope for a major difference in frequency content upon which to base a discrimination method. This is a possible explanation for the discouraging preliminary results using fan filtering, as discussed in Section IV.

A major unknown is the duration of the surface wave. The duration of the large-amplitude portion can be observed on the waveform, but smaller-amplitude signals may linger on for a prolonged period. This hypothesized "tail" to the surface wave train could arise from several factors:

- Ringing of the source — The dominant part of the source waveform will die out fairly rapidly, but there may be smaller oscillations continuing within the transducer. Since the surface wave represents the largest signal produced by the source, it follows that even small source vibrations can produce significant surface waves.

- Dispersion during propagation — If the velocity varies within the rock volume (as, for example, due to a slightly fractured near-surface layer), the surface-wave pulse will be dispersed with consequent elongation in time.

- Character of two-dimensional wave propagation — Cylindrical waves from a point source are not truly cylindrical waves, but it is possible that some of the effect may carry over.

Reflected Rayleigh Surface Waves — A joint or fracture which extends into the rock surface will have the capability of reflecting surface waves. These reflections will have the characteristic of more or less coherent propagation across the array, depending upon the smoothness of the reflecting plane. The propagation vector will like along the rock surface, but its direction will otherwise be unpredictable.

If the reflector were smooth, the resulting surface wave should be relatively constant in amplitude, waveform, and propagation direction across the array since the apparent source is at a relatively large distance. The opposite situation may occur in practice; rough reflectors may cause so much scattering of the reflected surface wave as to make it look almost like random noise. Beam forming will discriminate against horizontally propagating signals only to the extent that they are coherent across the array.

Ambient Non-source-generated Seismic Noise — We do not expect to encounter problems from this cause. For one thing, we are working in a high-frequency range where signals attenuate rapidly with distance, so that only nearby sources could contribute. For another, extraneous noise can be monitored prior to arrival of the seismic signal.

On the other hand, for very-low-level reflected signals, we cannot dismiss entirely this source of noise. Furthermore, some situations may present severe noise problems from machinery. The best technique here is signal enhancement through summation.

Side Reflections Other than Scattering — Side reflectors may exist which can produce coherent arrivals across part or all or the array. These will be characterized by a particular direction of arrival which differs from that of the target reflection. Their waveform may be very similar to that of the target reflection, although in general they will come from shorter distances and, hence, may contain higher frequencies.

Scattering — The most serious noise problems may arise from relatively incoherent signals from scatterers close to the receiver array. These may consist of small fractures, inclusions, rough rock surface or reflecting discontinuities, etc.

The signals will not be coherent across the array, but they will repeat fairly well from one source pulse to the next. Thus signal enhancement through summation can produce only moderate improvement at best. In principle, the best protection will come from summation from many array elements.

Instrument and Cable Pick-up Noise — Summation from multiple-source pulses will, if necessary, help to keep instrument noise within bounds.

2.1.3.2 Seismic Wave Attenuation — There are three types of energy loss which limit the range that can be achieved with a seismic reflection system. They are due to:

- Geometrical spreading
- Inelastic, frequency-dependent absorption
- Reflections at interfaces

Geometrical spreading losses result from the fact that the energy spreads out over a larger surface as distance increases. For plane reflecting objects which are comparable to the wavelength of the incident energy or larger, the loss varies inversely as the square of the distance. For objects small with respect to the wavelength, the loss varies inversely as the fourth power of the distance. Small anomalies at large distances will thus

be undetectable, but a small anomaly near a receiver position may scatter sufficient energy to produce a substantial perturbation of the received waveform as suggested in Section 2.1.3.

Inelastic attenuation increases with wave frequency in rocks of all types. It would then appear that low frequencies would give a better signal-to-noise ratio than higher frequencies and, therefore, greater depths of penetration. However, the power transmitted into the rock from a small seismic source increases with the square of the frequency, thereby tending to offset the increase in attenuation with frequency. Furthermore, resolution becomes poorer at lowest frequencies, providing a tradeoff between range and resolution.

We wish to estimate the amount of signal loss for the depths of penetration and rock types of interest in hard-rock excavations. These estimates will, in turn, provide estimates of the required signal processing gain to provide useful signal-to-noise ratios at maximum depths of penetration. Conversely, if the signal-processing gain is fixed, the expected maximum depth of penetration can be estimated.

Geometrical Spreading — An elastic-body P or S wave, propagating outward from a point source (and ignoring the nonuniformity of amplitude across the spherical wavefront from the directional radiation pattern of the source), suffers a loss in amplitude of a factor of two, or 6 db, for every doubling of distance traveled. This follows from the result that at sufficiently great distances from the source, the displacement amplitude of the wave varies as $1/R$ where R is the distance to the source. The energy in an elastic wave is constant, and, since the energy is distributed over an ever increasing sphere of area $4\pi R^2$, the geometrical spreading energy loss varies as $1/R^2$, or a factor of four for each doubling of distance.

Frequency-Dependent Attenuation — Geometrical spreading attenuation is independent of rock type, but inelastic attenuation depends both on rock type and on frequency content of the seismic wave. The most suitable parameter to characterize inelastic attenuation in rocks is $1/Q$, the specific attenuation factor, which is a reduction to dimensionless form of the more usual measures of attenuation. The quantity, Q, has been found experimentally by many investigators to be independent of frequency for a wide range of rock types. Typical values of $1/Q$ for various hard rocks are shown in Table 2-1.

2-6

Table 2-1. Internal Friction in Rocks, 1/Q*

Rock Type	1/Q (longitudinal vibrations)
Limestone, Pennsylvania	760×10^{-5}
Quartzitic sandstone	770
Gneiss, Pelham, Massachusetts	1800
Granite, Quincy	500 - 1000
Norite, Sudbury	340
Diabase, Vinal Haven	170
Gabbro, French Creek	590

*At ordinary pressure and temperature — selected from "Handbook of Physical Constants", p 92, (Birch, 1953)

The amplitude of a propagating harmonic wave, including both geometrical spreading loss and inelastic attenuation can be written as

$$A = A_o \frac{e^{-\alpha R}}{R}$$

The coefficient of attenuation α is related to $1/Q$ by

$$\alpha = \frac{\pi f}{vQ}$$

where f is the frequency and v is the appropriate phase velocity for the rock and the wave type.

Attenuation curves are shown in Figures 2-2 and 2-3 for two values of 1/Q which are representative of the range of values contained in Table 2-1. The ordinate is attenuation in db, referenced to the amplitude A_o of an elastic wave ($\alpha = 0$) at a distance of one meter. The abscissa is frequency. Distance (twice depth of penetration of reflected waves) is the parameter.

Discussion — The advantage of lower frequencies to achieve substantial penetration depths is apparent, particularly in lower-Q rocks, such as gneisses, as Figure 2-3 illustrates. On the other hand, Figure 2-2, which is representative of higher-Q rocks such as limestone or diorite, shows only a modest loss with frequency up to about 10 KHz. For example, a signal-processing gain of 36 db with a transducer operating at 10 KHz would provide the same signal-to-noise ratio for a reflector at a depth of 50 meters (R = 100 meters) as the same reflector at a depth of five meters. However, Figure 2-3 shows that the same situation requires a signal-processing gain of 119 db in the lower-Q rocks. Reducing the transmitted frequency to 5 KHz reduces the processing gain required to 59 db, which is more easily attained.
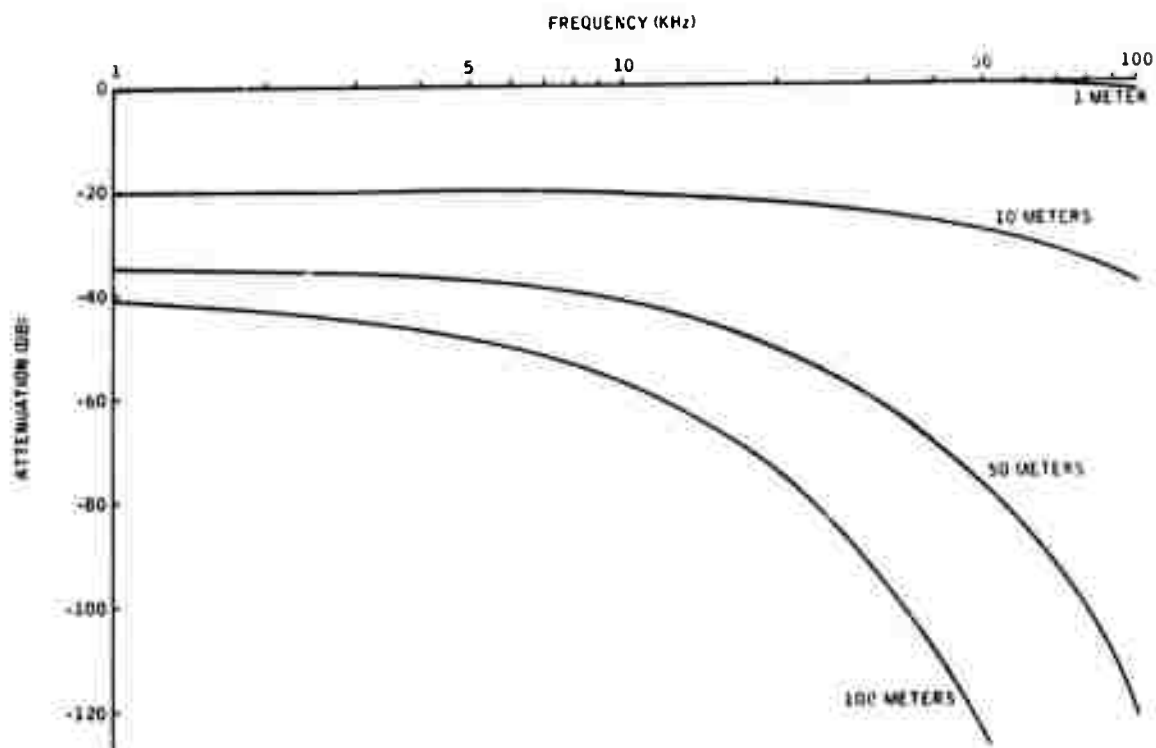
Figure 2-2. Propagation Loss Referenced to Elastic-Wave Amplitude at 1 meter -- Rock Q = 300
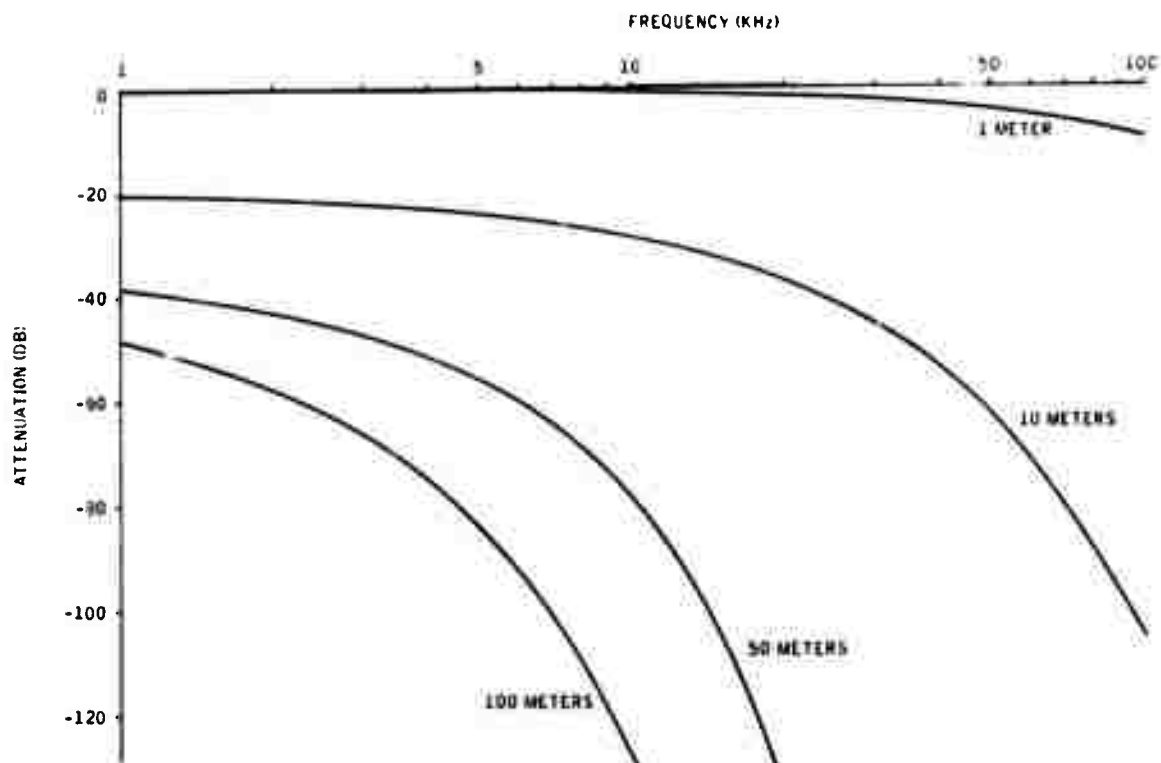
Figure 2-3. Propagation Loss Referenced to Elastic-Wave Amplitude at 1 meter -- Rock Q = 60

2-8

The disadvantages of lower frequencies include longer wavelengths with a correspondingly larger source transducer, larger array dimensions, and lowered resolution.

2.2 SYSTEM CONCEPT

The proposed seismic reflection system, with the exception of the source, is shown as a functional block diagram in Figure 2-4. The signals received on a two-dimensional array of sensors are combined to form a number of individual beams. The beamformer outputs are further processsed through filtering, cross-correlation, etc., and the final result displayed to an operator who makes an interpretation of the geologic situation from the displayed results.

To meet the time constraint requirements of rapid excavation, the data acquisition, processing, display, and interpretation will have to be accomplished in near-real time. This requirement represents a significant departure from conventional seismic technology, in which delays of weeks or months might be incurred between data recording and interpretation. One configuration which would meet this requirement is shown in Figure 2-5. The processor consists of a general-purpose minicomputer which provides control signals to the seismic source, samples the seismic signals received at the sensor array, performs the beamforming and associated processing, and generates signals to drive the output display. The major design problems consist of determining the array-processing algorithms which will produce the desired performance, specifying array configurations, and the form of the display.

2.2.1 Linear Array Processing for Underground Excavation

The use of groups or "arrays" offers several advantages over a single receiver:

- It provides directionality in the sensitivity pattern, so that waves arriving from some particular direction (for example, horizontally arriving reflections) can be favored against some other direction or against surface waves.

- It can be used to determine direction of arrival of some particular wave group.

- In the presence of noise, the array may be used to detect a small signal buried in noise or to recover the true signal waveform if it is distorted by noise.
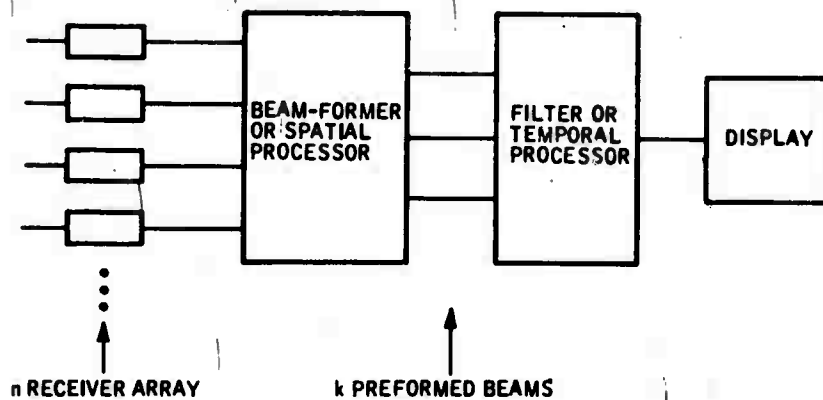
Figure 2-4. Signal Processor for Excavation Seismology
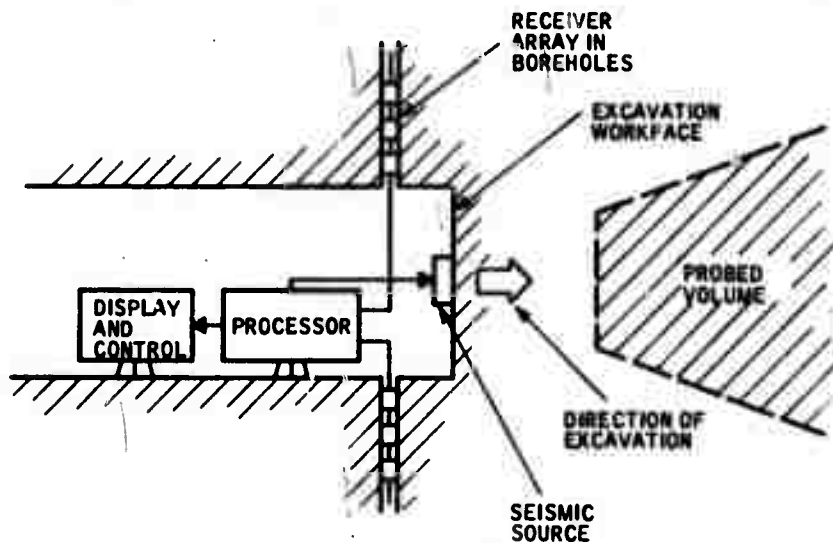
Figure 2-5. Possible System Configuration for Underground

The geometry of an array can be something as simple as two detectors placed along a line. The sum of their outputs will be greatest for a wave which reaches them both simultaneously, i.e., arrives perpendicular to the line. Other directions of maximum sensitivity can be achieved by delaying one of the outputs before the summation takes place. In practice, more complicated geometries can yield more selective results; in seismology, groups of dectors are used along straight lines, or along crossed lines, or in square grids. Examples of crossed arrays for earth-quake seismology include Tonto Forest (Arizona), Yellowknife (Canada), and Eskdalemuir (Scotland).

The essence of an array is that more than a single receiver is used--at least two, and normally many. The possible manipulations with an array reduce to the various ways in which the individual sensor outputs are modified and then combined. We will describe the principal manipulations in the simplest possible context of two sensors.

Consider first a wave incident first on a single detector, and then on two. detectors:
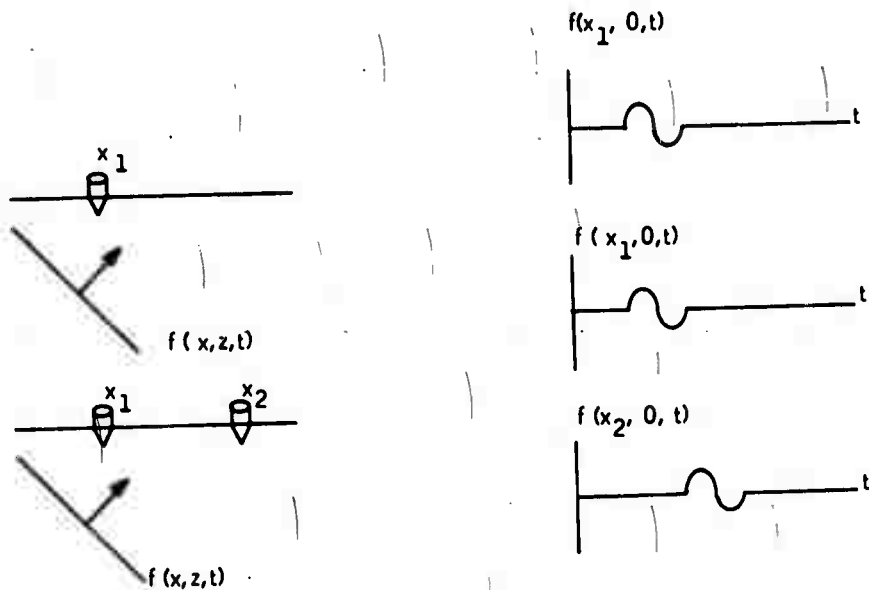
Much of array theory can be approached by considering the possible operations on the outputs from the two detectors, and by extension more than two. For example, the outputs can be summed to yield a single output:
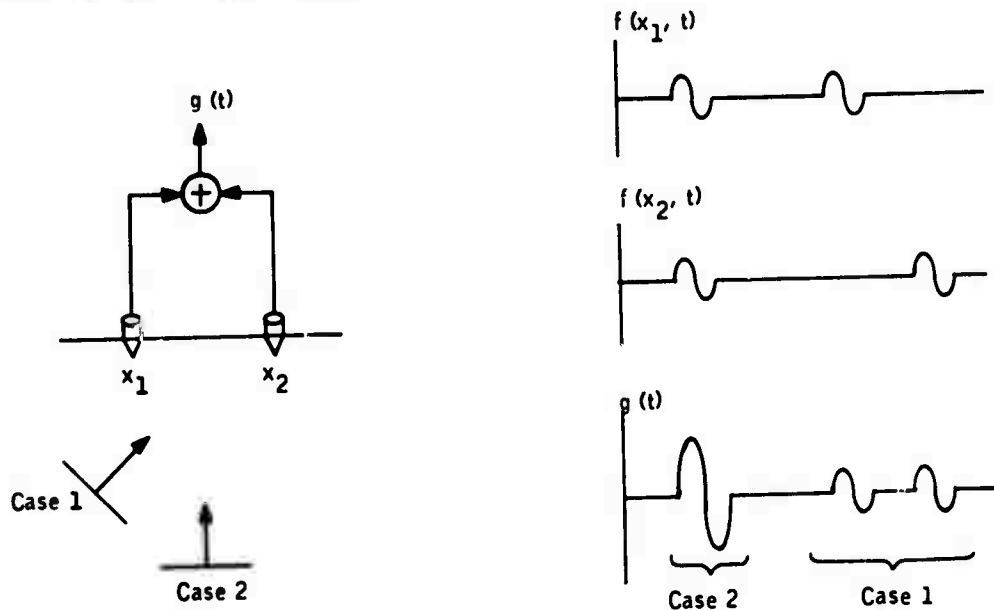
The use of "multiple geophones" in seismic exploration is an application of this method.

Alternatively, we could delay-and-sum the outputs to yield a single output:
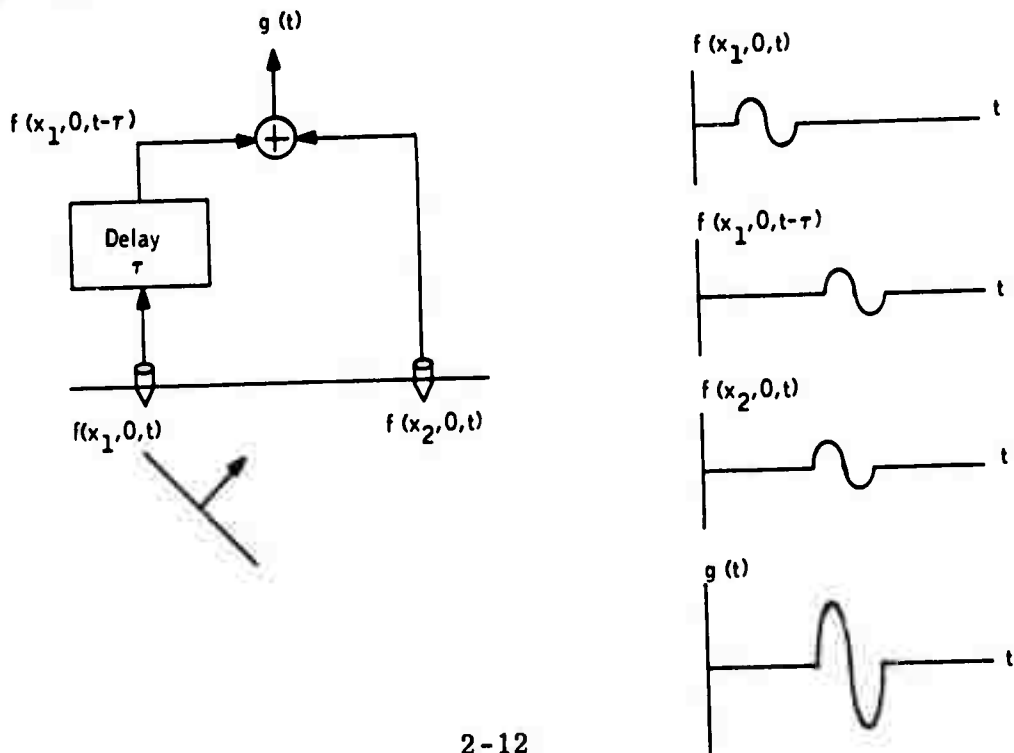
In the illustration, the delay τ has been chosen to yield constructive summation, but clearly this can be accomplished only if the delay is chosen with proper regard to:

- Direction of arrival

- Frequency, or wavelength

- Spacing between sensors

This approach and its extension to N receivers are analyzed in Sections 2.2.1.1 and 2.2.1.2.

A third possibility consists of individual filtering of each signal before summation:
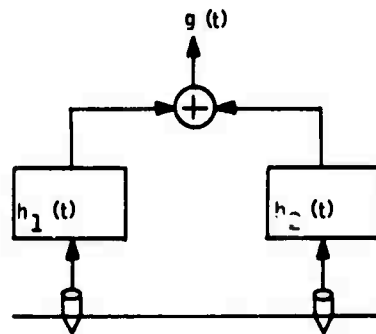
This type of array processing is known in seismology as multichannel filtering and represents about as complex a process as has found practical use.

It will be noted that this approach includes all of the preceding ones as special cases, since a simple time delay represents a particular type of filtering.

More complicated types of array processing can be visualized, as, for example, an intermixing of signals from adjacent receivers before summation or further processing:
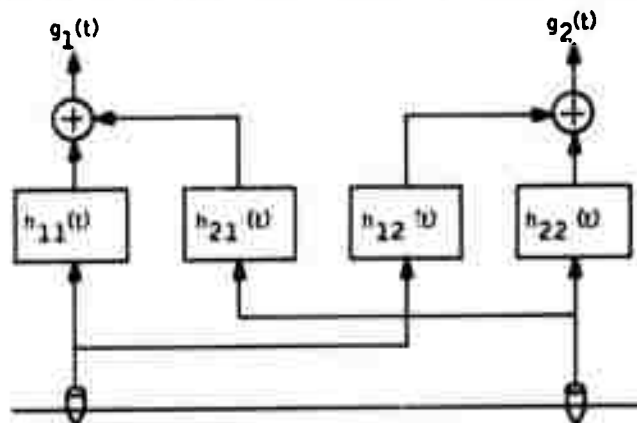
A simple version of this is known as compositing in seismic exploration, of which an illustration might be:
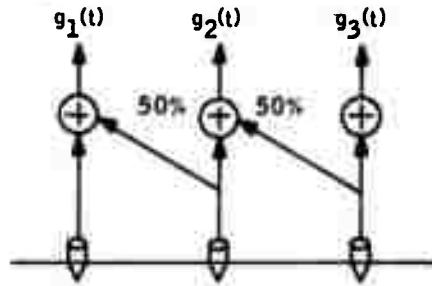
2.2.1.1 Beamsteering (or Delay-and-Sum) — In beamsteering (also known as delay-and-sum) the individual outputs are delayed in some prescribed fashion before summing. The purpose is to achieve directional sensitivity to the incoming waves. Straight summation of the inputs would be a special case of zero delay; this yields maximum sensitivity for broadside incidence.

First consider the almost trivial example of a plane wave incident upon an array consisting of only two detectors:
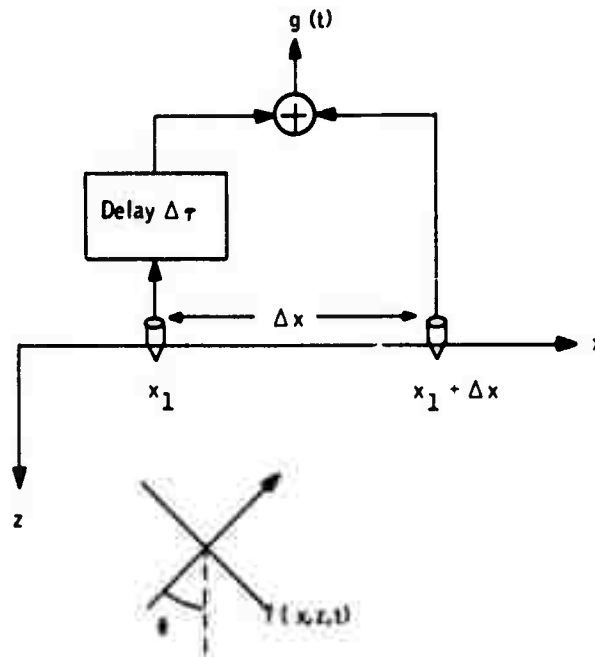
A plane wave propagating in positive x and negative z directions is

$$f(x, z, t) = A_o e^{i\omega \left[t - \frac{x \sin \theta - z \cos \theta}{v} \right]}$$

2-14

which becomes at z = 0:

$$f(x, o, t) = A_o e^{i[\omega t - k_x x]}$$

where we have replaced as follows:

$$k_x = \frac{\omega \sin\theta}{v} = \frac{2\pi}{\lambda_x}$$

In particular, the output at x_1 after delay $\Delta\tau$ becomes

$$f(x_1, o, t - \Delta\tau) = A_o e^{i[\omega t - \omega\Delta\tau - k_x x_1]}$$

and the output at $x_2 = x_1 + \Delta x$ becomes

$$f(x_1 + \Delta x, o, t) = A_o e^{i[\omega t - k_x x_1 - k_x \Delta x]}$$

and, summing

$$g(t) = A_o e^{i[\omega t - k_x x_1]} \left\{ e^{-ik_x \Delta x} + e^{-i\omega \Delta\tau} \right\}$$

$$= A_o \cos[\omega t - k_x x_1 - k_x \Delta x] + A_o \cos[\omega t - k_x x_1 - w\Delta\tau]$$

To quickly visualize the significance of this result, we note that the signals will interfere

- **Constructively, if phases differ by 0, 2π, 4π, ...**
- Destructively, if phases differ by π, 3π, 5π, ...

i. e.

$$\omega t - k_x x_1 - k_x \Delta x = \omega t - k_x x_1 - \omega\Delta\tau \pm \left\{ \begin{matrix} 2n \\ 2n+1 \end{matrix} \right\} \pi$$

or

$$\omega\Delta\tau = k_x \Delta x \mp \pi \begin{cases} 2n, & \text{constructive} \\ 2n+1, & \text{destructive} \end{cases}$$

$$= \frac{\omega \sin\theta}{v} \Delta x$$

Thus, for given values of v and Δx:

- For specified delay Δt, the response as a function of angle of arrival θ passes through successive maxima (both positive and negative) and zeros.

- The response pattern so computed is frequency dependent, so that a transient signal (containing multiple frequencies) will have a different response pattern for every frequency, except for the main lobe at $n = 0$, which occurs at the same location for all frequencies.

2.2.1.2 <u>Beamsteering with an Array of N Detectors</u> — Now consider a somewhat more general case than in the preceding subsection, namely N rather than two detectors. We retain certain simplifications, however: the detectors are equally spaced at intervals x, the delay introduced is proportional to distance along the array, and all detectors are equally weighted in the summation.

The array appears as follows:
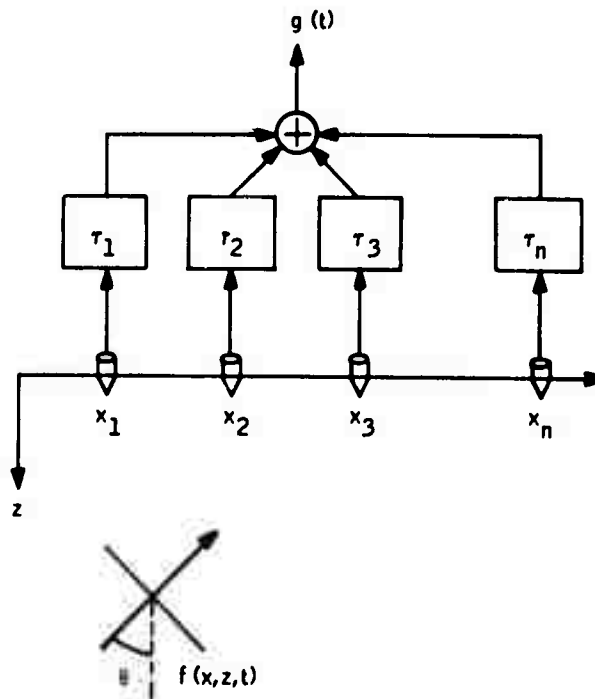
The contribution to g(t) from the nth detector is

$$f(x_n, o, t - \tau_n) = A_o e^{i [\omega t - w\tau - k_x x_n]}$$

Now the locations and time delays may be expressed as

$$x_n = x_1 + (n-1) \Delta x$$

$$\tau_n = \tau_1 + (n-1) \Delta\tau$$

and we can, without loss of generality, take the x = 0 location and the delay = 0 location at the center of the array. This means that the location and delay for the first detector become

$$x_1 = - \Delta x \frac{N-1}{2}$$

$$\tau_1 = - \Delta\tau \frac{N-1}{2}$$

and, for the nth detector

$$x_n = \Delta x \left[(n-1) - \frac{N-1}{2} \right]$$

$$\tau_n = \Delta\tau \left[(n-1) - \frac{N-1}{2} \right]$$

The output signal g(t) is now obtained from summation:

$$g(t) = \sum_{n=1}^{N} f(x_n, o, t - \tau_n)$$

$$= A_o e^{i\omega t} \sum_{n=1}^{N} e^{-i [\omega \Delta\tau + k_x \Delta x] \left[(n-1) - \frac{N-1}{2} \right]}$$

$$= A_o e^{i\omega t} \cdot \left| \frac{\sin N\phi}{\sin \phi} \right|$$

2-17

where

$$\phi = \frac{1}{2} [\omega \, \Delta\tau + k_x \, \Delta x]$$

The transfer function of a linear system can be expressed simply as the output-time-function when the input-time-function is a steady-state sinusoid of unit amplitude. Thus

$$H(k_x, \omega) = \frac{\sin N\phi}{\sin \phi} \quad , \quad \phi = -\frac{1}{2} [\omega \, \Delta\tau + k_x \, \Delta x]$$

$$H(\theta, \omega) = \frac{\sin N\phi}{\sin \phi} \quad , \quad \phi = \frac{\omega}{2} [\Delta\tau + \frac{\sin \theta}{v} \Delta x]$$

This expression gives the transfer function for a linear beamsteered array with equal spacing between detectors and equal weighting of detectors. It has been computed with x=0 and delay-time=0 associated with the midpoint of the array.

For example, for seven receivers (N = 7)

$$H(\theta, \omega) = 1 - 8 \sin^2 \phi + 16 \sin^4 \phi - \frac{64}{7} \sin^6 \phi$$

This function is plotted in Figure 2-6 versus θ for the case $\Delta t = 0$, $\Delta x = \frac{v}{2f}$ (half-wavelength spacing). In terms of parameter values typical for the hardrock excavation seismology problem:

f = 5000 Hz
v = 5 km/sec
λ = 1 m
Δx = 1/2 m
Array length = 6Δx = 3m

The same case is shown plotted in Figure 2-7 for beamsteering at θ = 15 deg ($\Delta\tau$= 50 μsec for the parameters listed above).

2.2.2 Nonlinear Array Processing

The principal advantage of the linear array processing techniques discussed in the previous subsection is that they may be so designed that a reflected signal, arriving from a particular direction, may be recorded without further distortion of the signal waveform.
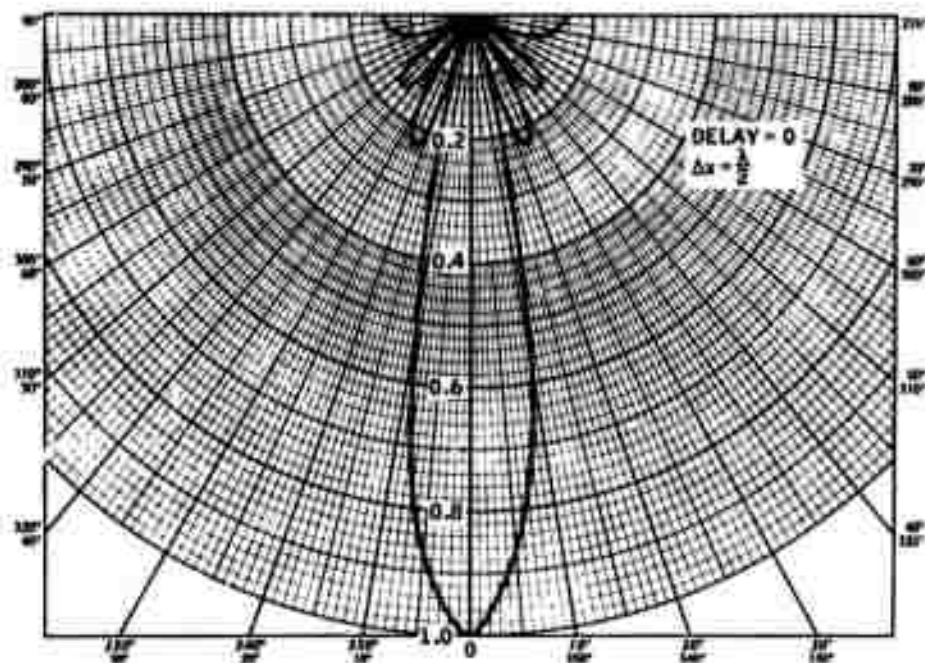
Figure 2-6. Beam Pattern for Seven Elements
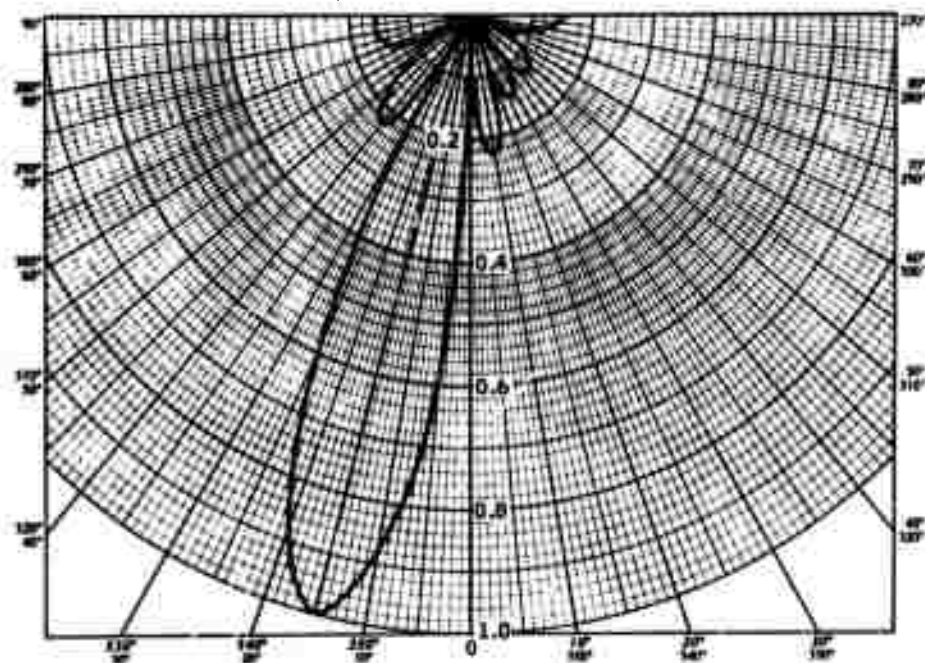
Figure 2-7. Seven-Element Array with Beam-Steering
at $\theta = 15$ degrees
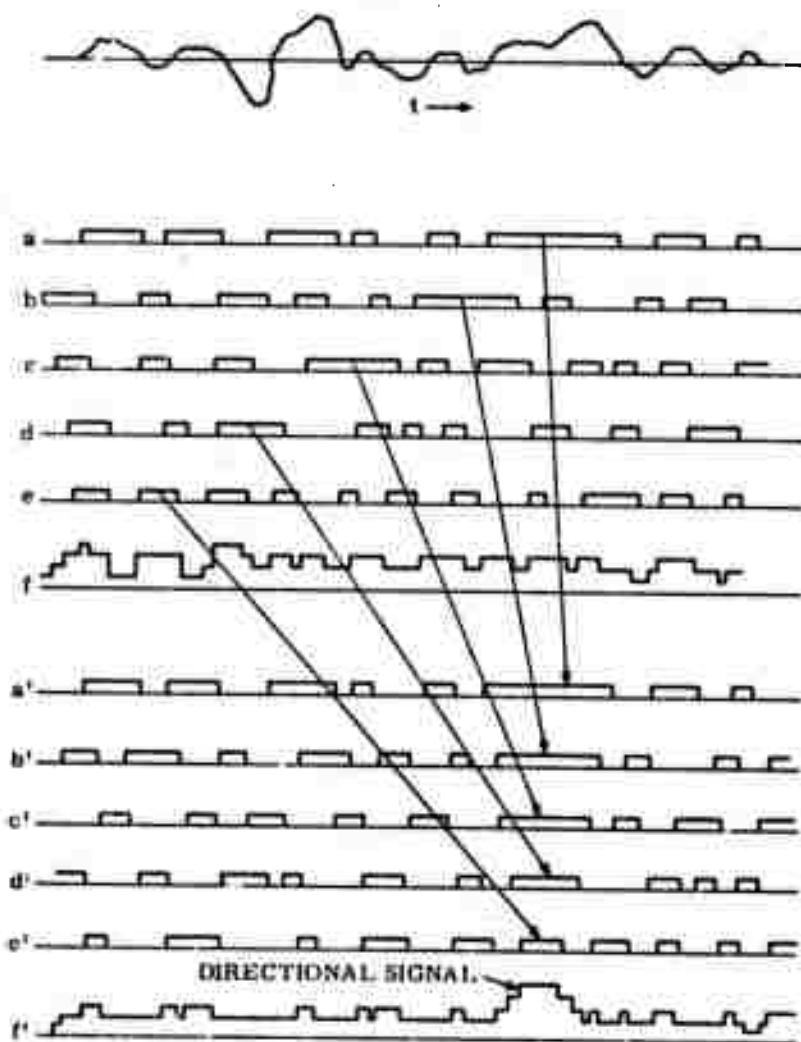
Figure 2-8. Illustration of Clipped Beamforming

Nonlinear methods do not share this property but can have certain other system benefits, such as reducing the number of receiver elements needed as well as computational requirements. The nonlinear techniques of principal interest in beamforming are (1) clipping, and (2) multiplicative beamforming.

When operating with clipped signals, we use only the polarity of the receiver output, which can then be represented by a single binary bit. The clipped array outputs can be delayed and summed to form a beam in a particular direction as Figure 2-8 illustrates. The top trace represents an analog receiver output whose clipped, or binary, version is shown as trace (a). Traces (b) through (e) represent the clipped output from other receivers in the array. Trace (f) which is the direct summation of the five binary signals (a) - (e), does not indicate any coherent signals for zero delay. However, (f') does indicate a coherent directional signal when the proper delays are introduced.

A further advantage of clipping is that amplitude variations between receivers, due to differences in sensitivity or coupling to the rock, become unimportant.

Multiplicative beamforming, or time-averaged product array processing (TAP), consists of the multiplication of the outputs of two beamformers, followed by lowpass filtering, to achieve more directionality than is provided by either individual beam (Figure 2-9). Any of the methods previously described for beamforming with line arrays can be employed as the initial beamforming operation.
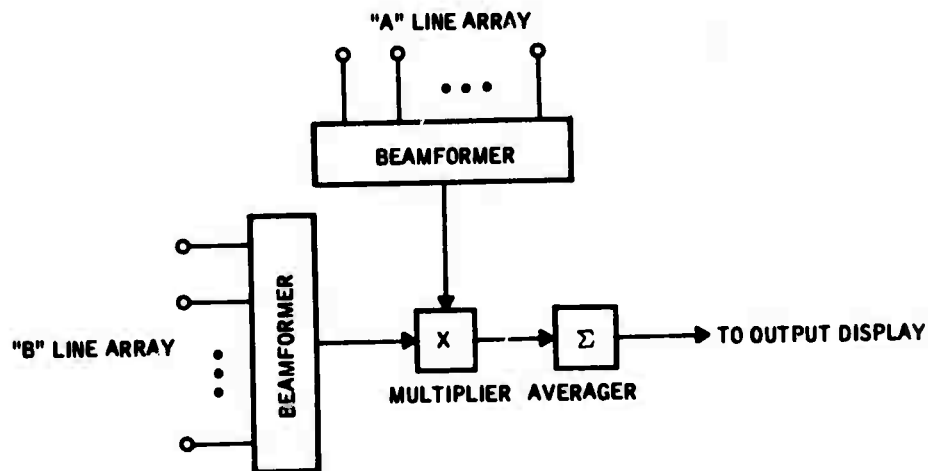
Figure 2-9. Multiplicative (TAP) Beamforming Using Perpendicular Line Receiver Arrays

2.2.3 Array Geometry for Underground Excavation

Figure 2-10 illustrates several two-dimensional array configurations which were considered for this application. A coherent seismic signal propagates across the array with apparent velocity v. As it does, time delays exist between the receiver outputs. From Figure 2-10(a), the time delay τ_i, referred to an arbitrary point P, which will "line up" all the receiver outputs, is given (for plane waves) by

$$\tau_i = \frac{r_i}{v_H} \cos (x - \alpha_i) = \frac{r_i}{v} \sin \theta \cos (x - \alpha_i)$$

(In general, the wavefronts will be curved, so that additional terms are needed in computing the necessary delay.)

First of all, we note that $\tau_i = 0$ if $\theta = 0$. This case corresponds to a reflection arriving along the z-axis, i.e., broadside to the array with infinite velocity and wavelength. For other values of θ, the computation of the delays for beamforming involve the coordinates of each receiver. To simplify the computations, special geometrical configurations such as those in Figure 2-10(b) through (e) are desirable. For example, for the circular array and circular cluster, the r_i are constant, while, for the symmetrical cross and L-shaped arrays, the α_i are constant. The computations are further simplified for these cases if the array elements are uniformly spaced.

The major problem with the use in rapid tunneling applications of array geometries with circular symmetry, such as (b) and (c), is that waves reflected from the sides of the tunnel would tend to arrive at all the receivers at the same time. Consequently, they would tend to interfere with reflections arriving from within the rock broadside to the array, the direction of principal interest.

The crossed line arrays, (d) and (e), do not have this problem; but, for linear processing (summation) of the receiver outputs, these configurations have poor beam patterns for azimuths at right angles to the direction of either line. This is because signals from these directions are always in phase on one of the two lines, and the output tends to be one-half the maximum output of the full array.

Birtil and Whiteway (Ref. 2) have shown how the crossed-line and L-shaped array response can be greatly improved by cross-correlating the summed outputs of the individual lines. The output of the correlation is then proportional to the product of the individual line responses, resulting in the formation of a narrow beam.

(a) GENERAL

(b) CIRCULAR

(c) CLUSTER

(d) SYMMETRICAL CROSS
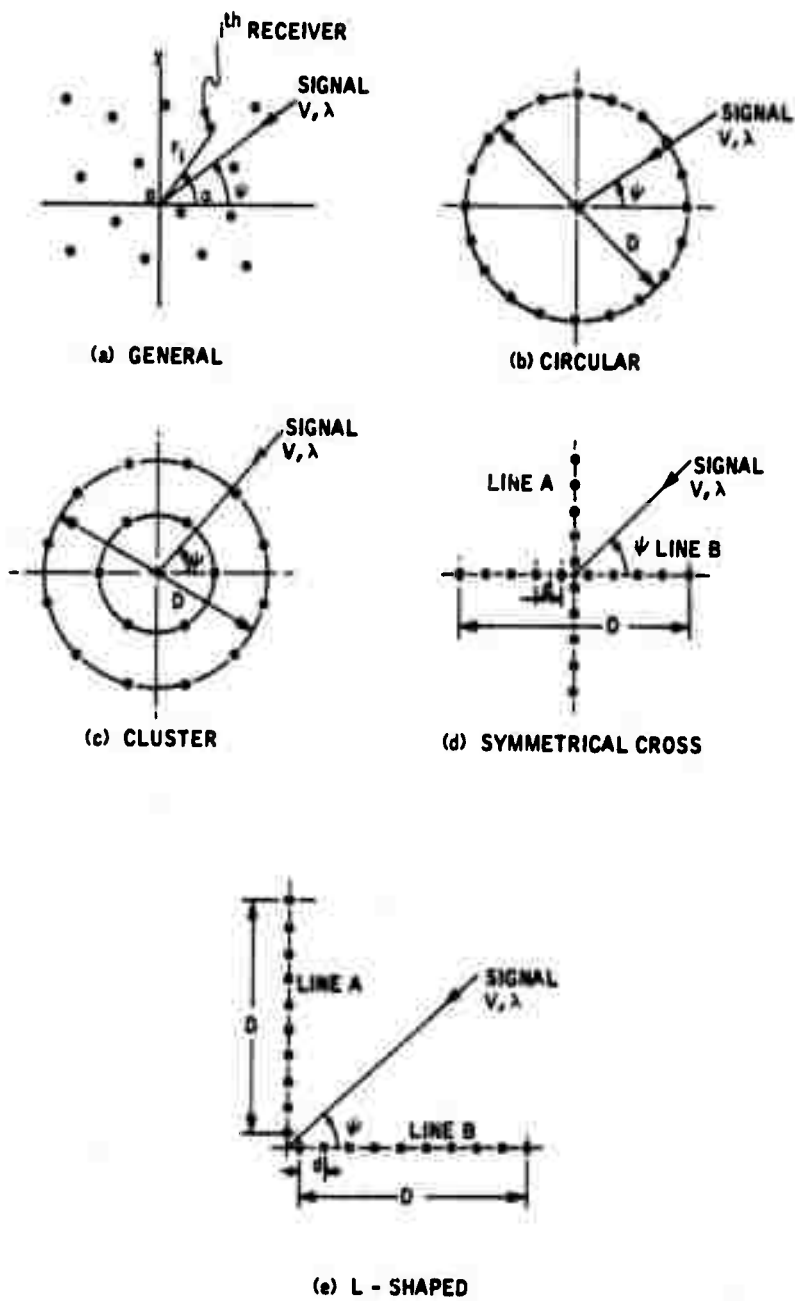
(e) L - SHAPED

Figure 2-10. Two-Dimensional Array Configurations
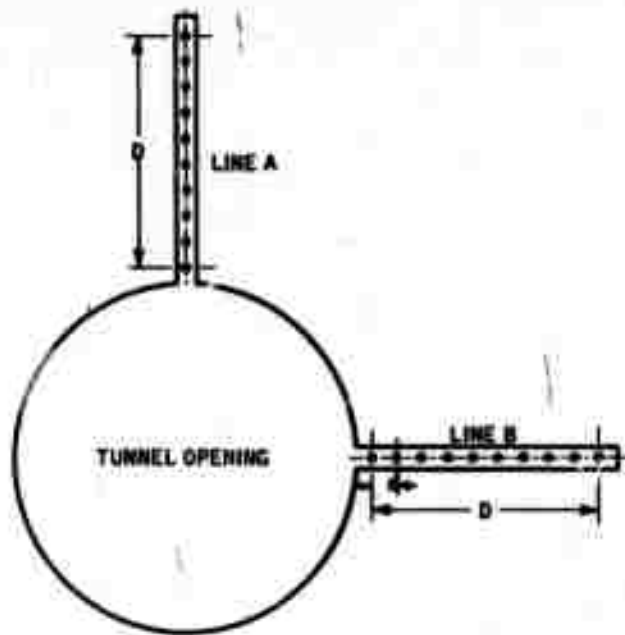
Figure 2-11. L-Shaped Array in Boreholes

2.3 USE OF BOREHOLES

2.3.1 Advantages

Several advantages from placing the receiver array in boreholes appear to be:

- Elimination of surface-wave interference
- Improved transducer-rock coupling
- Minimization of interference with tunneling operation

The reduction or elimination of surface-wave interference is based on the premise that surface-wave energy is substantially reduced at depths of one or two wavelengths and also from the fact that energy cannot propagate un-attenuated along the surface of a small hole. Consequently, signals received at depths of greater   than about 2 feet should consist principally of body waves. A further analysis is presented in Section 2.3.2.

Two problems in coupling a transducer such as an accelerometer to a rock surface are the roughness of the rock and the method of mounting. Techniques which have been used, such as grinding to provide a flat surface, and grouting or cementing the transducer to the tunnel face seem incompatible with a rapid excavation system. Furthermore, if the surface is not planar across the array, the out-of-planeness must be measured and corrected for in beamforming. Although tunnel-boring machines do produce a flat, though rough, surface, drill-and-blast methods do not. Normally, too, the drill-and-blast method fractures the rock to a depth of a few feet which may seriously reduce the transmission of seismic energy.

A drilled hole has a relatively smooth wall which should provide good transducer coupling. Also, the transducer can be mechanically wedged against the side of the hole, eliminating the need for bonding or grouting.

In Section 2.2 it was estimated that each line of an L-shaped array need be only 6 to 9 feet in length for operation at 5 KHz, corresponding to a typical wavelength of 3 feet. Thus, two perpendicular 8- to 10-foot holes of small diameter (AX) would have to be drilled in the sides of the tunnel. As shown in Figure 2-5, these can be drilled some distance from the face of the tunnel so as not to interfere with the tunneling. The two perpendicular holes determine a plane, so that out-of-plane time corrections would not be required.

2.3.2 Results from the Theory of Waves in Boreholes

The problem of the propagation of elastic waves in an empty cylindrical borehole was solved by Biot (Ref. 3). He showed that the surface wave on the interior of the hole, unlike the analogous Rayleigh wave on a plane boundary, is dispersive. The phase velocity increases with wavelength from that of Rayleigh waves to that of shear waves. No waves are propagated along the hole beyond a certain wavelength at which cutoff occurs. For hole diameter D, the cutoff wavelength is listed in Table 2-2 for various values of Poisson's ratio. For values appropriate to hard rock, signals of wavelength greater than about 1.5 D will not propagate along the hole. For D = 2 in. and λ_c = 3 in., the corresponding frequency range for hard rocks is 60 to 80 KHz which is too high to be of concern.

No cutoff occurs if the hole is filled with fluid. In this case, long wavelengths can propagate via coupling between the fluid and the elastic wall of the rock, the source of the well-known "water hammer" phenomenon. Consequently, dry holes are preferable.

The presence of the hole will have an insignificant effect on propagating body waves, so that a transducer in the hole will be sensing the true wave motion. This can be seen from curves of the division of energy between compressional

Table 2-2. Borehole Cutoff Wavelength

Poisson's Ratio, ν	Ratio of Cutoff to Diameter, λ_c/D
0	1.670
0.15	1.583
0.25	1.517
0.35	1.445
0.50	1.310

and converted shear waves for a compressional plane wave of wavelength λ incident on a hole of diameter D (Figure 2-12).
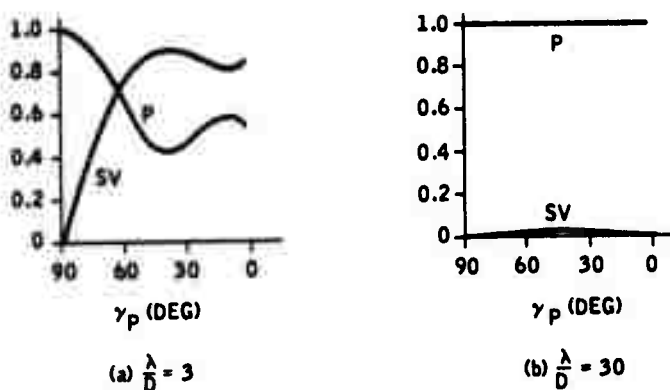
Figure 2-12. Effect of Hole on Propagating P-Wave

For the parameters used in Figure 2-12 (λ = 3 feet, D = 2 inches), $\lambda/D = 18$, which is closest to case (b), suggesting little effect of the presence of the hole on the incident P wave, regardless of angle of incidence γ_p (angle between borehole axis and P-wave direction of propagation).

2.4 SEISMIC SOURCES

The characteristics of the ideal seismic source include (1) short duration, (2) efficient radiation of compressional P waves, (3) uniform radiation pattern over a sufficiently wide solid angle, (4) sufficient radiated power for the required penetration, and (5) repeatable waveform.

The duration of the transmitted compressional waveform directly affects the capability of the reflection method to resolve two closely spaced reflectors. Seismic sources therefore are typically impulsive, explosives being commonly used. In recent years there has been a trend toward the use of nonexplosive sources such as electromechanical transducers and impact devices which are designed for efficient production of seismic energy in the frequency range of interest.

Because of absorption in rock of high frequencies and the need for prohibitively large arrays at long wavelengths, we are principally interested in frequencies near 5 KHz for the hard-rock excavation application. The most suitable receiver transducers in that frequency range are accelerometers. The particle acceleration in a plane stress wave is proportional to the time derivative of the stress pulse, since the particle velocity and stress have the same time dependence. The resulting acceleration for a triangular stress pulse, for example, is a one-cycle square wave as shown in Figure 2-13.
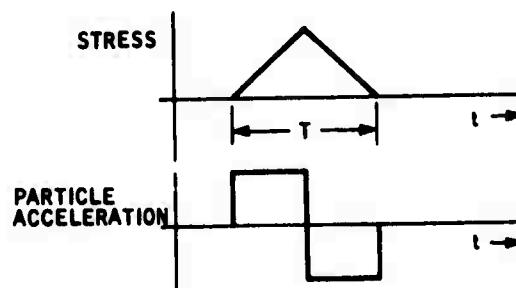
Figure 2-13. Particle Acceleration for Triangular Stress Pulse

2-28

The spectrum of the signal received for the example of Figure 2-13 has a maximum at $f_o = 1/T$. For $f_o = 5$ KHz, the corresponding stress pulse duration should be $T = 200$ μsec. For compressional wave velocities of 10,000 to 20,000 ft/sec, achieving this would provide a resolution of at least 3 feet and perhaps less.

In actuality, attenuation of high frequencies by absorption would result in a smoothing of the waveforms of Figure 2-13, which would result in the acceleration appearing more like a single cycle of a sinusoid of period T. If a simple stress pulse of one polarity cannot be achieved, then the resolution will be reduced. An example is found in the ringing of a piezoelectric transducer as described in Section III.

The possible locations for the seismic source are:

- On the rock surface
- Within a bore hole
  - Acting upon the bottom or end of the hole
  - Acting upon the cylindrical surface

It is of some interest to look at the radiation patterns for these source types and the relative efficiencies in generating compressional waves.

A surface source generates several modes of waves as indicated in Figure 2-14. The P waves are the only desired waves; the rest are potential interfering noise. In particular:

- The presence of the free surface produces surface waves plus a diffracted S wave
- The directionality of the source (force perpendicular to the surface) produces a radiation pattern which is not uniform

Miller and Pursey (Ref. 4) have calculated the displacement components for each wave type under the assumptions $R \gg a$ where R is distance and a is the radius of the source, and also for wavelengths $\lambda \gg a$. The corresponding radiation patterns for compressional and shear waves are shown in Figure 2-15 for the case of Poisson's ratio = 0.25, which is representative of hard rocks. Only the compressional wave is transmitted in the forward direction, which will be of principal concern in the underground excavation problem. Shear waves may predominate at larger angles, where they will be separable from P waves on the basis of direction of arrival or apparent velocity across the receiver array.

The radiation of surface waves is radially outward from the source.
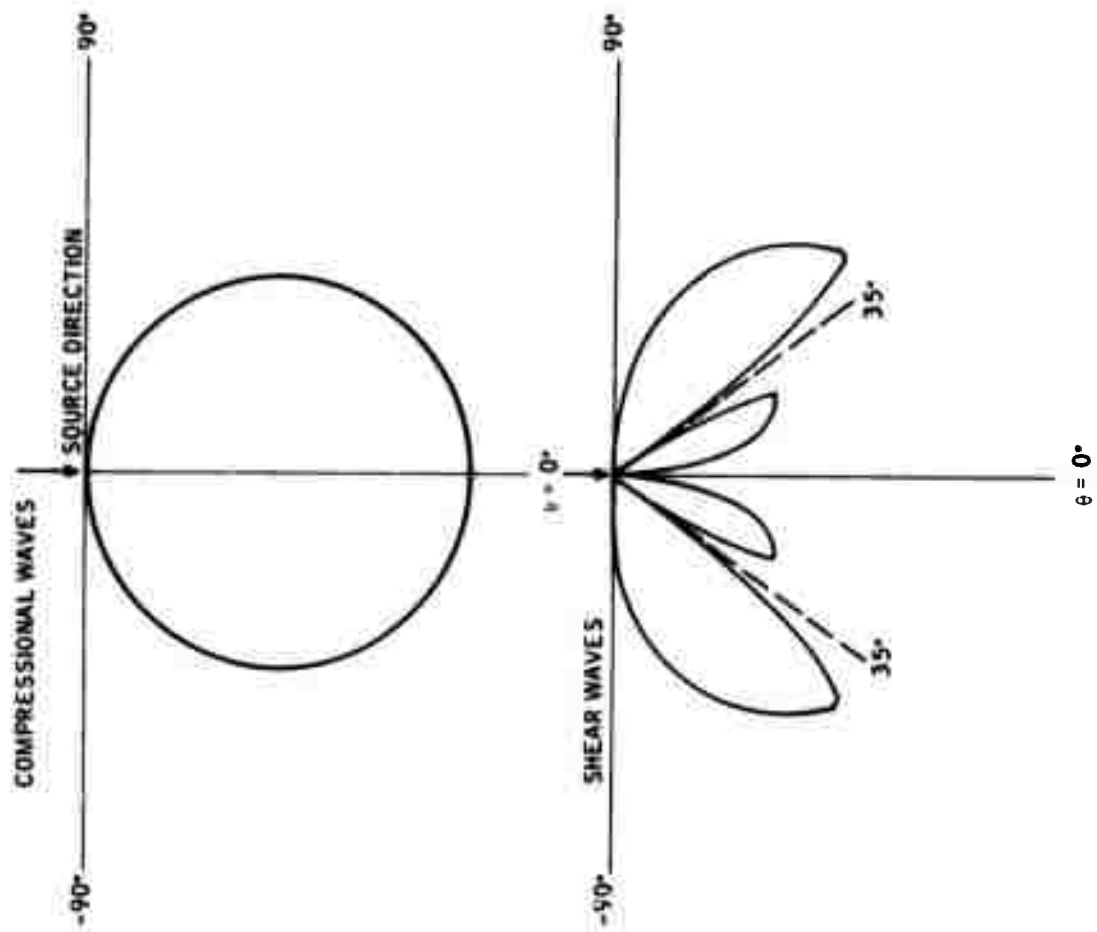
Figure 2-15. Radiation Pattern of Small Longitudinal Transducer
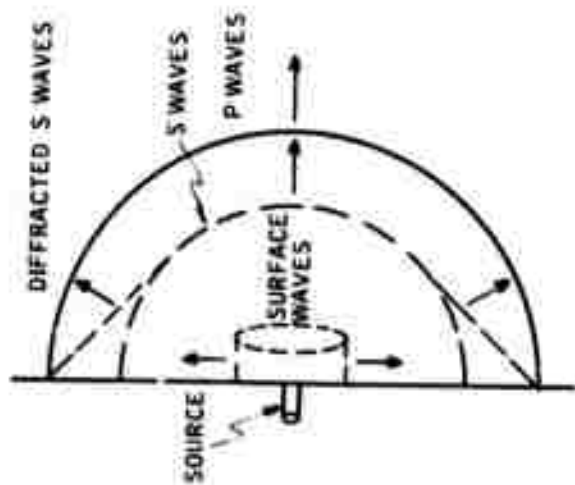
Figure 2-14. Seismic-Wave Modes Produced by a Force Transducer on a Rock Surface

The total power radiated by the source (Ref. 5) is

$$W = 4.836 \, W_o, \quad \text{with} \quad W_o = \frac{\pi f^2 F_s^2}{\rho v_p^3}$$

and the relative amounts of power radiated into individual waves are

Compressional	$W = 0.333 \, W_o,$	or 6.89%
Shear	$W = 1.246 \, W_o,$	or 25.77%
Surface	$W = 3.257 \, W_o,$	or 67.35%

A surface source is thus seen to be very inefficient in producing P waves, with less than 7% of the radiated power. Furthermore, the predominant surface waves attenuate less rapidly and are a source of interference for receivers which are also on the surface. The direct surface wave is not a serious problem because the initial part of the output of each receiver can be gated out until the direct surface wave has passed, with no significant loss of reflection data. However, reflection of surface waves from cracks and the sides of the tunnel can produce coherent interference throughout the time duration of interest.

A reasonable approach to reducing the surface-wave problem would be to put the source in a borehole. Since surface waves cannot propagate unattenuated along the hole (see Section 2.2), a source at sufficient depth should produce little or no surface wave energy. However, direct P and S waves and reflection from the tunnel free surface would then have to be provided for by array processing. A further argument for the source in a hole for drill-and-blast operations is the necessity to provide a consolidated rock medium for the source.

Calculations of the radiation patterns and energy partitioning have been made by Heelan (Ref. 6) for the use of a seismic source in a cylindrical cavity of radius a and length 2ℓ. The walls of the cavity are subjected to a uniform pressure P(t) of finite duration. Two types of waves are produced, a P wave and an SV wave, polarized along the direction of the cylinder axis.

The radiation patterns are shown in Figure 2-16. For a Poisson's ratio $\nu = 1/4$, approximately 60% of the power goes into SV and 40% into P. SV is beamed at angles of 45 degrees with respect to the borehole axis, and its maximum amplitude is about 1.6 times that of the P wave. The relative efficiency for generating P waves is much improved over a surface source, and the radiation pattern shows that the source could be used either with the borehole in the direction in which propagation is desired or perpendicular, with somewhat better efficiency in the perpendicular case (borehole in the side of the tunnel).
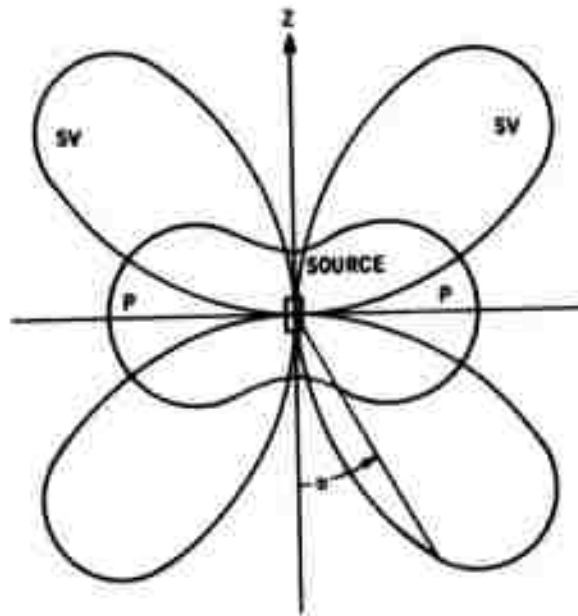
Figure 2-16. Variation of P and SV Amplitudes with ϕ when Source is Subjected to a Pressure

SECTION III
DESCRIPTION OF EXPERIMENTS

3.1 PURPOSE AND OBJECTIVES

The purpose of the experimental part of the excavation seismology program was to provide a realistic evaluation of seismic techniques before hardware development is undertaken. The use of seismic waveforms, recorded in a simple but representative geologic environment with breadboard models of transducer concepts, provided a more realistic evaluation of the performance of the various signal enhancement techniques than could otherwise be achieved.

The initial goals of the field program were to:

- Achieve repeatable seismic waveforms
- Accumulate a suite of waveforms for later analysis

Other goals, of lesser priority, were to:

- Compare methods of transducer coupling
- Identify noise problems and learn noise characteristics
- Evaluate various source waveforms
- Investigate methods of suppressing surface waves
- Develop optimum transducers
- Gain experience in hard-rock environment

3.2 TECHNICAL APPROACH

The approach used was to record a set of waveforms as might be received on an array of sensors using the basic instrumentation shown in Figure 3-1. A single transmitter and receiver were used which both eliminate the possibility of variations in transducer response and simplify the recording system. Either the transmitter or receiver was moved from one location to another to simulate an array of any size or configuration. This approach required the generation of a repetitive, stable seismic waveform which was easily achieved using a piezoelectric transmitter. The receiver was located either on the same surface as the transmitter for reflection measurements or on an opposing surface for transmission measurements.
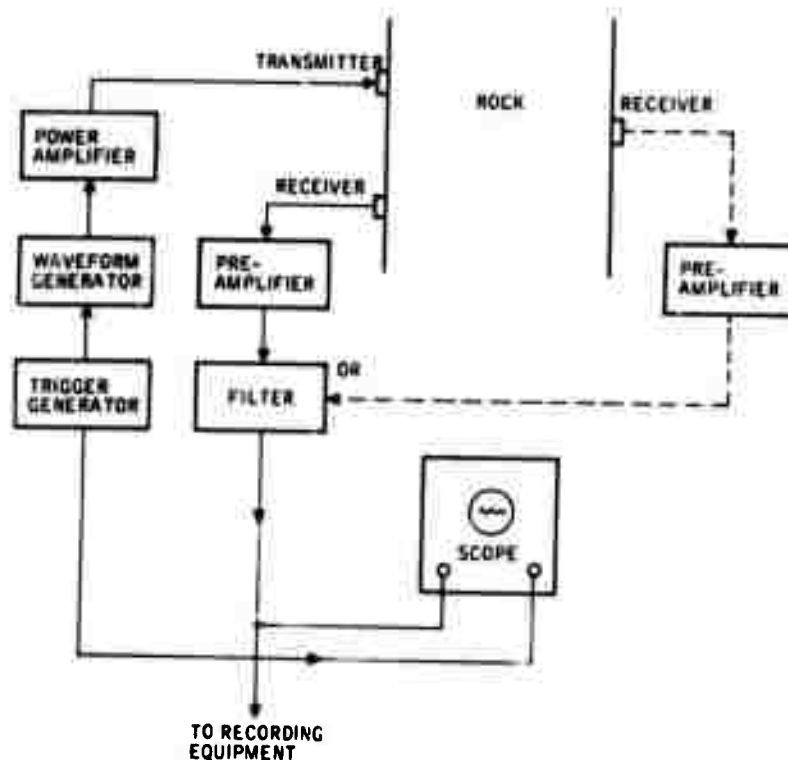
Figure 3-1. Basic Elements of Field Instrumentation

Rock surfaces were selected to provide a succession of geologic problems of increasing complexity. Thus, initial experiments involved large granite blocks with smooth surfaces which provided an ideal free-surface reflector and optimum conditions for transducer coupling. Successive recordings employed less ideal surfaces for both transducer mounting and as possible reflectors. These included rough, weathered, fractured surfaces and an intrusive dike. All of these field experiments were carried out on granite at quarries of the Cold Spring Granite Company near St. Cloud, Minnesota.

3.2.1 Transmission Measurements

For the transmission measurements, we selected a large volume of rock of uniform composition positioned so that the transmitter could be placed on one side and the receiver on the other. The thickness of the rock chosen (6 feet) was such that the direct compressional P wave could be observed on the receiver side with a minimum of interference from side reflections, shear waves and surface waves. The transmitted seismic waveform was then measured and changes observed as appropriate parameters were varied,

including receiver location, transducer coupling, source waveform and bandpass filter settings.

The receiver positions for the transmission measurements included a central one directly opposite the source transducer. Subsequent positions were along perpendicular straight lines through the "center" position at 3- to 6-inch intervals to a distance of about 4 feet.

3.2.2 Reflection Measurements

Reflections from a free surface were recorded at receiver positions on the same surface of the rock as the source transducer. As in the transmission measurements, the receiver positions were along perpendicular straight lines through the center (in this case, the source transducer) at 3-inch intervals. Seismic signals were recorded on perpendicular lines to simulate both line and crossed arrays, or "spreads."

In contrast to the transmission geometry, this experimental setup would not be expected to provide good measurements of the direct P wave along the surface because of the dominant surface wave and diminished amplitude of the P-wave radiation pattern of the transducer for θ = 90 degrees (Figure 2-15). However, the PP reflection at θ = 0 degrees should be optimized.

Experimental measurements of reflection from a free surface were chosen for the initial part of the study because:

- They provided the greatest possibility for early success in detecting, identifying and enhancing reflection waveforms.

- The free surface is possibly a good representation of rock fault or fracture.

Subsequently, recordings were made of possible reflections from less ideal reflectors such as observable fractures.

3.3 FIELD INSTRUMENTATION

A block diagram of the basic elements of the field instrumentation was presented in Figure 3-1. The seismic source repetitively transmits an acoustic signal into the rock volume. Timing and control circuits provide a trigger for the seismic source and establish the repetition rate. The timing and control circuits also provide synchronization and gating pulses to the display and recording elements. The received signal, after amplification and filtering, is displayed in real time on an oscilloscope and recording both on analog magnetic tape and chart recorders for subsequent analysis and processing.

3.3.1 Seismic Source

The seismic source consisted of a signal generator, amplifier and piezo-electric transducer. The signal generator consisted of two commercial pulse generators, Wavetek Model 134 VCG and Data Pulse Model 110A, whose outputs were summed to provide the double-pulse waveform required to minimize transducer ringing. Also, the Wavetek generator was used by itself to provide tone bursts, impulses, and other functions for comparative source-waveform investigations.

The waveform from the signal generator was amplified by a McIntosh 60-watt power amplifier which provides up to 200 volts across the transducer with an output impedance of 600 ohms. The frequency response was substantially flat up to 100 KHz.

The piezoelectric transducers used were fabricated by Honeywell for this program. These are longitudinal transducers, which provide a piston-like motion at the transducer-rock interface. Eight active elements are stacked as shown in Figure 3-2. The elements are electrically in parallel with a resulting static capacitance of 0.013 microfarad. The material used is Honeywell K-type, similar in properties to PZT-4, and it provides a K_{33} coupling coefficient for the stack of 0.65.

NOTE:
ARROWS INDICATE POLARIZATION (ELEMENTS IN STACK ARE ELECTRICALLY PARALLEL, MECHANICALLY IN SERIES). LENGTH = 2.5 INCHES, DIAMETER = 1.4 INCHES, CENTER MOUNTING HOLE DIAMETER = 0.4 INCH.
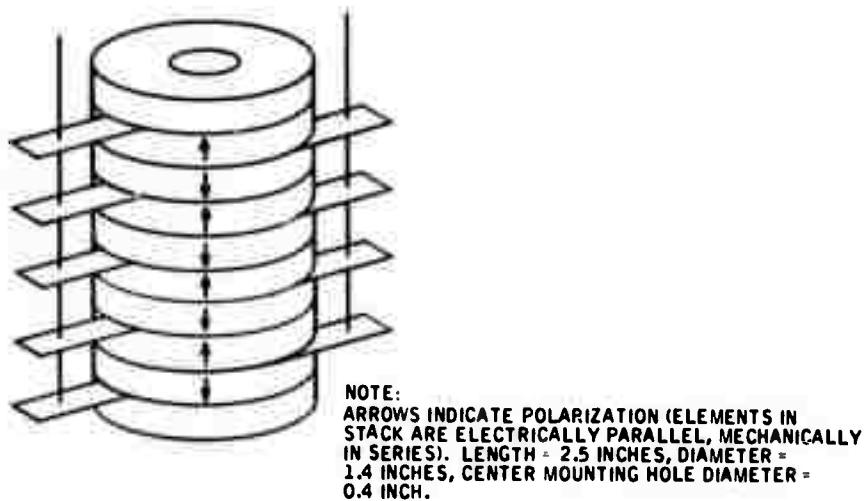
Figure 3-2. Piezoelectric Transducer Used for Field Experiments

Several other transducers with fewer active elements were constructed, all of them half-wavelength cylinders designed to be resonant at 20 KHz. The

piezoelectric K-type ceramic was used for the active piezoelectric elements, either with brass backing or directly air-backed. Aluminum, bonded to front surface of the ceramic, provided the coupling to the rock. A thin layer of petroleum jelly between the transducer and the rock excluded air in the interface and maximized power transfer.

A single hole was provided along the axis of the transducer to allow the transducer to be bolted to the rock. While this method of mounting appears to be satisfactory, it was found to be more convenient in the early stages of the field work to hold the transducer firmly pressed against the rock with a laboratory jack.

3.3.2 Receiver

The receiver included an Endevco Model 2225 accelerometer which has a high resonant frequency (80 KHz) for minimum distortion in the received waveform. The nominal sensitivity of the transducer is 0.65 mv/g. Transducer capacitance is 800 pF.

The accelerometer output was amplified by a battery-powered voltage pre-amplifier made by Radiation Electronics, Inc. (Model TA-5) which provided switch-selected voltage gains of 20, 40 and 60 db. The input resistance and capacitance of the connecting cable and amplifier were 370 K ohms and 38 pF, respectively. The amplified signal was filtered by a Krohn-Hite Model 3100 bandpass filter. The low-frequency cutoff was set at 100 Hz to reduce 60 Hz interference and the high frequency cutoff varied from 30 KHz to 60 KHz; the actual settings were not at all critical.

The accelerometer was mounted on the rock surface at each successive receiver position and the received waveforms recorded. Various methods of mounting were tried, including cementing with model plaster, petroleum jelly, and Permatex nonhardening gasket cement. The most suitable approach was simply to hold the transducer in position with a thin coupling layer of petroleum jelly.

3.3.3 Recording and Display

The received signal was displayed on an oscilloscope (HP Model 180A) with the sweep triggered externally by the same initiating pulse used to trigger the source signal generator. The received signal was also sampled. The sample-and-hold circuit was triggered by a pulse from the timing and control circuitry. The sampling trigger pulse was delayed with respect to the pulse which triggers the seismic source. Each time the source was triggered, the sampling pulse time delay was incremented, thereby slowly sweeping the sample time through the received seismic waveform. The delay was initially set to zero manually by a pushbutton switch.

The output of the sample-and-hold circuit was identical to the seismic waveform displayed on the oscilloscope, but with a greatly expanded time base. The longer time base permitted the permanent recording of the waveform on a Honeywell Model 550 X-Y recorder and on an FM channel of the Ampex FR-1300 magnetic tape recorder for later analysis and array processing experiments. Also recorded on magnetic tape were a pulse from the pushbutton initiating the slow sweep and a time-coded reference which was used for indexing and later identification of the recorded signal. The recorded initiating pulse provided a means of reestablishing precise time and synchronization relations for such subsequent processing as analog-to-digital conversion.

A two-channel Brush Model 220 strip chart recorder was used to monitor the tape-recorded signals as they were recorded. The time-coded reference was recorded on the strip chart, using the event marker pen. Any recorded waveform could then be relocated on the magnetic tape using the common time code. Descriptive annotations such as receiver location were written directly on the strip chart, and other pertinent information was recorded in a log book.

3.3.4 Timing and Control

The timing and control equipment included an Eldorado Model 1710 time code generator, two Beckmann Model 6014 preset accumulators, and pushbutton switch. The time code generator provided a precise 1-MHz oscillator signal as well as the time-coded signals for use as described above. The Beckmann accumulators counted the 1-MHz pulses to a preset value. When the preset value was reached, the counters automatically reset, provided an output pulse, and began counting again. Thus, if the number preset on one counter was N, the counter sent out a pulse every N microseconds. This pulse provided the trigger for the seismic source and the oscilloscope sweep. The second counter was set to N + n and sent out a pulse every N + n microseconds. This pulse was used to trigger the sample-and-hold circuit.

Typical values used were N = 50,000 and n = 2. Initially, the two counters were reset simultaneously with the manual pushbutton. After 50,000 μsec and every 50,000 μsec thereafter, that counter sent out a master trigger pulse, resulting in a source repetition rate of 20 per second. The second counter sent out pulses at 50,002 μsec, 100,004 μsec, etc., which consequently followed the master trigger pulse at intervals of 2 μsec, 4 μsec, etc. Thus, each sample occurred 2 μsec later on the received seismic waveform than the previous sample. Since one sample, representing an increment of 2 μsec of real time, was recorded every 50,000 μsec, the time base was expanded by a factor of 50,000/2, or 25,000. Frequencies were compressed by the same ratio, so that the nominally 20,000-Hz seismic signals became 0.8 Hz for recording purposes.

The pushbutton was used to simultaneously reset the two counters to zero and to initiate the internal sweep of the X-Y recorder.

Figure 3-3 is a block diagram of the system used for field recording, including seismic source, receiver, display and recording, and timing and control elements.

3.4 SEISMIC WAVEFORM EXPERIMENTS

3.4.1 Impulse Source

The first effort of the field work was to obtain the best possible waveform under the simplest conditions possible. A simple impulse would be the ideal transmitted waveform. Consequently, a voltage impulse was initially used as the source waveform. The source and receiving transducers were aligned on opposite faces of a homogeneous granite mass. The received signal is shown in the top trace of Figure 3-4.

The earliest arrival is the direct compressional, or P-wave, pulse as modified by the transmitting and receiving transducers and the intervening rock medium. The received waveform resembles a narrowband damped sinusoid which grades into following arrivals. It is apparent from the frequency of the damped sinusoid ($\sim$20 KHz) that the distortion results from "ringing" of the source transducer at its fundamental resonant frequency. Efforts were made to reduce the ringing by improving the coupling between the transducer and the rock load, but no substantial improvement resulted.

The remainder of the traces in Figure 3-4 were recorded at 3-inch intervals along a straight line. The seismic source was kept fixed. The receiver accelerometer was moved to each successive position between records. The accelerometer was held in place while each record was made with a thin layer of petroleum jelly used for coupling to the rock. Comparisons of the P-wave arrivals on the records of Figure 3-4 demonstrate a high degree of coherence and repeatability of the seismic waveform despite its ringing character.

3.4.2 Source Waveform Optimization

Various other types of source waveforms, including step function and single-cycle sine waves, were investigated experimentally in an attempt to more nearly approach the ideal seismic impulse. The source waveform which best meets this requirement consists of a combination of two pulses as developed by Brown (Ref. 7) for seismic model investigations.
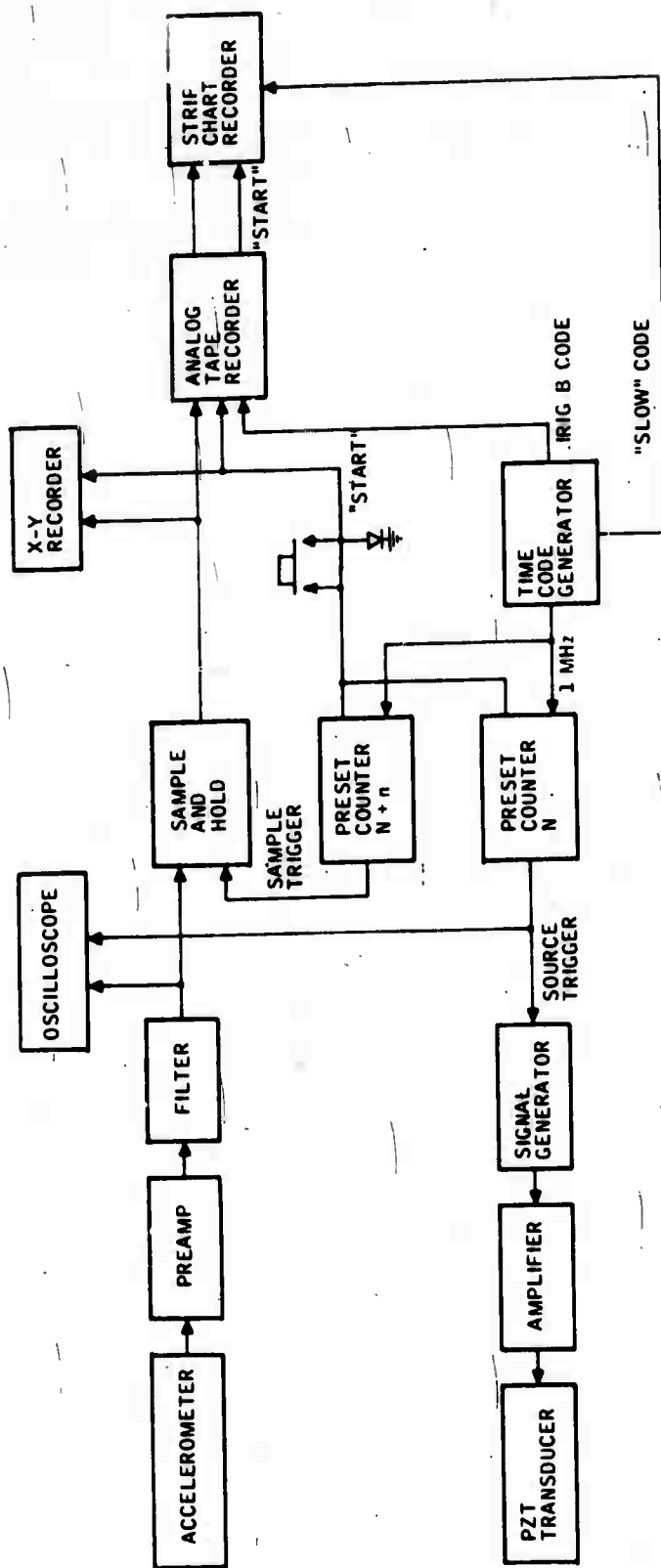
Figure 3-3. Field Recording System
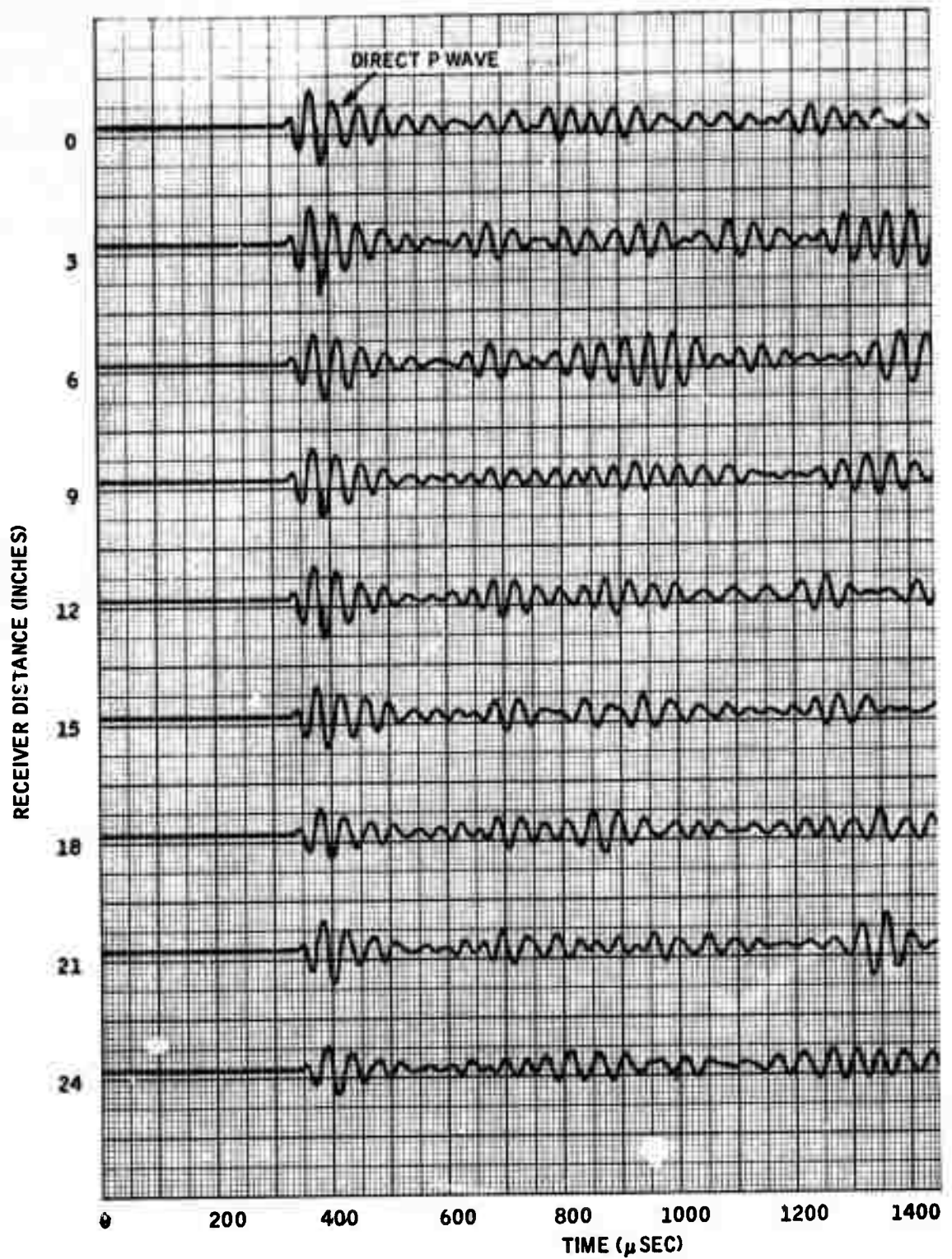
Figure 3-4. Seismic Transmission Through a 6-foot Granite Block Using an Impulse Source Waveform

In his dissertation, Brown derived the form of the electric field required to produce known simple transient stresses on the surface of a solid medium using a longitudinal piezoelectric transducer. The required excitation consists of the sum of two pulses, with different durations and amplitudes (Figure 3-5). The duration of the second pulse must be equal to the time it takes a signal to travel twice the length of the transducer. The fundamental resonance frequency of the transducer is determined physically by the same two-way propagation time, so that the required time T is the same as the period of the fundamental transducer resonance.

The amplitude required for the second pulse, relative to the first, depends in theory on the characteristic acoustic impedances of the transducer material and the rock. Since these were not known with the necessary degree of accuracy, it was necessary to experimentally adjust the amplitude of the second step to achieve the desired result.

In Figure 3-6, the two-level drive-pulse voltage is shown as it appears across the transducer. The small oscillations occurring after the first-level change are voltage fluctuations produced by the mechanical "ringing" of the transducer at its fundamental resonant frequency due to the piezo-electric effect. The following procedure was successfully used to optimize the parameters of the two-level drive pulse to reduce the ringing to a minimum and thereby produce a simple transmitted seismic pulse:

- The duration T of the second pulse was set equal to the period of the ringing as observed on an oscilloscope.

- The amplitude V_2 of the second pulse was adjusted to minimize the ringing as observed on the oscilloscope. The oscillations reverse in polarity at the minimum, so the adjustment is quite simple.

- The duration of the first pulse was set equal to or greater than the greatest time of interest on the received seismic signal.

The upper trace is the received seismic signal when the source function below was used to drive the transducer on a small granite block in the laboratory. The absence of ringing is apparent on the P wave. The large later arrivals consist primarily of surface waves.

3.4.3 Field Recordings Using a Two-Level Pulse

Seismic transmission and reflection profiles were recorded on a granite block using the two-level waveform as the source excitation voltage. The source transducer and receiver locations were the same as described previously for an impulse source voltage. The parameters of the drive voltage were optimized according to the procedure prescribed above and were not readjusted during the recording of the data.

PULSE GENERATOR 1

ADD

PULSE GENERATOR 2

(TRIGGERED FROM SAME SIGNAL)

(a)

(V$_2$ AND T CAN BE ADJUSTED TO PRODUCE SHORTEST IMPULSE RESPONSE)

(b)
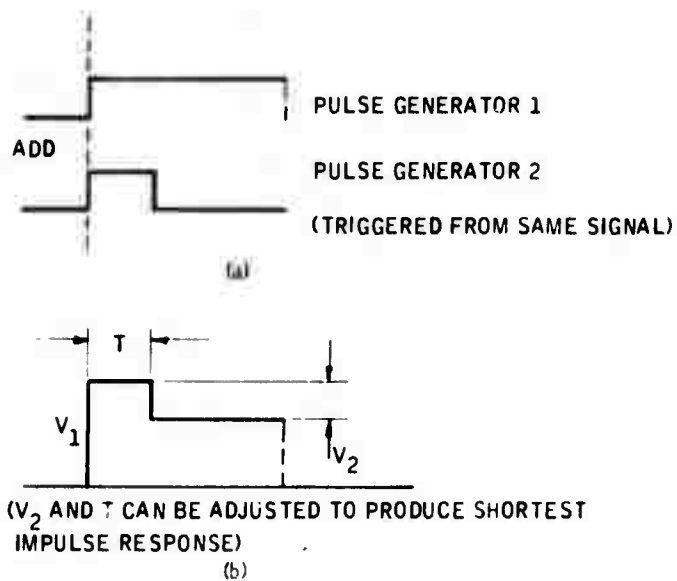
Figure 3-5. Two-Level Waveform Producing a Simple Seismic Pulse

TIME OF INITIAL STEP

SECONDARY PIEZOELECTRIC EFFECT (OSCILLATIONS)

SIMPLE P-WAVE

BOTH STEPS TURNED OFF

RECEIVED SIGNAL

INPUT WAVEFORM

TIME OF SECOND STEP

100 µS

TOP: .5V/CM
BOTTOM: 100 V/CM
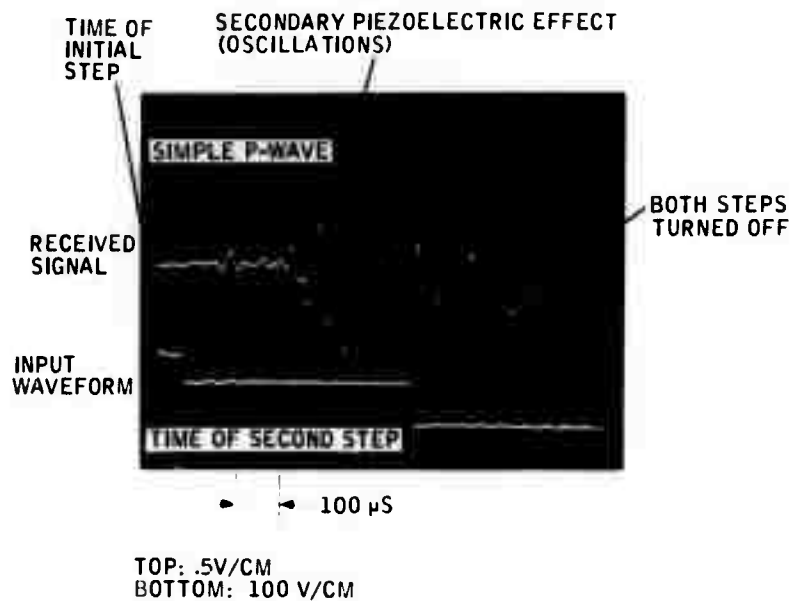
Figure 3-6. Effect of Two-Level Drive Pulse

3-11
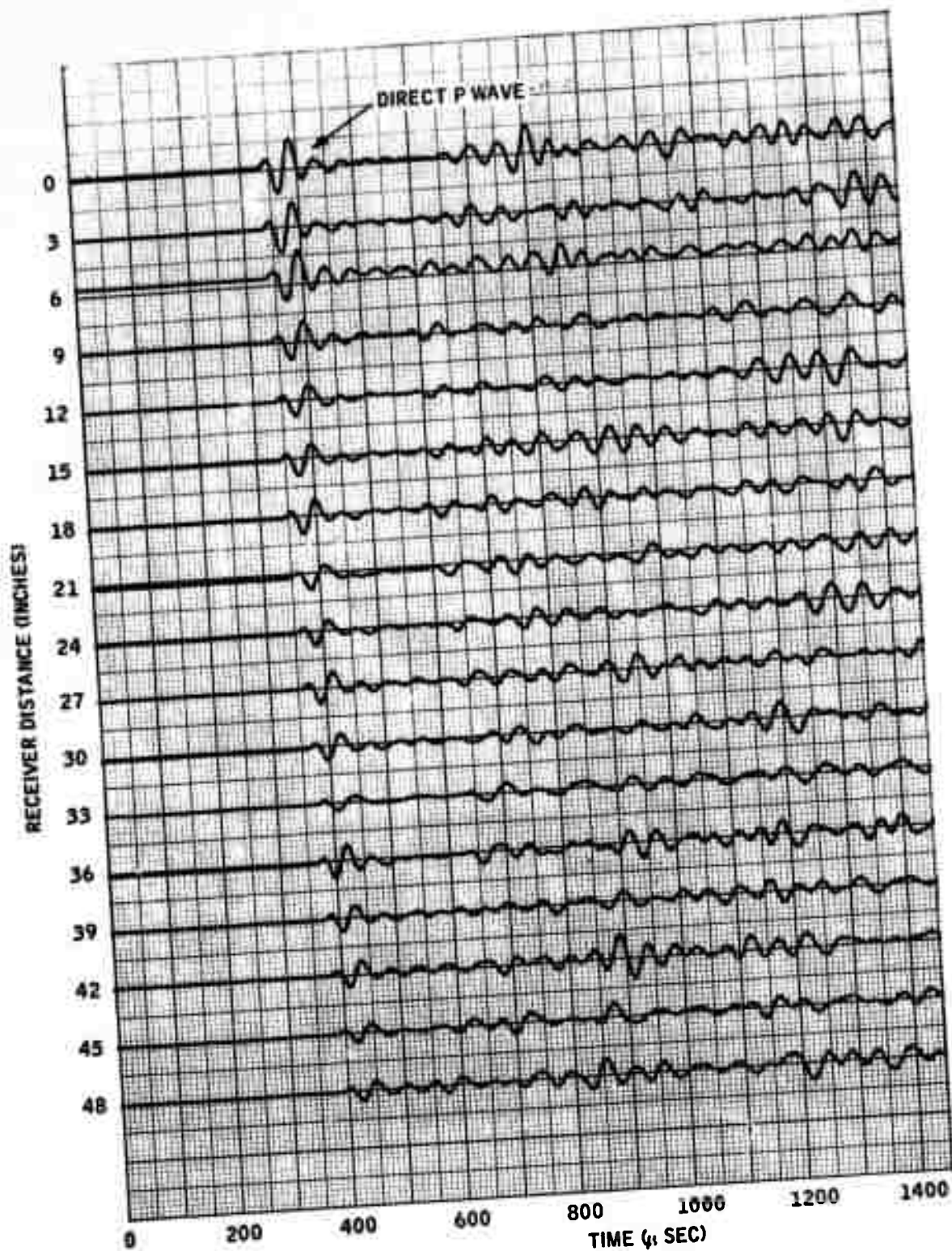
Figure 3-7. Seismic Transmission Through a 6-foot Granite Block Using a Two-Level Pulse Source Waveform

Figure 3-7 contains the seismic transmission measurements using the two-level source waveform, with the receiver locations the same as for the previous measurements for the impulse source function (Figure 3-4). Comparison of these two sets of data, particularly the first-arriving P wave, shows that the ringing has been significantly reduced with the two-level drive pulse, resulting in a more suitable waveform for seismic methods.

3.5 FREE-SURFACE REFLECTION DATA

Free-surface reflection data was recorded on the same granite block used in transmission measurements for seismic waveform optimization discussed in Section 3.4.2. The approximate block dimensions and array geometry are shown in Figure 3-8.
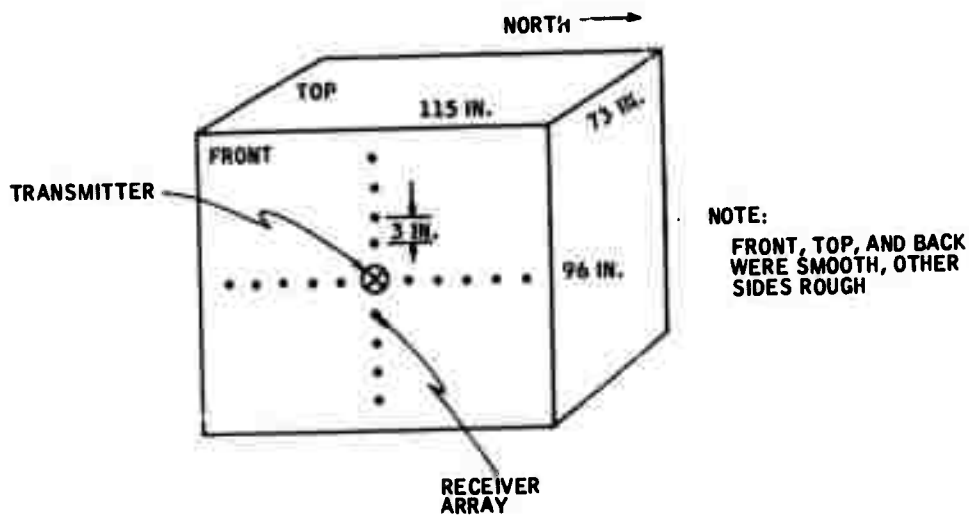
Figure 3-8. Free-Surface Reflection Geometry

Measurements were made using both an impulse excitation and the two-level optimized pulse. A representative set of records, taken at three-inch receiver intervals along a line to the north of the transmitter position, using the impulse source excitation, are shown in Figure 3-9. The predominant early arrival is the Rayleigh surface wave consisting of several cycles of ringing at the 20 KHz fundamental resonant frequency of the source transducer. The higher-frequency oscillation present at receiver locations near the source is probably due to another transducer mode resonance. This high-frequency oscillation is attenuated rapidly in propagation through the rock and has
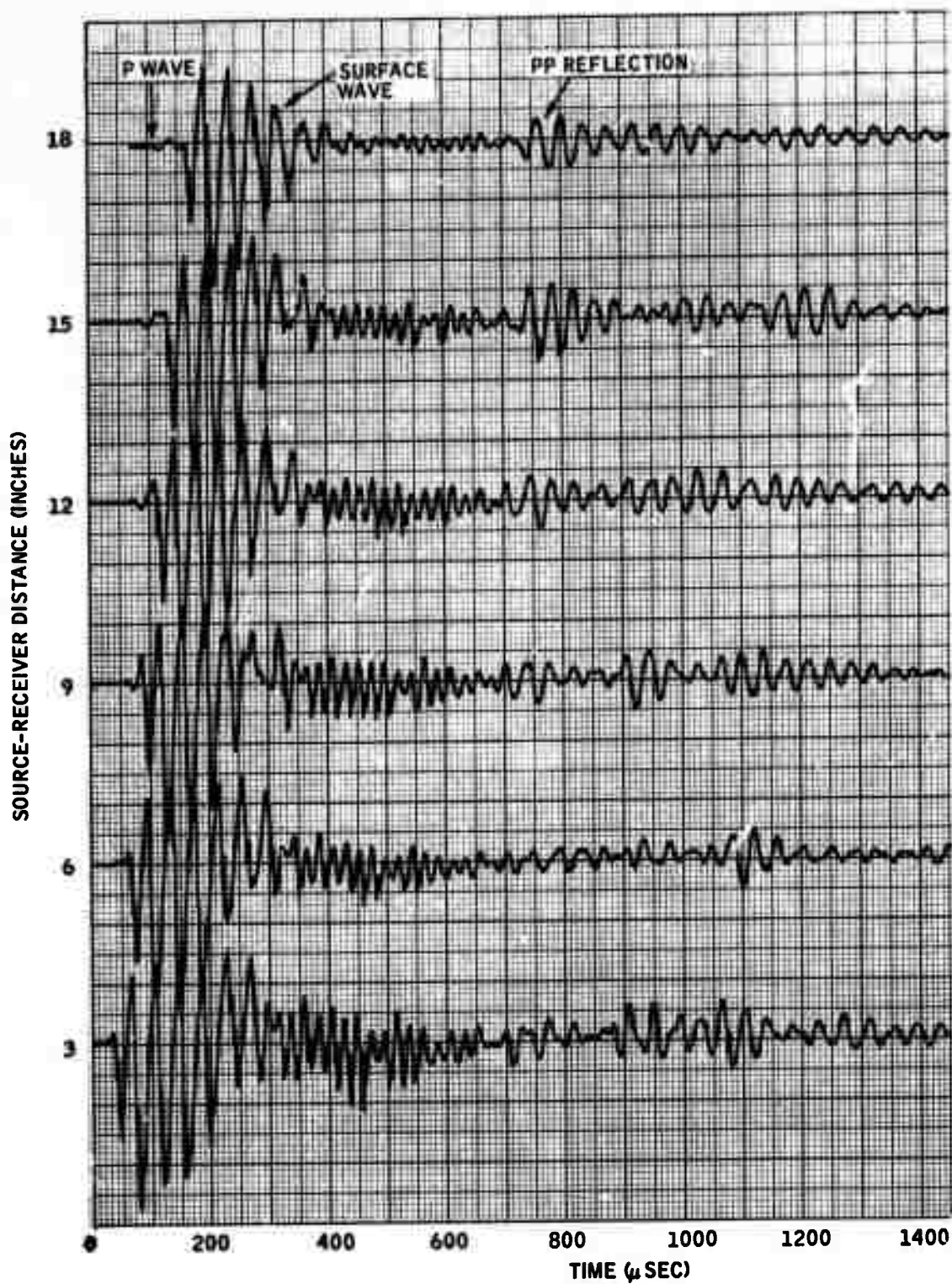
Figure 3-9(a). Reflection Seismogram Using Impulse Source
Waveform (receivers in-line with source to
18 inches)
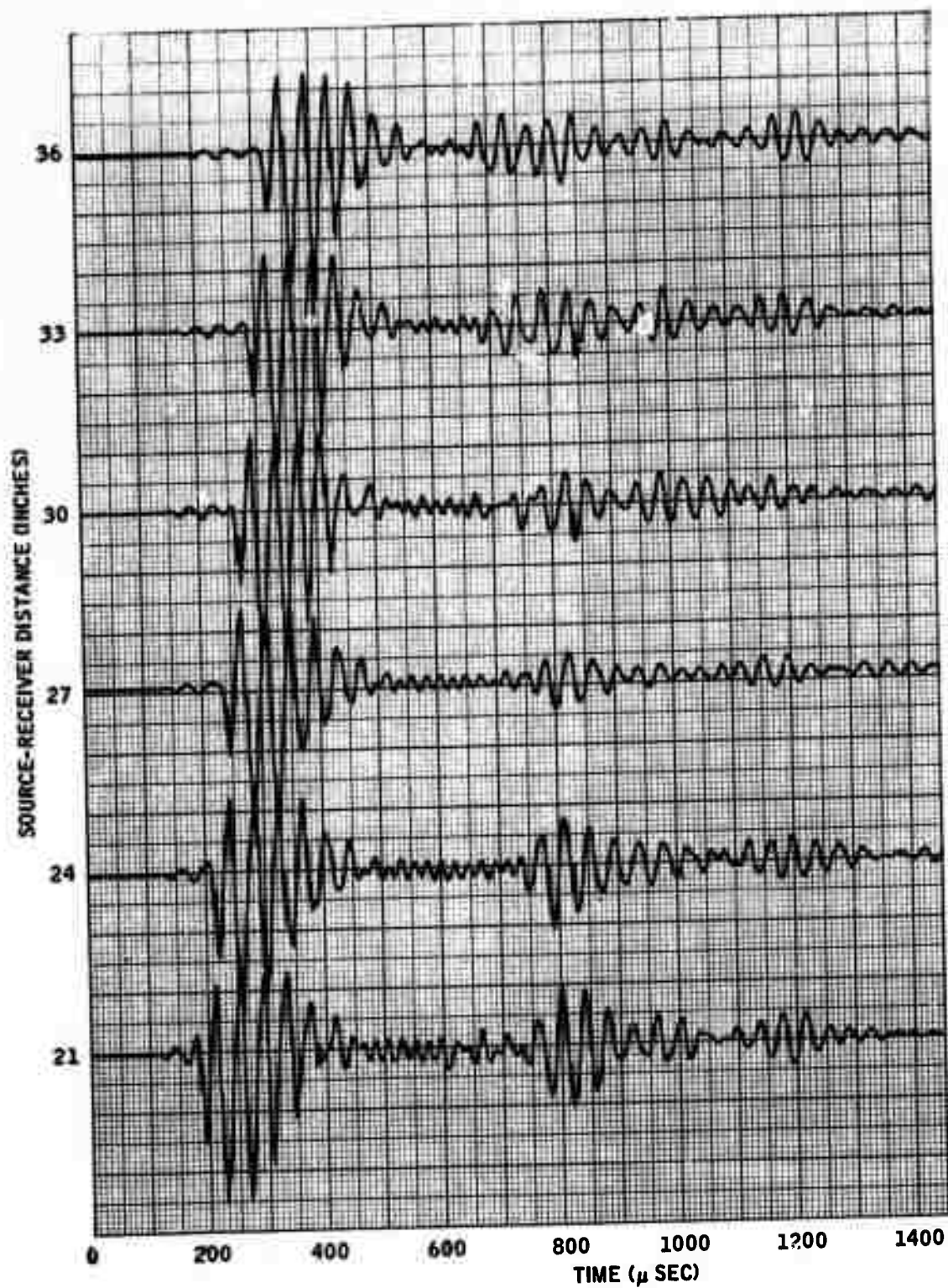
Figure 3-9(b). Reflection Seismogram Using Impulse Source
Waveform (receivers in-line with source
from 21 to 36 inches)

3-15
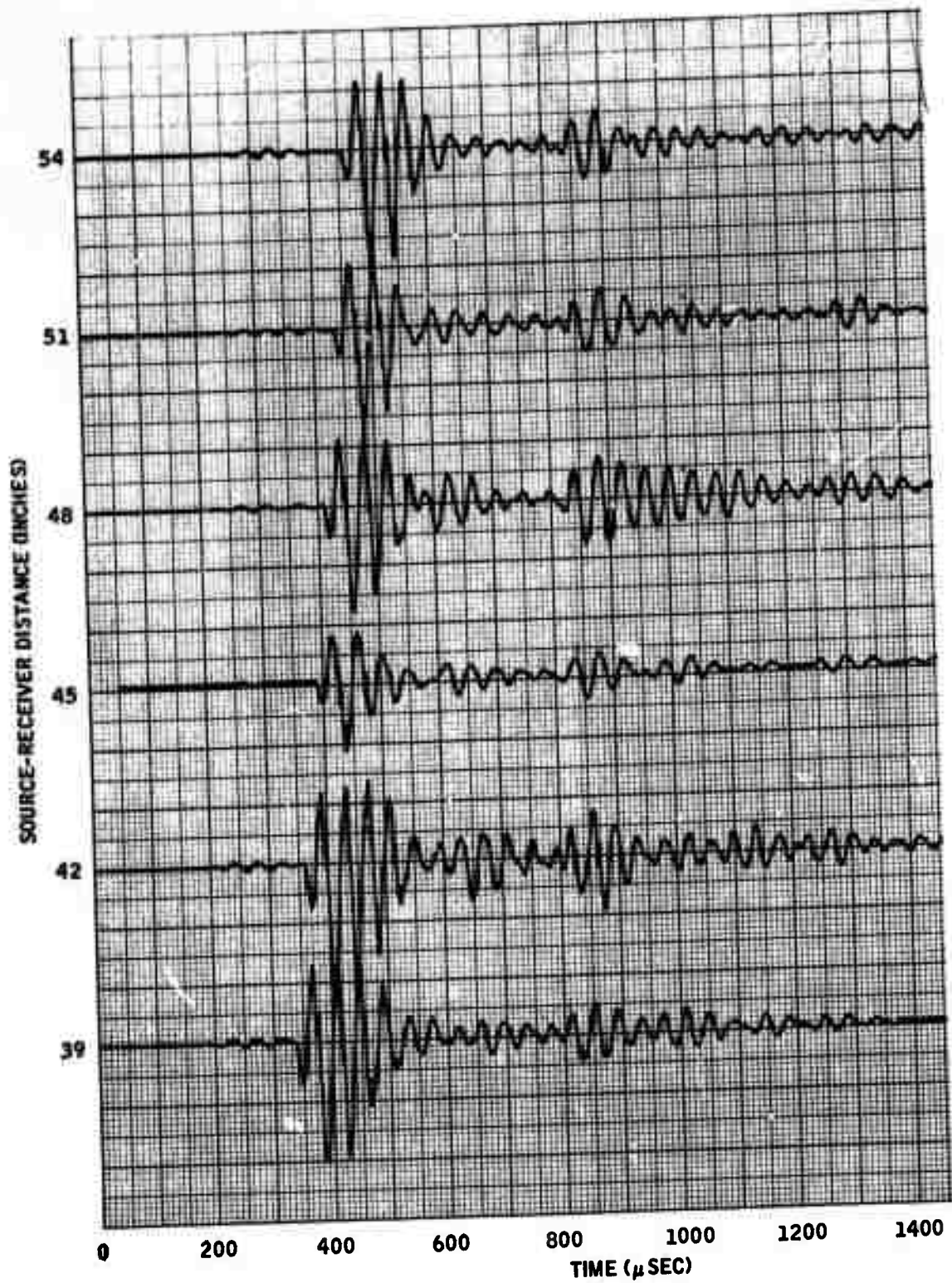
Figure 3-9(c). Reflection Seismogram Using Impulse Source Waveform(receivers in-line with source from 39 to 54 inches)

essentially disappeared at a transmitter-receiver separation of about 36 inches (it was also not in evidence on the transmission data, Figure 3-4, which traversed a path of more than 72 inches).

The reflected PP wave appears at about 750 microseconds. However, the narrowband ringing character of the wave detracts from the ability to distinguish it from other possible arrivals.

The corresponding set of data, using the two-level source pulse, appears in Figure 3-10. Comparison with Figure 3-9 illustrates the shortening of the surface-wave duration, the reduction of ringing effects, and the relative ease of distinguishing different wave arrivals. For example, the reflected surface wave from the edge of the rock, which interferes with the PP reflection at about 27 inches from the transmitter, can now be detected.

3.6 IN-SITU REFLECTION DATA

In addition to the free-surface reflection data described in Section 3.5, sets of data were recorded which represent more realistic geologic reflection problems. Two-level pulse excitation was used for these recordings. In this section, descriptions of three sites and representative examples of recorded data are presented.

3.6.1 Site A

Site A was located in an abandoned quarry of St. Cloud Gray ("charcoal") granodiorites. The transducers were emplaced on a weathered horizontal surface adjacent to the quarry pit. Figure 3-11 is a planview sketch, showing the receiver array layout and numerous vertical fractures and quartz veins. About 75 inches down from the edge of this surface, a horizontal fracture zone was exposed on the side of the pit (Figure 3-12). This fracture also was exposed on adjacent side of the pit, so it was considered likely that it extended beneath the receiver array, and would provide a seismic reflection.

Because of the rough and leached character of the weathered surface, we found it necessary to grind flat mounting pads for the transmitter and receiver positions. Again, petroleum jelly was used as a couplant between the transducer and the rock. Attempts to use the receivers on the porous surface without preparation by grinding resulted in significant variations in receiver sensitivy between adjacent locations.

Signals were recorded from receiver positions at three-inch intervals to 66 inches in a crossed-spread configuration. The data from two lines forming an L-shaped subarray appear in Figure 3-13.
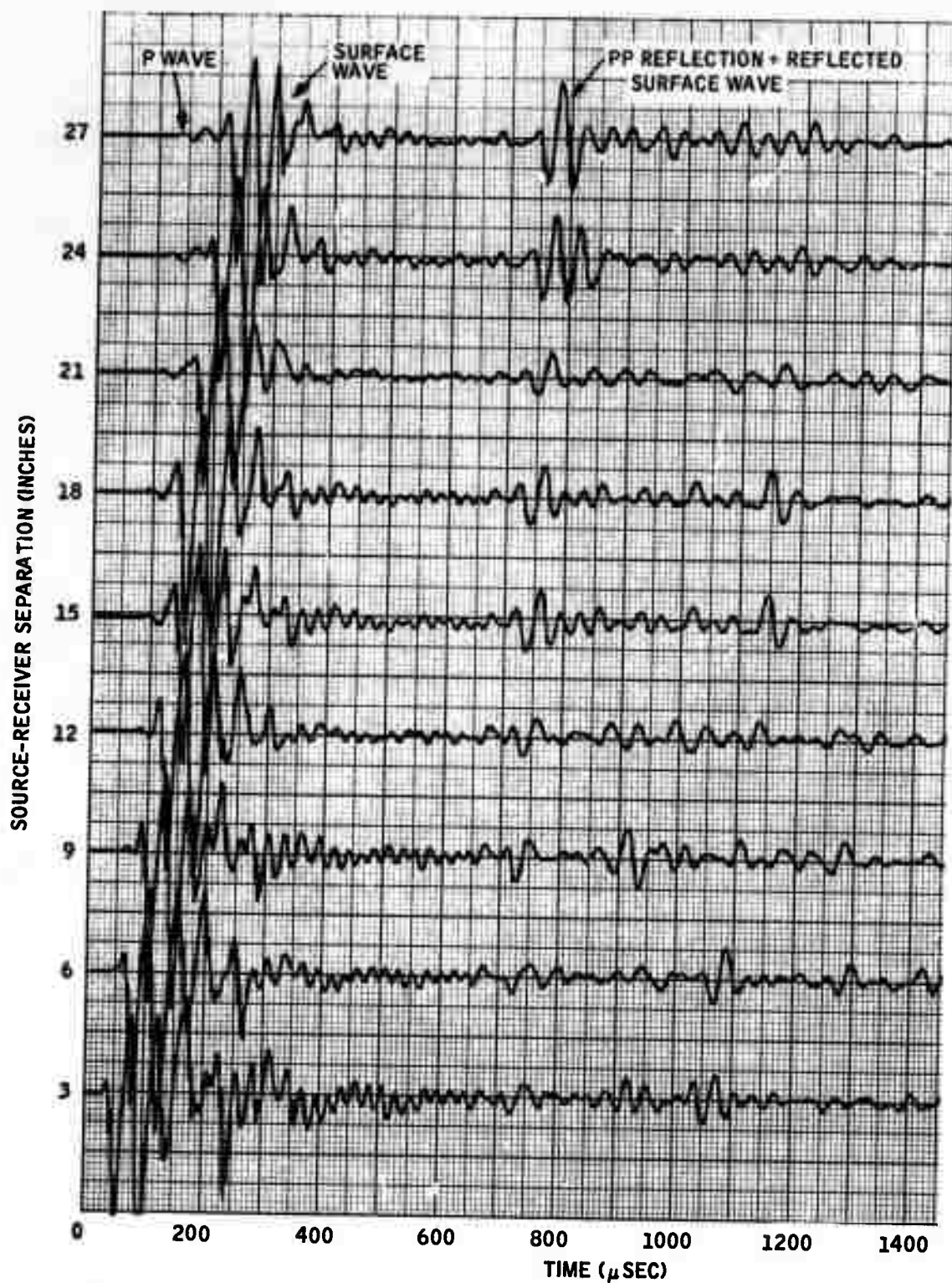
Figure 3-10(a). Reflection Seismogram Using Two-Level Pulse
Source Waveform, Producing a Simple Seismic
Signal (receiver in-line with source to 27 inches)

3-18
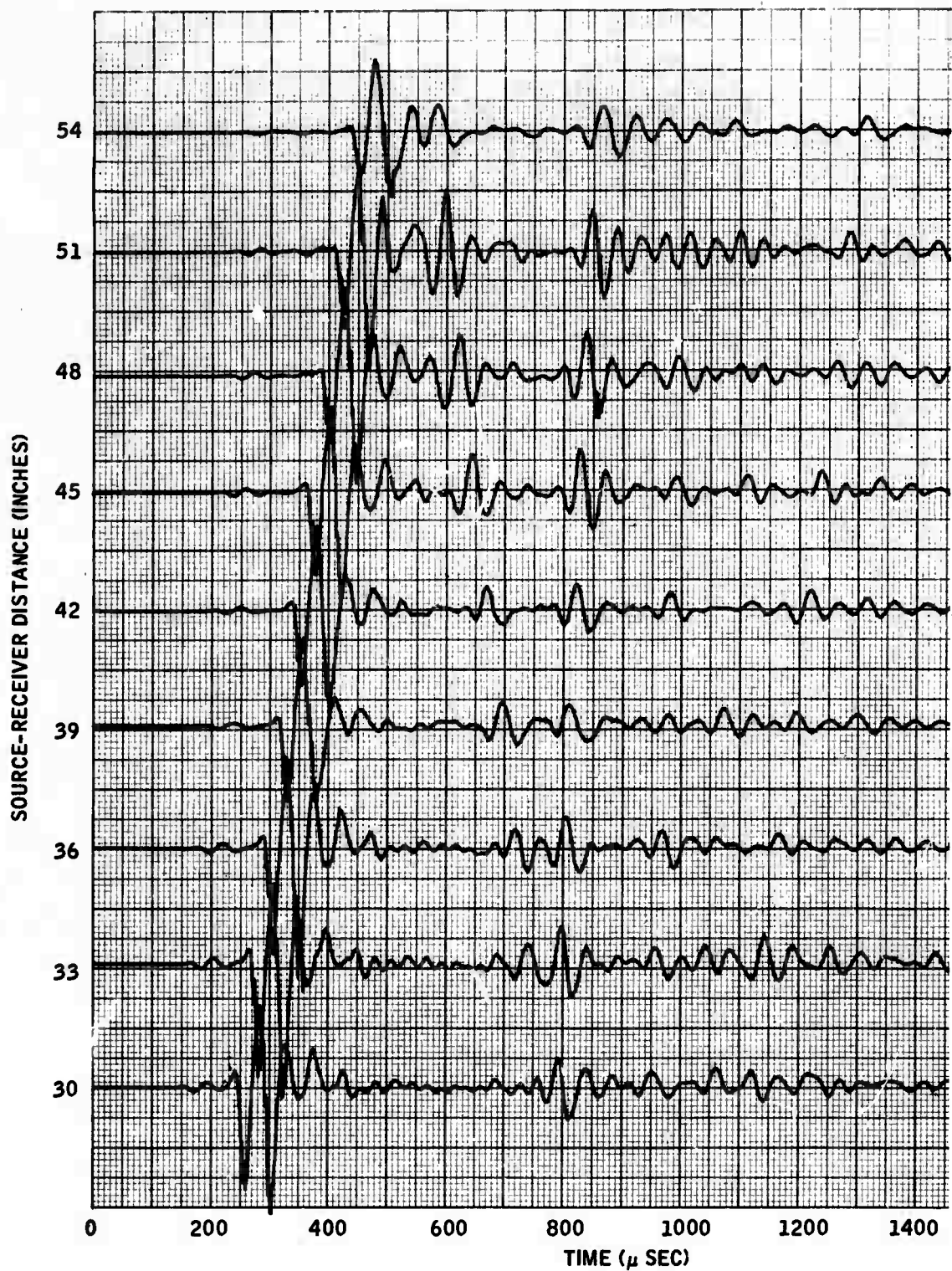
Figure 3-10(b). Reflection Seismogram Using Two-Level Pulse Source Waveform, Producing a Simple Seismic Signal (receiver in-line with source from 30 to 54 inches)

3-19
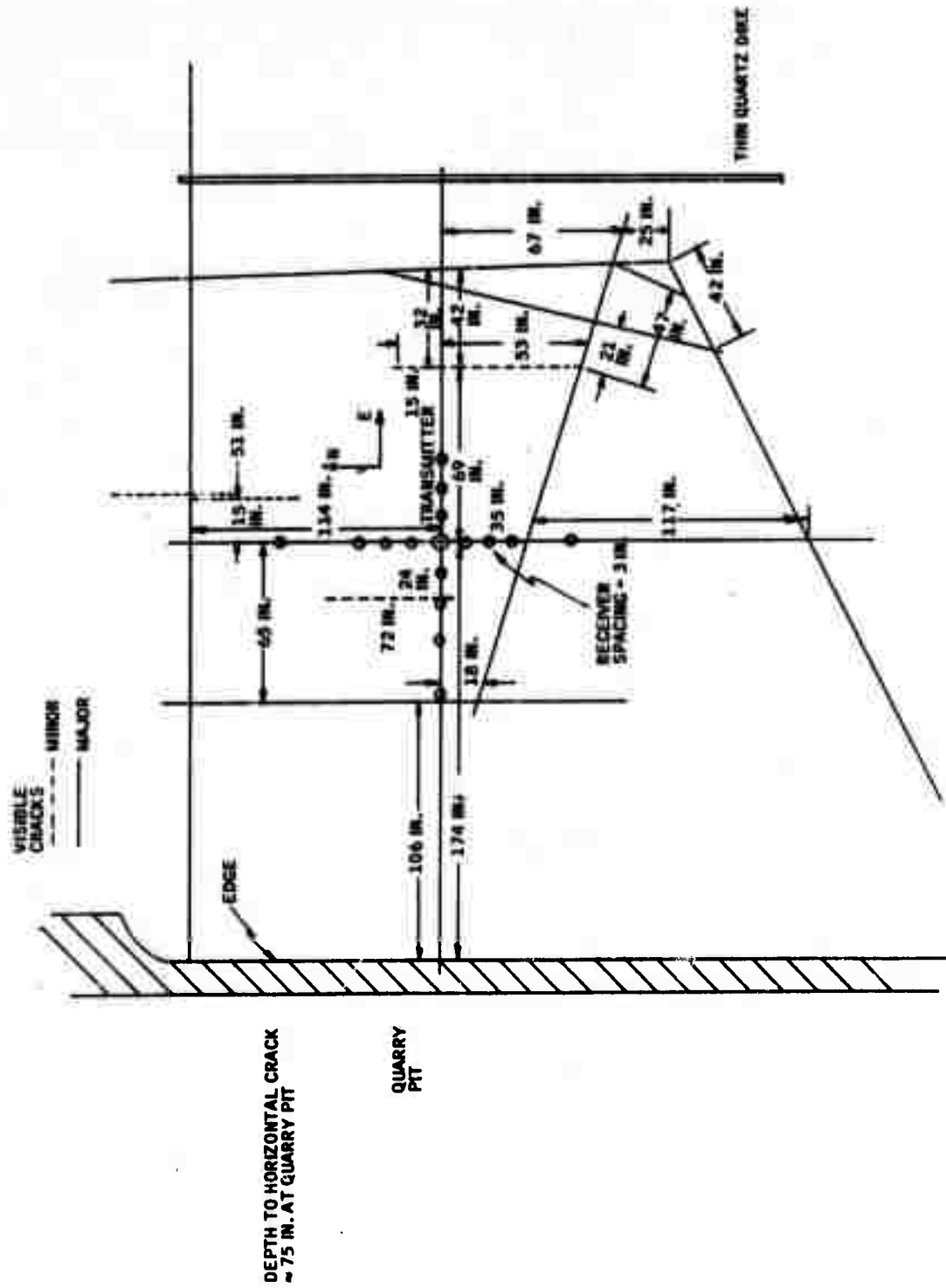
Figure 3-11. Plan View of Site A Test

Figure 3-12. Site A Fracture Zone
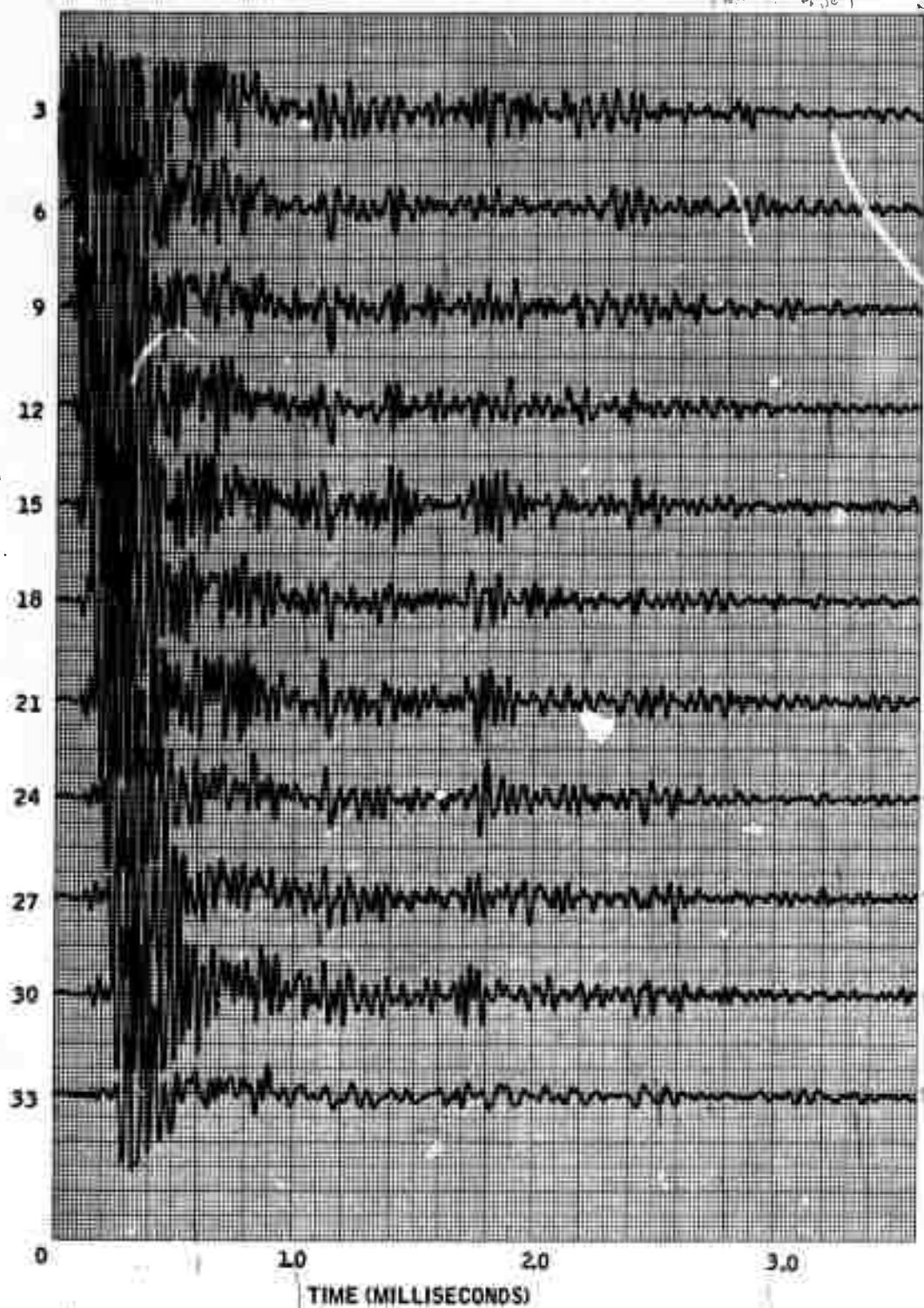
Figure 3-13(a). Site A Data (natural fracture) - North
(receiver in-line with source to 33 inches)

3-22
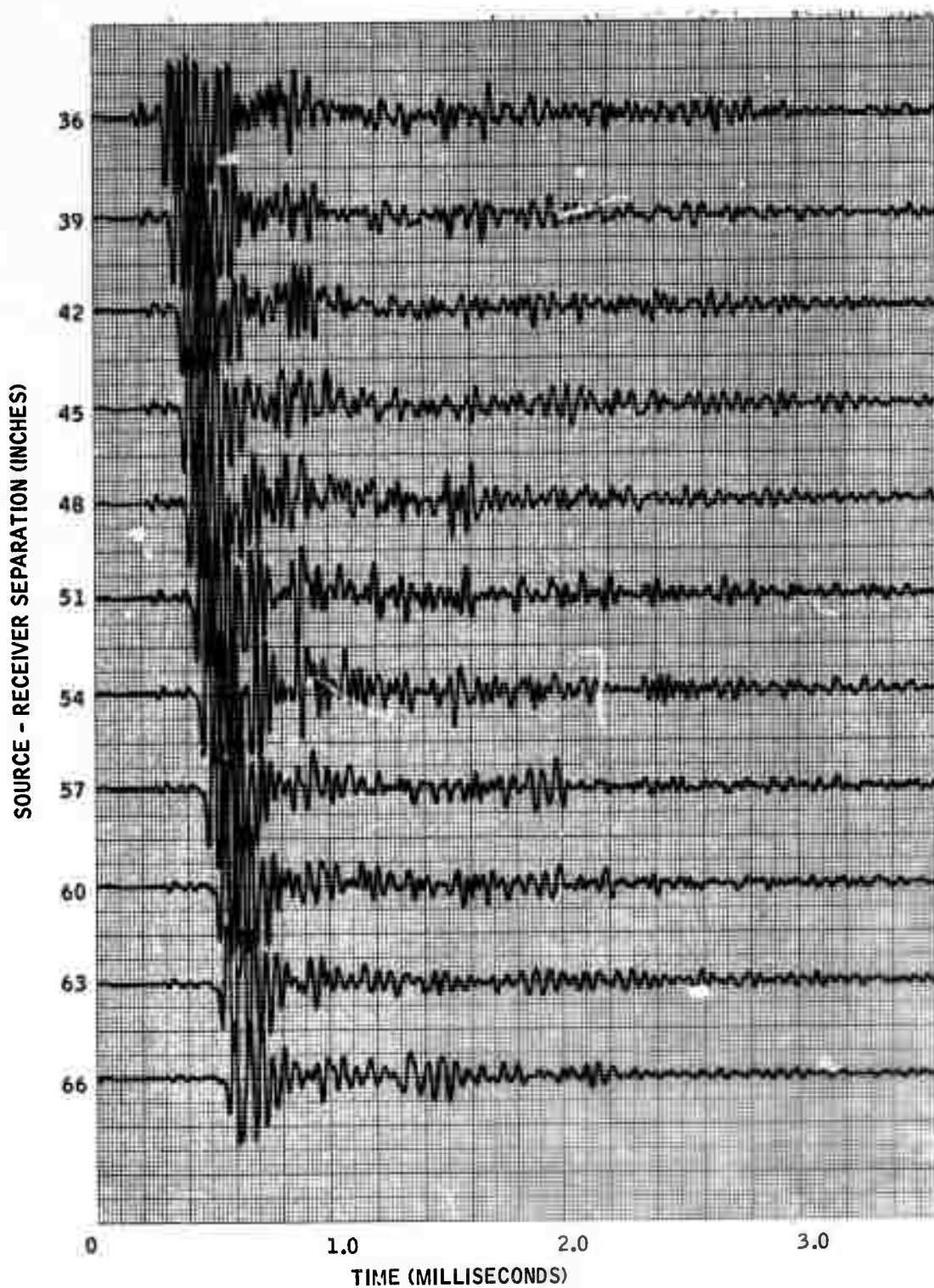
Figure 3-13(b). Site A Data (natural fracture) - North
(receiver in-line with source from
36 to 66 inches)

3-23
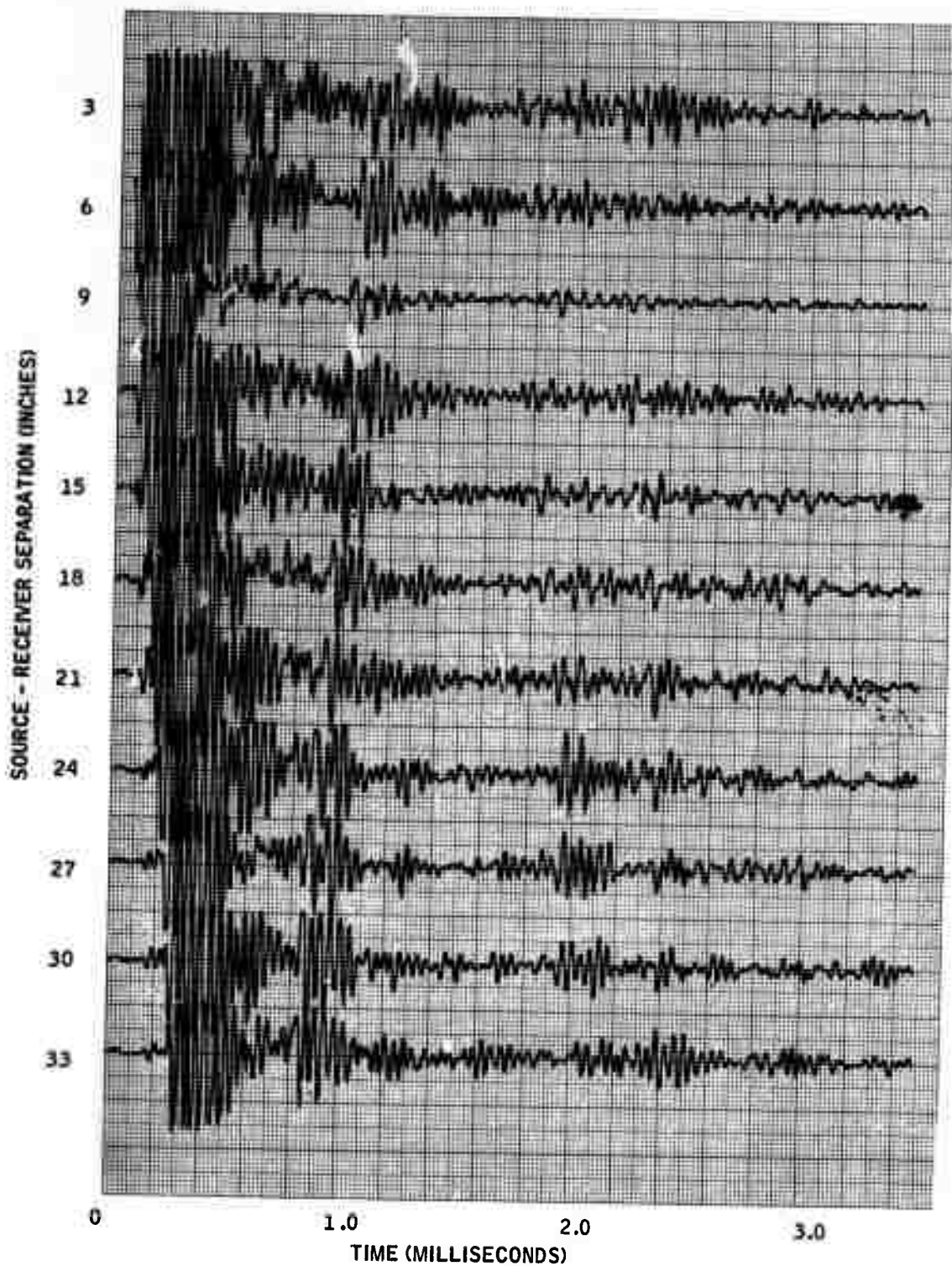
Figure 3-13(c).   Site A Data (natural fracture) - West
(receiver in-line with source to 33 inches)

3-24
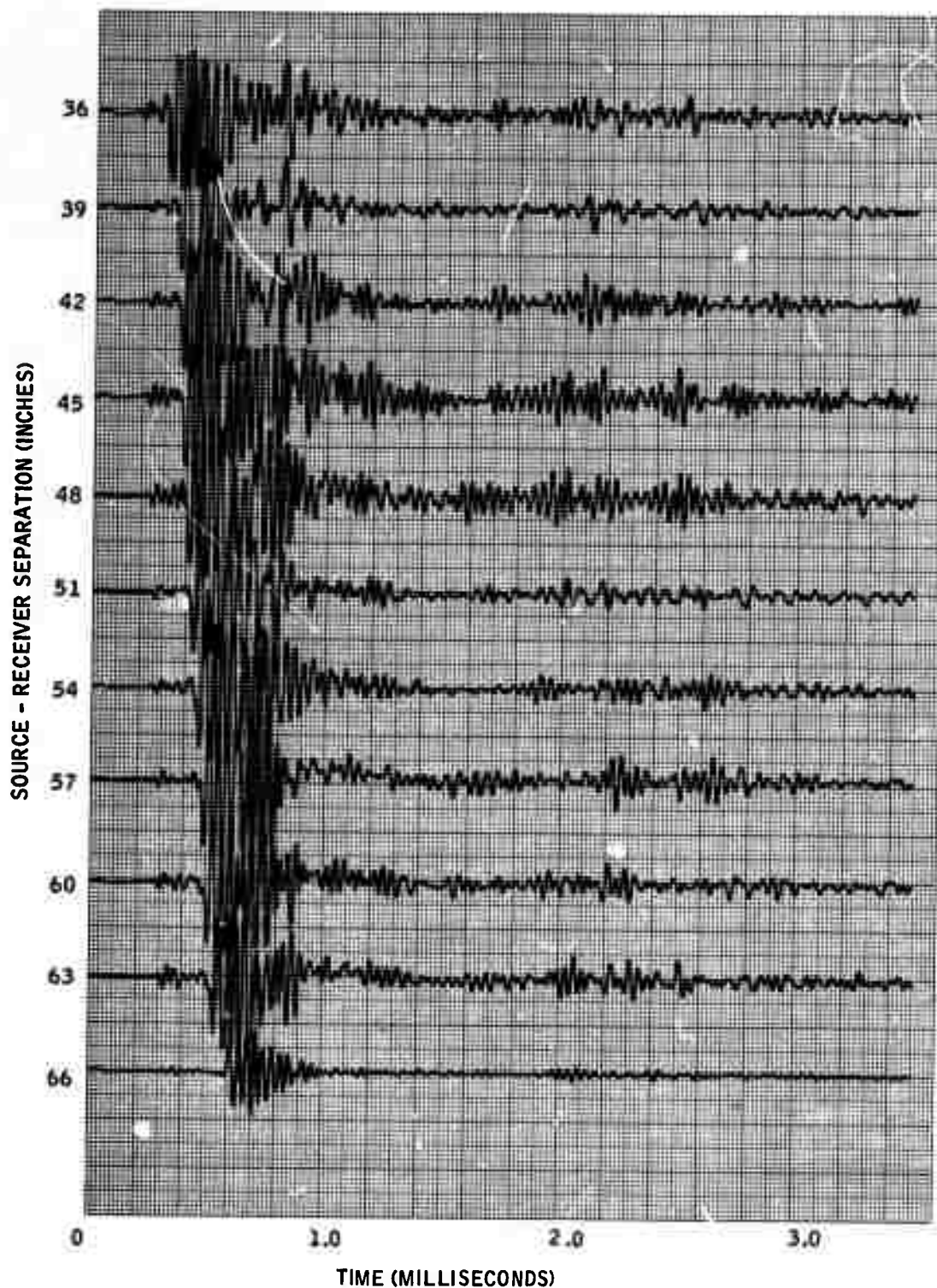
Figure 3-13(d).   Site A Data (natural fracture) - West
(receiver in-line with source from 36
to 66 inches)

3-25

Despite the use of the optimized two-level pulse excitation, the surface wave exhibits considerable oscillation, particularly at receiver positions near the transmitter. As the receiver is moved away from the transmitter, the waveform shortens somewhat, apparently because of attenuation of higher frequencies either by absorption or scattering by surface roughness and inhomogeneities. Later coherent events, which can be followed from trace to trace across the array and are probably reflected surface waves, also exhibit a simpler, lower-frequency waveform.

From the direct P wave, we estimate the P-wave velocity at this site to be about 18,300 ft/sec. The reflection expected from the fracture at a 75-inch depth should then appear at 680 μsec at a receiver near the transmitter to 740 μsec at the farthest receiver position. An examination of the data, however, does not show any obvious indication of a coherent arrival at that time.

3.6.2 Site B

Site B was located in another quarry in St. Cloud Gray grandiorite, which is currently being worked. As part of the quarry operation, a horizontal wire-saw cut was made 97 inches below the surface of a large ledge. The sawed surface represented a possible seismic reflector, although probably a very poor one because the opening would be closed by the weight of the rock above, and the smooth sawed surfaces would mate quite well and probably not appear as a discontinuity in acoustic properties to the incident wave.

The transducer array was located on the upper surface as shown in Figure 3-14. This surface was quite rough, and again some grinding preparation was required to mount the transducers. As in Site A, the transmitter was bolted to the rock with a bolt through the center of the transducer.

Because of the roughness of this surface, receivers were located only along the two legs of an L-shaped configuration as shown. Data was recorded in both directions to 57 inches. The data out to 33 inches is shown in Figure 3-15. The expected reflection time is about 950 μsec, but, if one is present, it is masked by reflected surface waves.

3.6.3 Site C

Site C was in a coarse-grained prophyritic granite which included a vertical basalt dike. The surface of the granite was very irregular but contained a smooth flat surface approximately parallel to the dike at a distance of about 62 inches which permitted the recording of a single line of receiver positions as shown in Figure 3-16. The purposes of this experiment were (1) to record signals in a different type of hard rock, and (2) to attempt to obtain reflections from the basalt-granite interface. The data is shown in
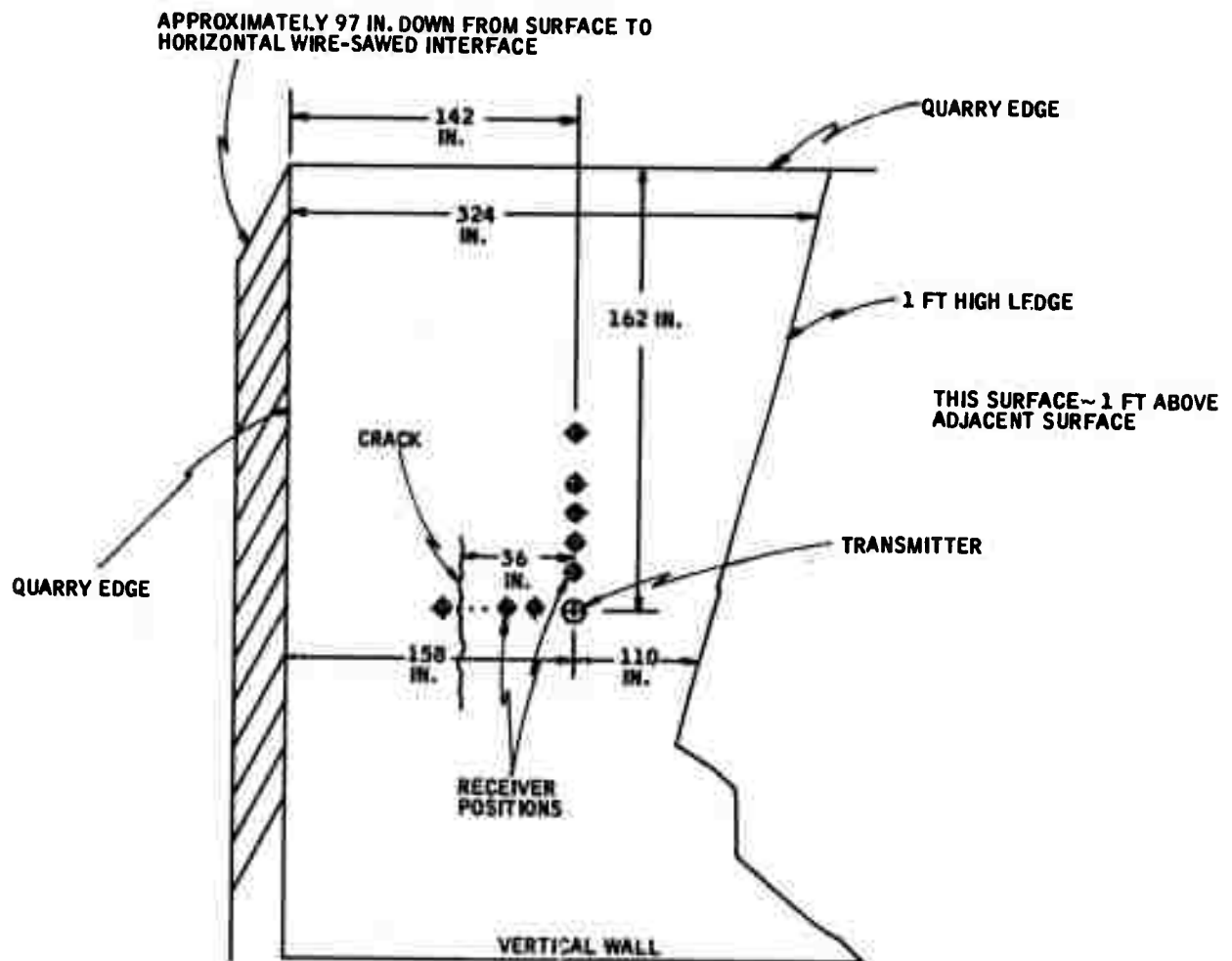
Figure 3-14. Plan View of Site B Test

TIME (MILLISECONDS)

SOURCE - RECEIVER SEPARATION (INCHES)
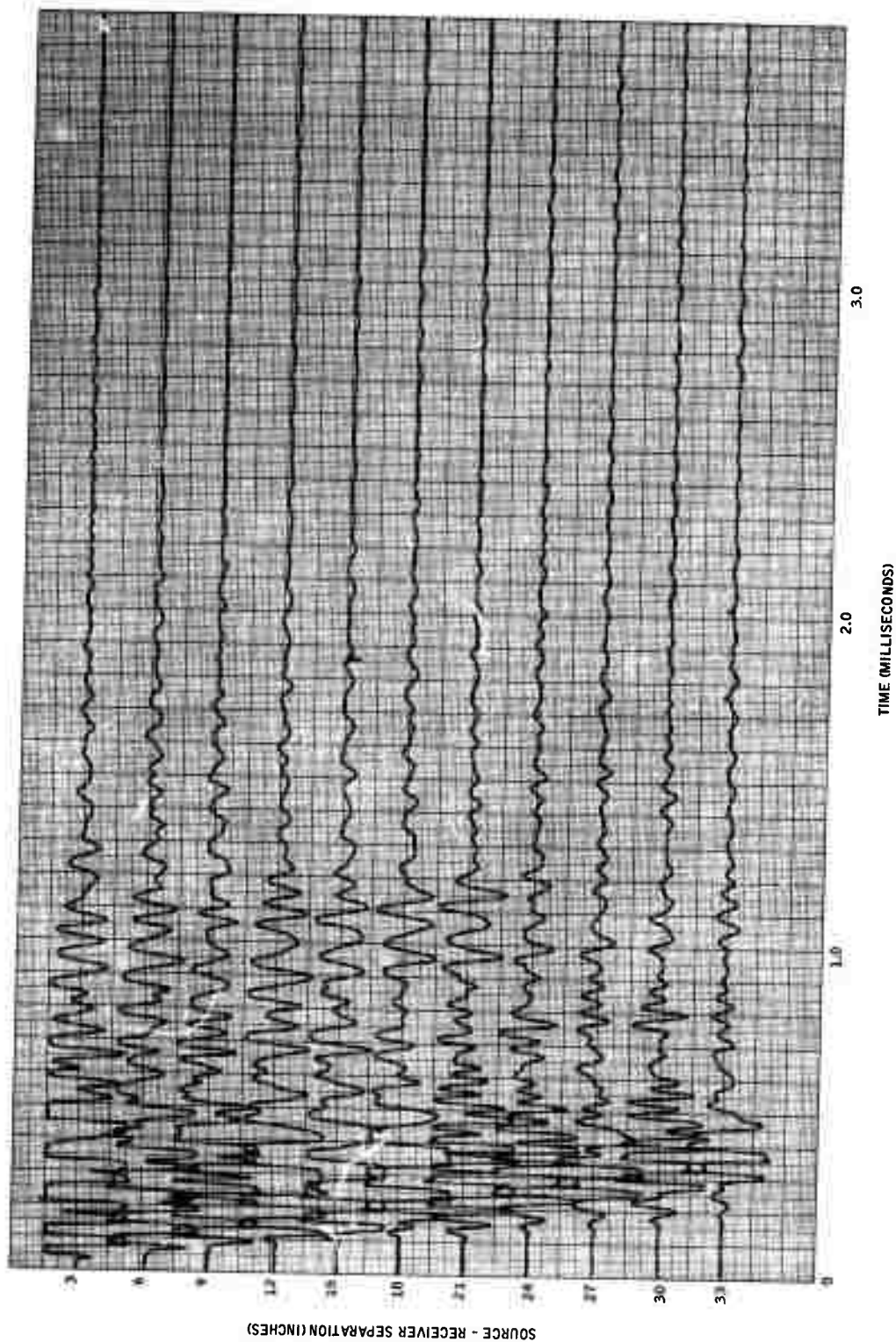
Figure 3-15(a). Site B Data - North
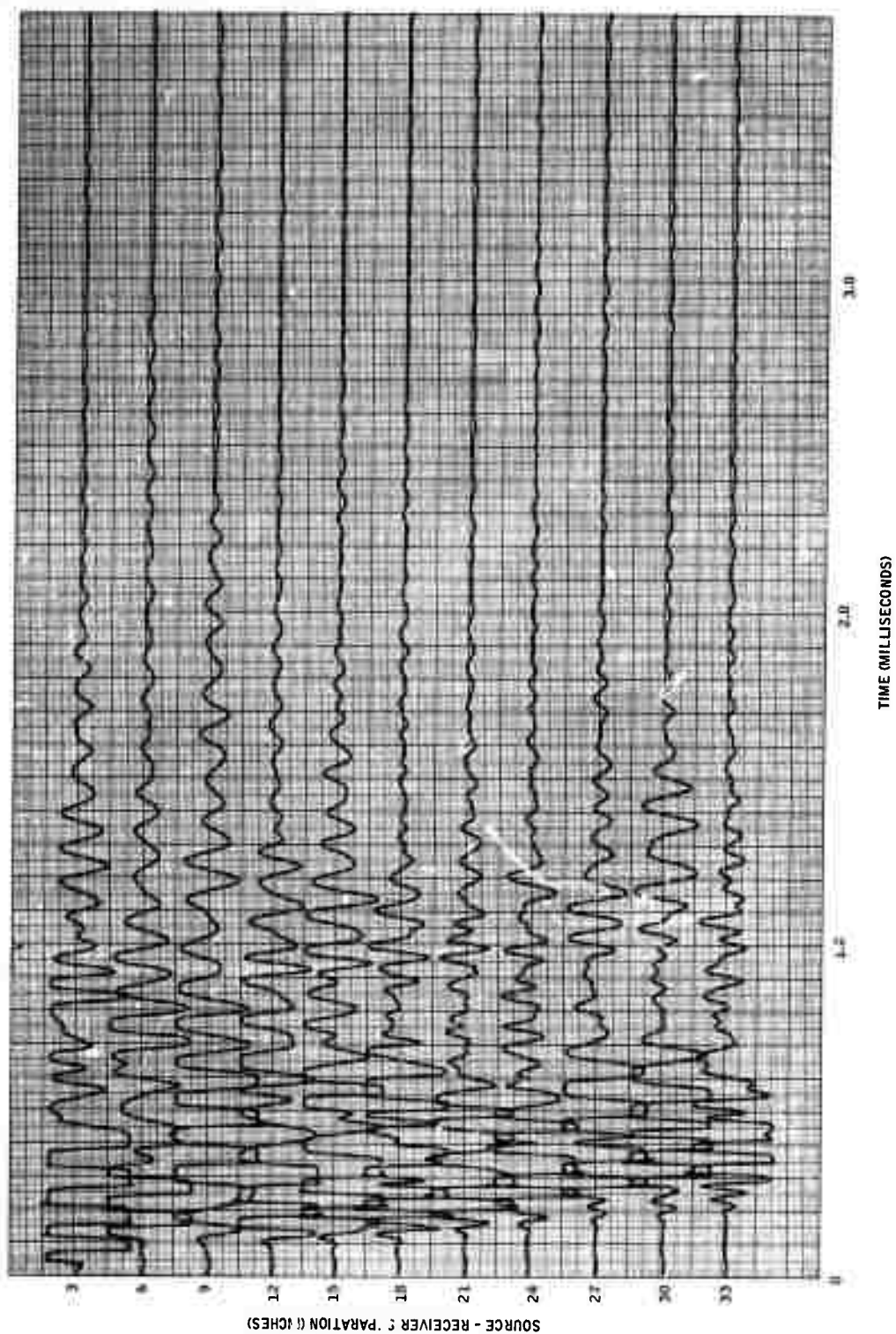
Figure 3-15(b). Site B Data – West

3-29
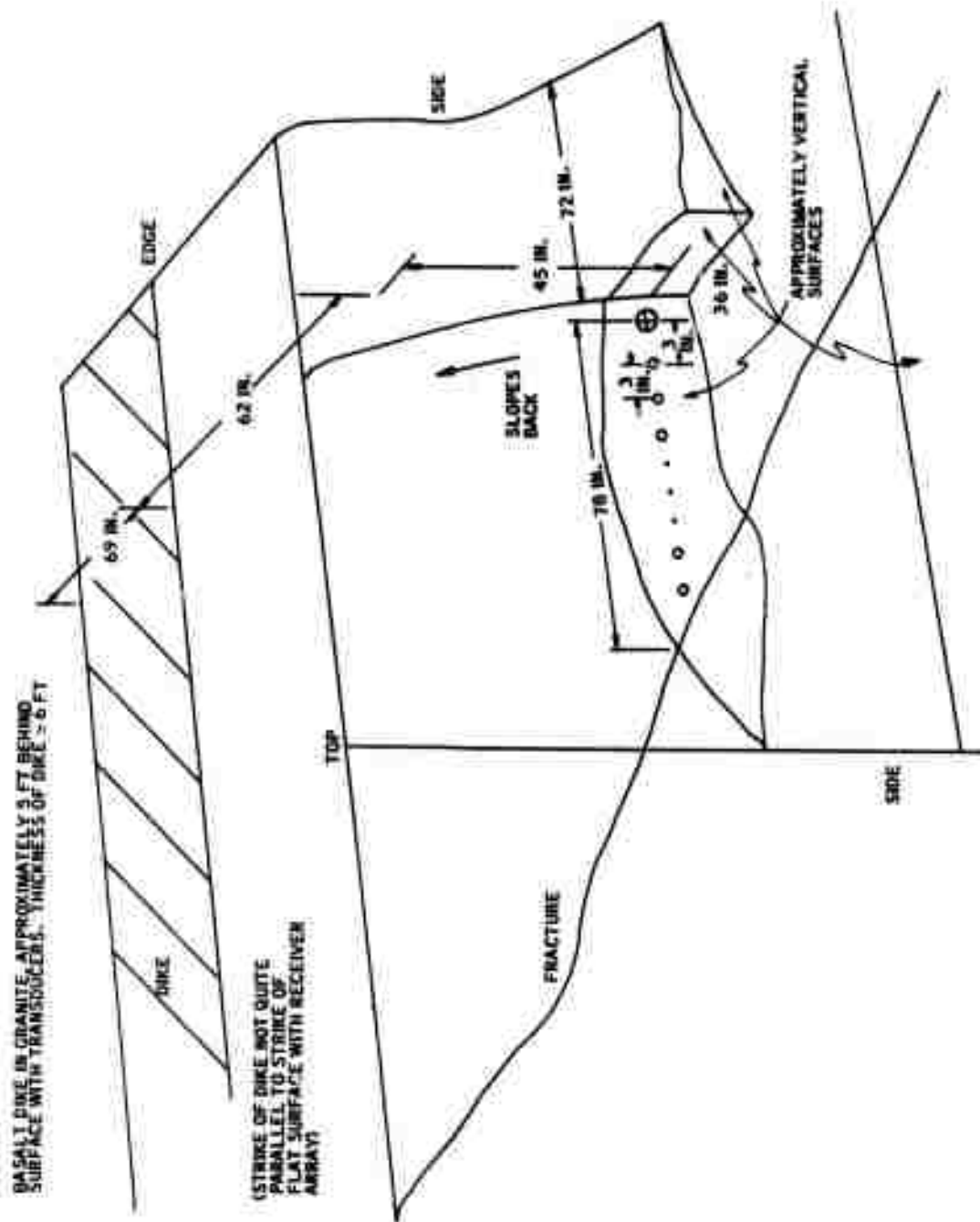
Figure 3-16. Site C Geometry

Figure 3-17. The P wave velocity, from direct P wave measurements, was estimated at 15, 700 ft. /sec. A reflection from the basalt would then be expected at about 660 μsec. An event, which can be followed across most of the array, does exist at that time as indicated in Figure 3-17 but does not have the correct time-distance relationship for the basalt reflection. It is probably a surface-wave reflection from the diagonal fracture about 36 inches below the transmitter.

3.7 SEISMIC MODEL DATA

Two-dimensional laboratory seismic models provided the initial data for array processing performance investigations and also have been used for preliminary studies of possible techniques for surfacewave suppression. Thin sheets are used with transmitter and receivers positioned along the edge of the sheet. The instrumentation and recording system were similar to those used in the field (Figures 3-1 and 3-3), except that analog magnetic tape recording was not employed, the data being digitized directly.

The seismic model consisted of a plexiglass sheet, 4 x 3 feet in size. The transmitter was placed on the long side, 22 cm from the edge. Successive receiver locations were 10 cm apart. The position of the transmitter was kept fixed.

For the transmitter and receiver, ceramic transducers with high mechanical Q, lead zirconate-lead titanate (PZ-PT) ceramics materials are used. These were obtained from the Honeywell Ceramic Department and are K-type materials in various shapes and sizes. Those used in the experiment are cylindrical with a length of 0.7 cm and a diameter of 0.8 cm. This size transducer is used for the transmitter only. For the receiver, a smaller size gives better results. The receiver transducer is also cylindrical in shape but measures 0.35 x 0.5 cm.

Devices to hold the transducers were constructed as shown in Figure 3-18. The holders provide both mechanical mounting for the transducers against the model and also a means for applying an electrical signal.

For the tra.. . !..: assembly, a brass rod 1/2 inch long and the same diameter as that of transducer is used for backing and also serves the purpose of electrical connection. For the receiver assembly, a 1/2-inch aluminum rod with same diameter as that of the small receiver transducer is used. It was noticed that use of brass or aluminum as backing material does not change the waveform significantly.
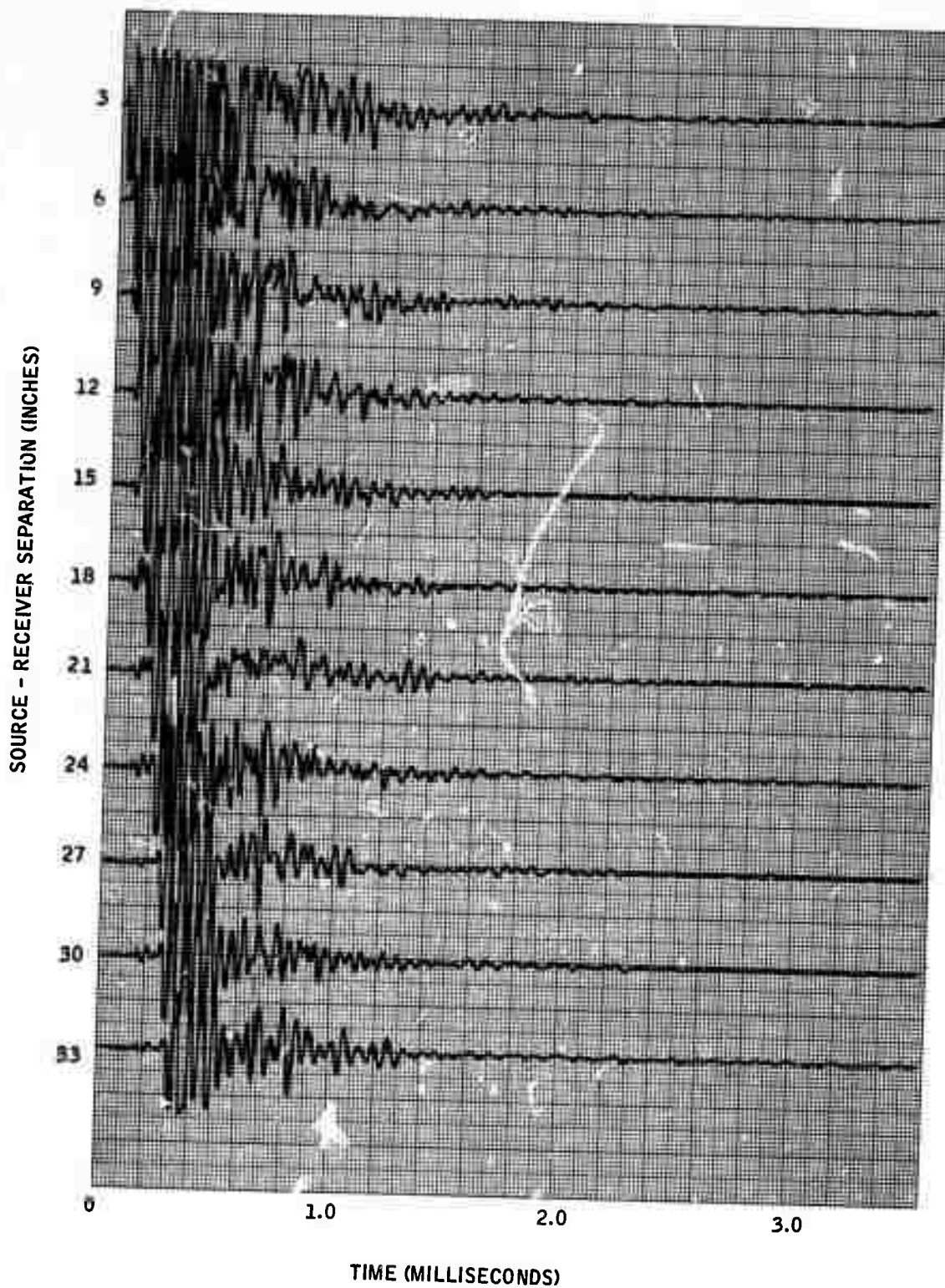
Figure 3-17(a). Site C Data - Basalt Dike (receiver in-line with source to 33 inches)

3-32
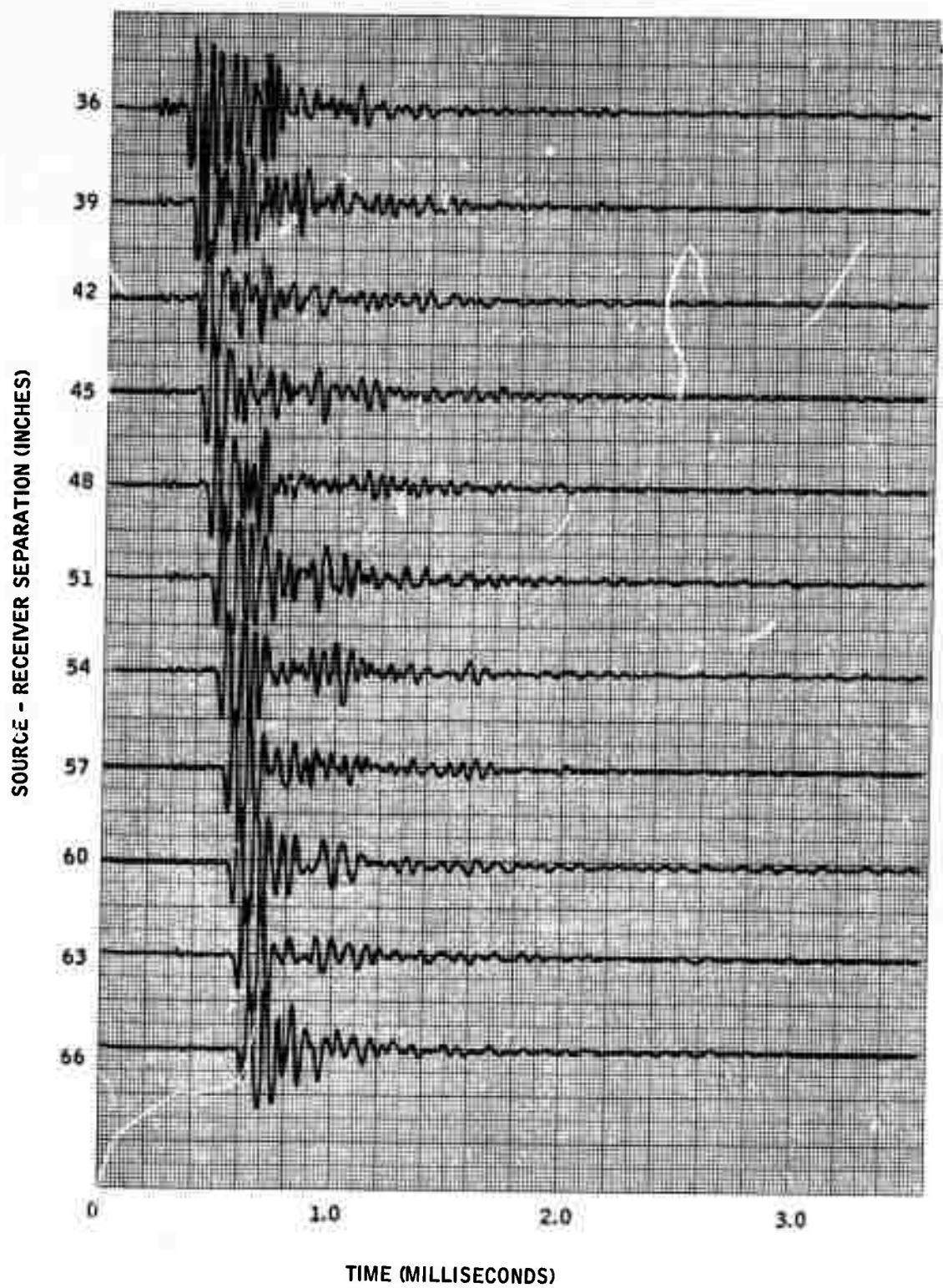
Figure 3-17(b). Site C Data - Basalt Dike (receiver in-line with source from 36 to 66 inches)
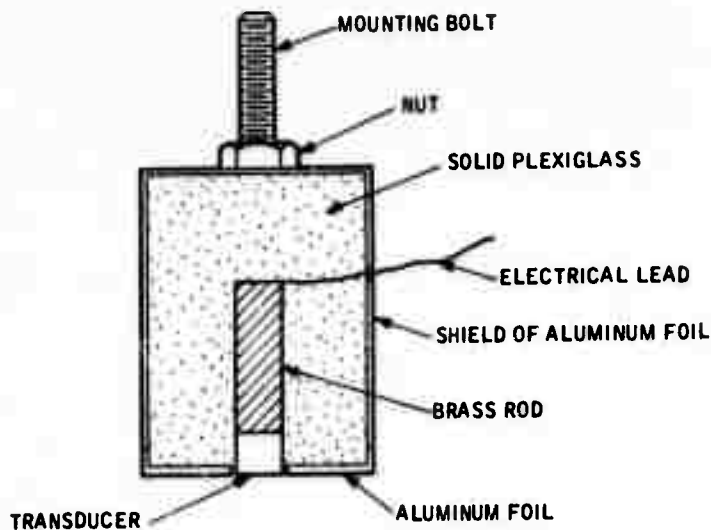
Figure 3-18. Model Transducer Holder

The data recorded on this model is shown in Figure 3-19. Its qualitative similarity to field data from hard-rock environments is apparent. Several distinct seismic arrivals were easily identified from travel-time plots as direct P waves, the PP reflection from the bottom of the sheet, direct surface waves, and reflected surface waves from the sides of the sheet. The amplitudes of the reflected P waves, however, are very small compared to the reflected surface waves.
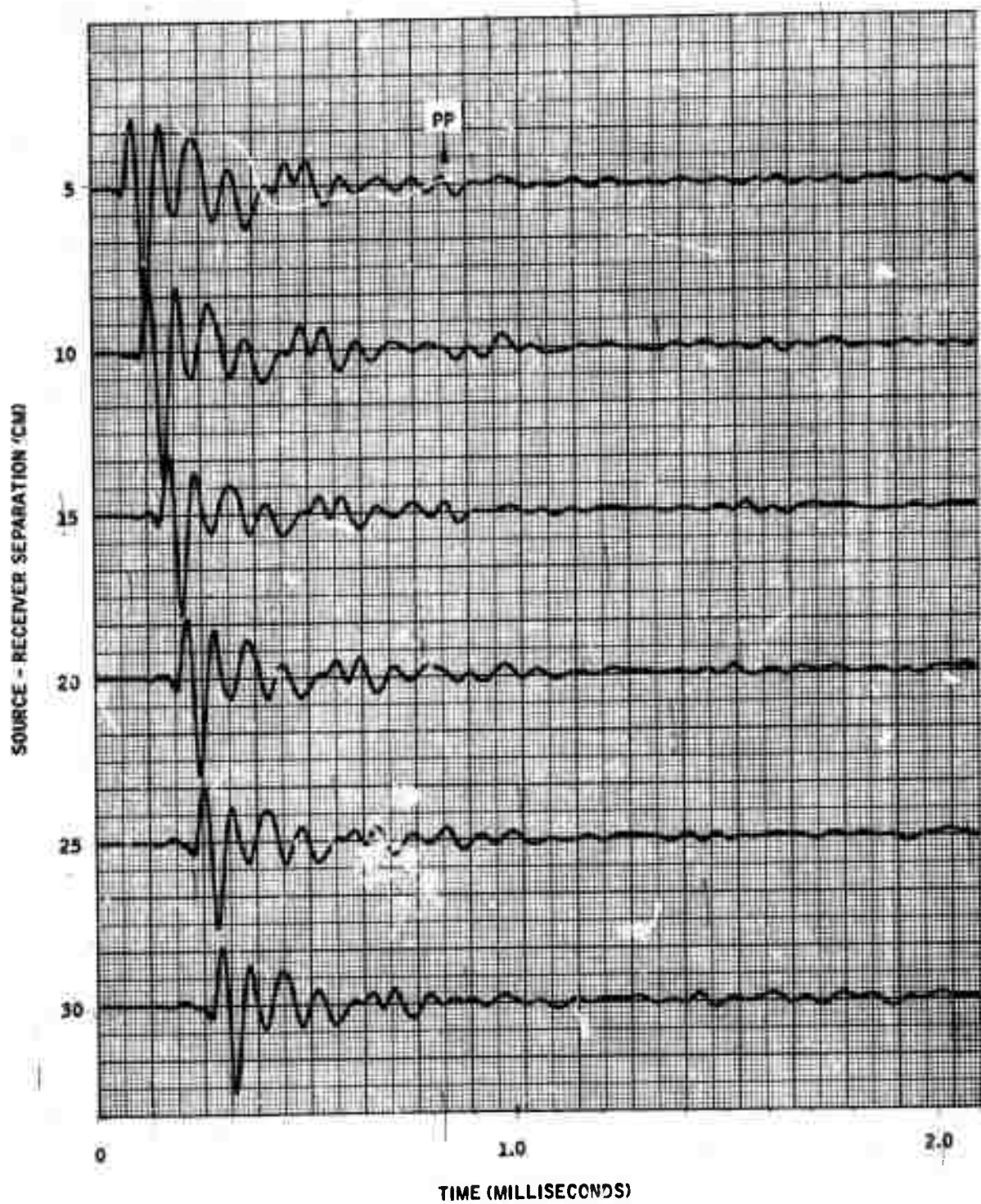
Figure 3-19(a). Seismic Model Data (receiver in-line with source to 30 cm)
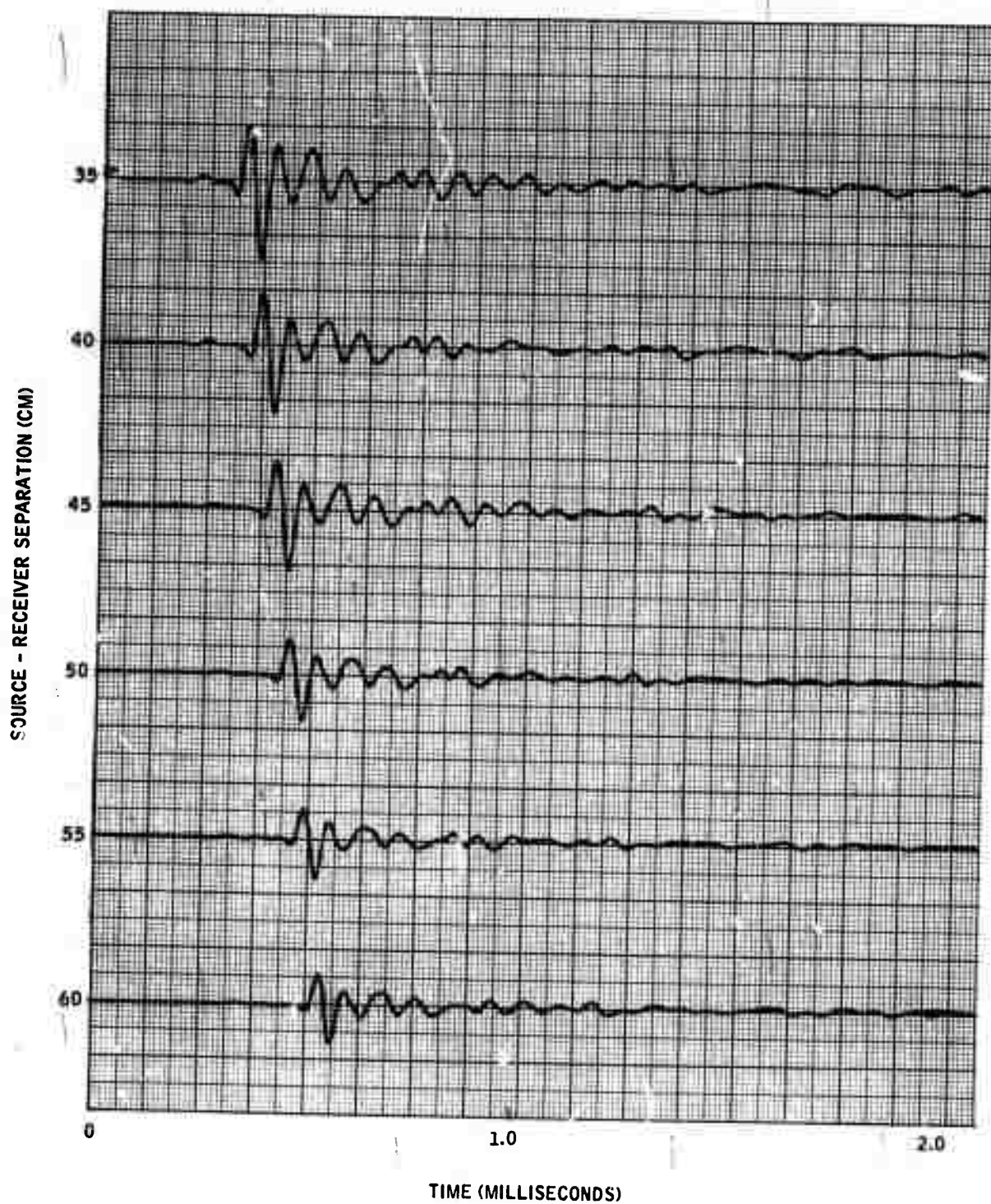
Figure 3-19(b). Seismic Model Data (receiver in-line with source from 35 to 60 cm)
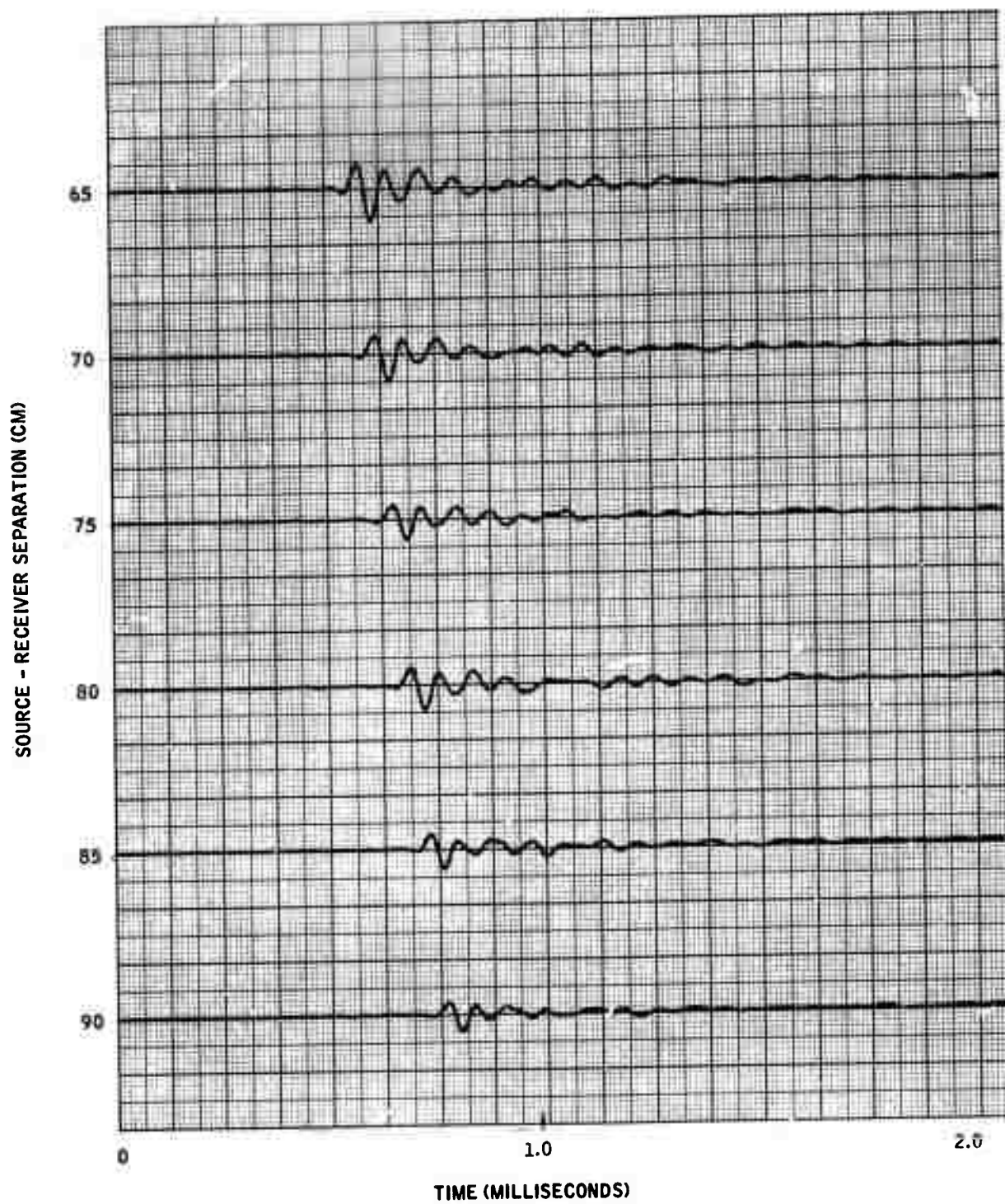
Figure 3-19(c). Seismic Model Data (receiver in-line with source from 65 to 90 cm)

3-37

SECTION IV
ARRAY PROCESSING RESULTS

4.1 PROCESSING TECHNIQUE SELECTION CONSIDERATIONS

Selection of a manageable set of array-processing techniques to be experi-
mentally tested for excavation seismology from among the myriad of tech-
niques available must be guided both by the nature of the signal and inter-
ference phenomena to be encountered and by the practical constraints of a
field-portable implementation. Array processing techniques vary in com-
plexity from simple DIMUS (DIgital Multibeam Steering, Ref. 8) beamform-
ing to optimal multichannel Wiener filtering. The latter, for example, is no
doubt too complex for a field portable implementation, but in addition, is
also probably unsuitable for this application because of the high degree of
coherence between the signal and interference fields.

The primary interferences resulting from active probing of the medium
are direct and reflected surface waves. Not only is more pulse energy
coupled into the surface wave than the compressional wave, but the surface
wave suffers only cylindrical spreading loss, whereas the compressional
wave suffers spherical spreading loss.

Constancy of the medium permits coherent ensemble averaging over repeated
pulse transmissions, hence random noise is not a significant interference.
Ensemble averaging will not suppress coherent interference, however.

The medium of interest is locally homogeneous, with relatively isolated
discontinuities such as fractures and boundaries. In addition, the transmitted
signal is a short-duration sinusoidal pulse. Therefore, the reverberant field
within any time interval of the order of a pulse duration is best characterized
by a limited number of directional arrivals which are coherent replicas, ex-
cept for phase, of a desired P-wave reflection. We cannot, for example,
rely upon a dense distribution of random scatters to decorrelate the rever-
berant field from the signal such as occurs in ocean acoustics.

As a result of these properties of the primary interference field, optimal
array-processing techniques which are based upon statistical independence of
the signal and noise, and depend upon quasi statistical stationarity in their
derivation, did not appear attractive in this application. Rather, the more
conventional beamforming techniques seemed most suited to the excavation
seismology problem. Not only have they been proven adequate for suppressing
directional interferences in many applications of radar, sonar and seismic
signal processing, but their relative simplicity and general ease of imple-
mentation was also a significant factor in this choice.

The desire for simplification of the system also leads to the selection of a multiplicative array configuration. Nonlinear beamforming can produce the desired beam pattern with far fewer elements than that required by linear beamforming (Ref. 2, 9). Based on operational considerations and recommendations in Reference 2 an L-shaped array was chosen. After linear beamforming on each of its arms, the two beams are correlated to produce the desired pattern from the L-shaped array. Although correlative beamforming results in a loss in array gain relative to linear beamforming (Ref. 10), this loss is not sufficient to negate the advantages in reduced system complexity.

4.1.1 Numerical Experiments Performed

As a result of the above considerations, initial experimental studies of phased array processing on the two-dimensional model commenced with simple stacking or delay-and-sum beamforming and Dolph-Tchebyscheff shaded (Ref. 11) linear beamforming. To these were added a fixed-null beamformer seeking to null the direct surface wave prior to beamforming, fan filtering (Ref. 12, 13) and DIMUS (Ref. 8) beamforming. Inadequacies in all but DIMUS when applied in correlative beamforming on the three-dimensional granite block data led to tests of an adaptive zero-memory/least-squares processor (Ref. 14, 15). Poor performance of this processor prompted consideration of its extension to a finite-memory configuration. However, examination of the complexity of this processor, coupled with the fact that it is unlikely that more than one interference will arrive within one pulse period, resulted in an adaptive-null processor that seeks to null an arrival not in the beam prior to beamforming. Refinements of the adaptive-null processor to reduce its complexity led finally to what is termed a DIMUS/adaptive null processor because it operates solely on hard-clipped (one-bit) data.

4.1.2 Conclusions

Of the several array processors examined in this study, the DIMUS and DIMUS/adaptive null are best, on the whole, based upon performance and simplicity of implementation. The reason that this is the case is a direct result of the fact that the primary interferences are relatively slowly propagating surface-wave pulses, either direct or reflected.

A basic limitation of conventional linear beamforming for discrimination against pulsed sinusoids is that an off-beam-axis interference pulse does not fill the array with coherent energy. On the leading edge, the pulse has not reached all the elements in the array, in which case the effective aperture of the array is reduced. Also, in the case of shaded beamforming, the

shading weights of the reduced aperture array are no longer appropriate. On the trailing edge, the decaying oscillatory tails of the pulse do not satisfy both the amplitude and phase relationships of coherent propagating sinusoids that give these beamformers their characteristic response in the sidelobe region of the beam pattern. In addition, attenuation and dispersion of the pulse as it propagates across the array, plus nonuniform coupling of the transducers to the medium, further act to destroy those critical amplitude and phase relationships.

Clipped data array processing alleviates all of these problems in one fell swoop. High-amplitude leading edges of strong interferences are clipped to a common level with all other signals; hence the effects of reduced array aperture are minimized. The oscillatory tails and the propagation medium have a reasonably high degree of phase stability. Since clipping restores amplitude coherence while maintaining phase coherence (to one-bit accuracy), improved beamforming within and on the tails of off-axis interference pulses is achieved.

Clipping does have adverse effects as well. It broadens the pulses considerably since the tails are weighted equally with the peaks. Also, detection of a weak signal coincident with a strong coherent interference does not appear likely with a single line array using DIMUS beamforming. However, as will be seen, correlation of orthogonal line arrays can yield a detectable signal in this case.

In Section 4.2, the array processing technique descriptions and experimental results of this study are summarized. This section is supplemented by Appendix A, which gives mathematical descriptions of the processor algorithms, and by Section 4.3, which presents and discusses a selection of processor output records from the various experiments. Appendix C discusses array design considerations and DIMUS beam patterns for the L-shaped pair of correlated orthogonal arrays.

4.2 PERFORMANCE MEASURES

The experimental results from the various array processors and experimental setups examined in this study are summarized and compared by use of two average signal-to-interference ratios. These performance measures are:

R_{PE} — the peak reflected P-wave signal/average energy ratio (averaged over the stack of processed records)

R_{PP} — the peak reflected P-wave signal/peak interference ratio (averaged over the stack of processed records)

4-3

More precisely, if $C_j(n)$, $1 \leq n \leq N$, is the jth processed sample data record in a stack of J records

$$R_{PE} = 10 \log_{10} \left\{ \frac{1}{J} \sum_{j=1}^{J} \frac{C_j^2(n_p)}{\frac{1}{N} \sum_{n=1}^{N} C_j^2(n)} \right\} \quad (db)$$

$$R_{PP} = 20 \log_{10} \left\{ \frac{1}{J} \sum_{j=1}^{J} \frac{C_j(n_p)}{C_j(n_I)} \right\} \quad (db)$$

where n_p is the sample point for a reflected P-wave maximum, and n_I is the sample point for an interference maximum.

R_{PE} is not quite the signal-to-noise ratio performance measure that is usually desired. Because it was not possible to estimate the PP waveform so as to remove it from the data, the average energy over the record includes the desired signal component. However, for short pulses and long records, the signal contribution will be negligible.

A stack of four records (J = 4) was used in the averages for R_{PE} and R_{PP}. In all experiments, the driver was positioned at the end of the uniformly spaced line array, as illustrated in Figure 4-1. Numbering the elements in sequence from the driver, the processed record stacks were formed by beamforming in turn on arrays composed of elements 1 to K_A, 2 to $(K_A +1)$, 3 to $(K_A + 2)$ and 4 to $(K_A + 3)$. In every case, the K_A element arrays were phased relative to a PP arrival at the origin.
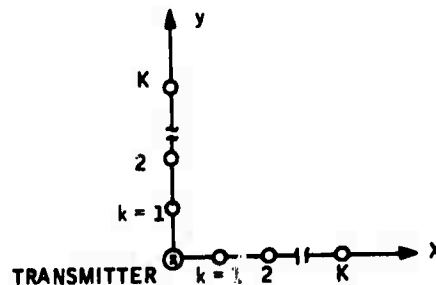
Figure 4-1. Orthogonal Line Array Geometry

It is convenient to discuss the study results in approximately the chronological order that the various processing techniques were tested. Because data from the two-dimensional models was obtained first, the initial phase dealt with conventional linear beamforming techniques. Later, when data from the granite block and Charcoal Quarry was obtained, three-dimensional nonlinear and adaptive array processing techniques were examined. The subsequent discussion will be divided along these lines.

4.3 LINEAR BEAMFORMING

The linear array processors tried first on the two-dimensional model data were delay-and sum, Dolph-Tchebyscheff shaded beamforming, a fixed null beamformer and the fan filter. For notational simplicity, these are abbreviated D&S, D-T, FN and FF, respectively, in the discussion.

Mathematical descriptions of these processing algorithms are presented in Appendix A as processors P-1: D&S, P-2: D-T, P-4: FN and P-5: FF. Only brief prose descriptions of the processors will be given here.

4.3.1 Delay-and-Sum Beamformer

D&S refers to phasing the array so that the desired directional signal adds coherently before summing the element outputs with equal weights. D&S beamforming is optimal for a single directional signal in additive noise that is uncorrelated and of equal intensity across the array. However, it can have poor response to directional interferences in the sidelobes of its beam pattern. This technique is known as "stacking" in seismic exploration.

4.3.2 Dolph-Tchebyscheff Beamformer

Amplitude weighting (shading) of the array element outputs can improve the beam pattern in the sidelobe regions, but at the expense of the width of the main lobe. D-T shading (Ref. 11) is an optimal weighting in the sense that it minimizes the width of the mainlobe for a predetermined peak sidelobe response level. Theoretical D&S and D-T beam patterns for a five-element line array are compared in Figure 4-2. Half-wavelength element spacing and phasing for normal incidence ($\phi = 0°$) is assumed. The notation D-T/L, where L refers to the peak sidelobe response relative to the peak mainlobe response in decibels is used here and throughout this discussion.

Formulas for computing D-T weights may be found in References 16 and 17. In this study, D-T shaded arrays of $K_A = 5$, 9 and 13 elements, and at shading levels of -20 db, -30 db and -40 db, were tried. In every experimental setup tested, the ratio of the element spacing to surface wavelength
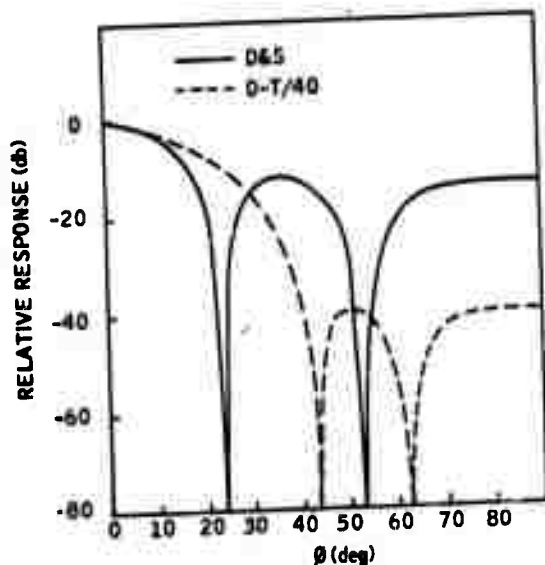
Figure 4-2. Theoretical Beam Patterns,
$K_A = 5$

satisfied $d/\lambda_s \geq 1/2$. Since the D-T weights are independent of d/λ_s under these conditions, the D-T weights tabulated in sequence in Table A1 of Appendix A were valid throughout the study.

4.3.3 Fixed-Null Processor

Since the primary interference in the two-dimensional model data was the direct surface wave, the FN processor attempts to null the direct surface wave from the kth element output by subtracting an estimate of the surface waveform obtained from the $(k+1)^{st}$ element prior to D-T beamforming. This is a simplified, suboptimal version of the optimal processor for nulling a single directional interference (Ref. 18, 19).

The optimal processor (e.g., the DICANNE processor of Reference 19 in the case of a single interference only) uses every element in the array for estimation of the interference waveform. However, the optimal processor performs significantly better than the simpler FN processor only when the trace velocities of the interference and desired signals are nearly equal. This is illustrated in Figure 4-3, where the normalized array gain of the DICANNE and FN processors are compared for the case of a desired signal incident on the line array normal ($\phi_0 = 0°$) as a function of the angle of incidence of the interference (ϕ_1). In this comparison, it is assumed that the signal and the interference have the same wavelength. The normalization is with respect to the array response in the absence of the interference (i.e., 0 db implies perfect nulling of the interference with no loss in signal power).

4-6

It is seen that the DICANNE processor is theoretically significantly better than the FN processor only when $\phi_1 \cong \phi_0$, and then only for the larger arrays. For this reason, the simpler FN processor was chosen for testing.
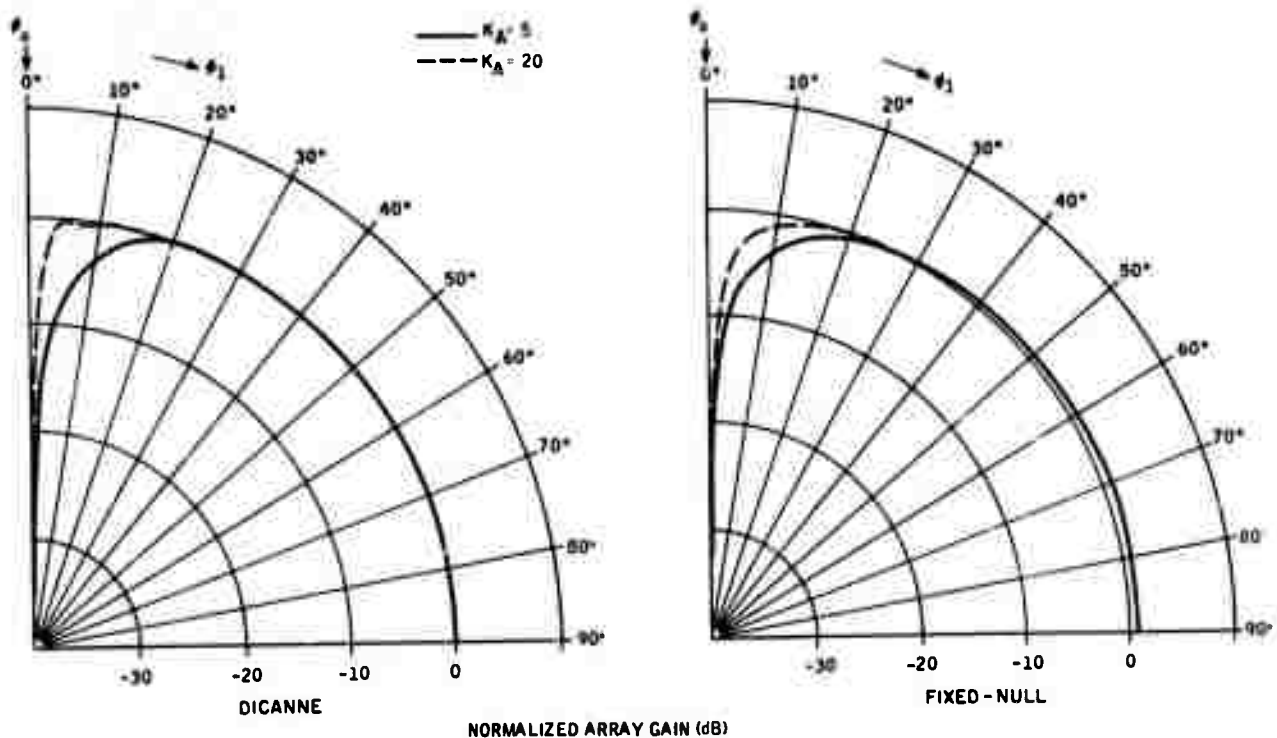
Figure 4-3. Comparison of DICANNE and Fixed-Null Processors in Nulling a Single Interference

4.3.4 Fan Filter

The fan filter (Ref. 13), or pie slice filter (Ref. 12), is so named because its transfer function in the (frequency, wavenumber) plane is unity within a fan-shaped region, and zero outside that region. It is a lowpass frequency filter and highpass velocity filter. In the case of the two-dimensional model data, which had a time sample interval of 2 μsec and element spacing d = 5 cm, its lowpass cutoff frequency was 250 KHz, and its highpass cutoff velocity was 25 km/sec. These cutoffs are more than adequate, theoretically, to pass the 20-KHz pulse and reject the 1.2-km/sec surface wave.

4.3.5 Two-Dimensional Model Results

R_{PE} and R_{PP} array-processing results were compiled as a function of array size, K_A, for the two-dimensional model. Gain settings of the analog amplifiers during digitization are referred to as low-gain and high-gain in the following discussion. In the low gain case, the direct surface wave was linearly reproduced. At high gain, the direct surface wave was allowed to limit, but the remainder of the traces were held in the linear range, yielding an increase in signal-to-interference ratio.

Several modifications to the basic processors tested on the seismic model/low-gain data are reflected in Figure 4-4 and 4-5.

In addition to various D-T shading levels, the effect of gain compensation to equalize the amplitude of the interference from element to element was examined (indicated by a circle around the symbol of a given processor). Gain compensation (based on the peak amplitude of the direct surface wave at each element) was expected to improve the performance of all processors. However, it is seen that it had negligible effect on their performance in almost every case.

The fan filter was tested on both steered (FF/S) and unsteered (FF/US) arrays. There was concern that the effects of near-field beamforming on the image source of the PP wave would alter the uniform interelement propagation delays inherent in the direct surface wave sufficiently to destroy the phase relationships necessary for its suppression by beamforming. However, it is seen that these effects are negligible relative to dephasing the array with respect to the PP wave.

Failure of D-T shaded beamforming to significantly improve suppression of surface waves over that achieved with D&S beamforming is no doubt largely due to the limitations of conventional beamforming in discriminating against off-axis interference pulses that were discussed in Section 4.1. The almost complete lack of effect of changes in shading level over the range -20 db to -40 db seen in Figures 4-4 and 4-5 is felt to substantiate this interpretation. Superior performance by the FN processor indicates that the most effective method of reducing pulsed interferences is by nulling with coherent estimates of the interference pulse prior to beamforming on the desired signal.

The performance measure R_{PP} is in some respects more significant than R_{PE} because an interference peak is more likely to be mistaken for a P-wave reflection. In the model data, the peak PP wave was about 20 db below the peak surface wave at the input. From Figure 4-5, it is seen that the D&S, D-T and FF beamformers achieve about 20-db gain in peak signal-to-interference ratio for the larger arrays. Significantly, the FN processor achieves a 25-db gain with just five elements, but does not improve significantly with an increase in the number of elements. This is seen as additional evidence that
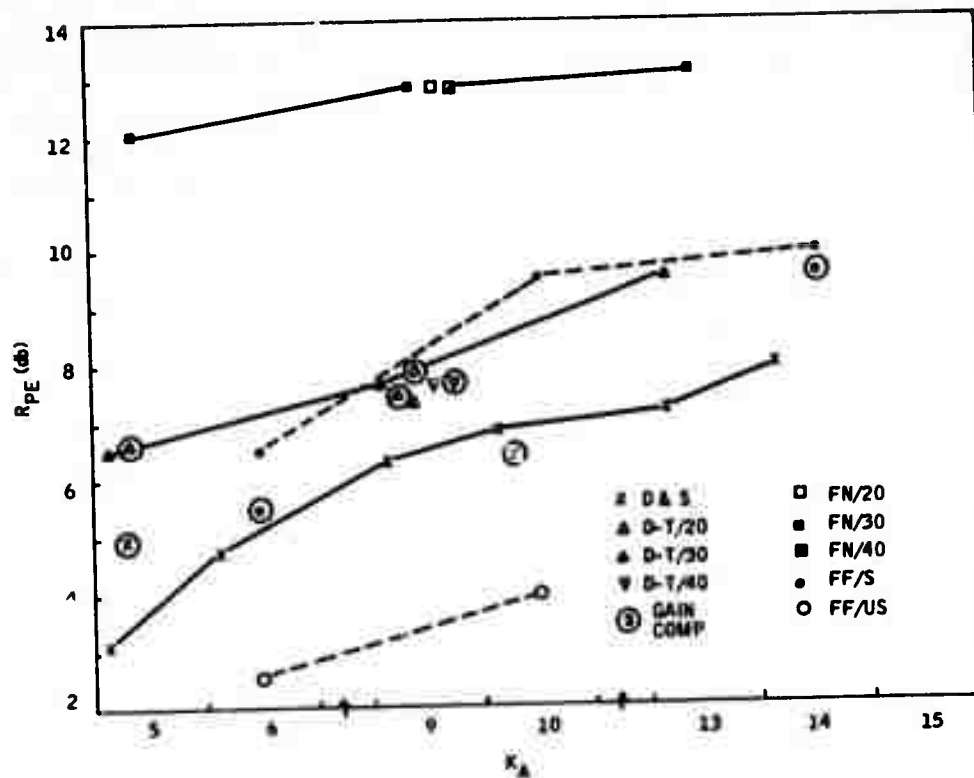
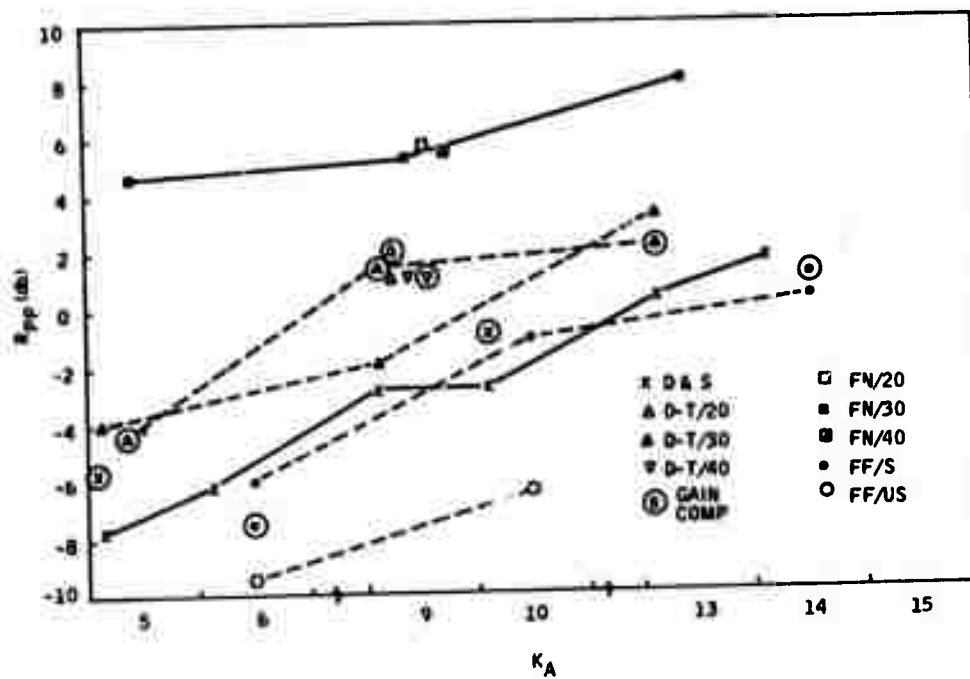Figure 4-4. R_{PE} versus K_A - Seismic Model/Low Gain

Figure 4-5. R_{PP} versus K_A - Seismic Model/Low Gain

4-9

nulling is a more effective method of suppressing surface-wave interferences than beamforming.

Based on the results of processing the model/low-gain data, -30-db D-T shading without gain compensation was chosen for processing additional data with the D-T and FN processors.

Linear beamforming results for the model/high-gain data are presented in Figures 4-6 and 4-7. Increased input signal-to-interferences ratio (S/I) has the expected result on the output R_{PE} and R_{PP}. The D&S and D-T beamformers benefit most by the increased S/I, especially for the smaller arrays. Increasing the array size has even less effect on this data than on the low-gain data. Again, FN processing was superior, particularly for small arrays.

The depth of the P-wave reflecting surface in the experimental model was small compared to the desired penetration depths for the future system. Since the low-gain data represented the greater challenge to array processing that increased penetration depths would occur, it was decided to concentrate on processing of the low-gain data in the remaining experiments.

4.4 NONLINEAR AND ADAPTIVE BEAMFORMING

The results of orthogonal array correlation using the D&S, D-T, FN and FF processors on the granite block data are presented in Figures 4-8 through 4-13. Three orthogonal line arrays, forming two pairs of L-shaped arrays, were available. These are denoted by their orientation on the source face of the block: S (south), U (up) and N (north), with the possible correlation pairs (SXU) and UXN).

An improvement in the D-T shaded beamformer performance for the granite block relative to the model would be expected because here the ratio of element spacing to surface wavelength $d/\lambda_s = 0.5$.

This is a better ratio for suppression of surface waves aligned with the array axis than the $d/\lambda_s = 0.82$ of the seismic model since the latter places the surface wave near a grating lobe in the beam pattern. However, the PP wave was not detectable with this processor except for the largest array, $K_A = 13$, and just barely so there.

The fan filter fared no better and was definitely inferior to the D&S beamformer on the low-gain data. On the high-gain data (Figures 4-12 and 4-13) it showed substantially more improvement than did the D&S, D-T and FN processors relative to the low-gain data but not sufficiently to make it viable in this application, particularly since its R_{PP} was still well below 0 db. High-gain runs are not presented for the (UXN) array pair since there was a bad section on the high-gain data tape for the north array which included the arrival time of the PP pulse.
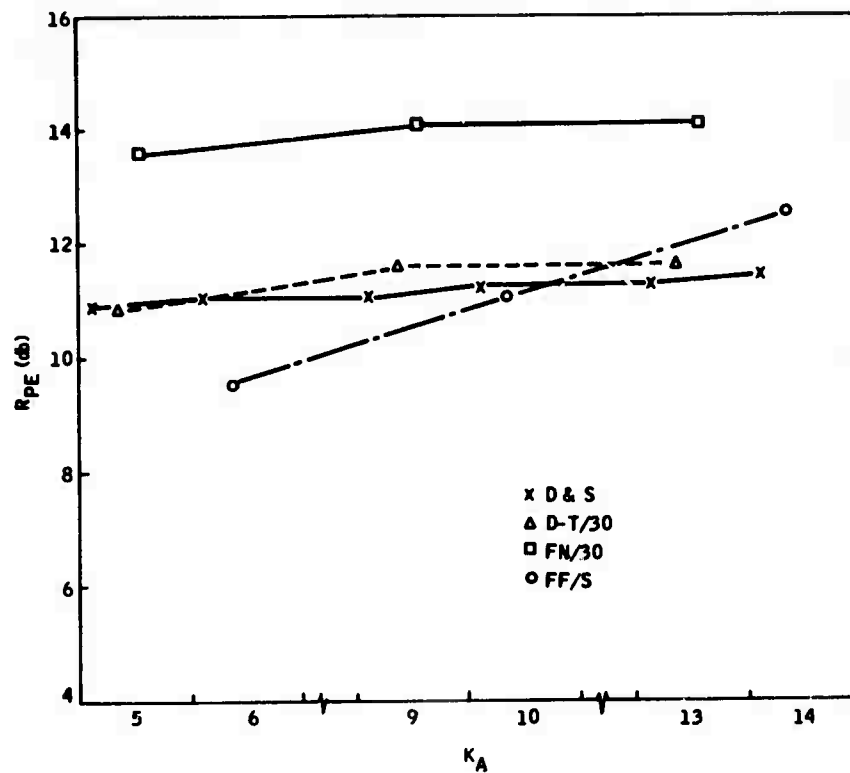
Figure 4-6. R_{PE} versus K_A - Seismic Model/High Gain
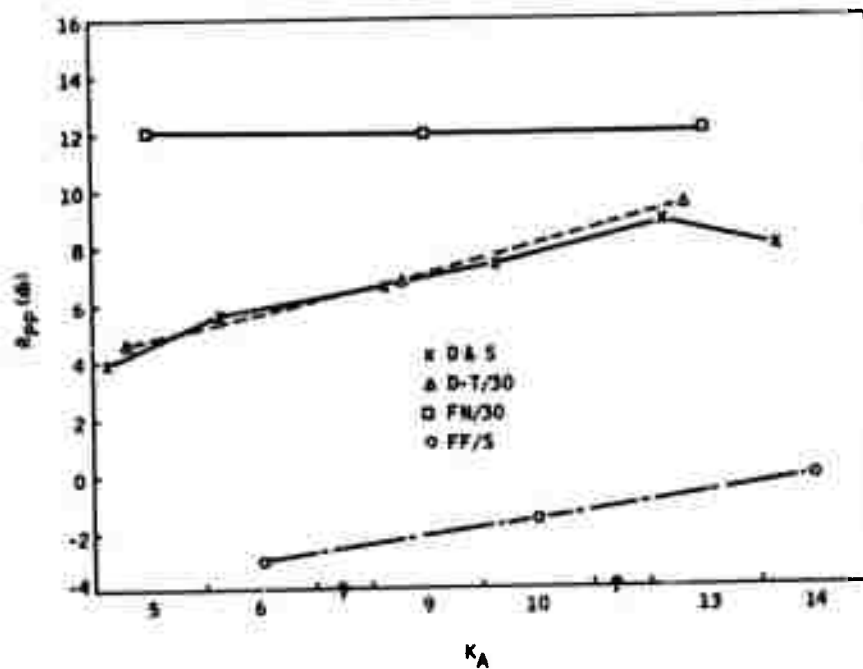
Figure 4-7. R_{PP} versus K_A - Seismic Model/High Gain

4-11

Figure 4-8. R_{PE} versus K_A - Granite Block/Low Gain (SXU)

Figure 4-9. R_{PP} versus K_A - Granite Block/Low Gain (SXU)

Figure 4-10. R_{PE} versus K_A - Granite Block/Low
Gain (UXN)

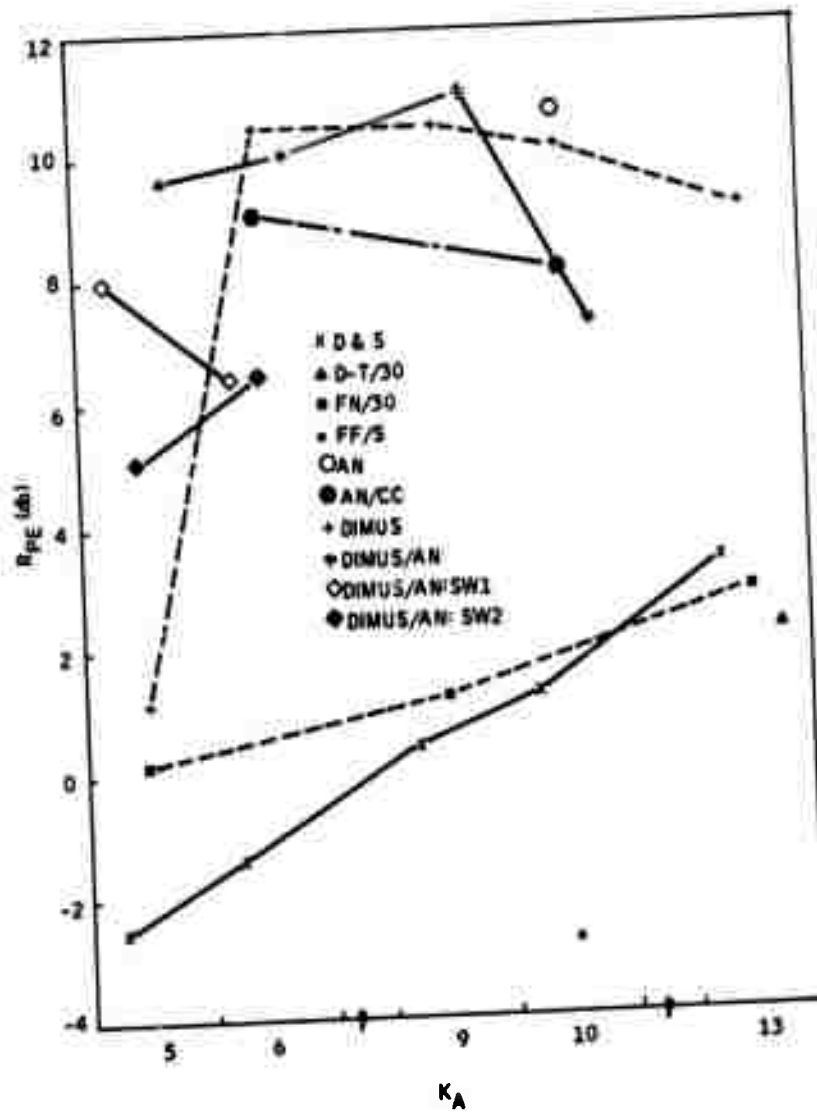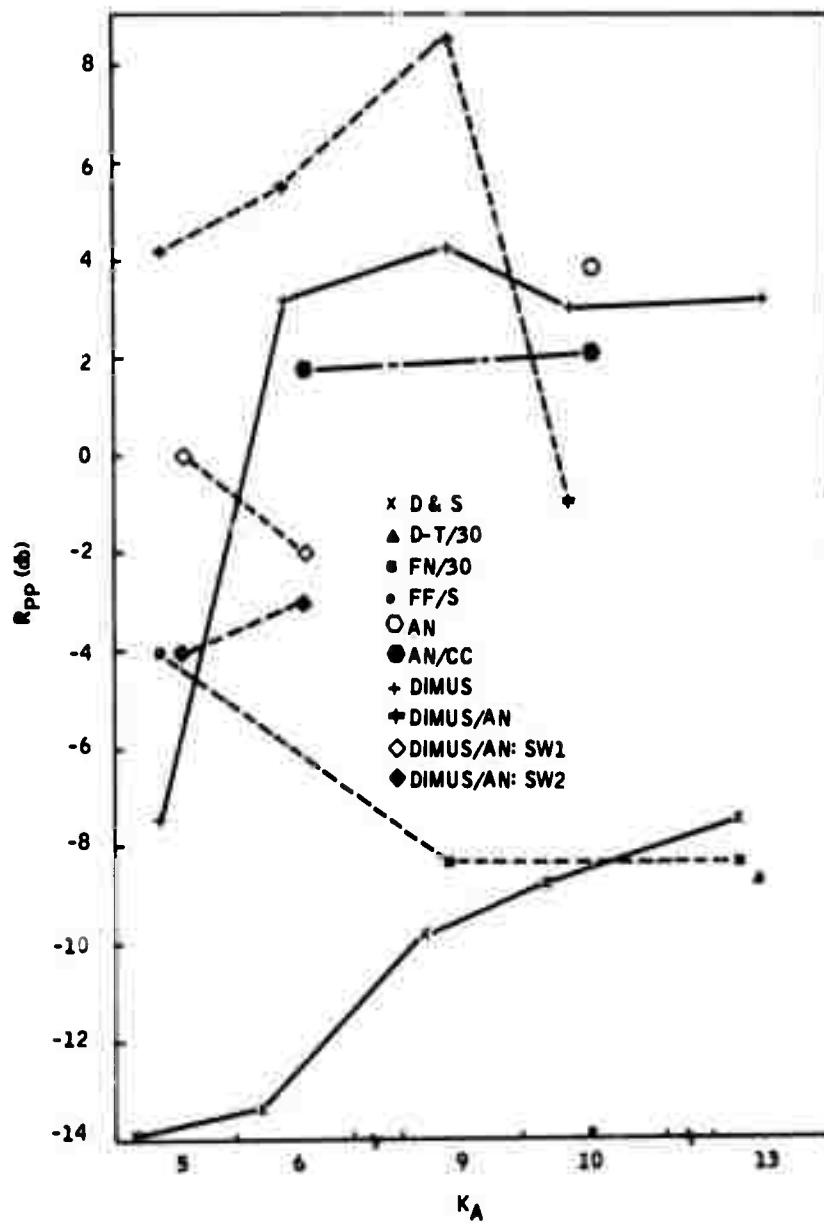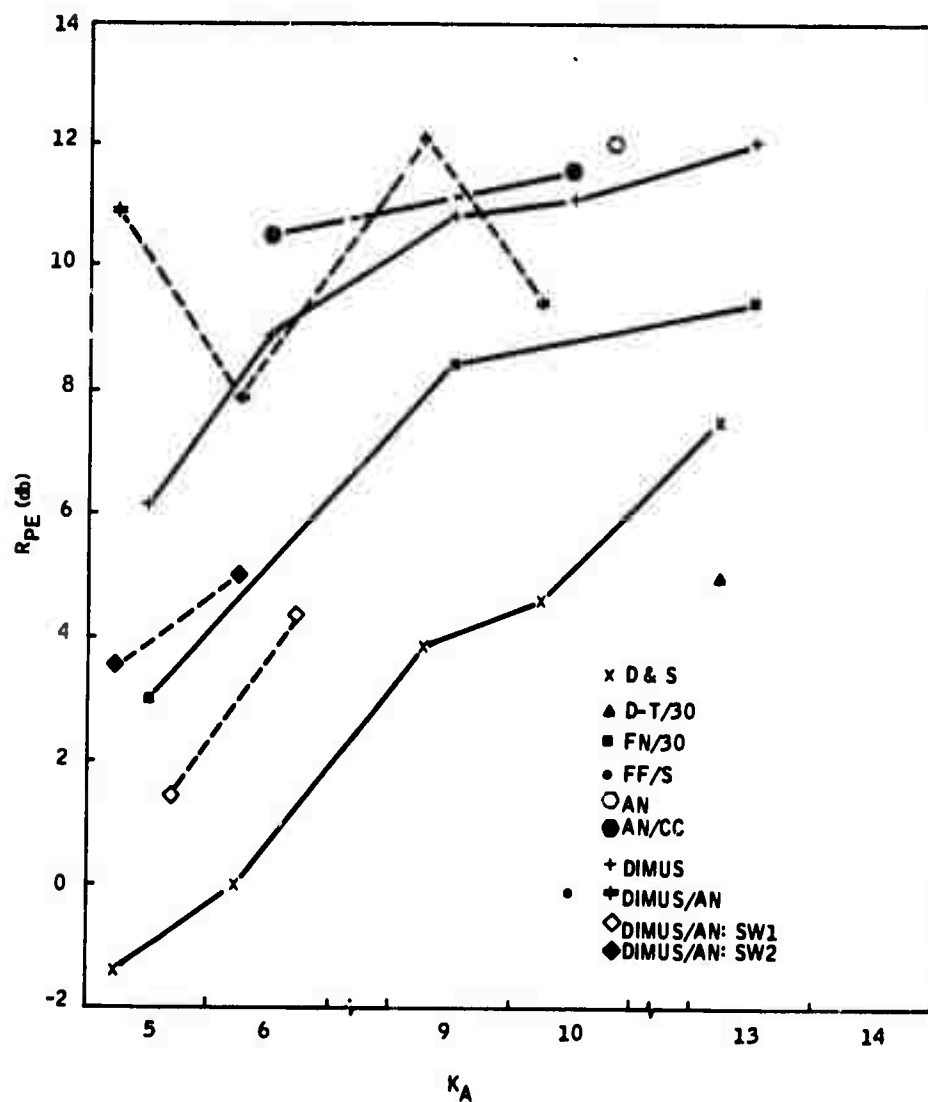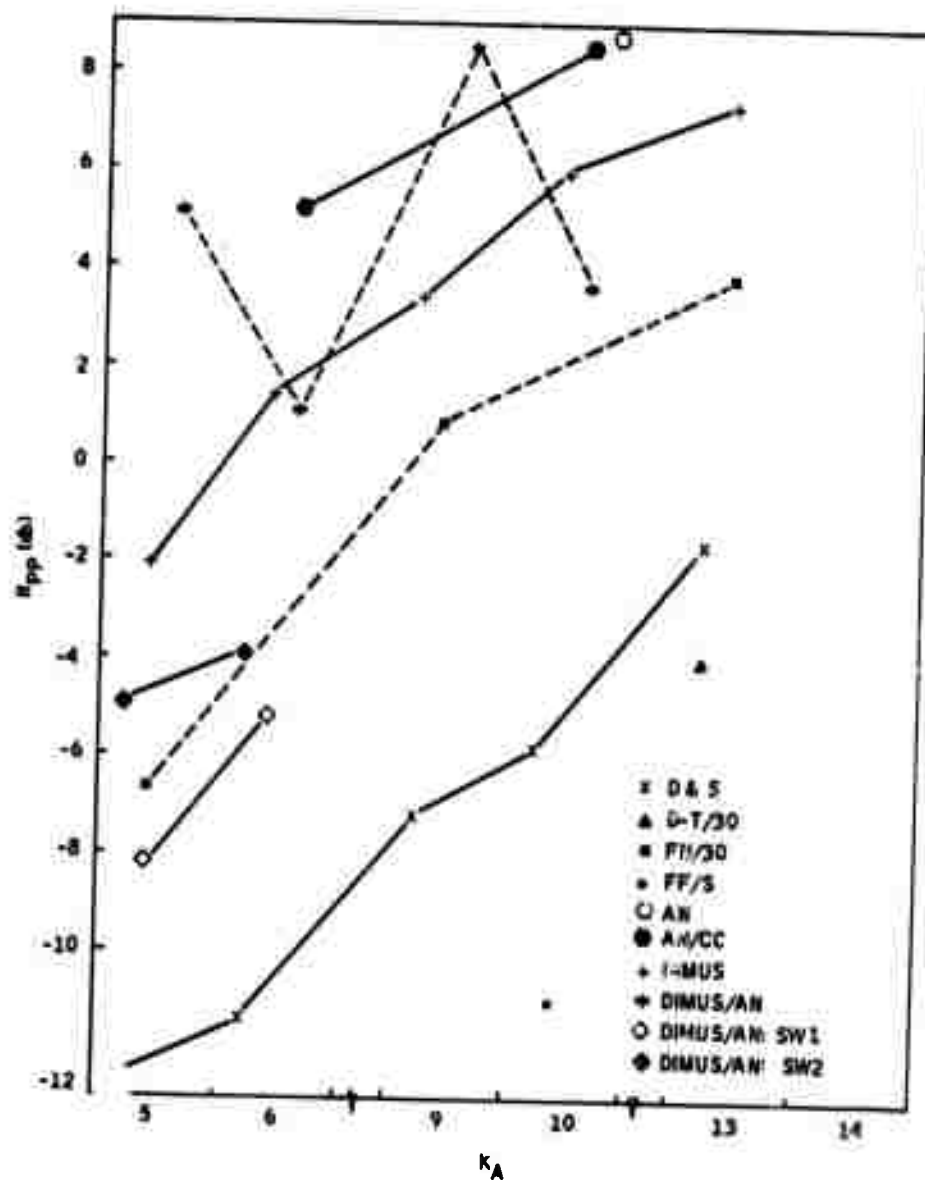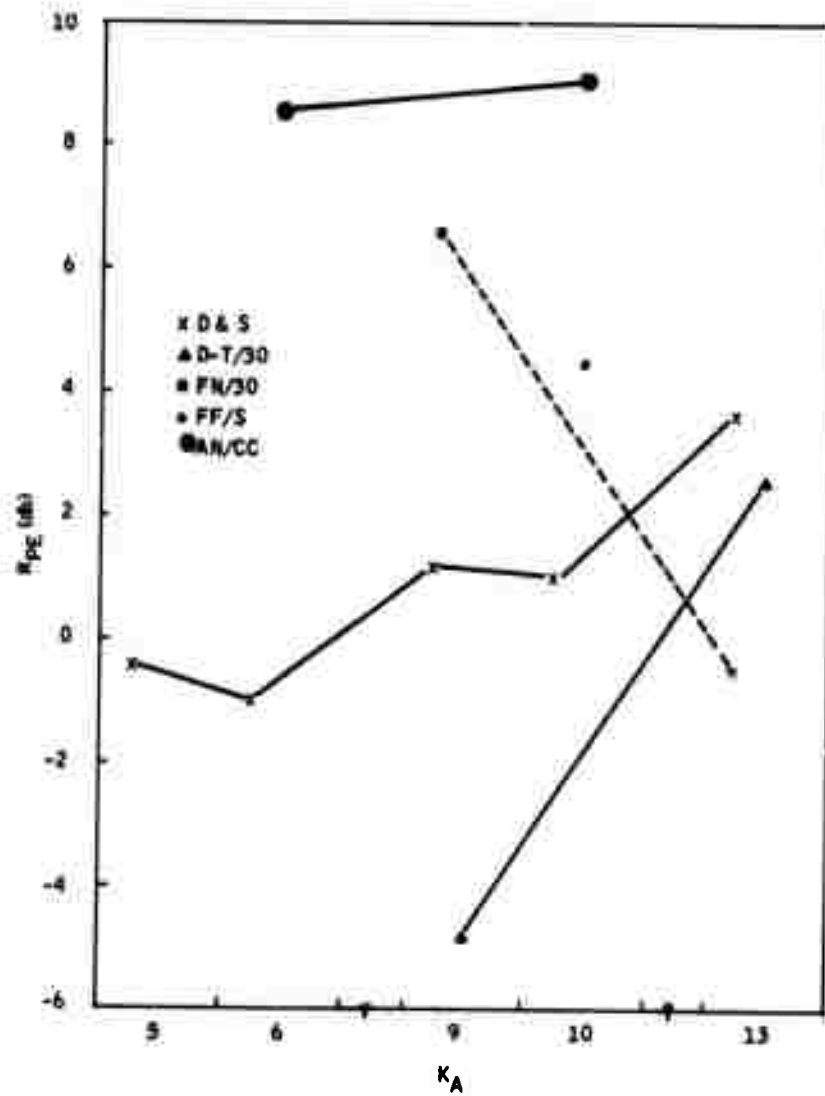Figure 4-11. R_{pp} versus K_A - Granite Block/Low Gain (UXN)

Figure 4-12. R_{PE} versus K_A - Granite Block/High Gain (SXU)
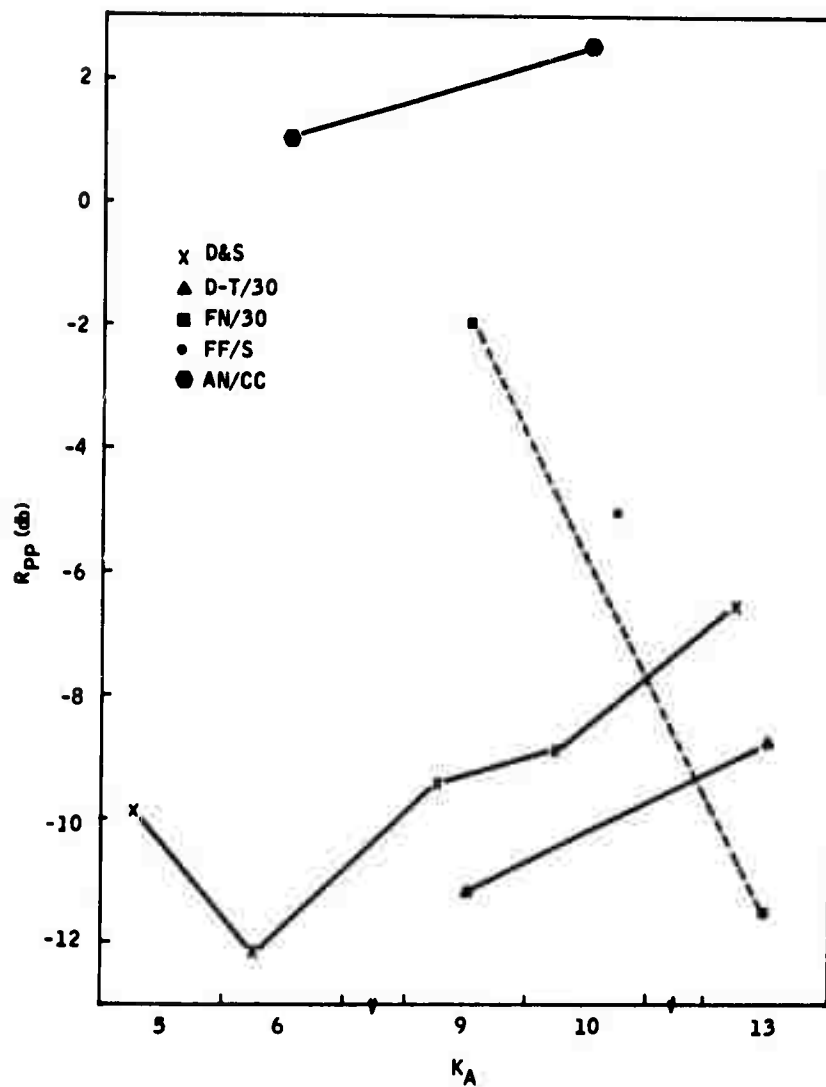
Figure 4-13. R_{PP} versus K_A - Granite Block/High Gain (SXU)

D&S beamforming was somewhat better for the (UXN) pair than the (SXN) pair, but again not particularly encouraging with respect to R_{pp}.

The FN processor is not suited for general application because it requires a priori knowledge of the angle of incidence of the interference it is nulling. However, the geometry of the granite block experiment was such that the image sources for the surface-wave reflections were approximately aligned with the array axes. This permitted nulling of a surface-wave reflection on one of the orthogonal arrays, thereby effecting a null in the correlated pair. The (UXN) pair, Figures 4-10 and 4-11) turned out best for the FN processor. Here, reasonably acceptable performance was achieved for the larger arrays.

4.4.1 Zero-Memory, Least-Squares Processor

The first attempt to improve array processing results on the granite block data involved least-squares processing with a signal fidelity constraint (Ref. 14, 15). This form of processing is similar to adaptive Wiener filtering (Ref. 20, 21) in that a least-squares criterion is used. However, rather than constrain the processor by specifying the signal correlation function to prevent nulling the desired signal, the processor is constrained by requiring that a desired signal on the beam axis pass undistorted.

The zero-memory version, described in Appendix A, is the simplest form of this processor. It is essentially just a weighted, delay-and-sum beamformer wherein the weights are adaptively trained to minimize the total input energy, subject to the fidelity constraint. Kobayashi (Ref. 15) reported reasonable success with this simple version using a steepest-descent and conjugate-gradient-weight training algorithms. These algorithms were tried with no success.

The processor algorithm was then recast in a form suitable for a recursive inversion of the array covariance matrix, as described in Appendix A. Here it was noted that occasionally the covariance matrix, $\tilde{R}$, was ill conditioned, as evidenced by failure of the product of $\tilde{R}$ and its inverse to produce the identity matrix. This could be cured by increasing the averaging window to something substantially greater than one pulse period (~ 100 μsec), but this was incompatible with our desire to adapt to new arrivals at intervals of the order of a pulse period. The ill conditioning of $\tilde{R}$ is no doubt related to the fact that the covariance matrix for a sinusoidal signal on a $K_A > 2$ array is singular. In any event, the records from this processor were unintelligible, and hence no results are presented here. Examples of ZM/LS processed records are presented in Section 4.3 for reference.

Extensions to finite-memory, least-squares processing of this type were considered, but abandoned as impractical. It is known that the optimal processor for nulling directional interferences obtains maximally coherent estimates from every array element to null the interference on each element.

Since the maximum propagation time for the surface wave across the array is $(K_A -1)d/v_S$, approximately 100 weights per element would be required to utilize the full resolution of a five-element array for data sampled at 2-μsec intervals in this case where d = 3 inches and v_S = 10,000 ft/sec. The filter could probably be thinned to reduce the dimensions of the matrix inversion implied by the above example, but the fact remains that a high-dimensional matrix inversion, or its iterative equivalent, would no doubt be required. This, coupled with the fact that the zero-memory version was not the least bit encouraging in this application, led to abandoning the finite-memory, least-squares processor.

4.4.2 Adaptive Null

Since the fixed-null processor had shown promise, even with the granite block data, an adaptive-null technique was tried. This processor, designated AN in the figures, essentially optimizes the fixed null by scanning for an off-beam-axis correlation maxima between adjacent elements. Since this signifies an interference, a maximally coherent estimate of the interference waveform is then obtained and subtracted from the element in question. The AN processor is described in Appendix A.

The rationale behind the simple AN processor is that it is unlikely that more than one interference will arrive during any given interval of the order of a short pulse length. Should two or more interferences with different trace velocities arrive at the same time, the performance will be degraded, of course. This also will be the case if the desired P-reflection and an interference arrive simultaneously with different trace velocities but comparable amplitude. However, if the signal is strong compared to the interference, no null will be applied. If the signal is weak, the estimate of the interference will be improved. In either of these latter two cases, the performance will be as desired.

Results from the AN processor were quite gratifying, as seen in Figures 4-10 through 4-13. Improvements of from 8 to 12 db over D&S beamforming for KA = 10 placed the signal in the detectable range, especially for the (UXN) array. Correlation windows of 100 μsec were used in this processor.

4.4.3 Adaptive Null/Clipper Correlator

Because the surface interference image sources lie in the near field of the array, a scanning correlation for each element pair is required in general for the AN processor. Since this is time consuming and costly, a clipper correlator was substituted. The adaptive null/clipper correlator (AN/CC) is discussed in Appendix A. Although about 2-db processing gain was lost by the AN/CC relative to the AN processor in the (SXU) array, the negligible loss for the (UXN) array prompted trying the adaptive-null technique on one-bit data.

4-19

4.4.4 DIMUS/Adaptive Null

The DIMUS/AN processor operates exclusively on hard-clipped data, as described in Appendix A. The results are somewhat mixed, indicating loss in processing gain for some array sizes, and gains for others, relative to AN processing. However, the general acceptability of this technique, coupled with its simplicity relative to other techniques discussed so far, make the DIMUS/AN a reasonable candidate for implementation in this application.

The performance drop in DIMUS/AN for the even-element arrays in both the (SXU) and (UXN) beams is perplexing. It appears to result from carrying more than one bit in the element data after subtraction for nulling.

4.4.5 DIMUS/Adaptive Null: Sliding Window

For long data records, a more efficient method for computation of the inter-element clipped correlations is to slide the correlation window, as described in Appendix A, rather than using the stepped, nonoverlapping windows. This permits a different correlation maximum to be determined at each sample instant.

DIMUS/AN:SW1, 2 results plotted in Figures 4-8 through 4-13 are for sliding windows of 50- and 100-μsec widths. It is seen that use of a sliding window is definitely inferior to the stepped correlation window. This suggests that the interelement correlation maximum is not a good instantaneous indicator of the phasing for the best interference estimate.

4.4.6 DIMUS

The success of the DIMUS/AN processor prompted trying straight DIMUS beamforming (see Ref. 8 and Appendix A). Actually, DIMUS beamforming had been tried earlier on the two-dimensional model data with what seemed like poor results. Upon reexamination of the model DIMUS processed data, it was discovered that what first appeared to be strong reflected surface-wave interference following onset of the PP-wave pulse was actually oscillations in the tail of the PP pulse which were accentuated by clipping.

In any event, the results of DIMUS beamforming with orthogonal correlated arrays on the granite block data are quite good (Figures 4-8 through 4-11), relative to DIMUS/AN and all other processors. Certainly DIMUS must be considered as a prime candidate for implementation in this application.

As a further test, the DIMUS-derived processors were applied to the model data. These results are shown in Figures 4-14 and 4-15. Comparison of these with the linear processors of Figures 4-4 and 4-5 shows that they perform as well as the best linear processor on this, the most favorable data.
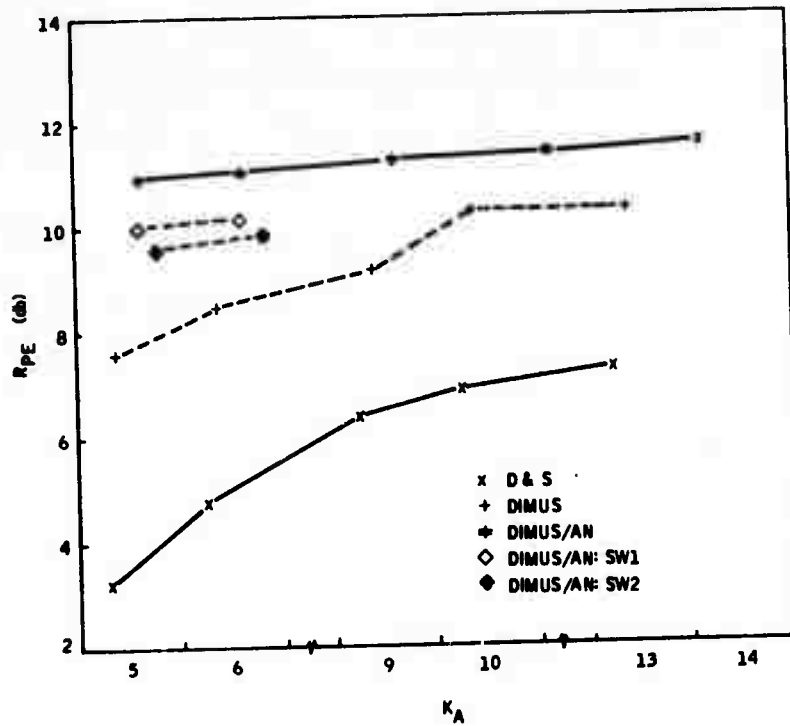
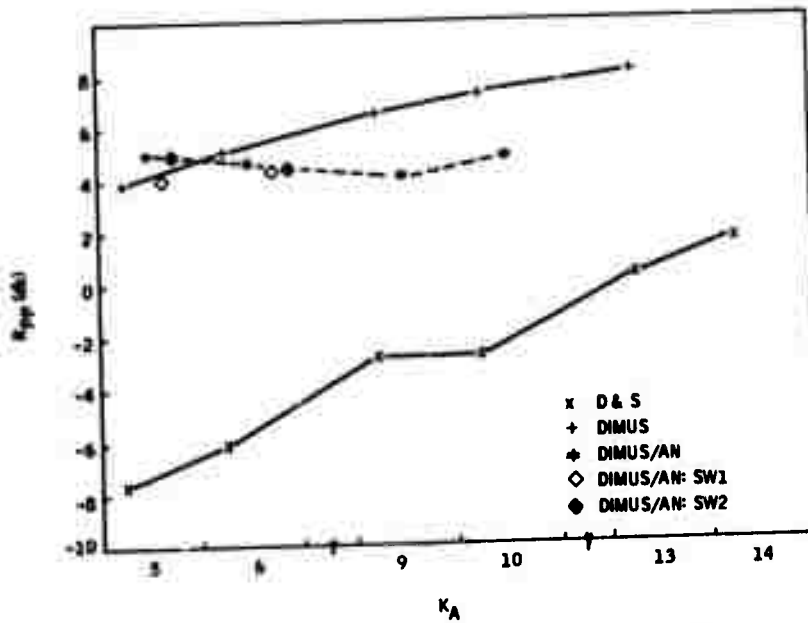Figure 4-14. R_{PE} versus K_A - DIMUS Performance for Seismic Model Data

Figure 4-15. R_{PP} versus K_A - DIMUS Performance for Seismic Model Data

Absent in the preceding discussion have been results from these processors on in-situ data gathered at the quarry sites. However, there was no consistent detection of a P-wave reflection from the natural fracture that was expected in the site A data. For this reason, the data was not reduced and presented in this summary of results. However, it is discussed in Section 4.5.

In spite of the failure of either DIMUS or DIMUS/AN to detect a PP wave in the Charcoal Quarry data, it is recommended that these two processors be selected for continued study of array processing in Phase II. Although their average performance measures were often comparable, and DIMUS is the simpler of the two, it is felt that DIMUS/AN has qualities not possessed by DIMUS. In comparisons of processor records in Section 4.5, it will be seen that DIMUS/AN can present a more easily detected signal than DIMUS, even though both have comparable average performance indices. This, plus the somewhat limited data base for this study, make it judicious to keep both array processor options open at this stage of the program.

4.5 DISCUSSION OF PROCESSOR OUTPUT RECORDS

In many respects, the average performance measures, R_{PE} and R_{PP}, used to summarize results in Sections 4.3 and 4.4 need to be supplemented with qualitative descriptors. Two processors with comparable R_{PE} and R_{PP}, as measured here with a priori knowledge of the signal arrival times, can have considerably different detectability to an operator not possessing this information. Also, some processors, particularly the DIMUS-related processors, appear to have higher detectability than these average performance measures would indicate.

Because of the large number of record stacks represented in the averaged data of Sections 4.3 and 4.4, only a fraction of the runs can reasonably be exhibited here. Even by limiting the plots to one (usually) representative sample for each processor per experimental setup, the number of figures required is quite large. In all but the Charcoal Quarry data, the record lengths are 1.4 msec. A scale of 0.1 msec/cm is used throughout. The sequence of numbers K_S designates the starting element (element numbers in sequence from the driver) for each array in the stack. In most cases, the stack sequence is $K_S = 1, 2, 3, 4$. However, due to an error in reprogramming the processors for production runs, a number of stacks have the sequence $K_S = 1, 2, 4, 7$. Since all arrays were phased relative to the origin at the source, this discrepancy does not invalidate the results.

4.5.1 Seismic Model

Several seismic arrivals can easily be identified on the model data of Figure 3-19. The most obvious arrivals are plotted on a travel-time curve in

Figure 4-16. All of the plotted points are calculated from peaks and troughs rather than first motion. Some theoretically calculated arrivals are also plotted as dotted lines. The slight variations in the observed and the theoretical travel-times is because the observed arrivals represent peaks and troughs rather than first motion.

From the slope of the lines in the travel-time curve, the P-wave velocity is found to be 2350 m/sec and the surface wave velocity 1175 m/sec. It was not possible to identify the direct S wave on the seismogram. Previous studies also indicate this difficulty in identifying the direct S wave.

The outstanding events on the seismograms are identified as PP, surface waves, and reflected surface waves from the sides of the model.

The image source to the parallel reflecting boundary on the seismic model was at 182 cm. Since the P-wave velocity $V = 2.3$ km/sec, the PP signal is expected at 0.79 msec.

The model presented a clean separation of the direct surface wave and reflected P wave, with no interfering surface-wave reflections present within the 1.4-msec record. As a result, every processor provides a detectable signal on the basis of the alignment of the PP waveforms in the stacks, irrespective of their average performance measures, R_{PE} and R_{PP}.

Some of the salient features to be noted in the results presented in this section (Figures 4-17 through 4-32) are:

- The lack of effect of gain compensation on the processed direct surface waveforms (compare Figures 4-17 and 4-18 for D&S, Figures 4-19 and 4-20 for D-T).

- Alteration of the processed surface waveform by change in D-T shading, but failure to achieve uniform suppression over the trace (compare Figures 4-21 and 4-22 for D-T/20 and D-T/40).

- The random noise-like character of the processed surface waveform for DIMUS and DIMUS/AN (Figures 4-25 through 4-28). This is the reason that these processors are so effective in suppressing the direct surface wave in correlation of orthogonal line arrays. Clipping the direct surface waves also greatly improves the linear processors (Figures 4-29 through 4-32), though the fan filter benefits least.

- Broadening of the pulse by accenting the tails as a result of clipping (Figures 4-25 through 4-28). Since the processed PP pulse level is high over 40% of the record for DIMUS and DIMUS/AN, the R_{PE} performance measures for these processors are therefore somewhat pessimistic.

4-23
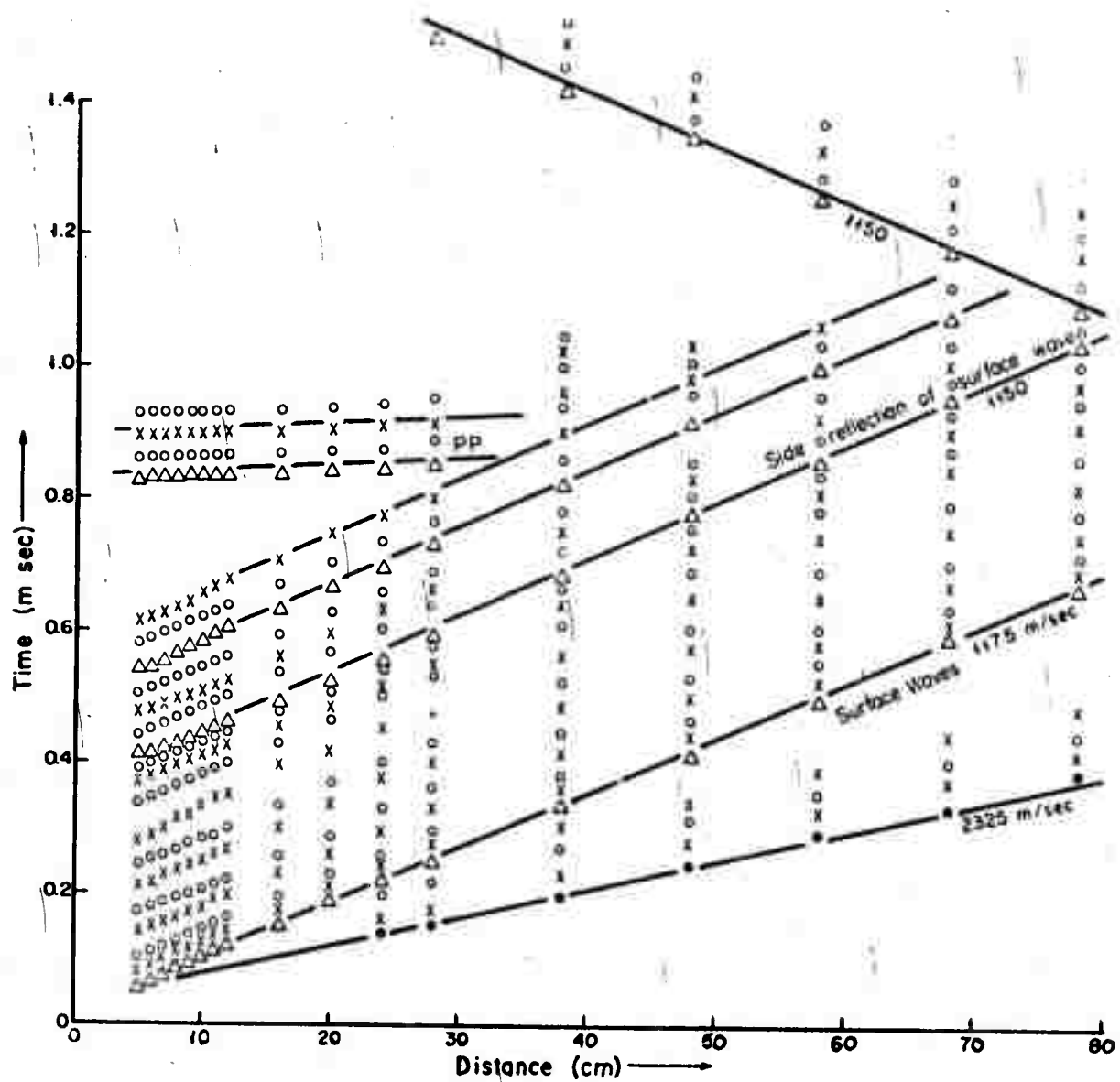
Figure 4-16. Travel-Time Curves for Seismic Model

Figure 4-17. Seismic Model, Ten-Element Delay-and-Sum Beamformer

Figure 4-18. Seismic Model, Ten-Element Delay-and-Sum
Beamformer - Gain Compensated
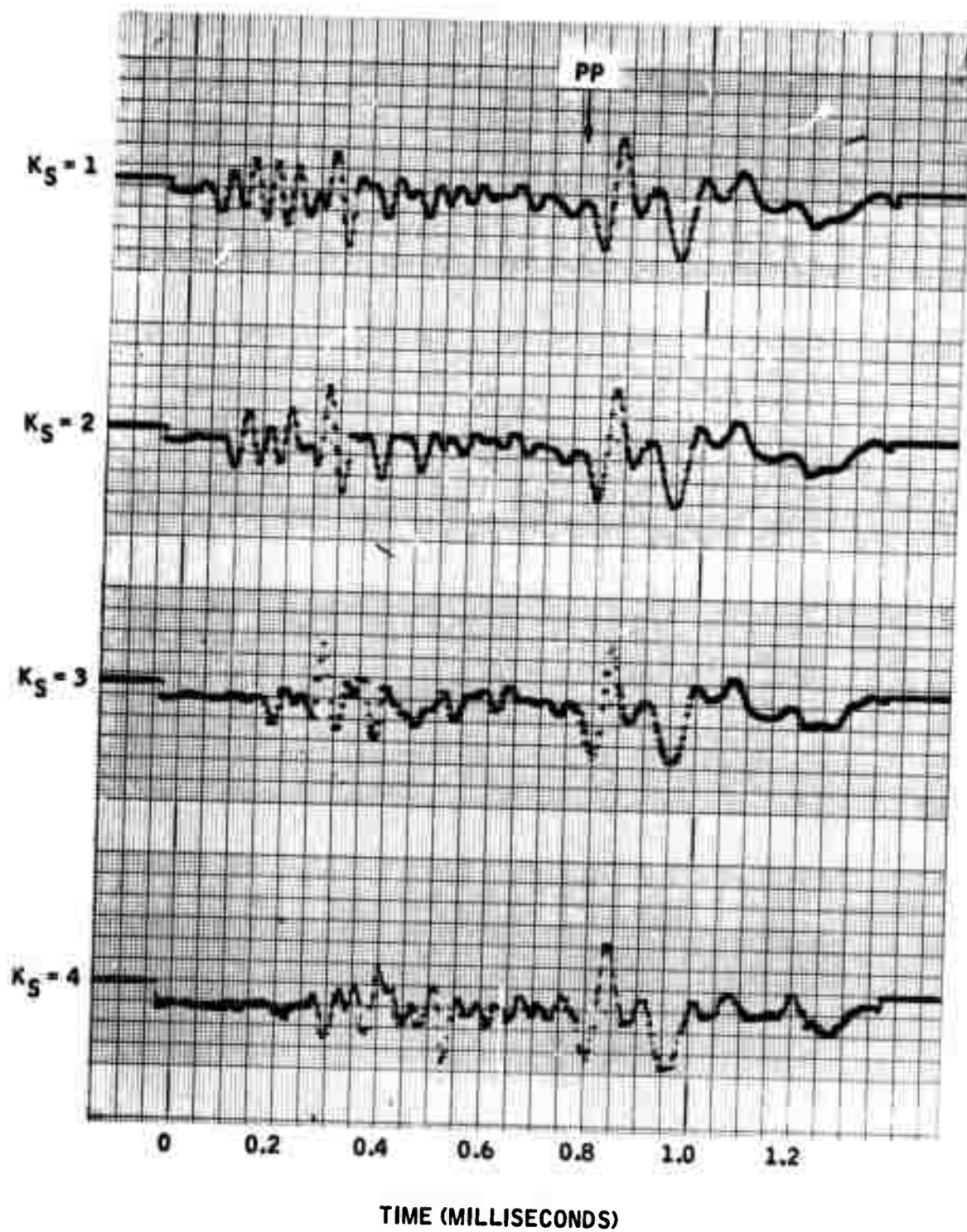
Figure 4-19. Seismic Model, Nine-Element Dolph-Tchebyscheff Beamformer

4-27

Figure 4-20. Seismic Model, Nine-Element Dolph-Tchebyscheff
Beamformer - Gain Compensated

4-28
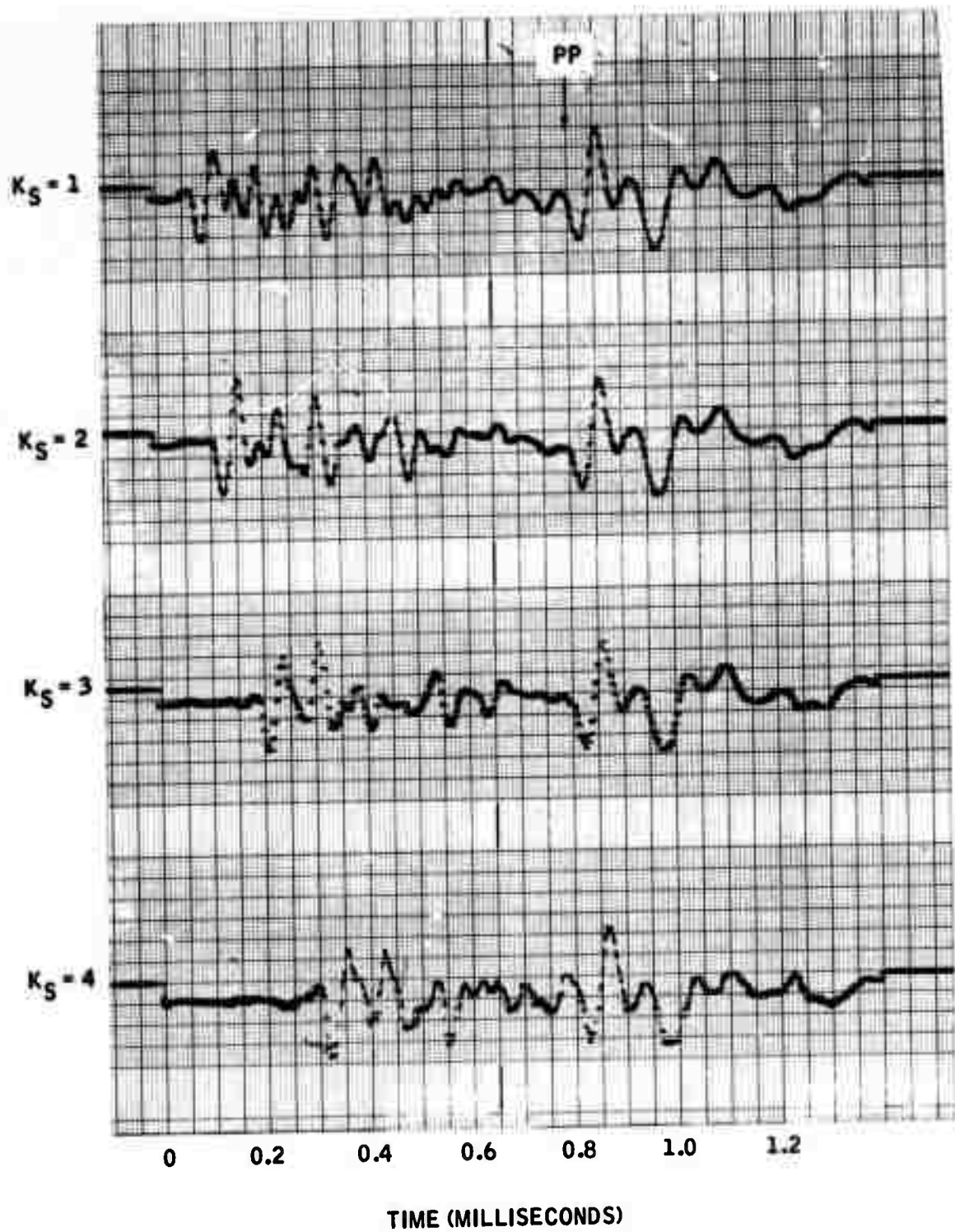
Figure 4-21.   Seismic Model, Nine-Element Dolph-Tchebyscheff
Beamformer - 20-db Sidelobes
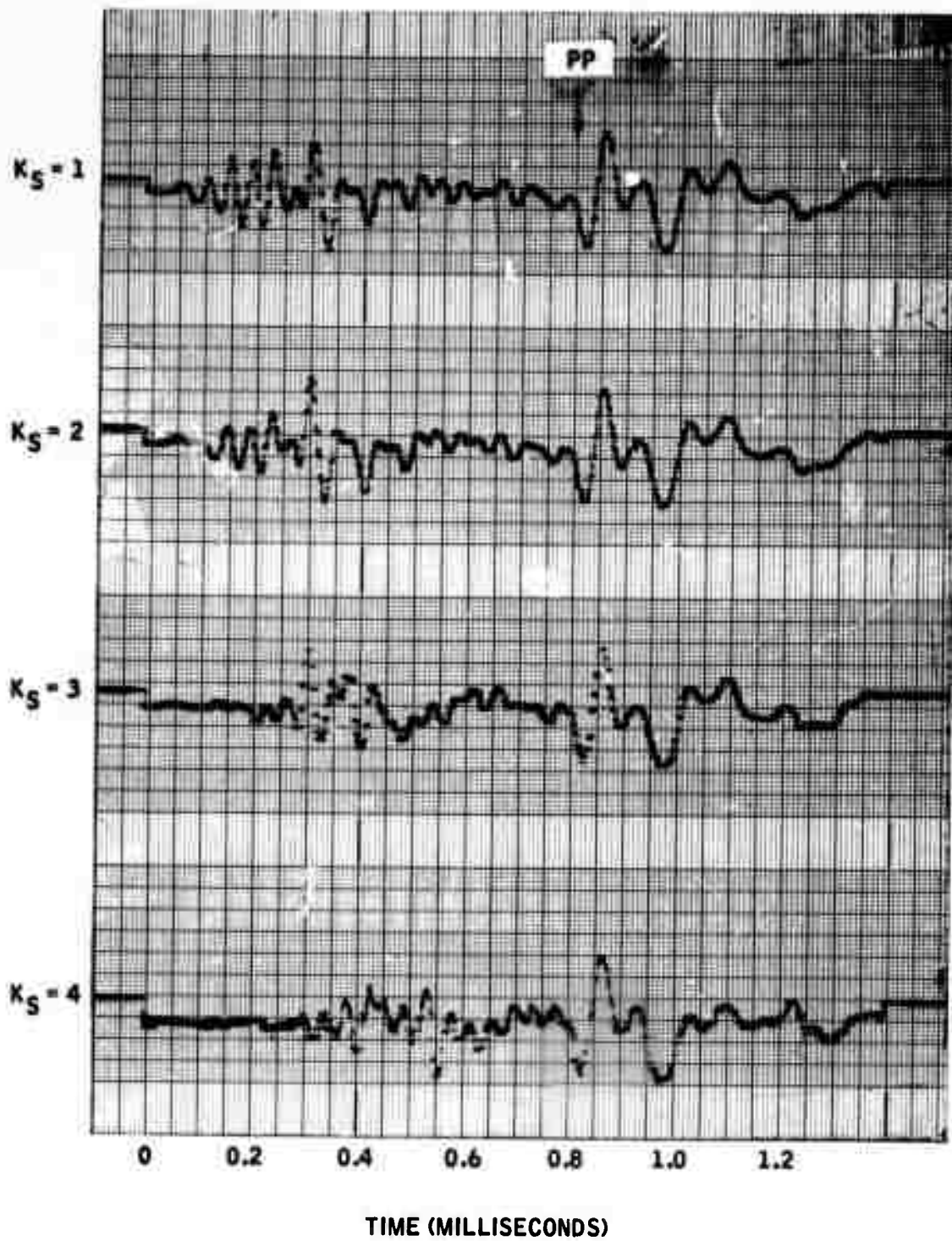
Figure 4-22. Seismic Model, Nine-Element Dolph-Tchebyscheff
Beamformer - 40-db Sidelobes

4-30

Figure 4-23. Seismic Model, Fixed-Null plus Nine-Element Dolph-Tchebyscheff Beamformer - 20-db Sidelobes

TIME (MILLISECONDS)
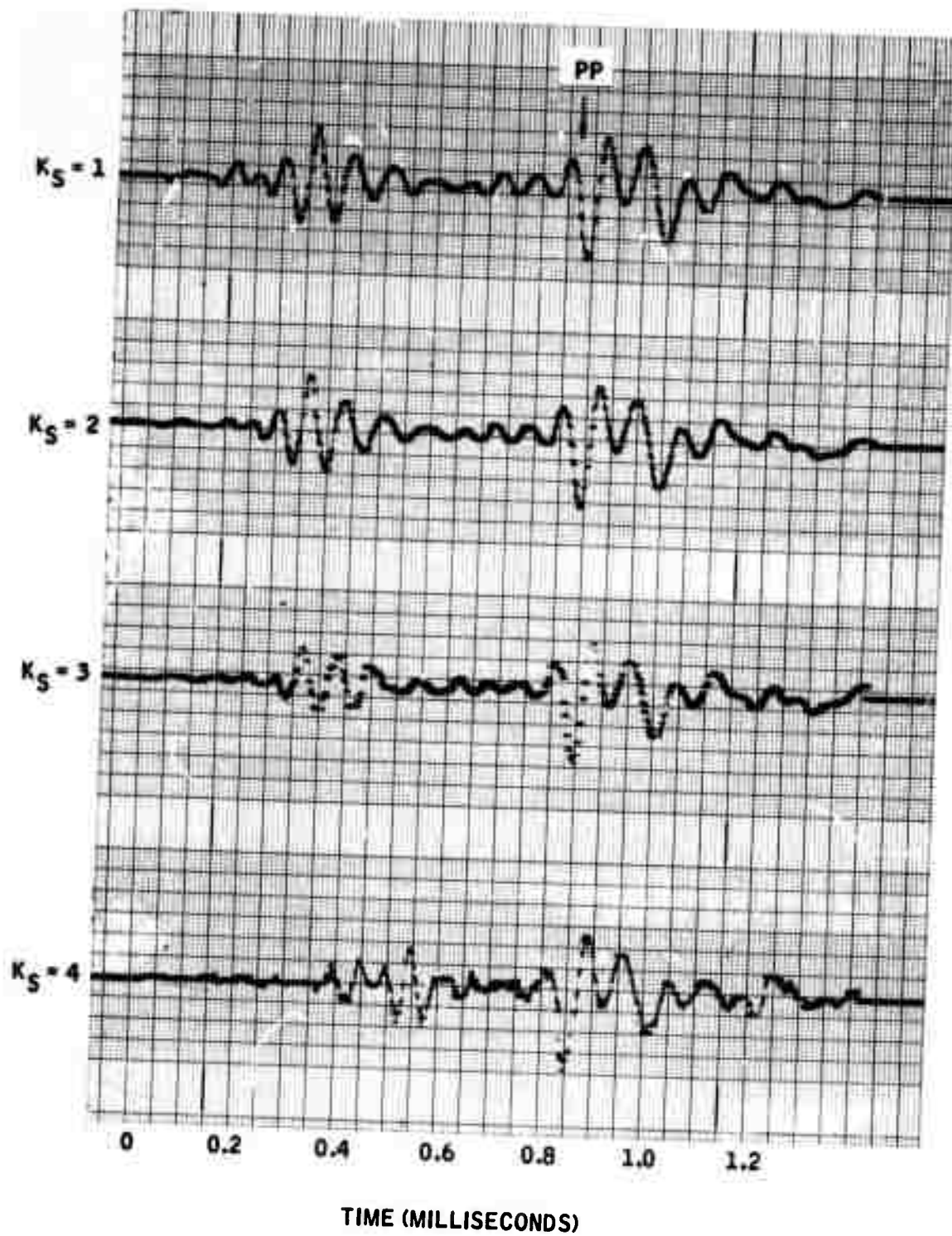
Figure 4-24. Seismic Model, Fixed-Null plus Nine-Element Dolph-Tchebyscheff Beamformer - 40-db Sidelobes
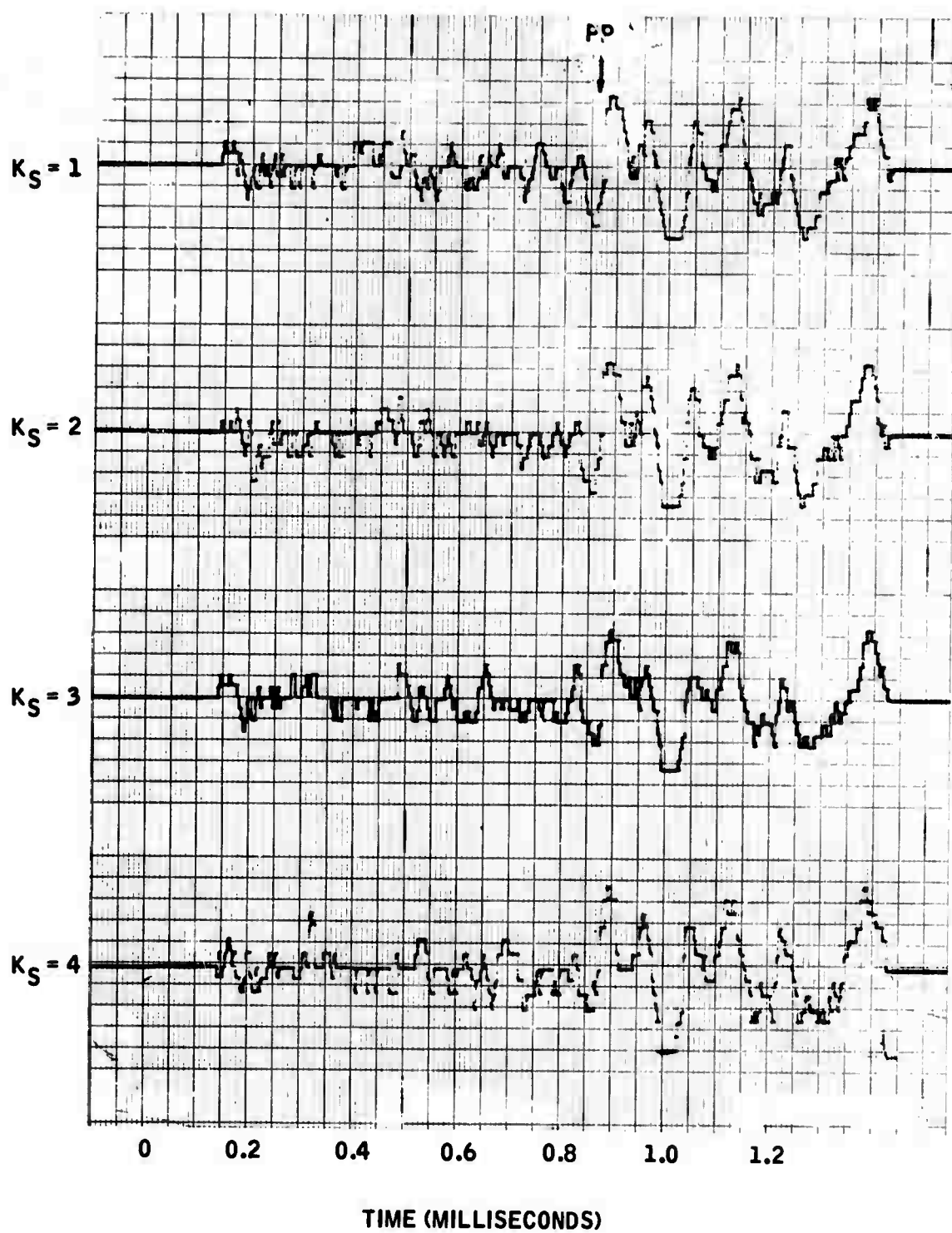
Figure 4-25.   Seismic Model, Six-Element DIMUS Beamformer

4-33
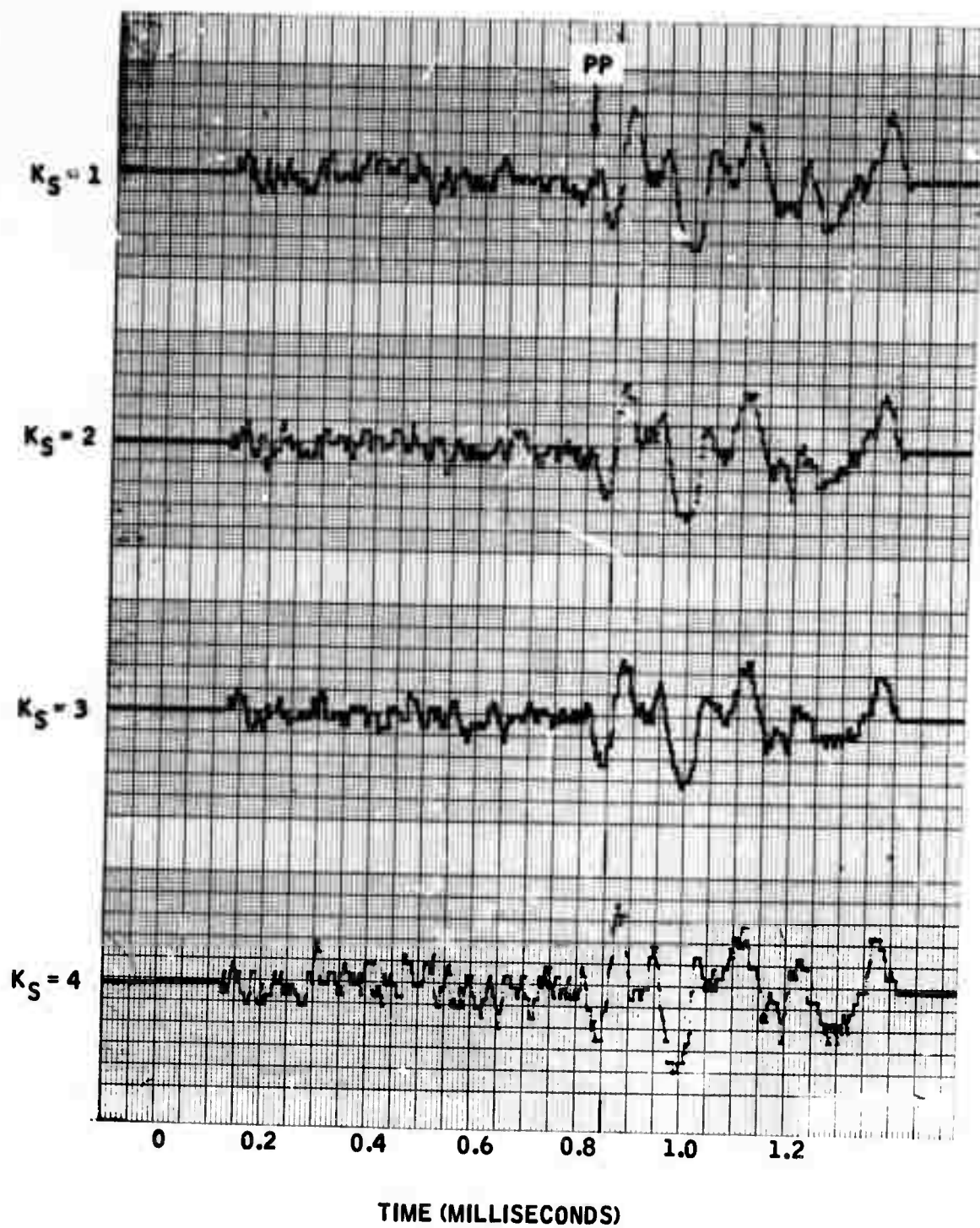
Figure 4-26. Seismic Model, Ten-Element DIMUS Beamformer

TIME (MILLISECONDS)
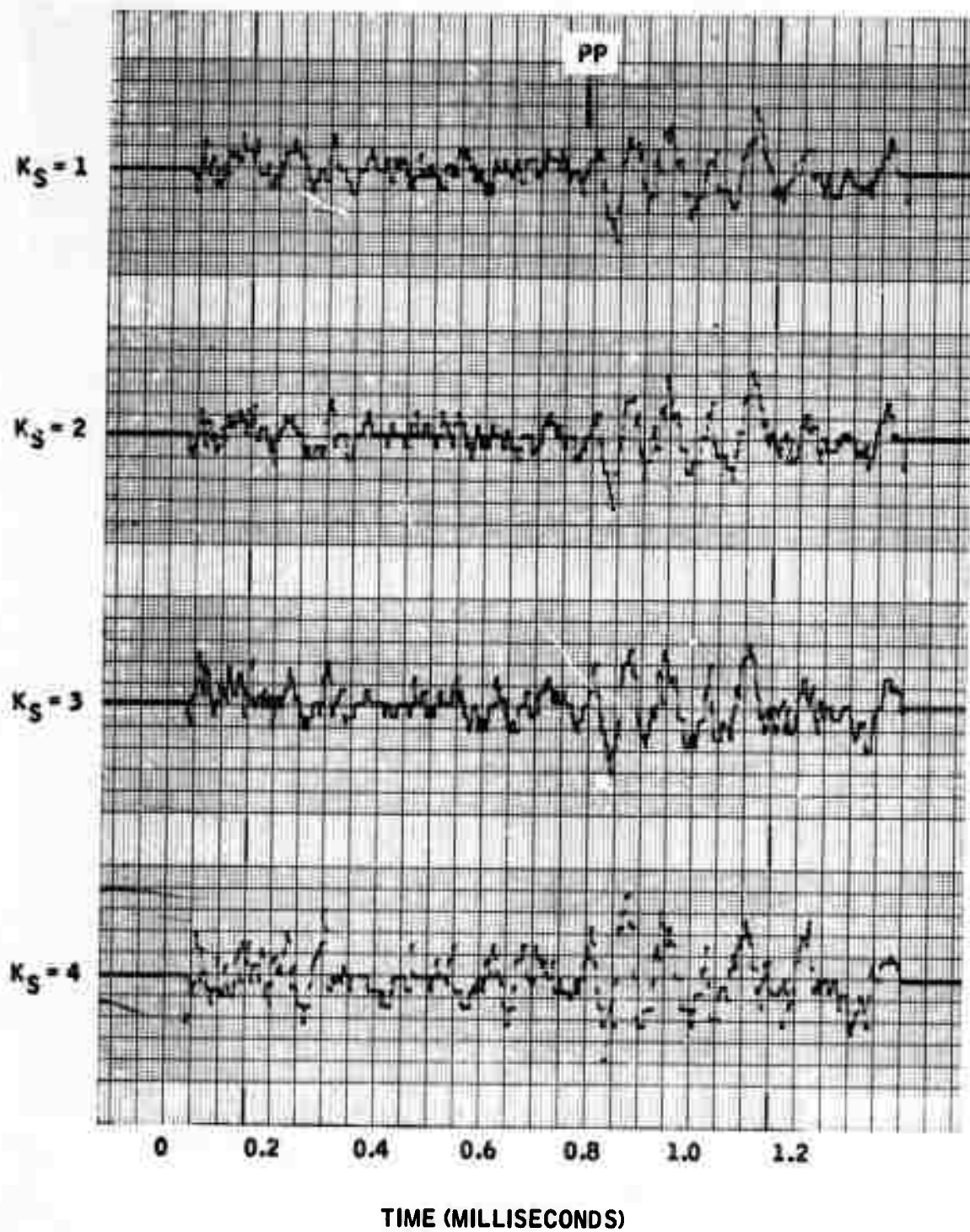
Figure 4-27. Seismic Model, Six-Element Adaptive-Null plus
DIMUS Beamformer

4-35

Figure 4-28. Seismic Model, Ten-Element Adaptive-Null plus DIMUS Beamformer
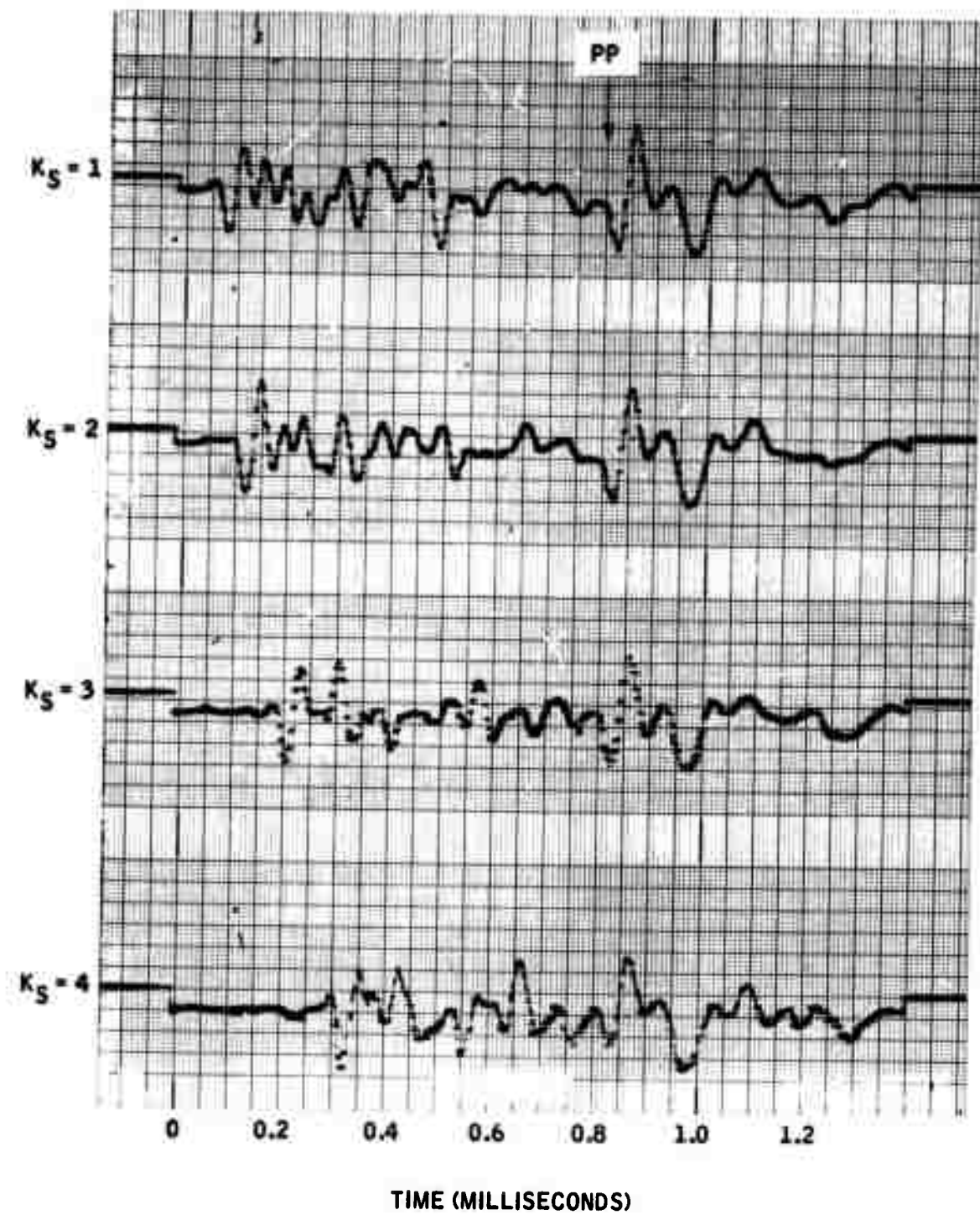
Figure 4-29. Seismic Model, Ten-Element Delay-and-Sum Beamformer - High-Gain Data
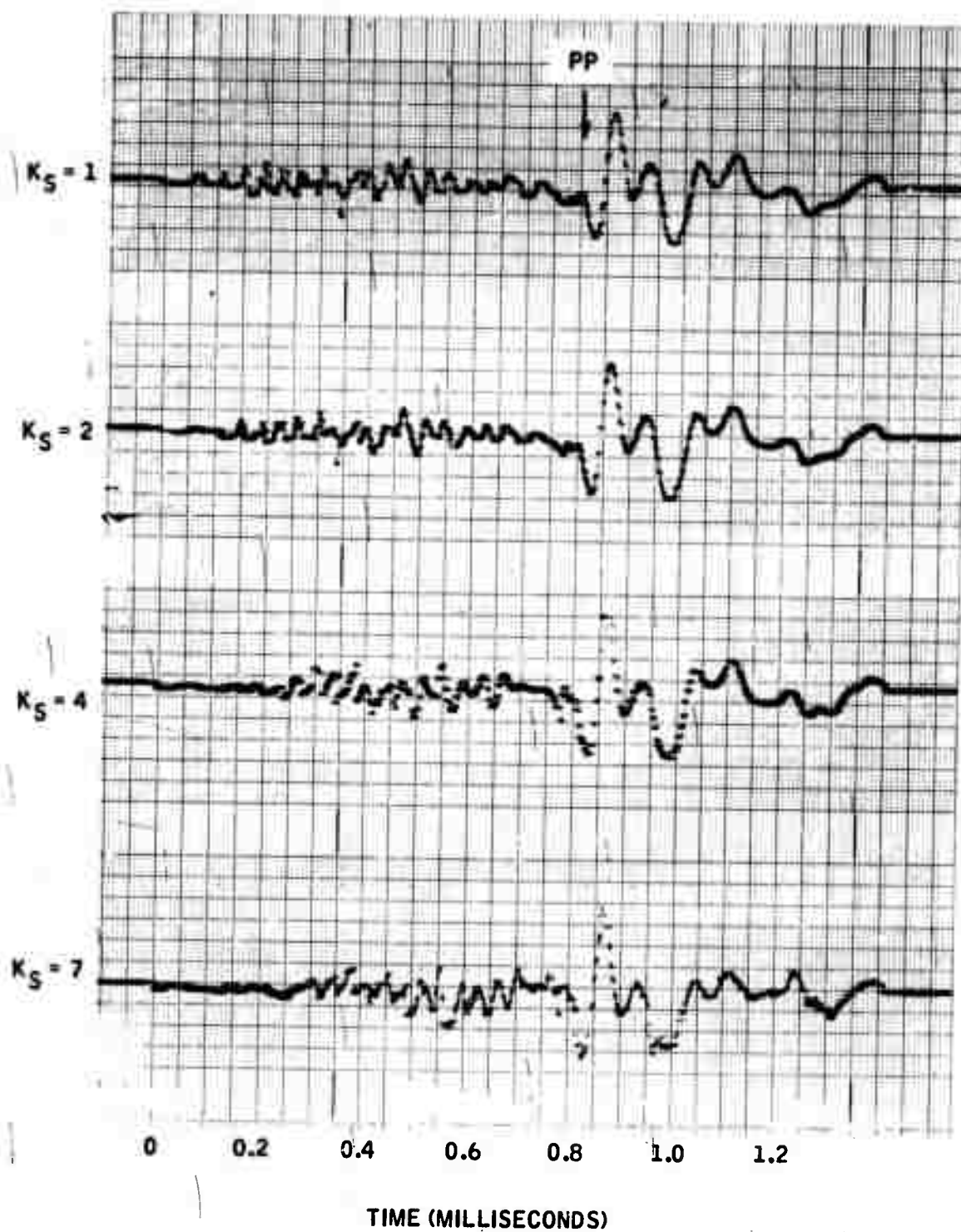
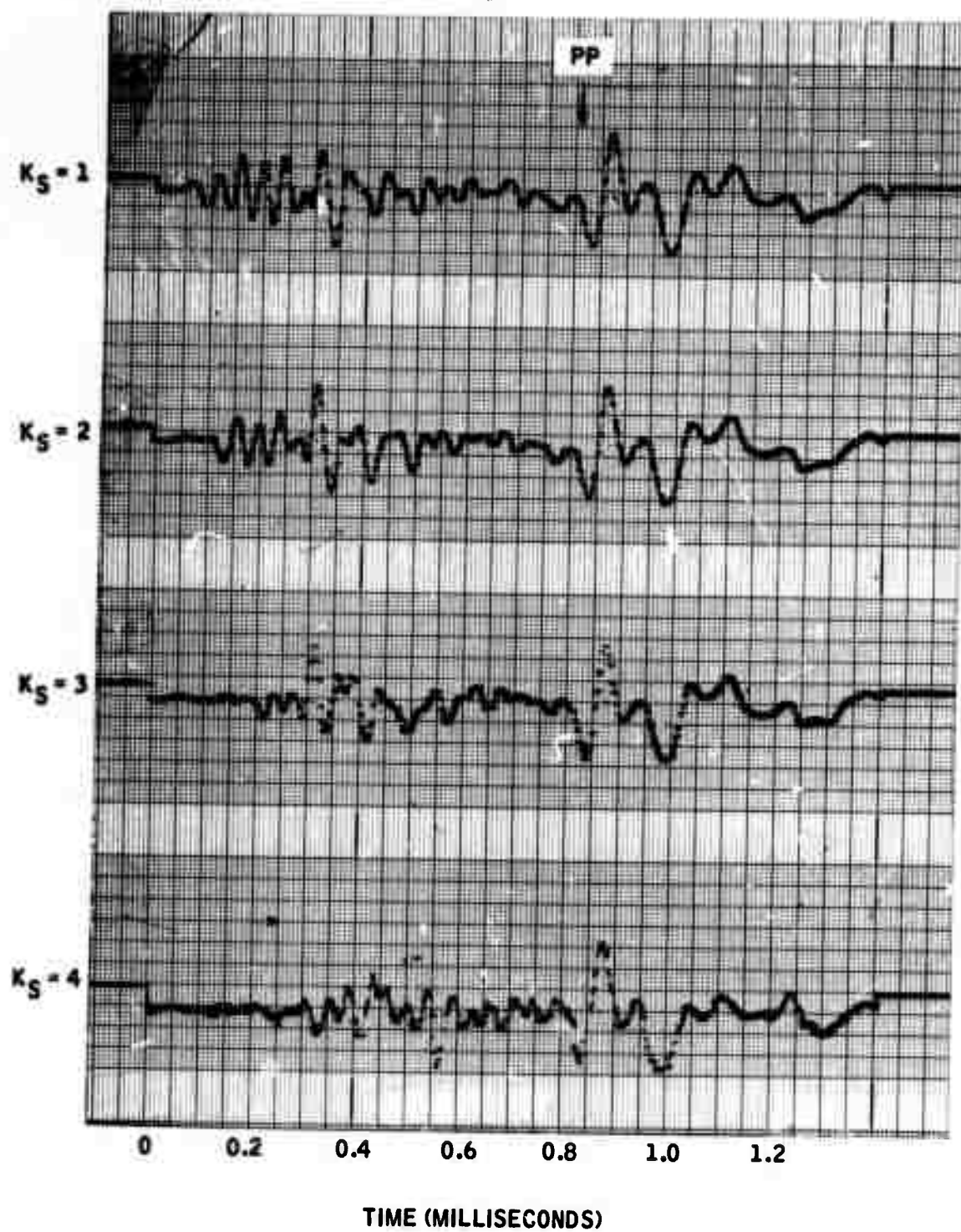Figure 4-30. Seismic Model, Nine-Element Dolph-Tchebyscheff
Beamformer - High-Gain Data

4-38

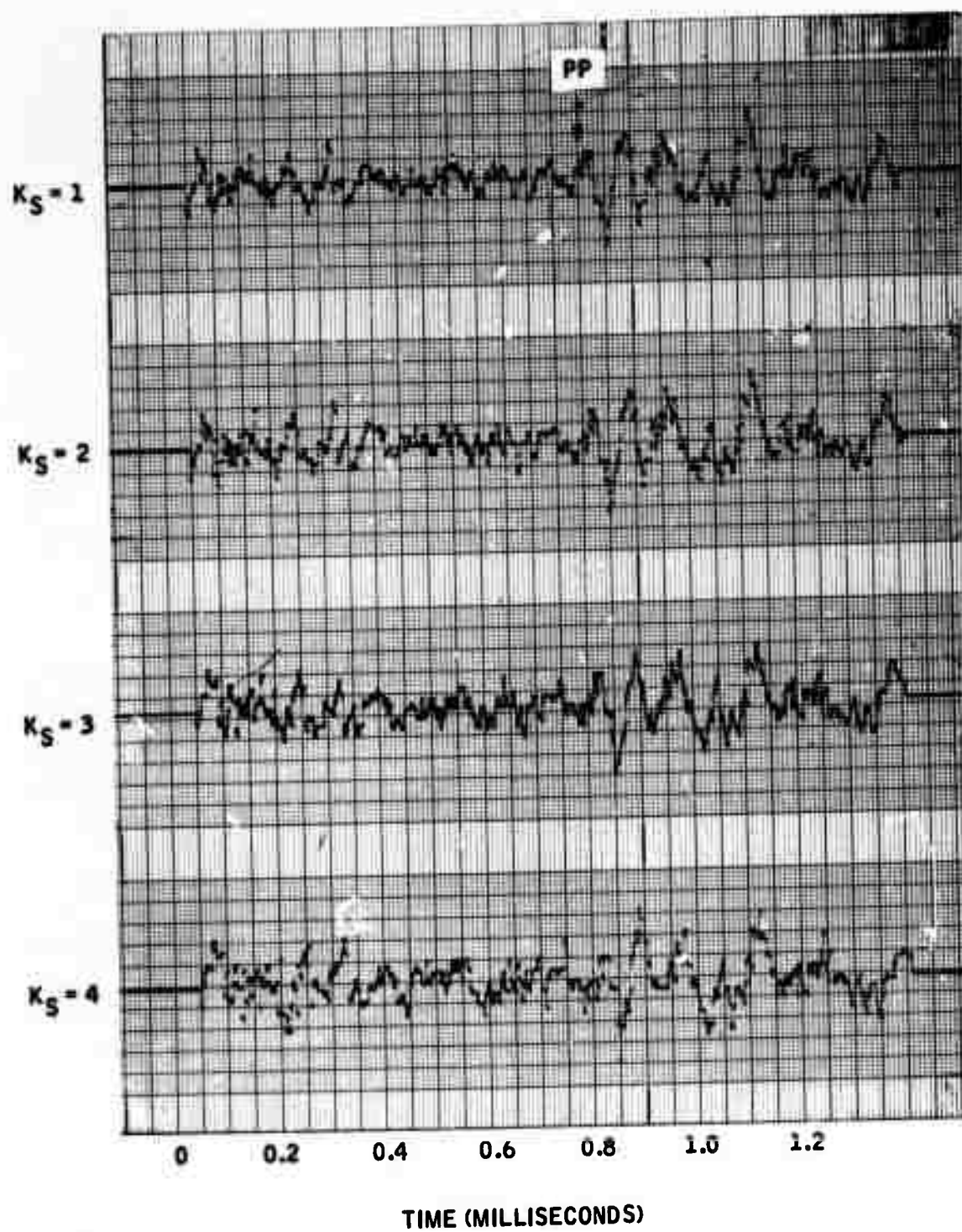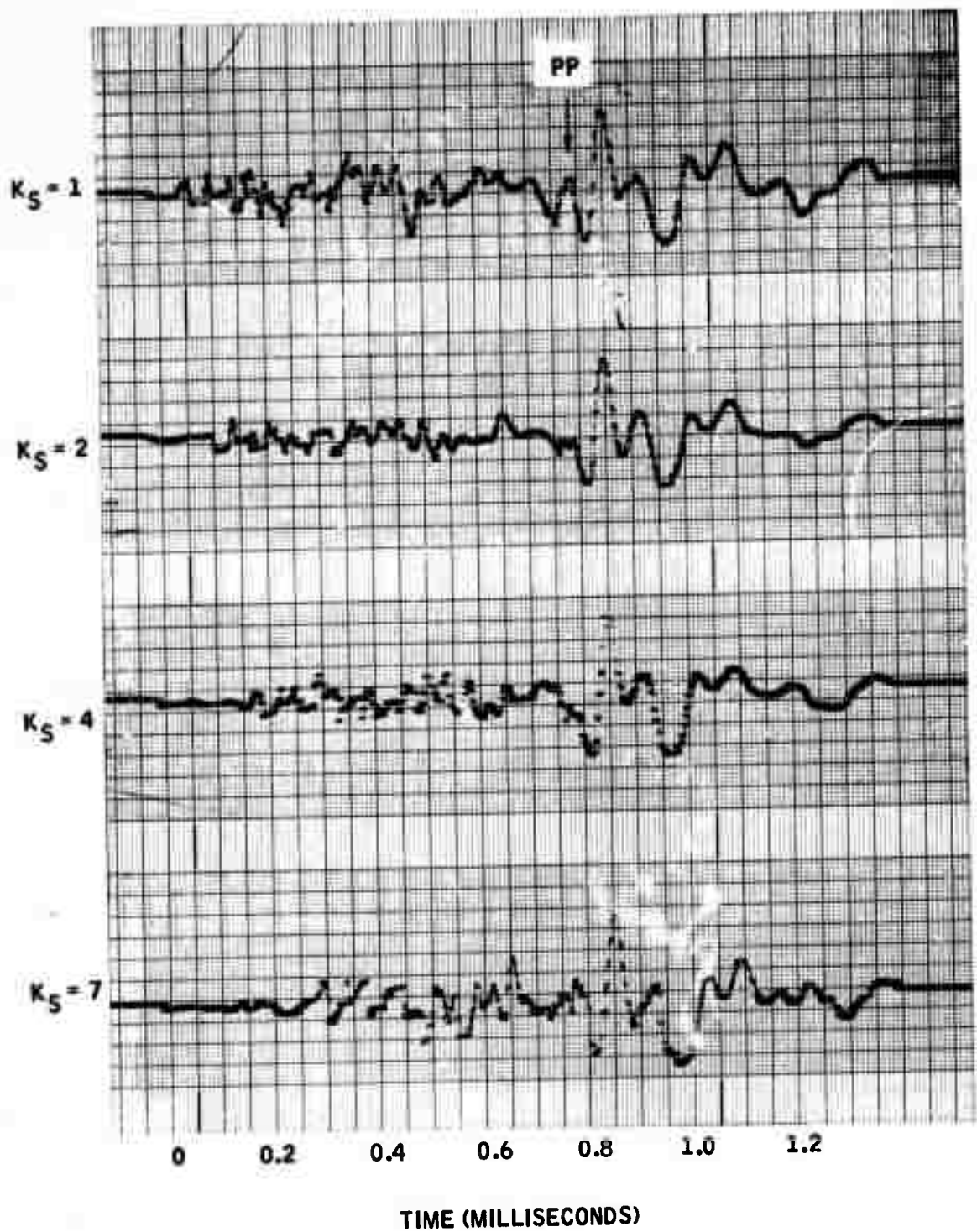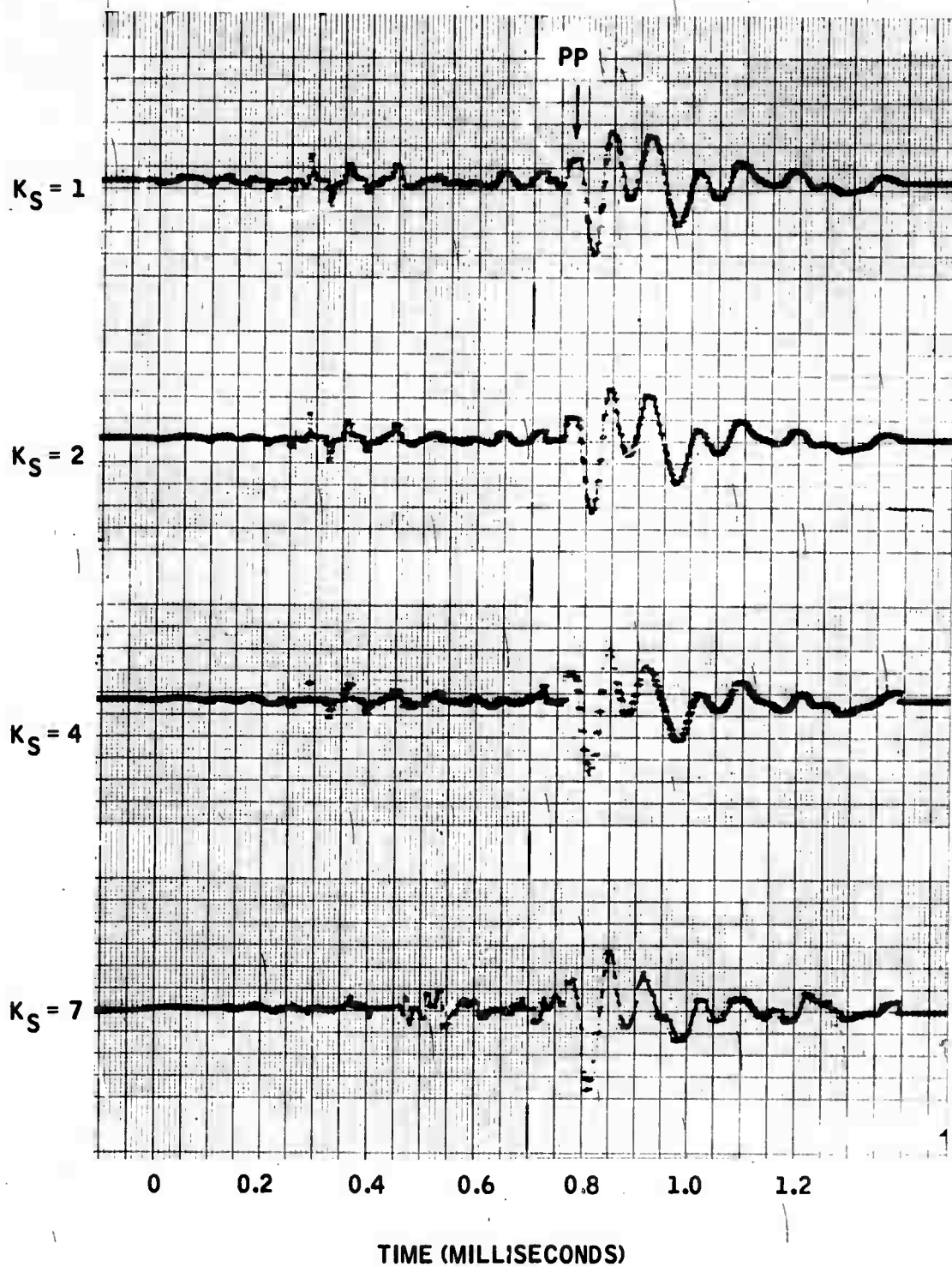Figure 4-31. Seismic Model, Nine-Element Fixed-Null plus Dolph-Tchebyscheff Beamformer - High-Gain Data
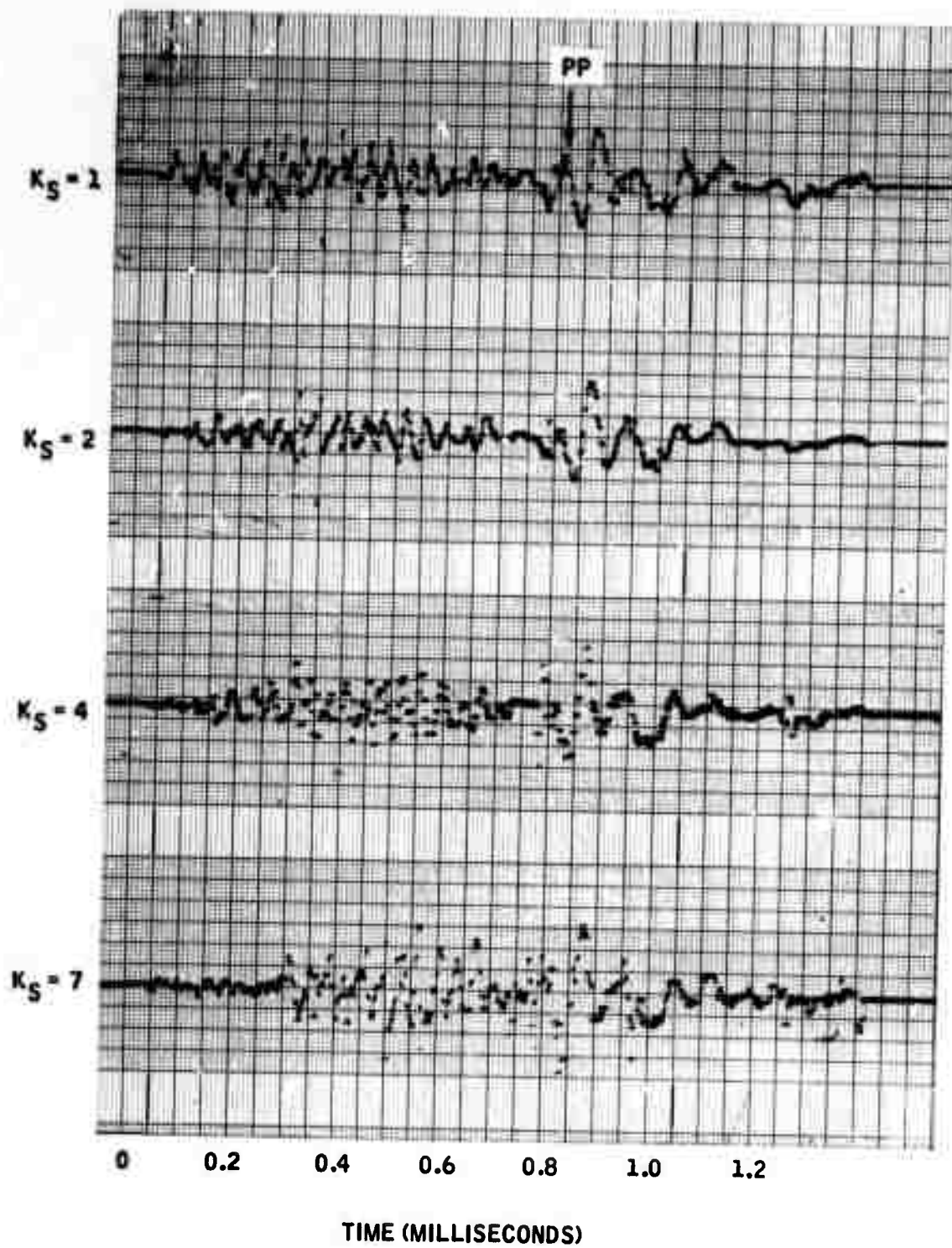
Figure 4-32. Seismic Model, Ten-Element Fan Filter - High-Gain Data

4-40

- The qualitatively superior performance of DIMUS to all other processors in this instance, in spite of its somewhat lesser ranking based on R_{PE} and R_{PP}.

There is still the question of DIMUS performance when reflected surface-wave arrivals coincide with PP arrivals. The granite block provided ample test of this situation, and as will be seen, orthogonal array correlation alleviates this problem considerably.

4.5.2 Granite Block

Three mutually orthogonal arrays, designated South, Up, and North, provided two orthogonal TAP beams, (SXU) and (NXU), for the granite block experiment (see Figure 3-8, Section III). A parallel reflecting boundary at a depth of 6 feet, coupled with V_p = 17,000 ft/sec yielded an expected arrival time of 0.71 msec for the PP wave at the origin. However, the boundary at the bottom of the block at about 3.5 feet from the source, coupled with a surface-wave velocity of 10,000 ft/sec, indicated that a reflected surface wave could also be expected at about the same time. Since this boundary was parallel with the S and N arrays, beams steered on the PP wave with these two arrays would also be steered on this surface reflection as well.

In addition to the bottom boundary, the top boundary surface reflection is expected at about 0.87 msec at the origin, and again approximately normal to the S and N arrays. Although the side boundaries are rough, they are approximately parallel with the U array and yield reflected surface-wave arrivals at about 0.88 msec and 1.0 msec which are approximately normal to the U array. Figure 4-33 is a travel-time plot for the data of Figure 3-9 (the S array).

The D&S and D-T/30 TAP beams were completely dominated by the direct surface wave with no indication of a P reflection, as illustrated in Figures 4-34 through 4-37. The FN/30 processor helped reduce the direct surface wave and yielded a detectable PP pulse, especially in the (NXU) beam (Figure 4-41). It should be mentioned that the 0.1-msec correlation window was not centered on the sample point, but rather started at the sample point in these data. Therefore, the PP maxima occur at about 0.65 msec rather than at about 0.7 msec.

The S and U processed array outputs for FN/30 are shown in Figures 4-38 and 4-39 to illustrate the processed waveforms before multiplication and averaging. In the S-array output, oscillations commence at about 0.6 msec or about 0.1 msec prior to the expected arrival of the PP and bottom-reflected surface waves. This is probably surface-wave reflection from a hole in the source face near the bottom of the block. The approximately normal surface-wave reflection from the top is not as evident in the K_S = 1 and 2 traces as in the K_S = 4 and 7 traces.

4-41
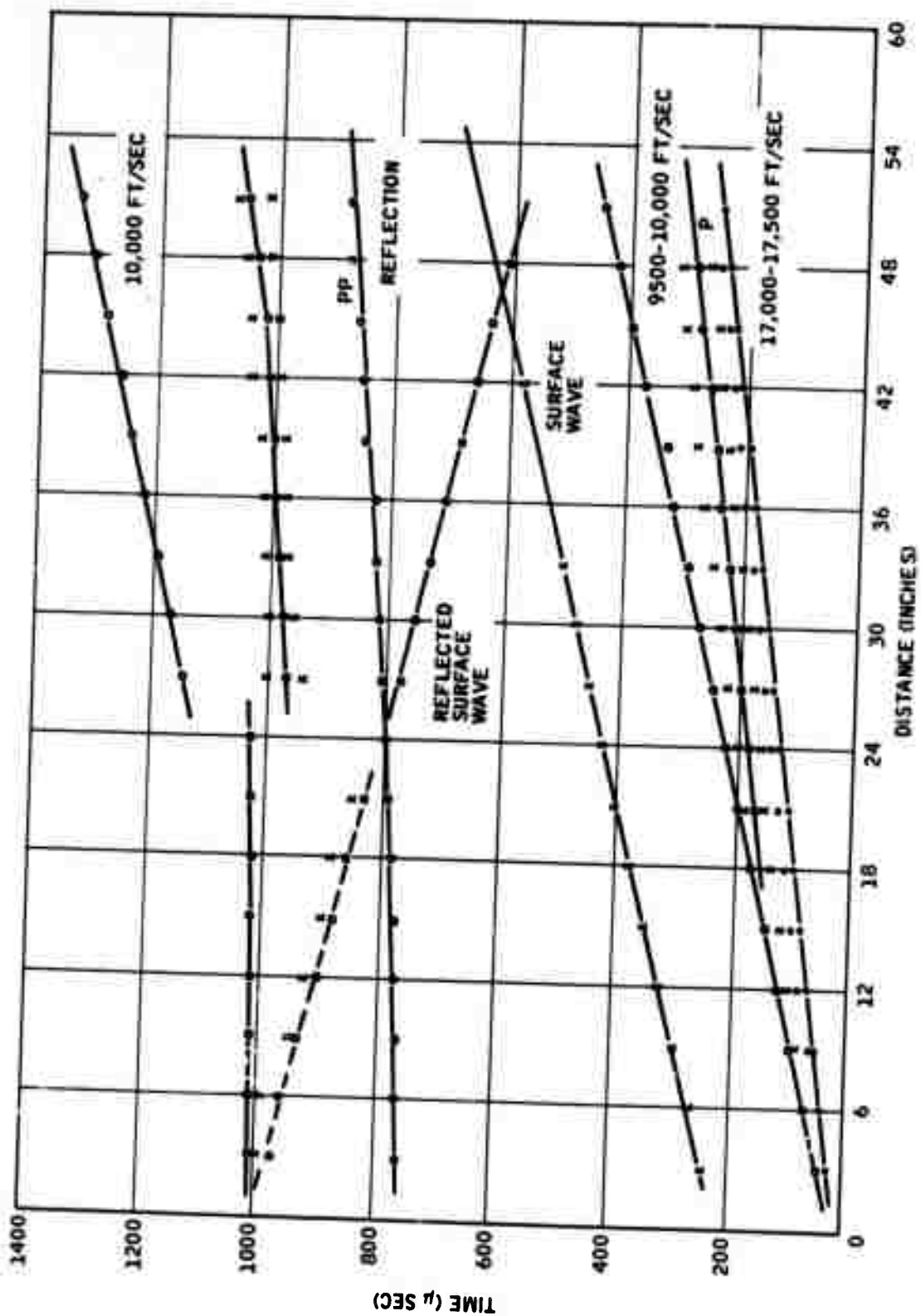
Figure 4-33. Travel Times for Granite Block S-Array

Figure 4-34. Granite Block, Cross-Correlation (SXU) of Delay-and-Sum Beams

Figure 4-35. Granite Block, Cross-Correlation (NXU) of Delay-and-Sum Beams

4-44

Figure 4-36. Granite Block, Cross-Correlation (SXU) of D-T Weighted Delay-and-Sum Beams

4-45
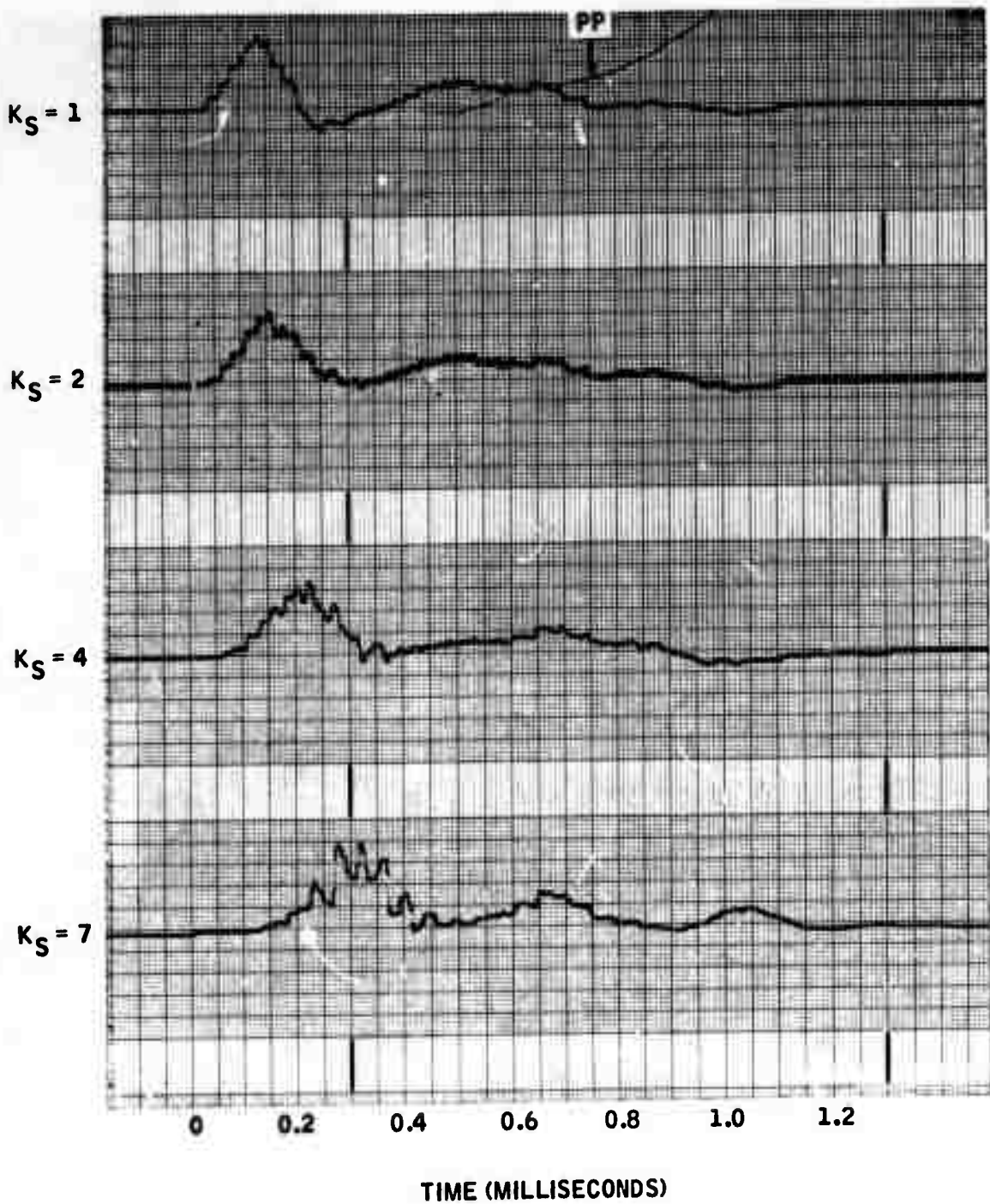
Figure 4-37. Granite Block, Cross-Correlation (NXU) of D-T Weighted Delay-and-Sum Beams

4-46
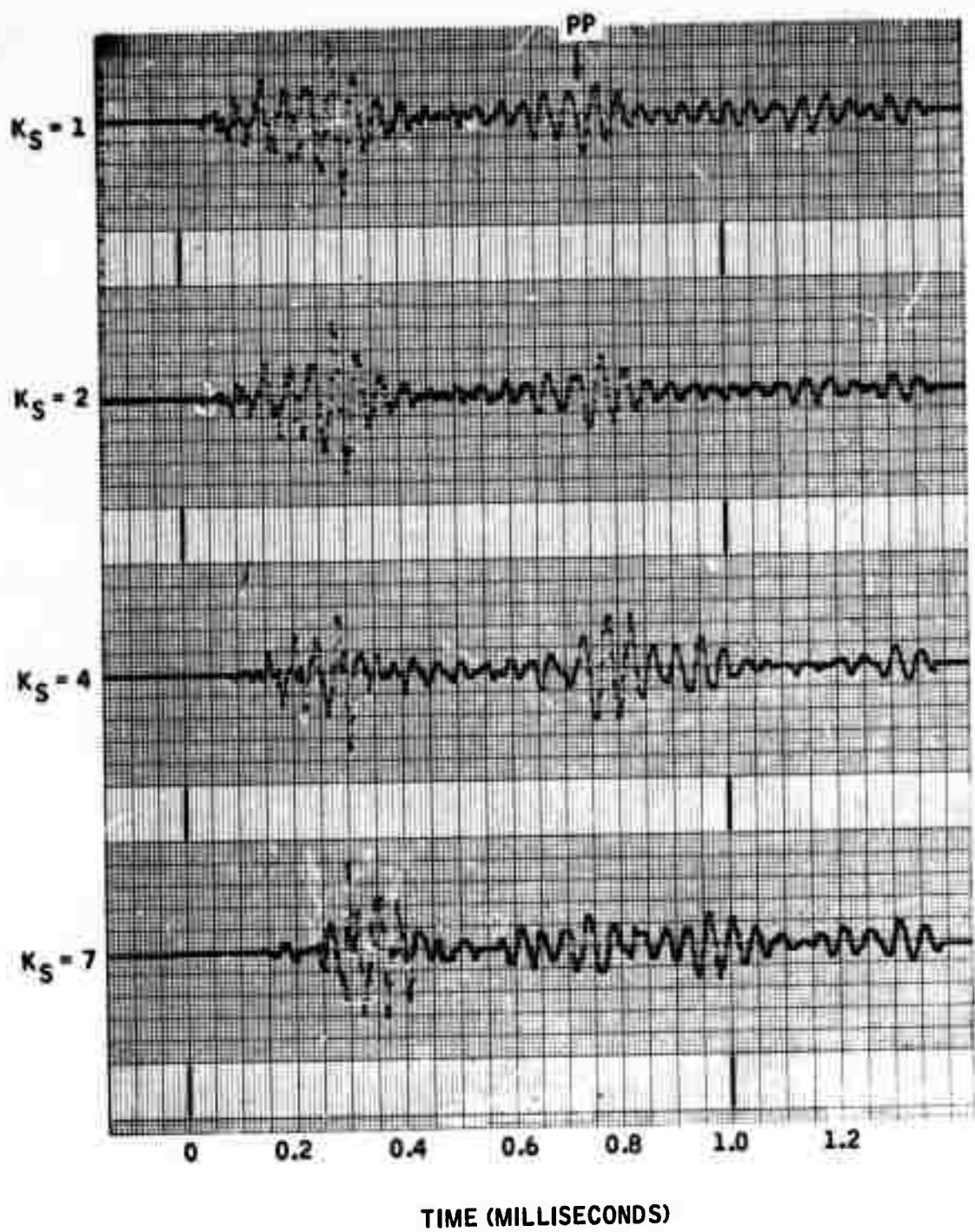
Figure 4-38. Granite Block (S), Fixed-Null plus D-T Weighted
Delay-and-Sum Nine-Element Beam
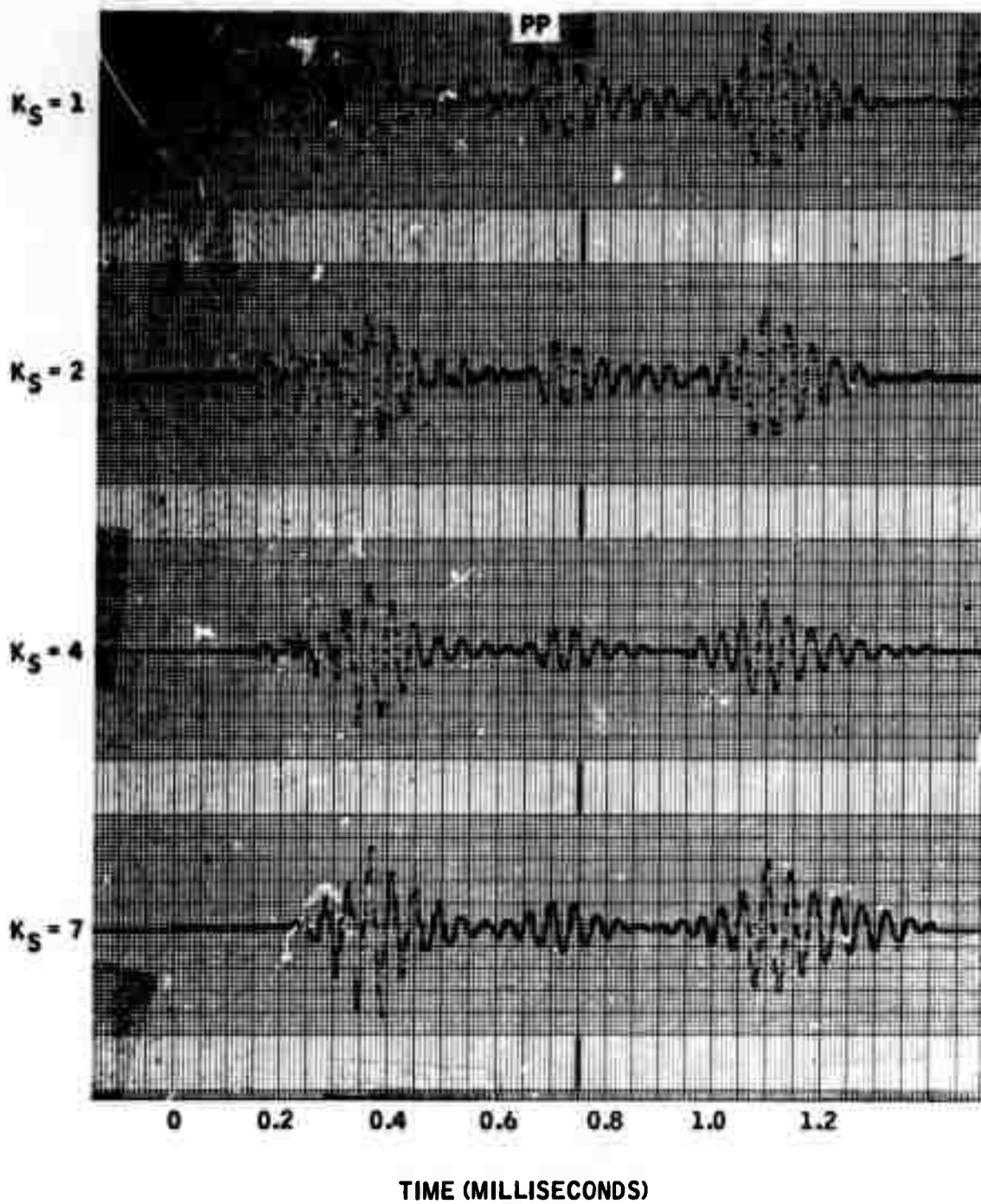
Figure 4-39. Granite Block (U), Fixed-Null plus D-T Weighted
Delay-and-Sum Nine-Element Beam

The PP wave is quite evident in the U-array output because the coincident bottom-surface-wave reflection is aligned with U array and therefore nulled by the FN/30 processor. Also note the strong surface-wave reflection from the south sidewall commencing at about 1 msec.

Failure of the $K_S = 7$ arrays to produce a PP correlation peak in the (SXU) beam, Figure 4-40, can be traced to a 90-degree phase shift between the S and U outputs in the vicinity of 0.7 msec. This seems to be due to surface-wave interference distorting the waveform in the S array.

Fan-filter results are shown in Figures 4-42 and 4-43. In contrast to the FN processor, the FF U-array trace exhibited no discernable PP arrival. In the (SXU) and (NXU) beams, relative maxima at 0.7 msec are just barely discernable.

Beamformer outputs from the S and U arrays with adaptive zero-memory/ least-squares processing, and their TAP beam, are shown in Figures 4-44 through 4-46. The lack of any evidence of a PP reception, plus the relative complexity of this processor, led to its rejection for this application.

DIMUS processing results are illustrated in Figures 4-47 through 4-51. In the case of a six-element array, Figures 4-47 and 4-48, suppression of the direct surface wave is good, as it was in the seismic model data. Normally incident surface-wave reflections appear to correlate with their orthogonal counterparts, but with the aid of vertical visual correlation down the stack, it is reasonable to say that these would be rejected while the vertically aligned maxima at about 0.7 msec would be accepted as a PP arrival. Note a symmetric averaging window was used in these runs, so there is not a 50-μsec shift in the time base as in the FN case.

The ten-element U-array DIMUS beamformer output shown in Figure 4-49 is revealing because none of the isolation of the PP waveform that was evident in the U array for the FN/30 processor (Figure 4-39) is evident here. Instead, there is a broad train of high-amplitude oscillations covering the range 0.4 to 0.8 msec, roughly. However, in the (SXU) and (NXU) beams, a clearly defined peak at the PP-wave arrival time is evident, and there is no doubt of a detection. Maxima at about 0.5 msec would no doubt lead to an erroneous detection in the (SXU) case but probably not so in the (NXY) case. It is apparent that DIMUS processing requires multiplication and averaging of orthogonal beams to be effective in this application.

Adaptive-null processing results are shown in Figures 4-52 through 4-56. Because of the constraint that prevents nulling of an interference on the beam axis, we see the bottom-reflected surface wave prevalently in the S and N records. However, in the U array, this interference is nulled quite effectively, and the PP waveform is quite evident. As a result, the (SXU) and (NXU) show well-defined maxima (at 0.65 msec because of a nonsymmetric averaging window, again) at the PP arrival time. Residual direct
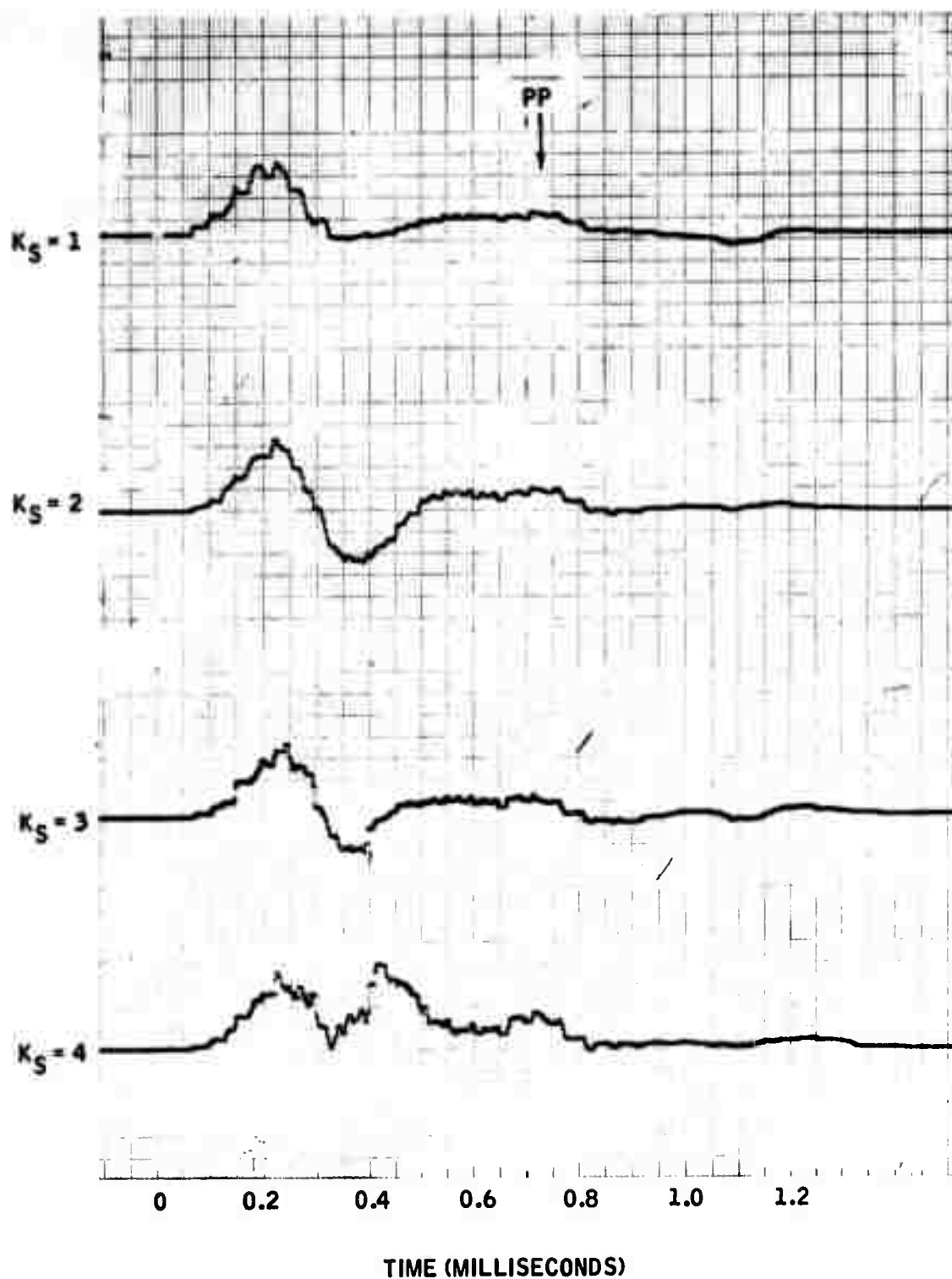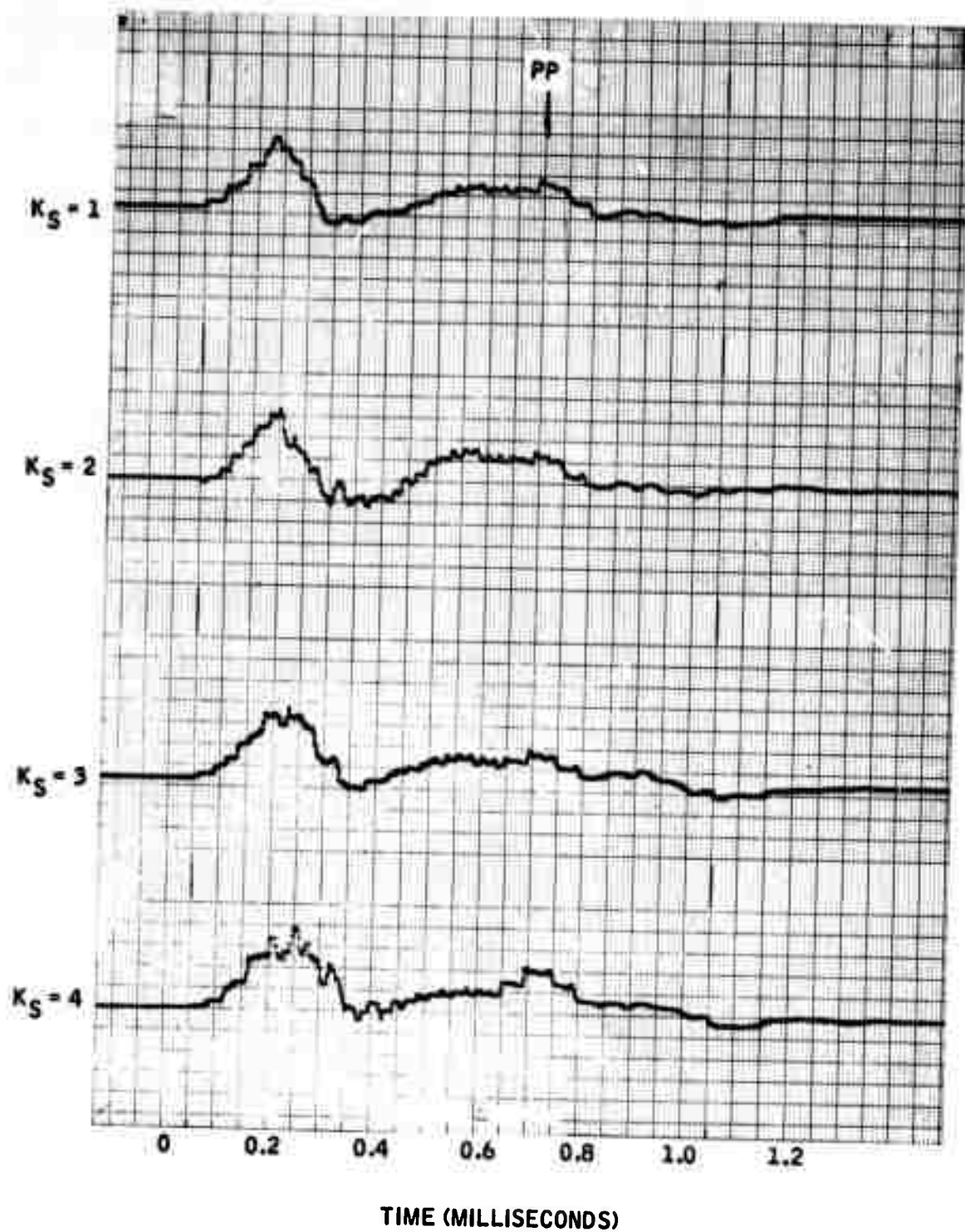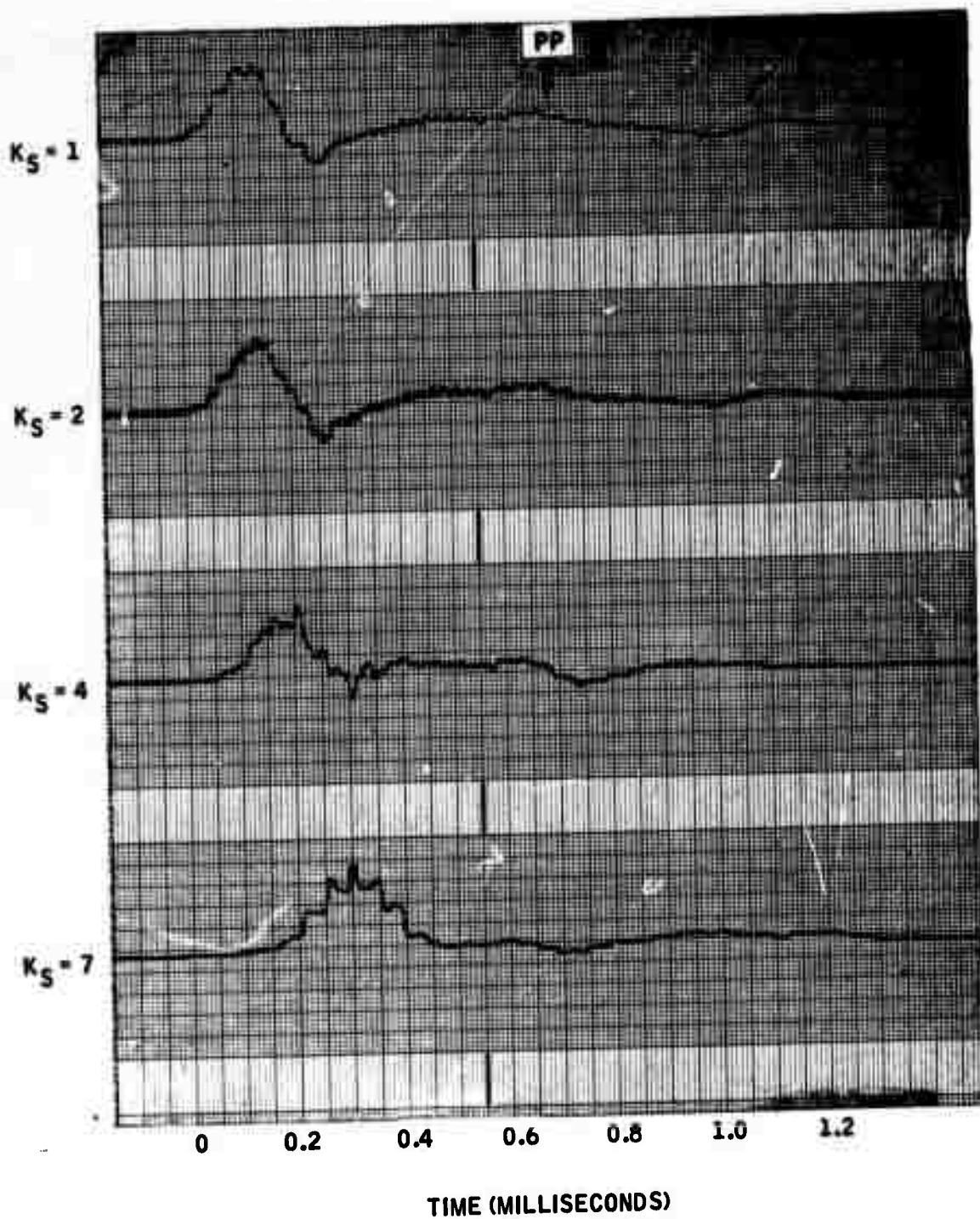
4-49

Figure 4-40. Granite Block, Cross-Correlation (SXU) of Fixed-
Null plus D-T Weighted Delay-and-Sum Beams
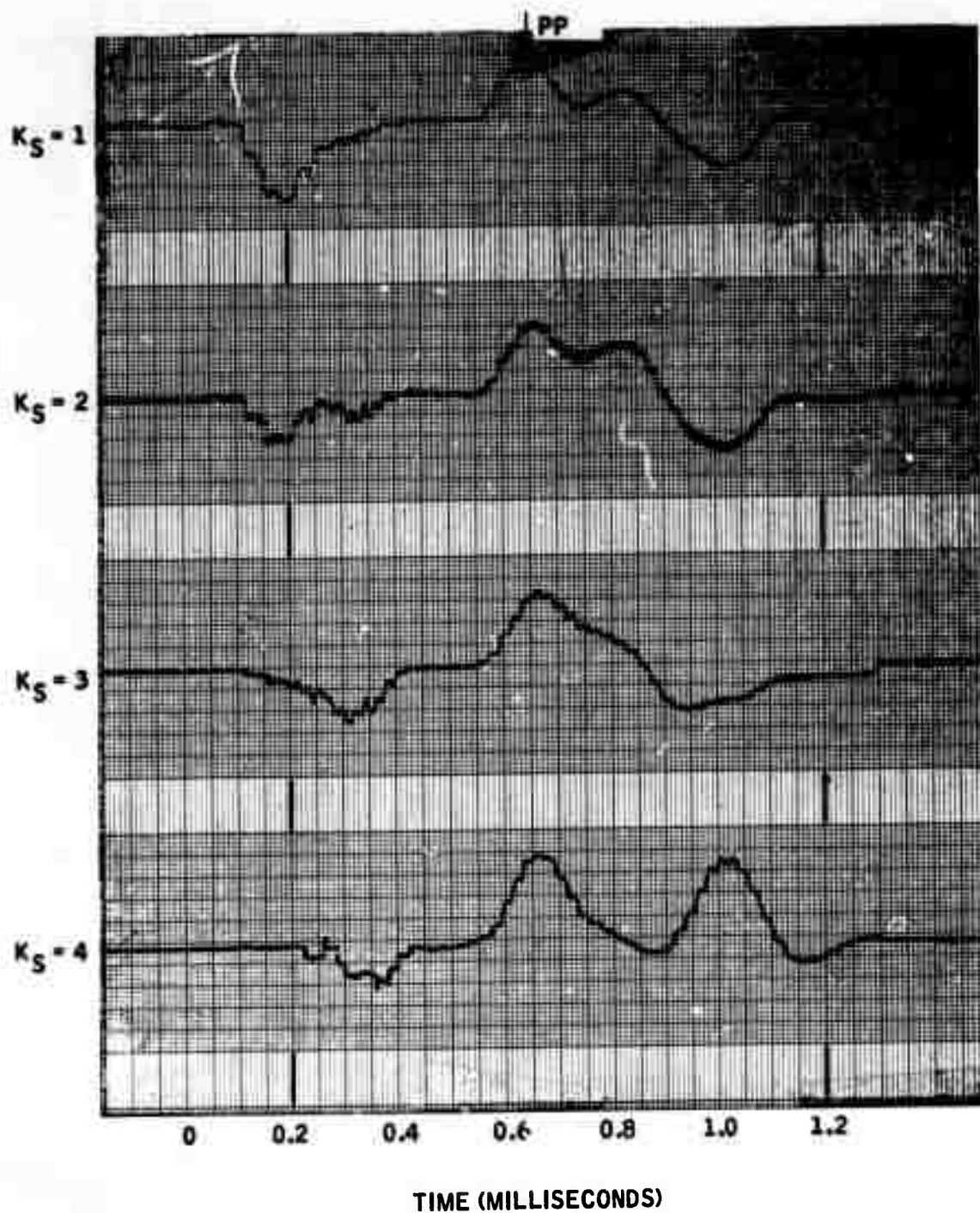
Figure 4-41. Granite Block, Cross-Correlation (NXU) of Fixed-
Null plus D-T Weighted Delay-and-Sum Beams

4-51

Figure 4-42.   Granite Block, Cross-Correlation (SXU) of Fan Filter
Ten-Element Beams
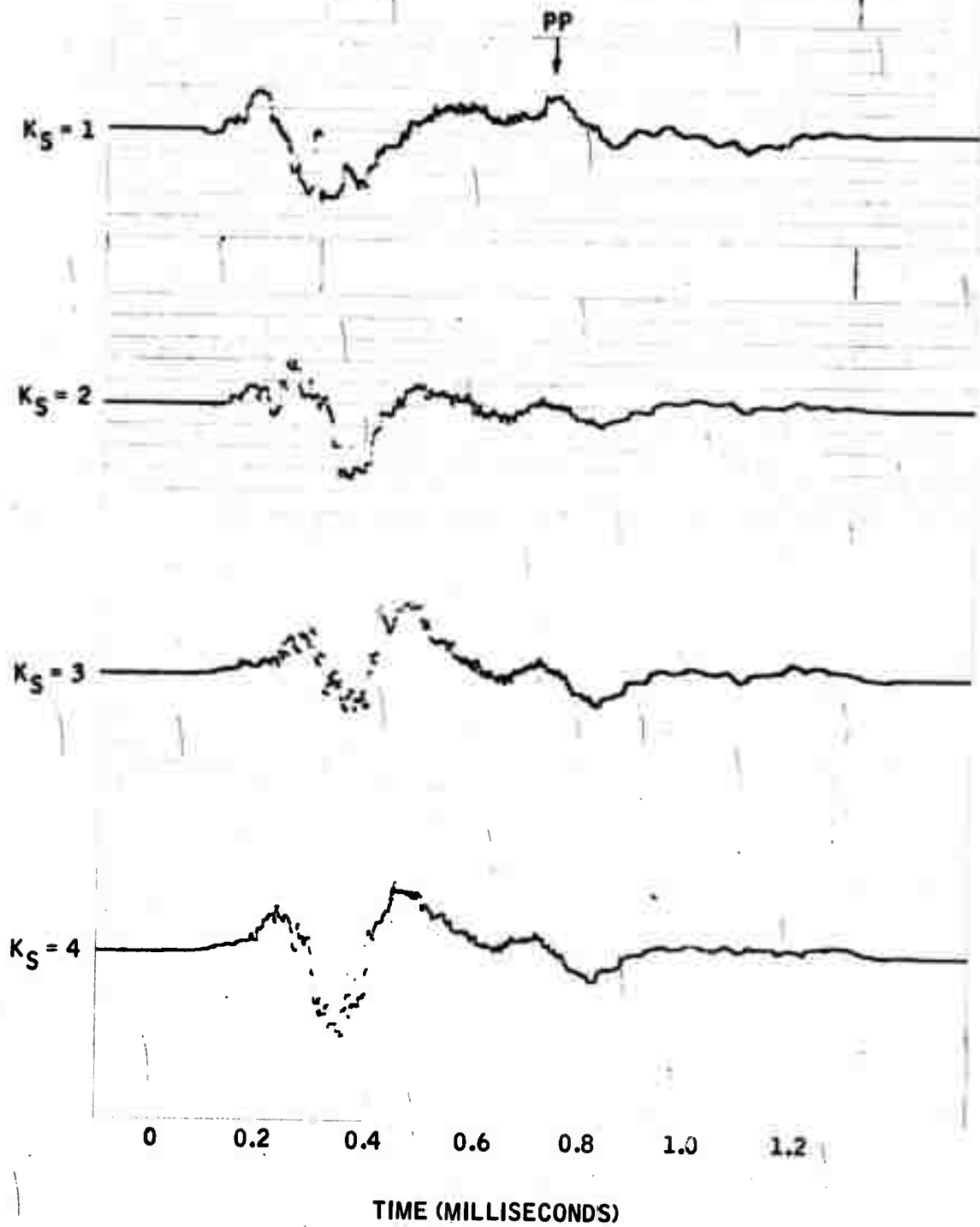
Figure 4-43. Granite Block, Cross-Correlation (NXU) of Fan Filter Ten-Element Beams
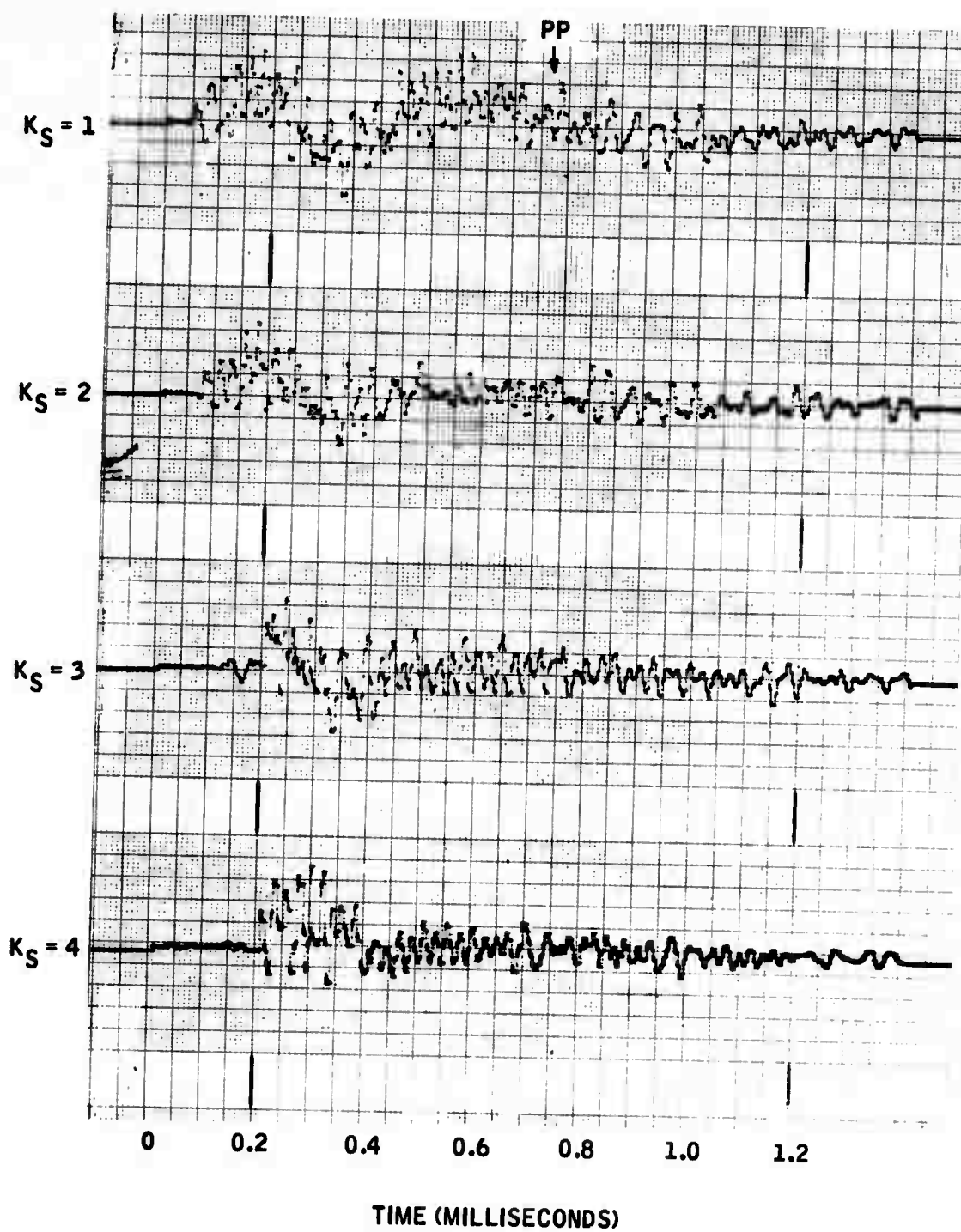
Figure 4-44. Granite Block (S), Adaptive Least-Squares Five-Element Beamformer

TIME (MILLISECONDS)
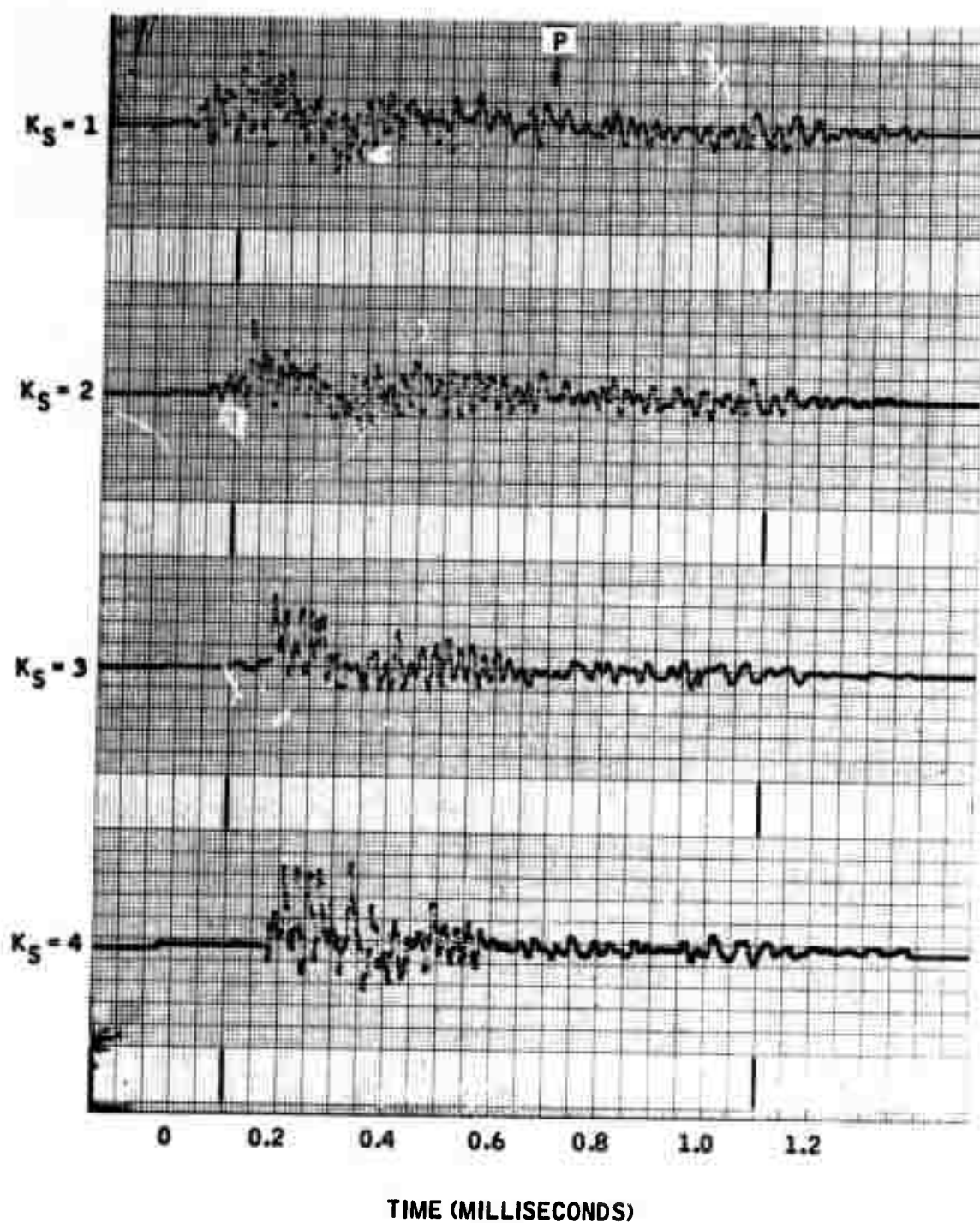
Figure 4-45. Granite Block (U), Adaptive Least-Squares Five-Element Beamformer

4-55

Figure 4-46. Granite Block Cross-Correlation (SXU) of Adaptive Five-Element Beams

4-56

TIME (MILLISECONDS)

Figure 4-47. Granite Block Cross-Correlation (SXU) of Six-
Element DIMUS Beams
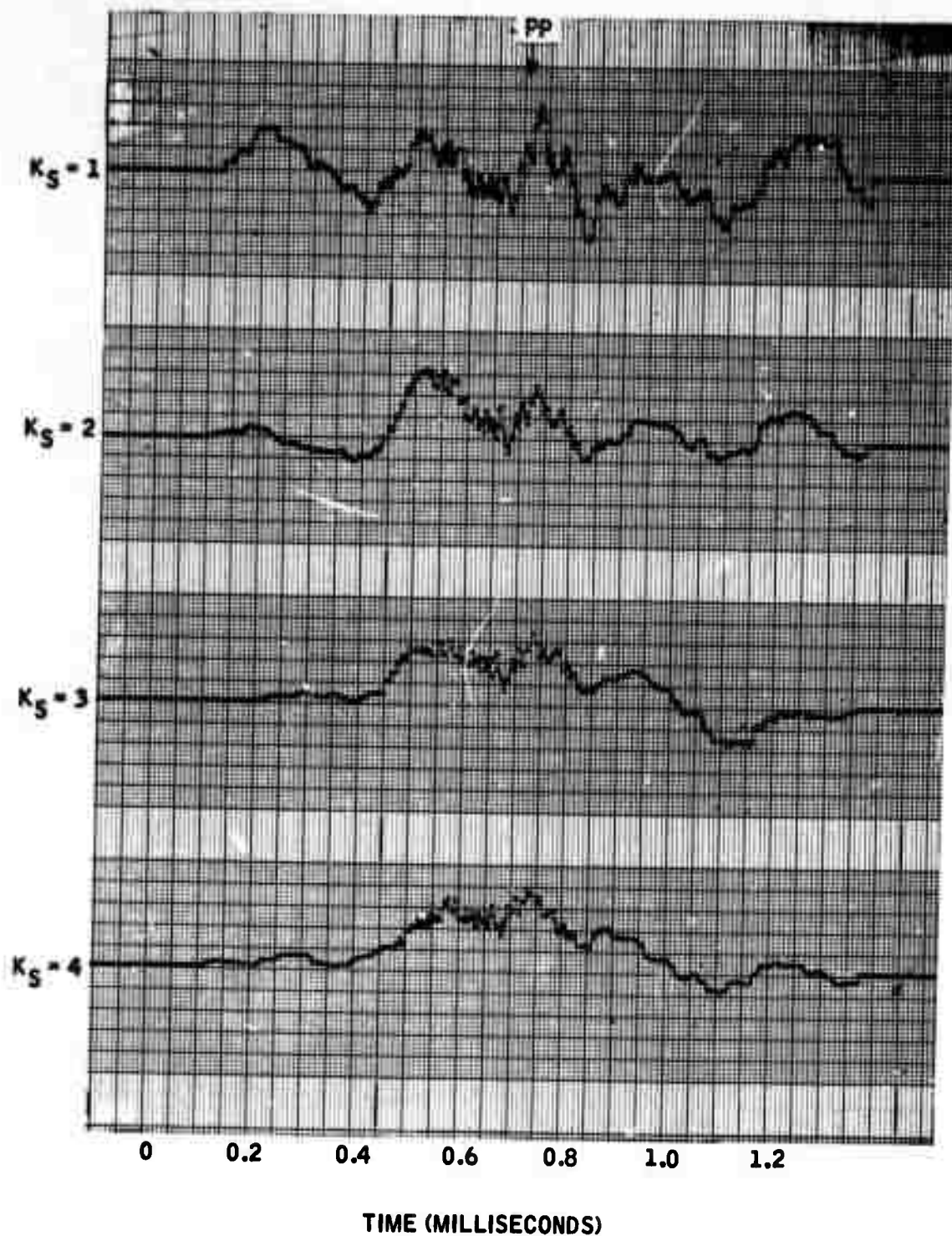
Figure 4-48. Granite Block Cross-Correlation (NXU) of Six-Element DIMUS Beams

4-58
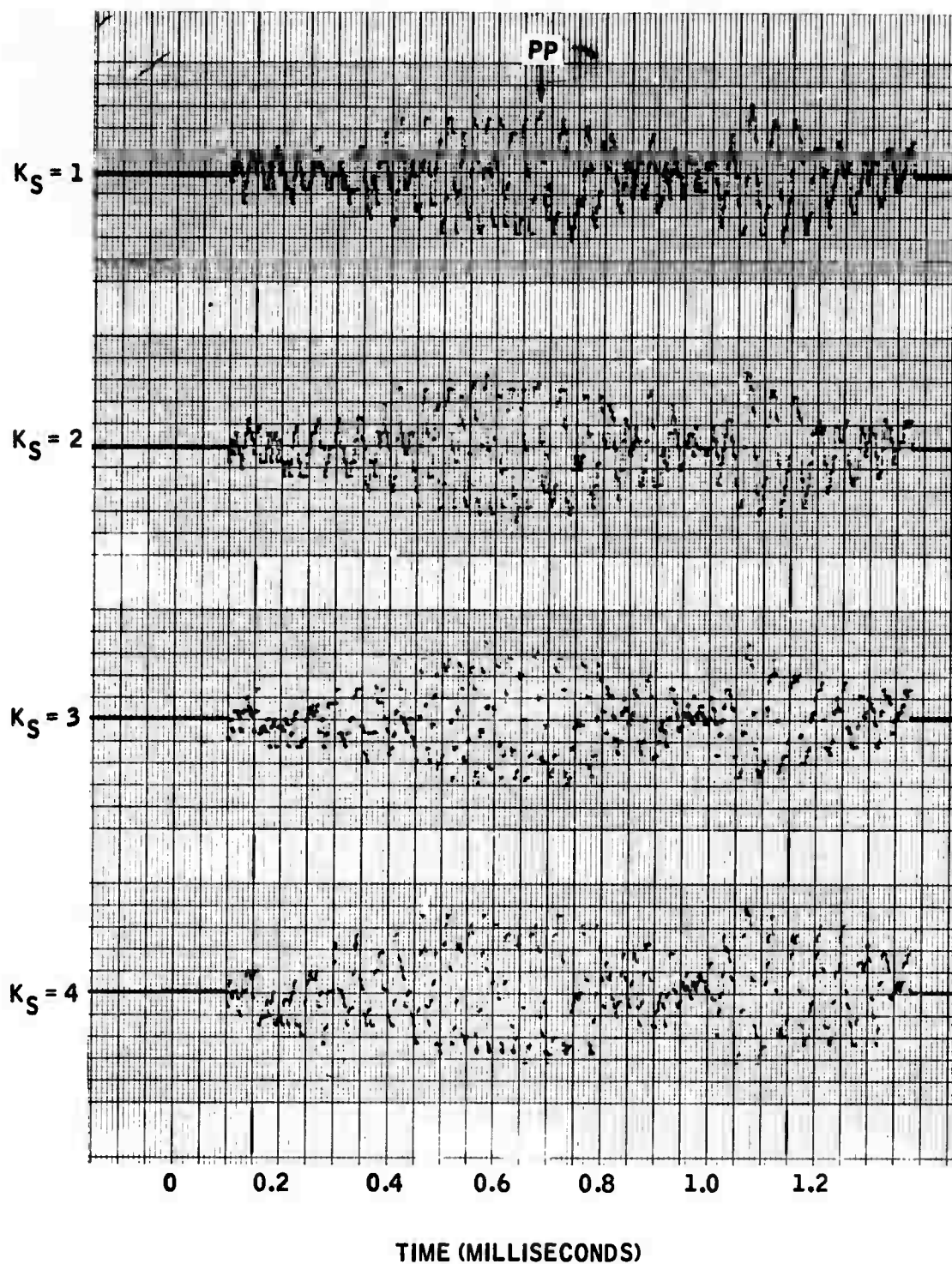
Figure 4-49. Granite Block (U), Ten-Element DIMUS Beam

4-59
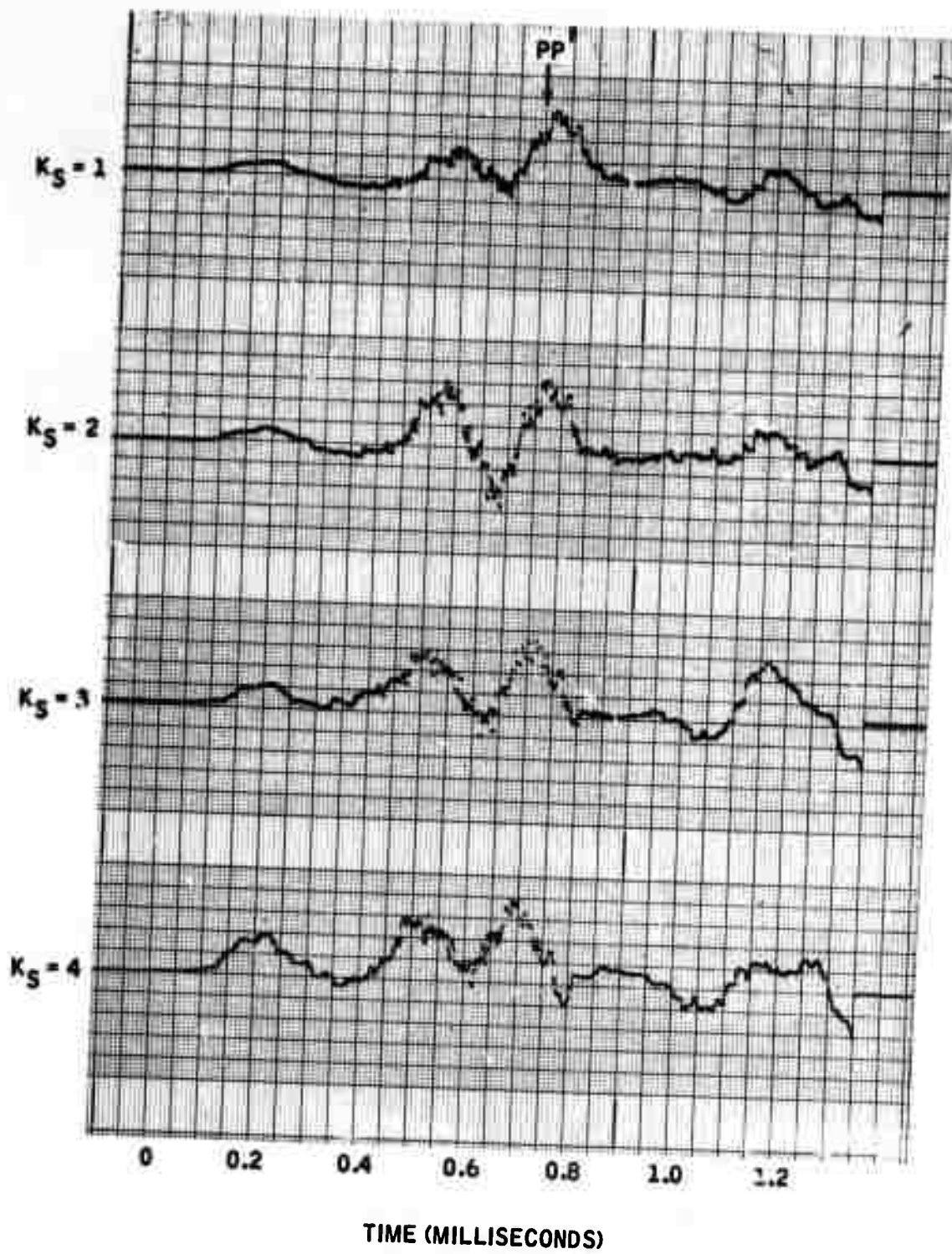
Figure 4-50. Granite Block, Cross-Correlation (SXU) of Ten-Element DIMUS Beams

4-60

TIME (MILLISECONDS)
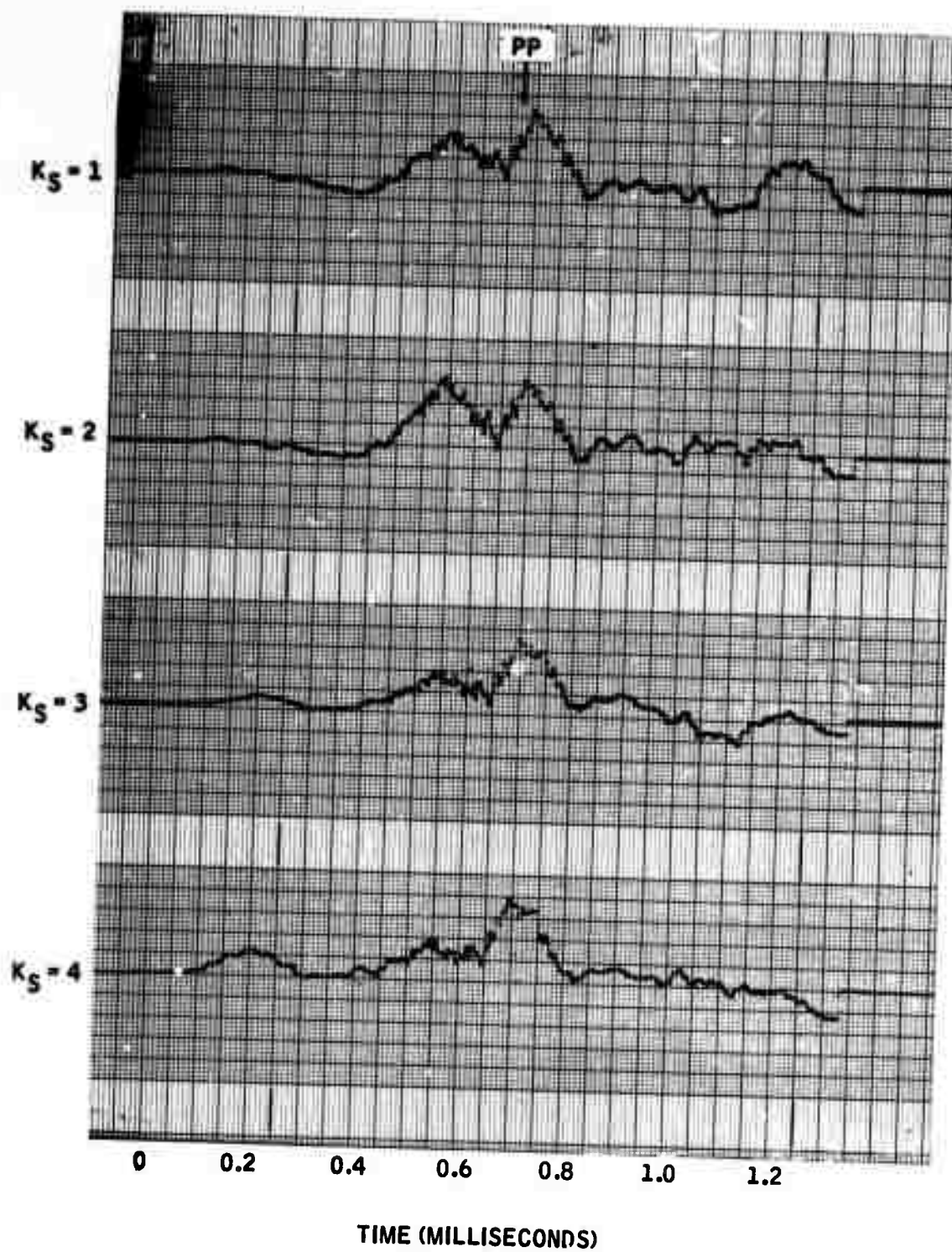
Figure 4-51. Granite Block, Cross-Correlation (NXU) of Ten-Element DIMUS Beams

4-61

surface-wave maxima correlated on three of the four traces from the (SXU)-array pair might be confusing, but no evidence of similar correlation is seen in the (NXU) output.

The AN/CC TAP beams are presented in Figures 4-57 and 4-58. Because these were substantially the same as the AN results, the final simplification of DIMUS/AN processing was pursued.

DIMUS/AN TAP beams for a five-element array are given in Figures 4-59 and 4-60. Failure of the K_S = 3 and 4 traces to have the same waveform in the vicinity of the peak as the K_S = 1 and 2 traces would probably hamper detection by the (SXU)-array pair. However, the (NXU) maxima are sufficiently similar to yield an unambiguous detection.

The U-array DIMUS/AN for a nine-element array (Figure 4-61) illustrates how the addition of the adaptive null to DIMUS can improve the PP clipped waveform detection. Here we see evidence of a PP arrival rising above the background that was not observable in the DIMUS beamformer output for the U array (Figure 4-49).

DIMUS/AN (SXU) and (NXU) outputs for the nine-element arrays are shown in Figures 4-62 and 4-63. In both cases, good suppression of interferences is achieved, resulting in unambiguous detection of the PP return.

4.5.3 Charcoal Quarry (Site A)

The Site A quarry experiment used a set of four orthogonal arrays designated North, East, South and West. A natural fracture at a depth of 75 inches, and apparently parallel with the array plane (Figure 3-12, Section III) was expected to yield a PP reflection which would arrive at the origin at about 0.74 msec for a P-wave velocity of 17,000 ft/sec. Several surface cracks and boundaries at the site (described in Figure 3-11, Section III) were sources of reflected surface wave. The location of the image sources for the major surface discontinuities, and the expected arrival times for reflected surface waves at the origin, are shown in Figure 4-64.

D&S beamforming results from ten-element arrays are shown in Figures 4-65 through 4-68. The strongest correlation results from the direct surface wave in every case. In the (NXE) and (SXE) cases, there is a slight indication of reflected surface-wave arrivals from the (-1.5 feet, -5.5 feet) and (-11 feet, 0 feet) image sources starting at about 0.55 and 1.1 msec, respectively. In the (SXW) and (NXW) TAP beams, the (-1.5 feet, -5.5 feet) image source has a much stronger effect because it presents a more nearly normal wavefront to the W array than any other.
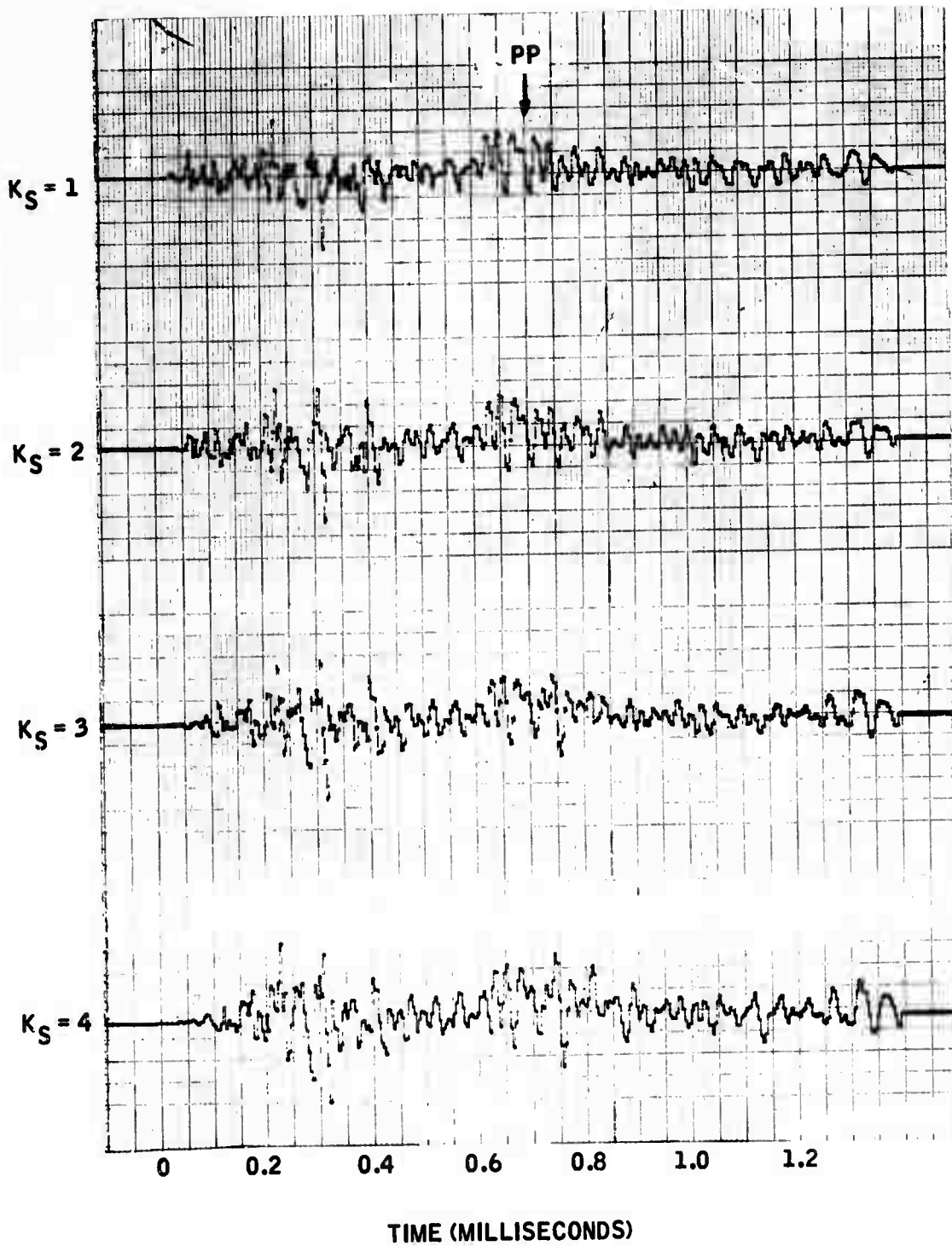
Figure 4-52. Granite Block (S), Ten-Element Adaptive-Null Beam
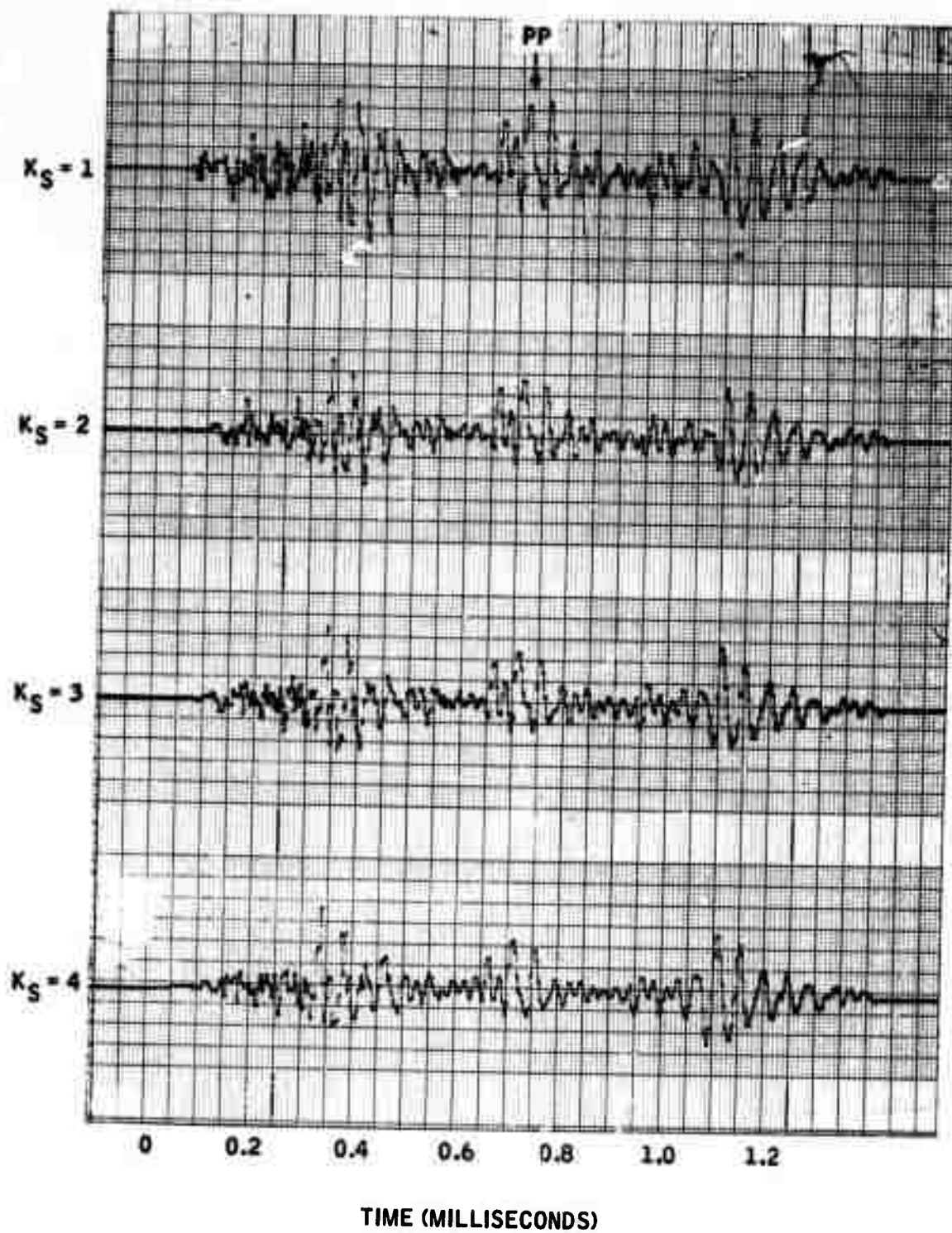
Figure 4-53. Granite Block (U), Ten-Element Adaptive-Null Beam

4-64
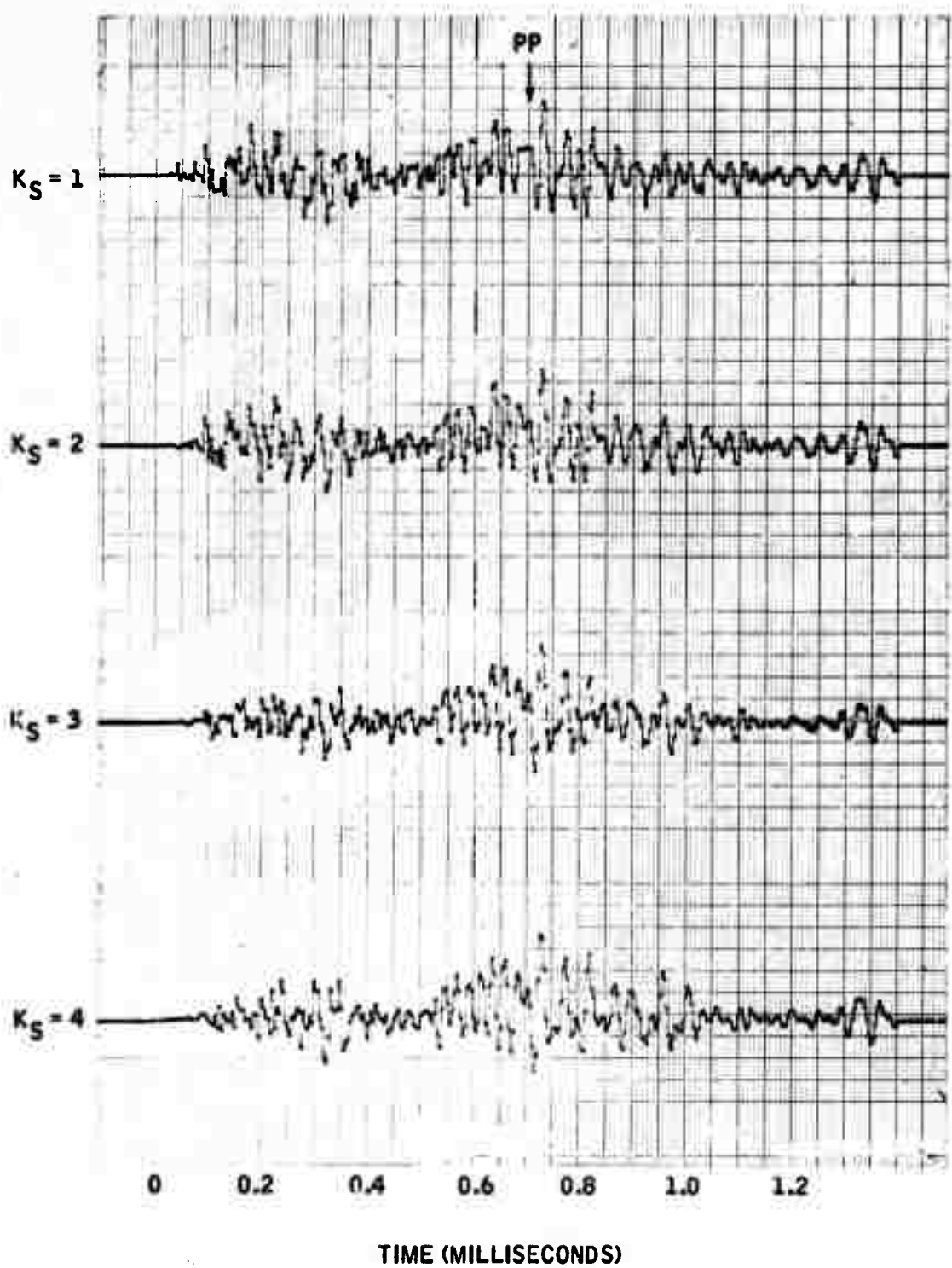
Figure 4-54. Granite Block (N), Ten-Element Adaptive-Null Beam
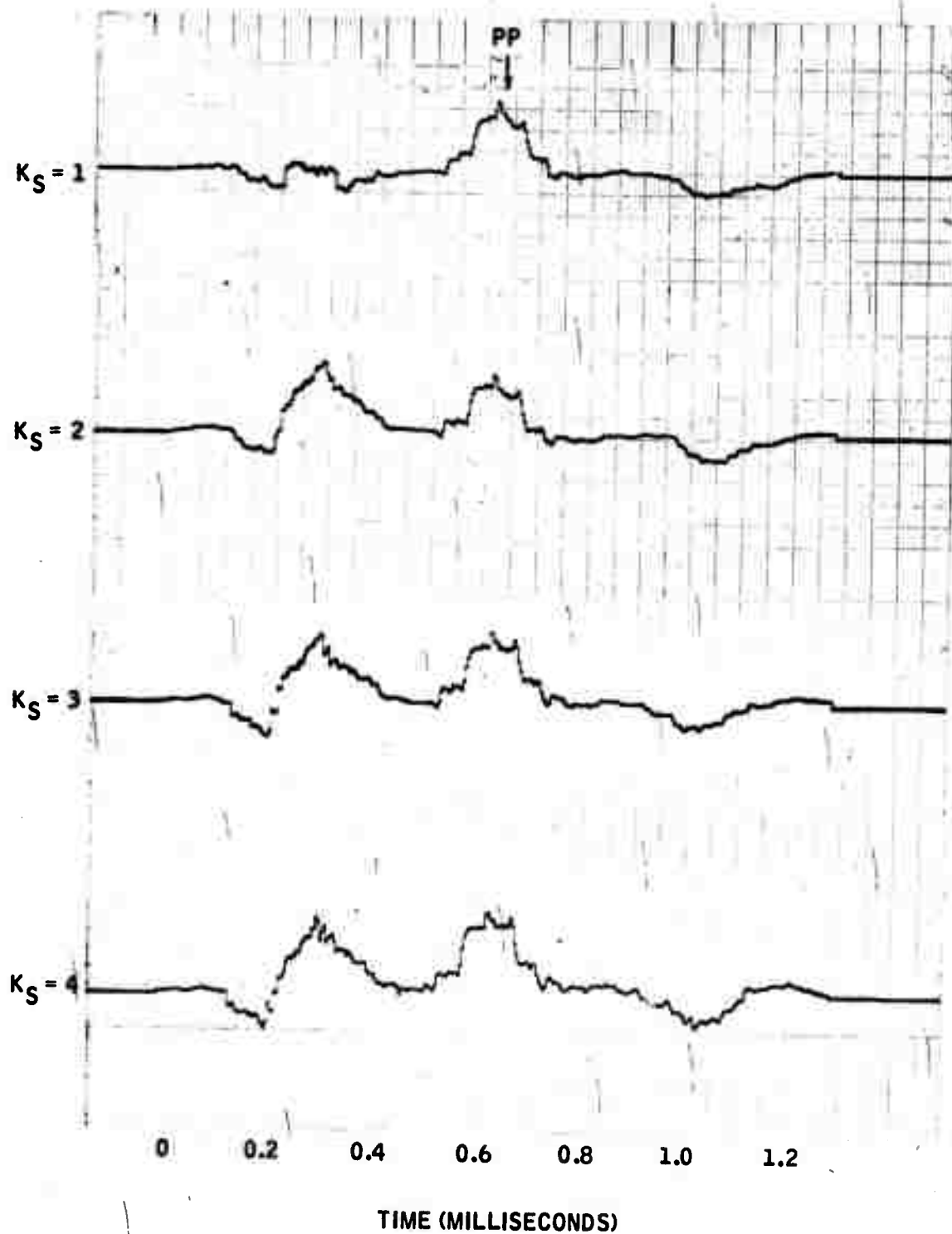
Figure 4-55. Granite Block, Cross-Correlation (SXU) of Ten-Element Adaptive-Null Beams
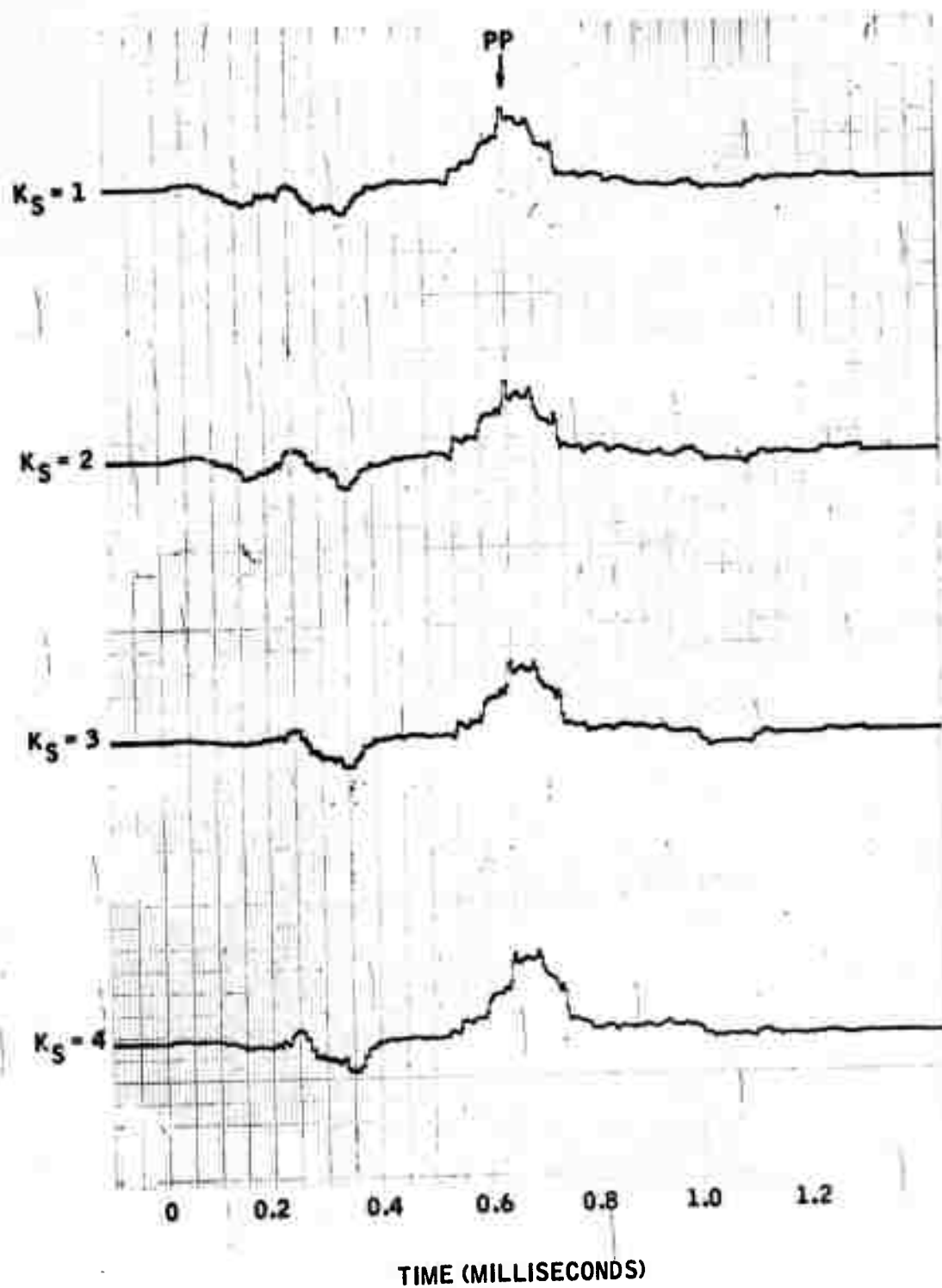
Figure 4-56. Granite Block, Cross-Correlation (NXU) of Ten-Element Adaptive-Null Beams

4-67
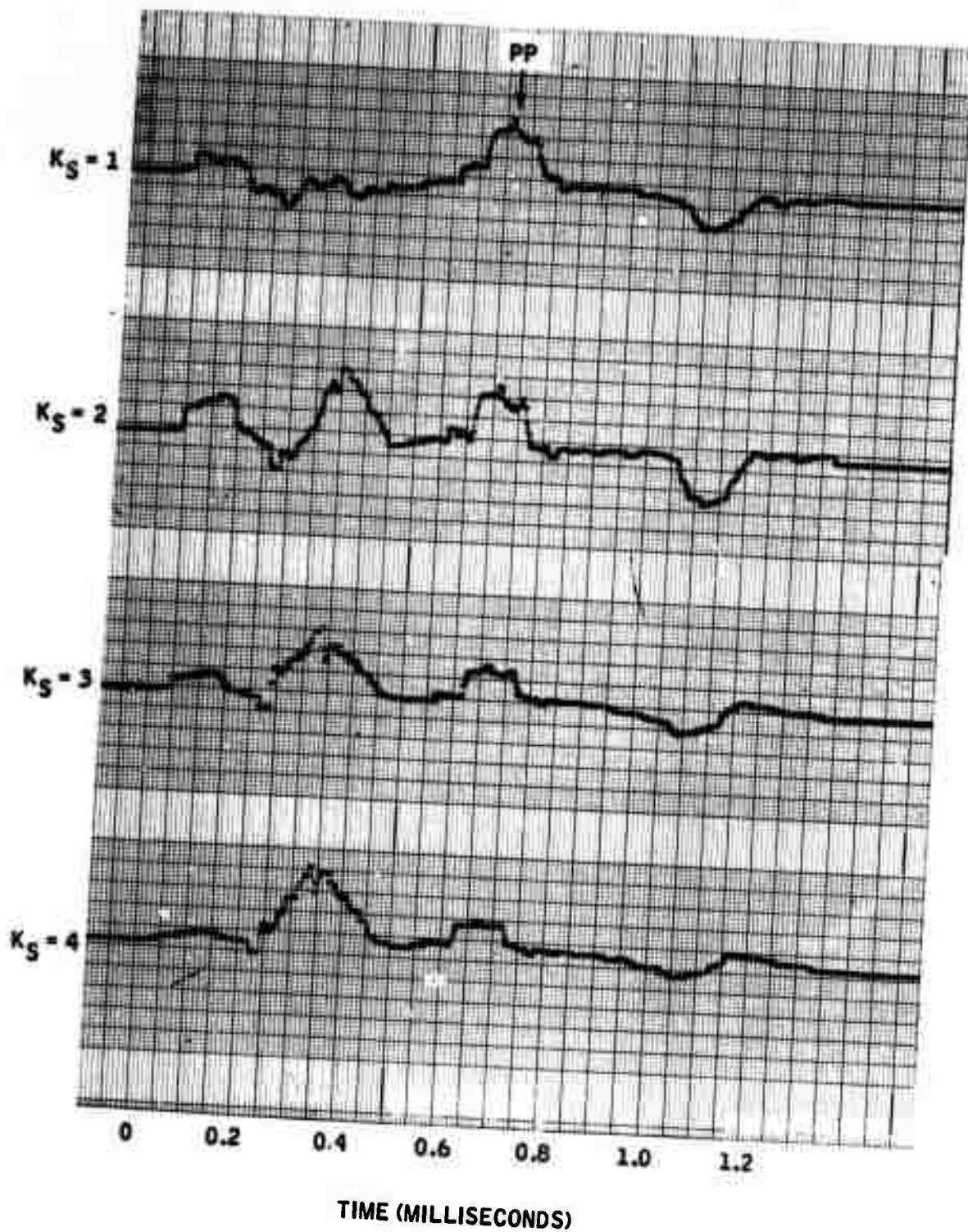
Figure 4-57. Granite Block, Cross-Correlation (SXU) of Adaptive-Null (clipper correlator) Beams

4-68

TIME (MILLISECONDS)
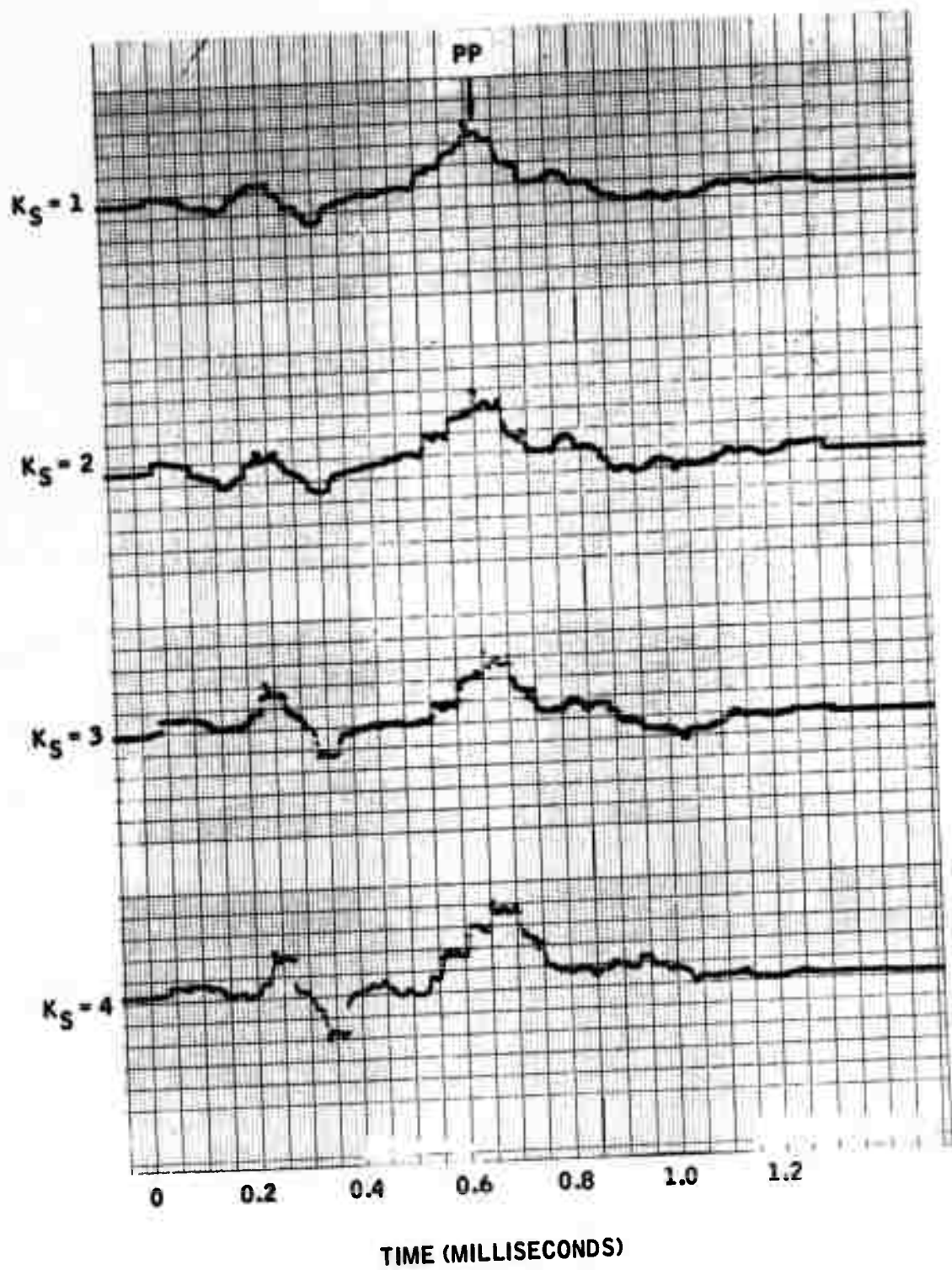
Figure 4-58. Granite Block, Cross-Correlation (NXU) of Adaptive-Null (clipper correlator) Beams
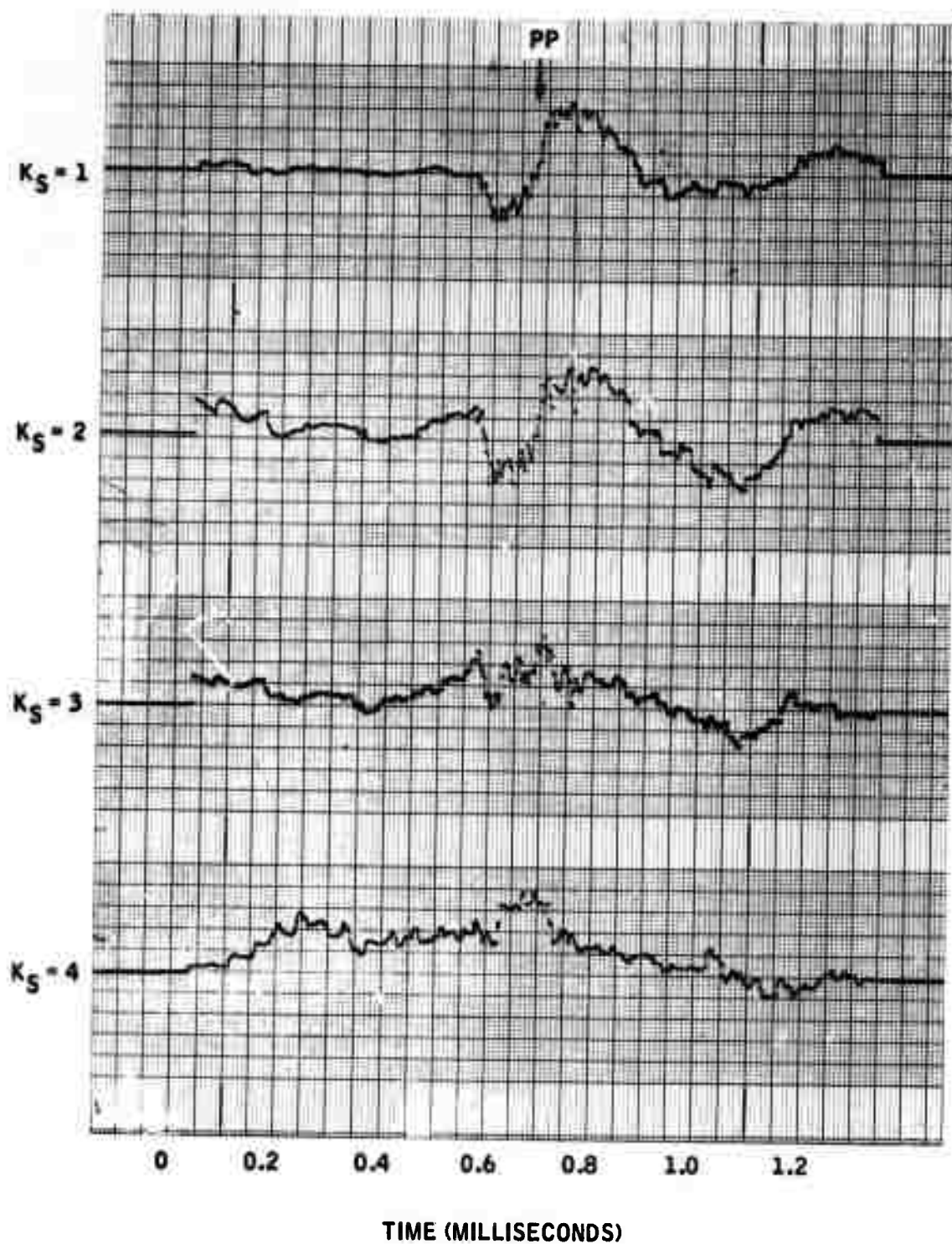
Figure 4-59. Granite Block, Cross-Correlation (SXU) of Five-Element DIMUS/AN Beams

4-70
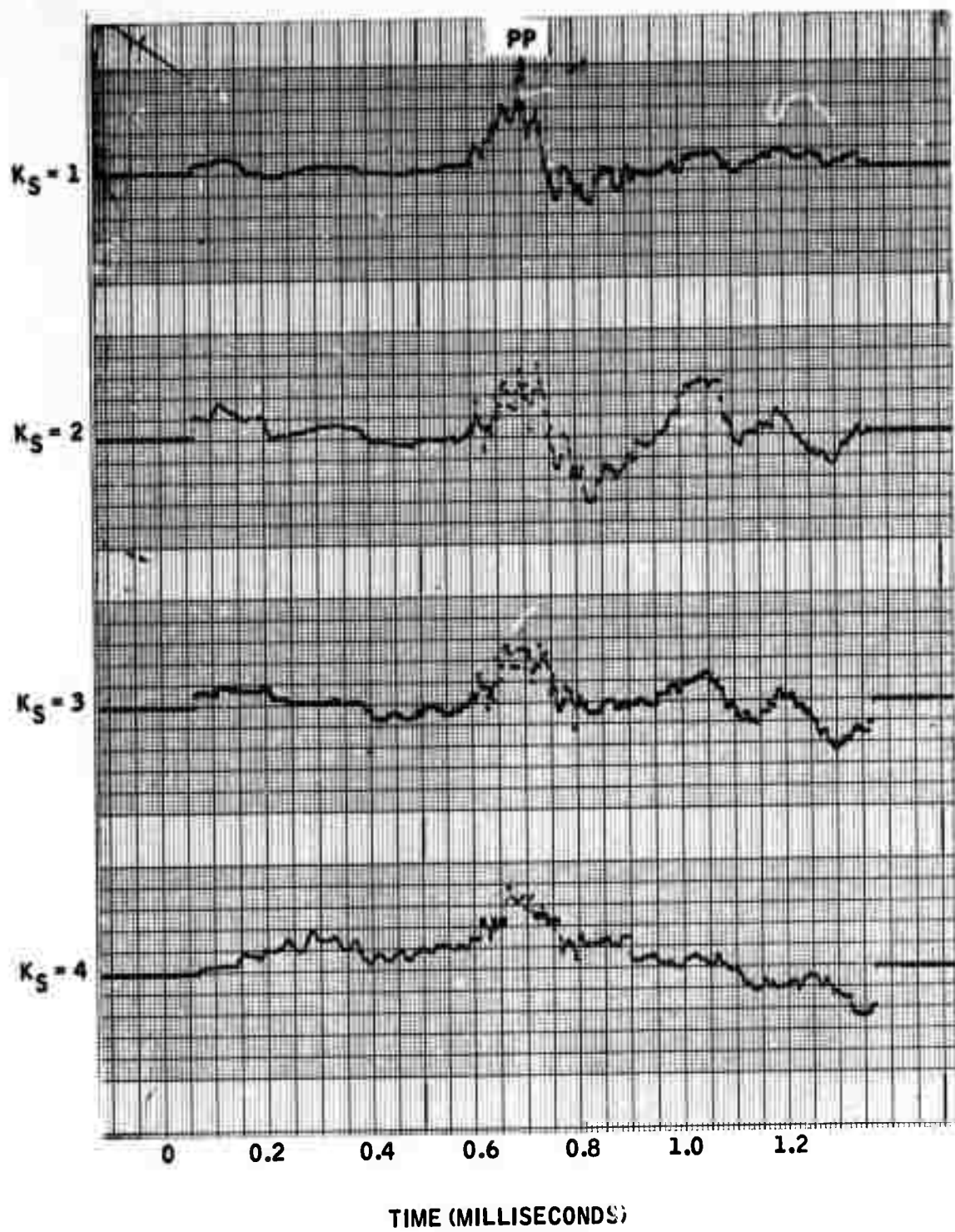
Figure 4-60. Granite Block, Cross-Correlation (NXU) of Five-Element DIMUS/AN Beams

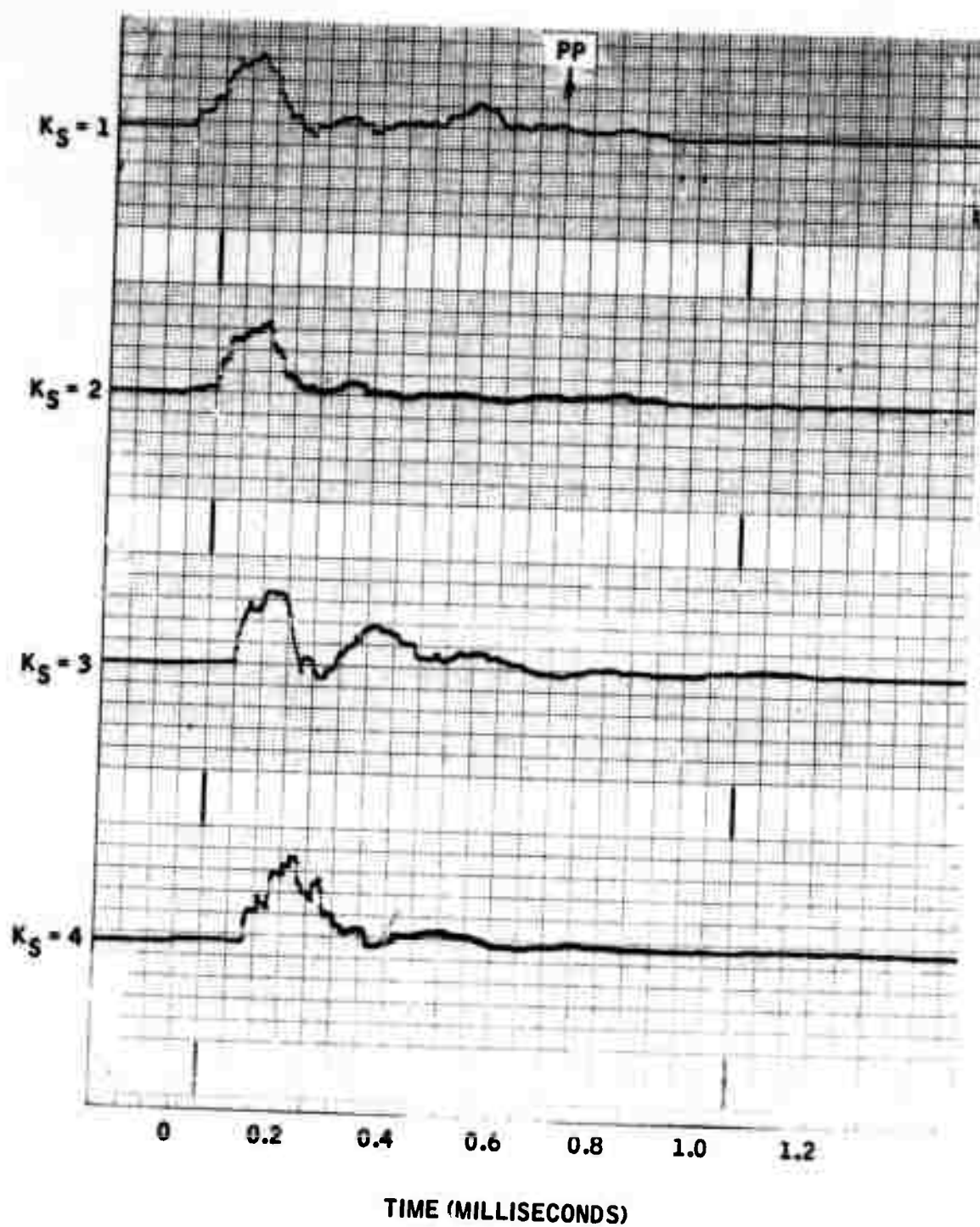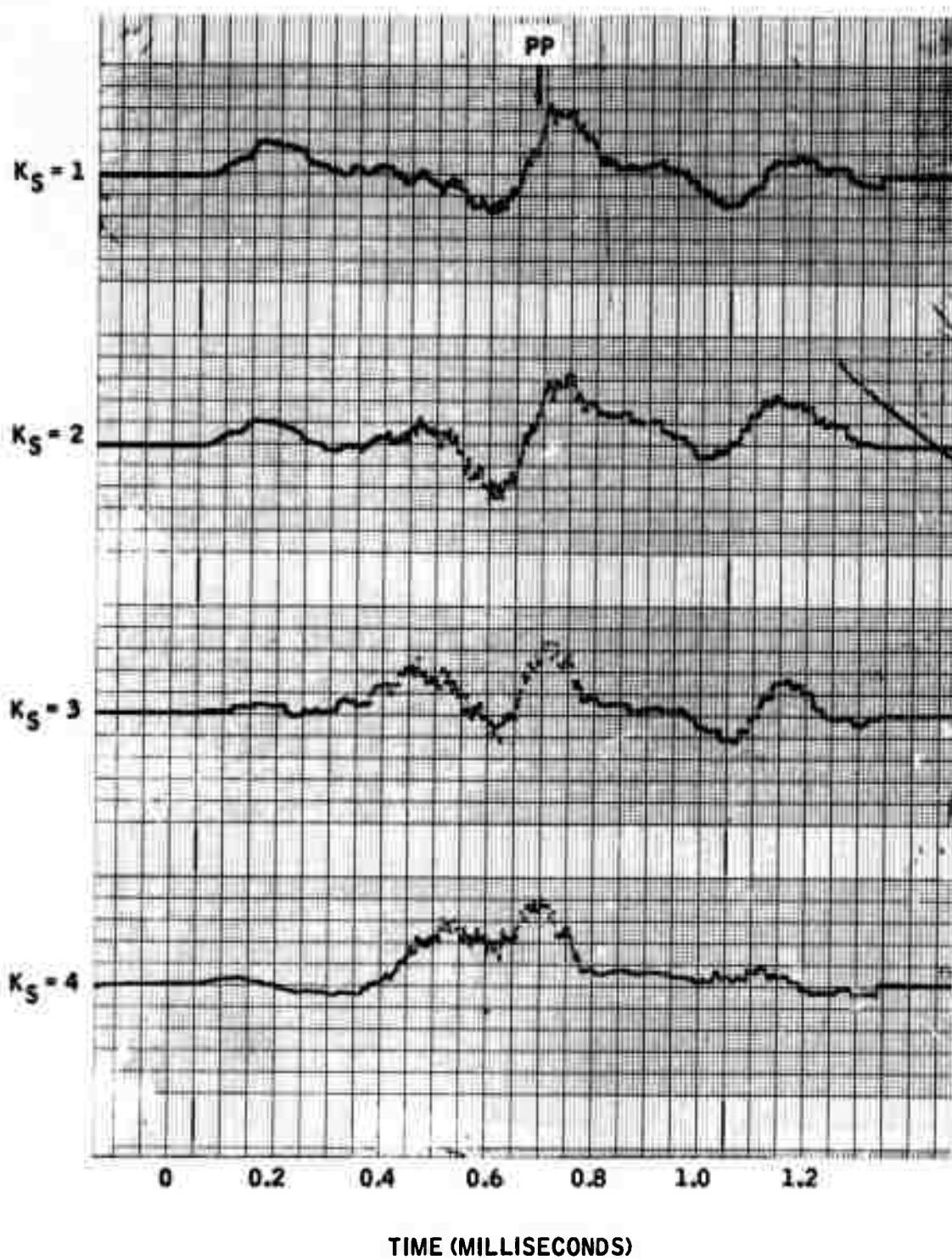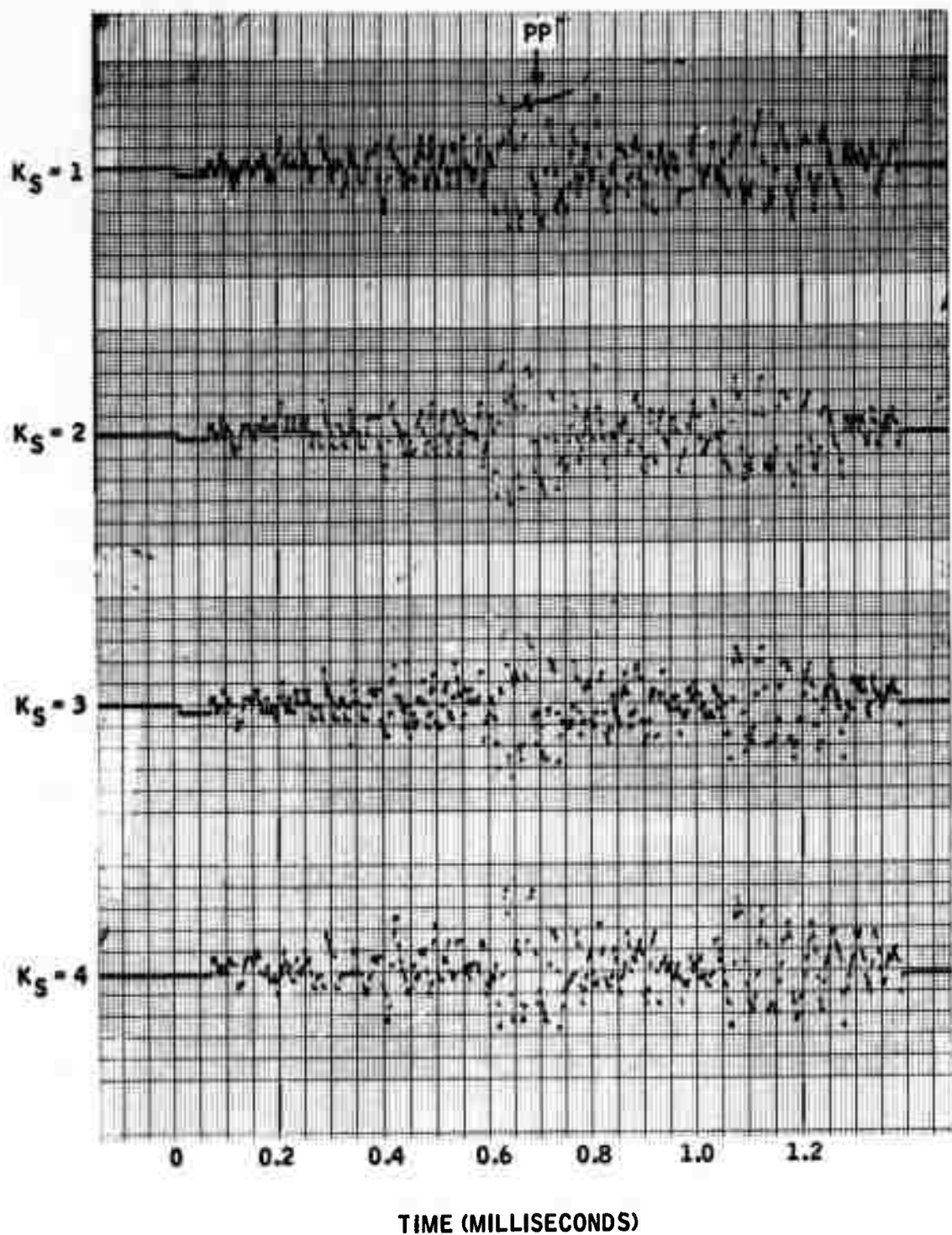Figure 4-61. Granite Block (U), Nine-Element DIMUS/AN Beam
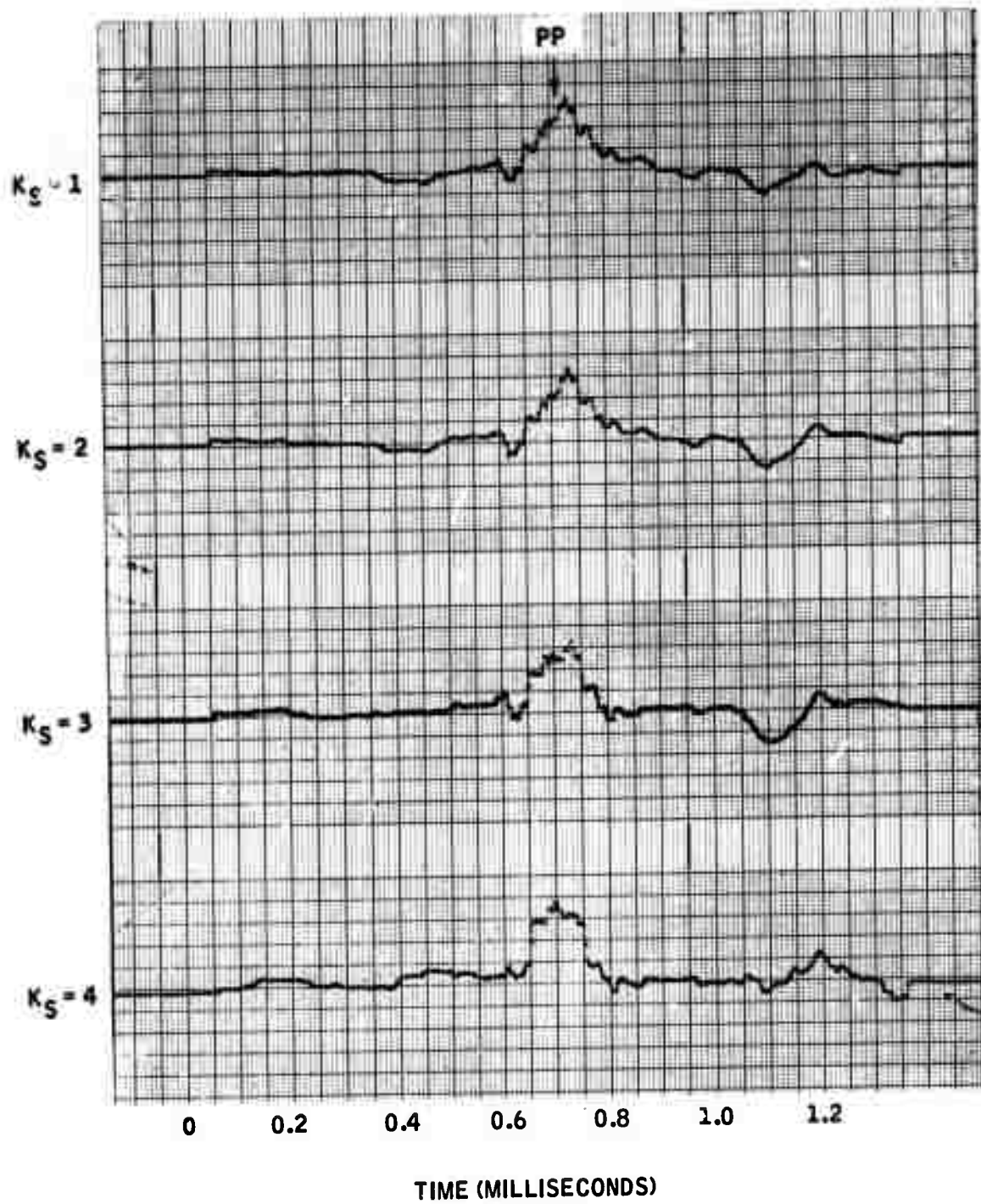
Figure 4-62. Granite Block, Cross-Correlation (SXU) of Nine-Element DIMUS/AN Beams
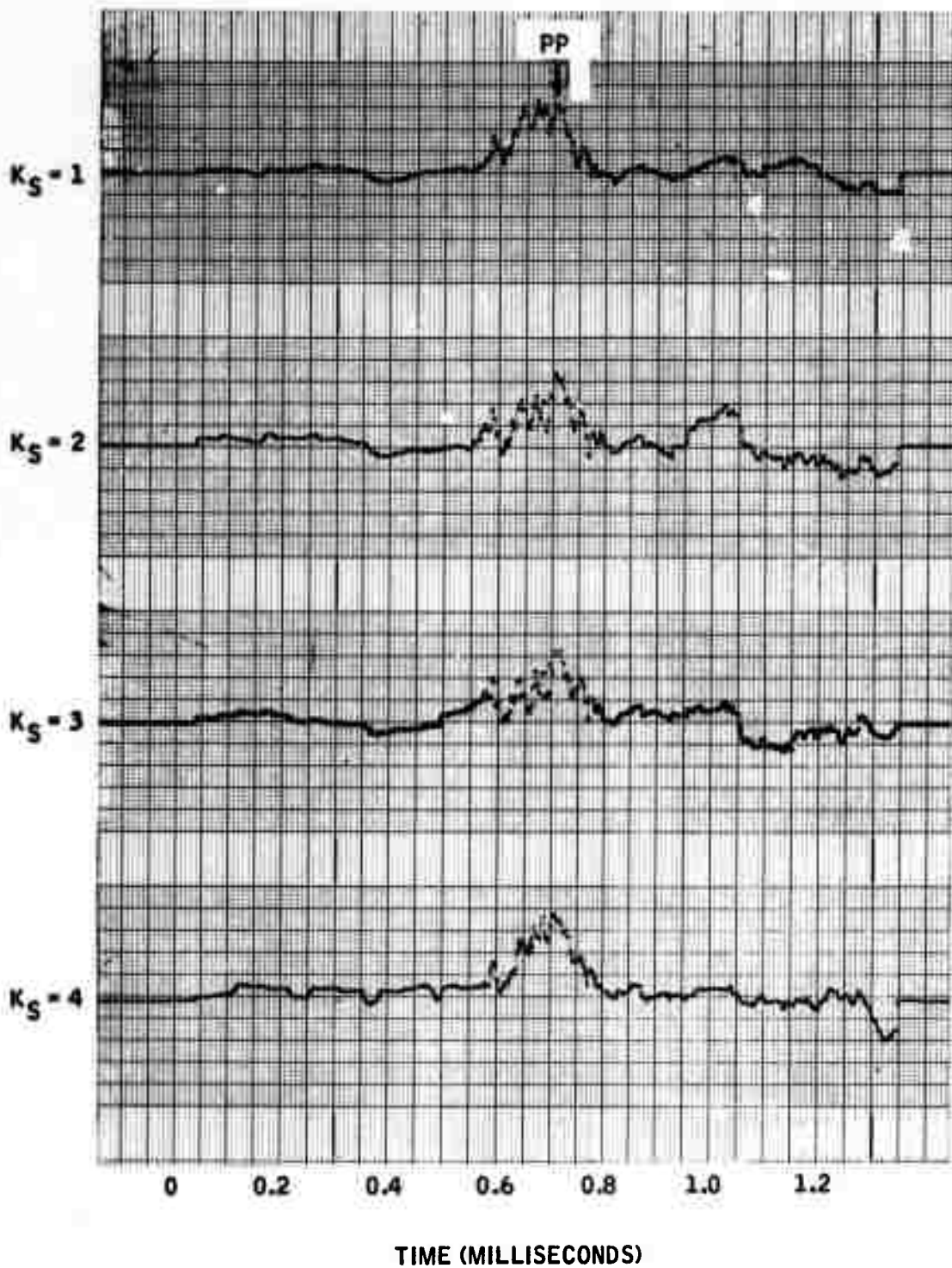
Figure 4-63. Granite Block, Cross-Correlation (NXU) of Nine-Element DIMUS/AN Beams

4-74
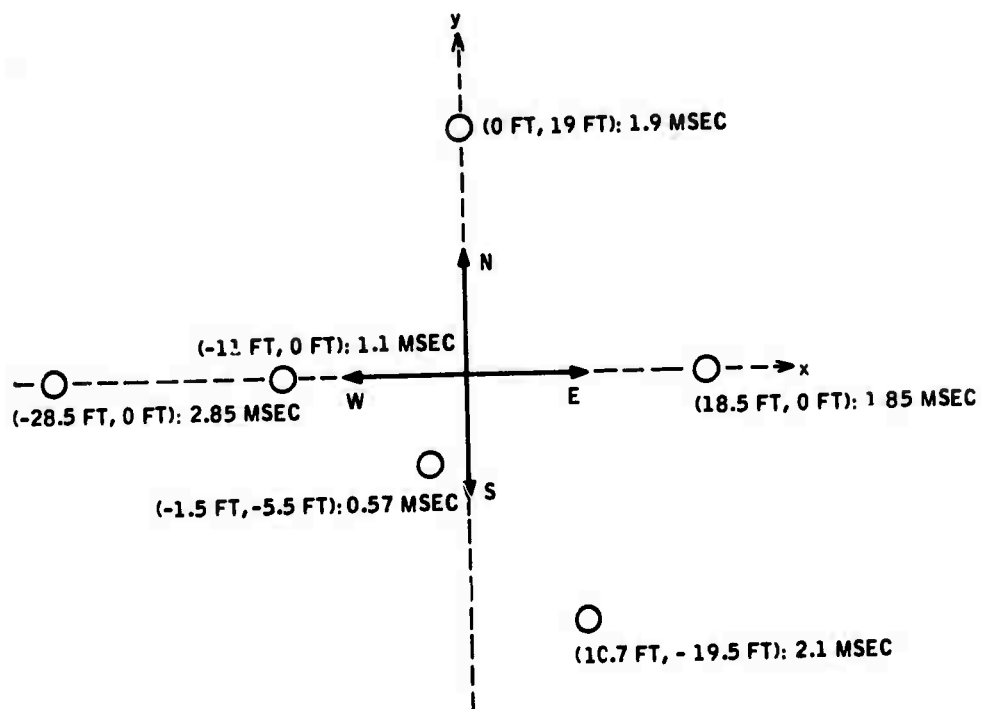
Figure 4-64.   Image Sources for the Major Surface Reflectors
in the Charcoal Quarry Setup
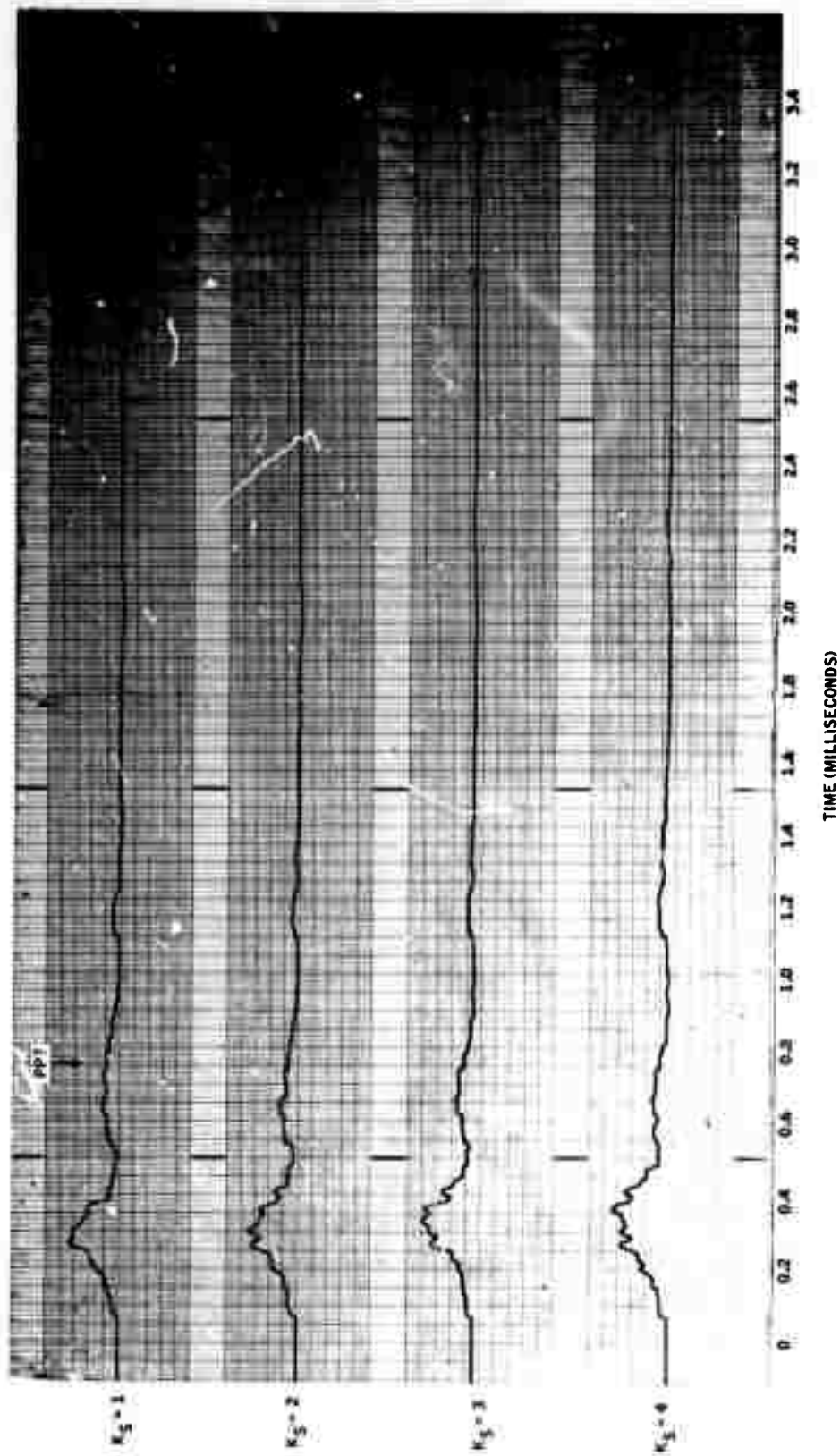
Figure 4-65. Charcoal Quarry, Cross-Correlation (NXE) of Ten-Element Delay-and-Sum Beams
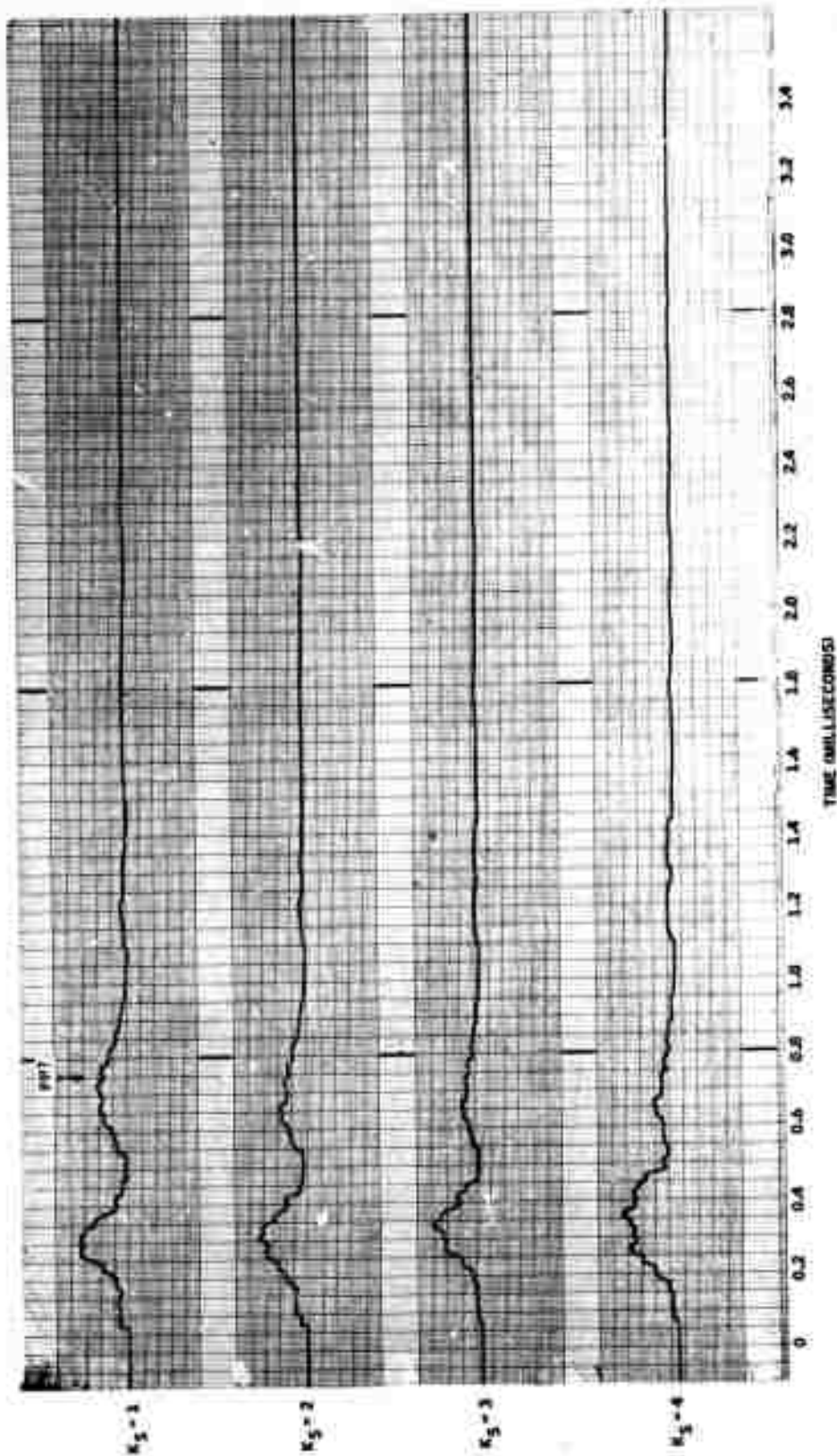
Figure 4-66.   Charcoal Quarry, Cross-Correlation (SXE)
of Ten-Element Delay-and-Sum Beams
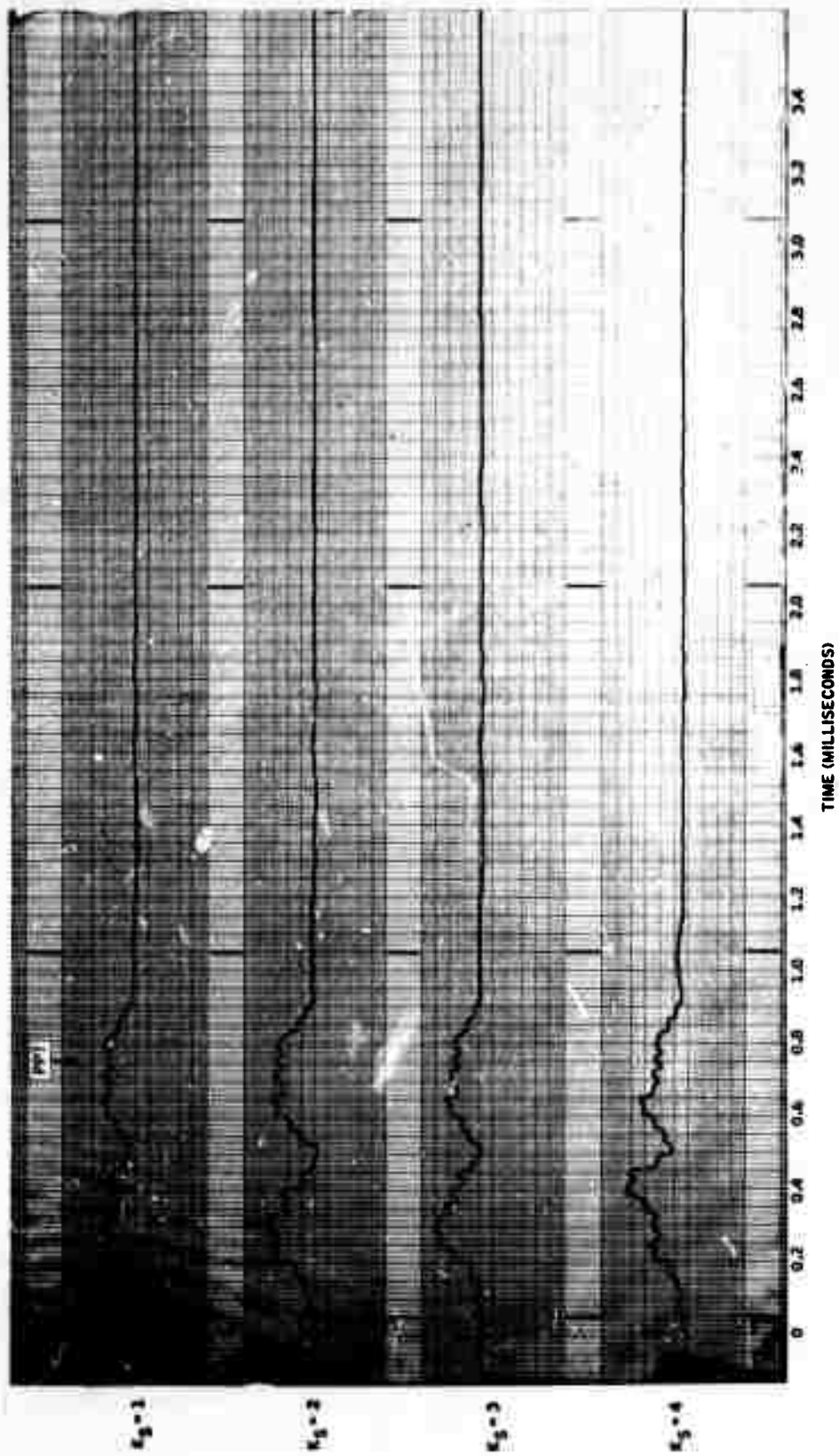
Figure 4-67. Charcoal Quarry, Cross-Correlation (SXW) of Ten-Element Delay-and Sum Beams
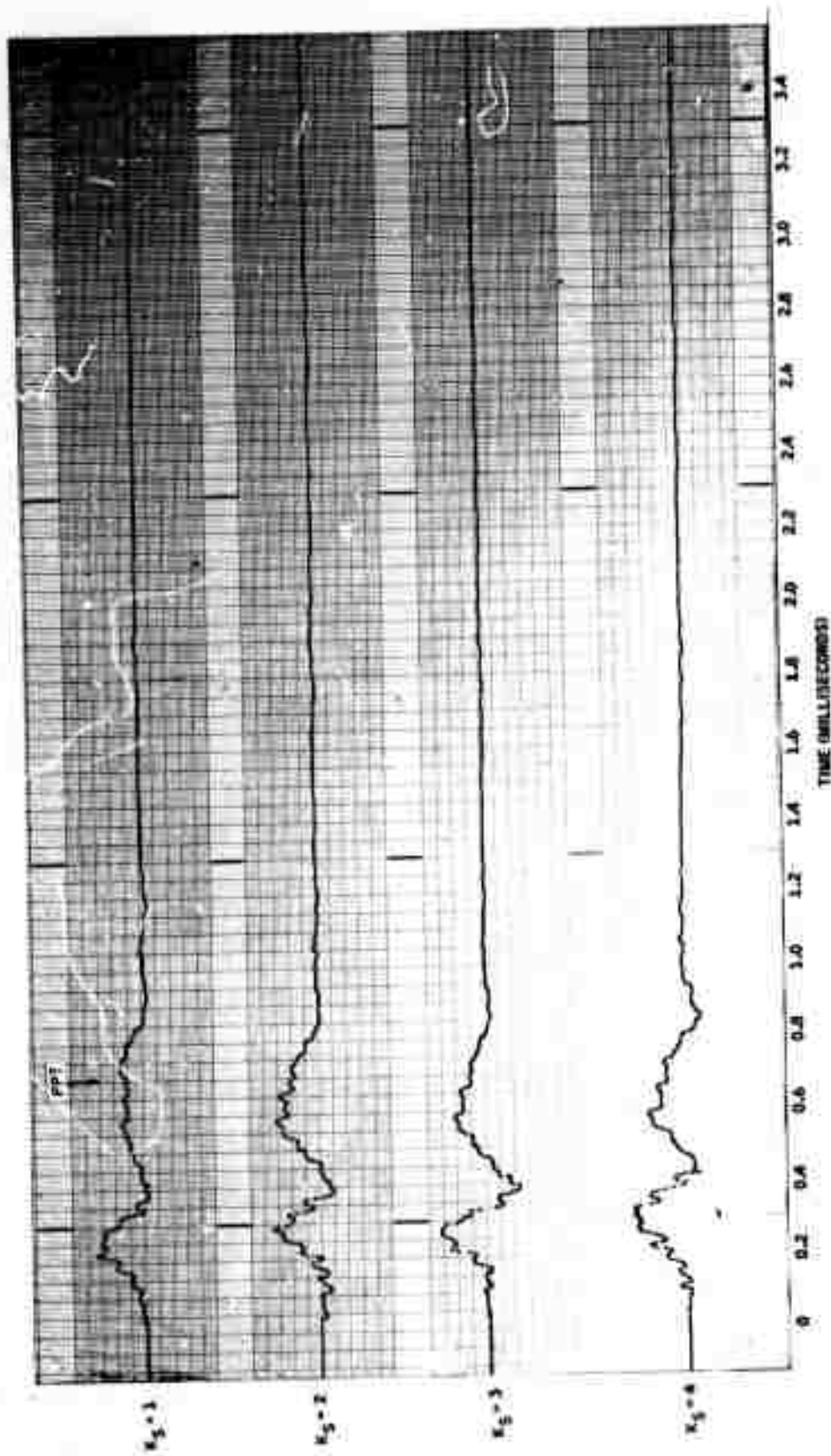
Figure 4-68. Charcoal Quarry, Cross-Correlation (NXW) of Ten-Element Delay-and Sum Beams

DIMUS beamforming results are presented in Figures 4-69 through 4-72. Generally, these records are quite random, exhibiting few maxima which correlate vertically on the stack. Exceptions occur in the (NXE) output in the ranges 0.45 to 0.55 msec and 2.1 to 2.3 msec. These most likely result from surface waves. One other exception occurs in the (SXW) pair where a vertical correlation on the stack can be seen in the vicinity of 0.75 msec. This could be the expected P-wave reflection, but since it is evident only on this pair, little confidence can be placed upon this interpretation.

An indication of a fairly strongly correlated but out-of-phase return is seen at the end of a number of DIMUS records. This may be the surface reflection from the quarry ledge, although it occurs a little later than expected.

Finally, DIMUS/AN TAP outputs for the Charcoal Quarry data are shown in Figures 4-73 through 4-76. Here there are quite a few more maxima that correlate vertically on the stacks. However, most of them can be associated with reflected surface waves. An exception is again the (SXW) pair where, as in the case of DIMUS, a vertical correlation of stack waveforms is observed in the vicinity of the expected PP-wave arrival time. In this case, the peak occurs closer to 0.8 msec, but the correlation extends over an interval including the expected arrival time. Again, however, it cannot be said that a detection occurred with confidence since it appears on only one of the array pairs.
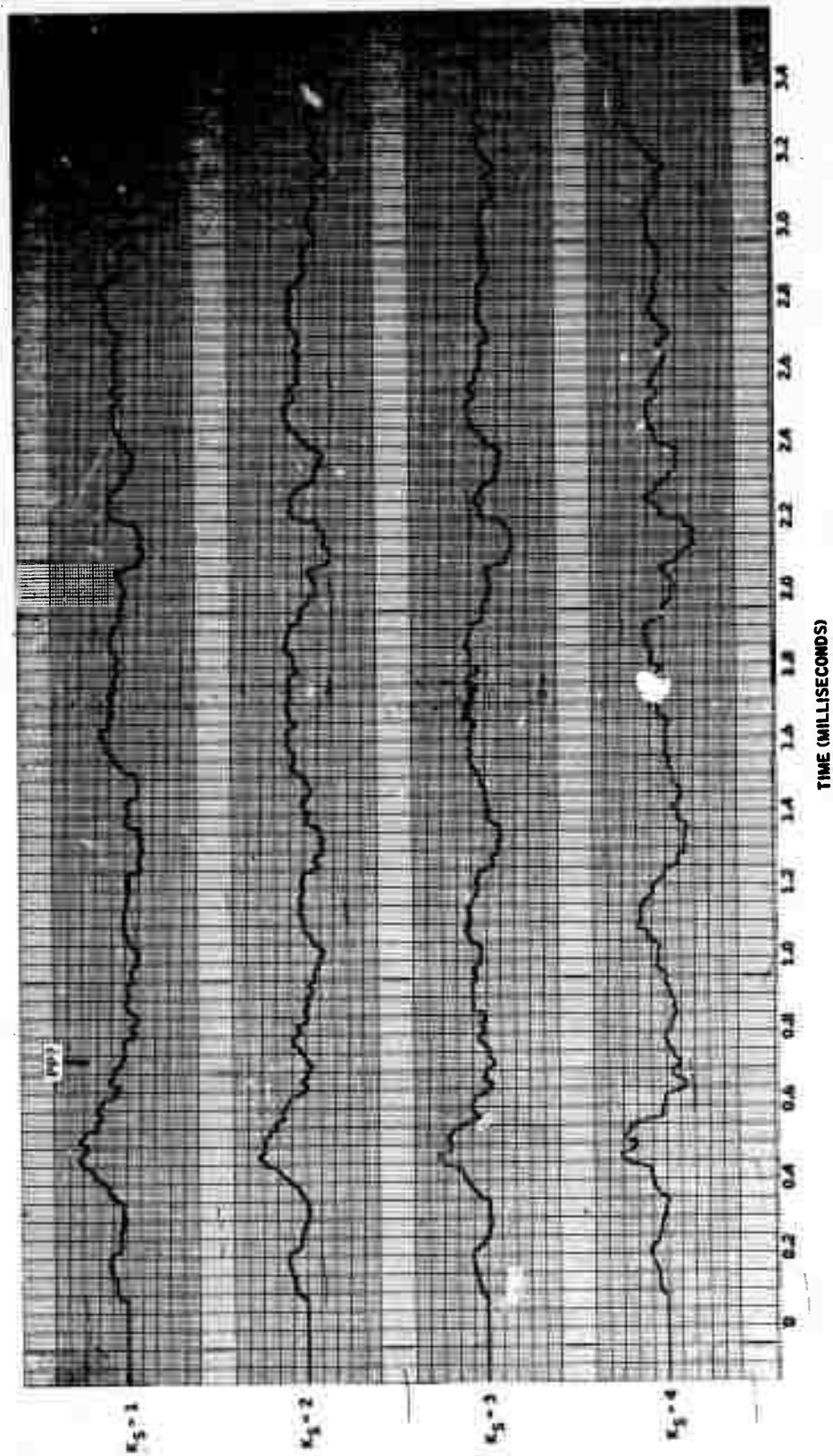
Figure 4-69. Charcoal Quarry, Cross-Correlation (NXE) of Ten-Element DIMUS Beams
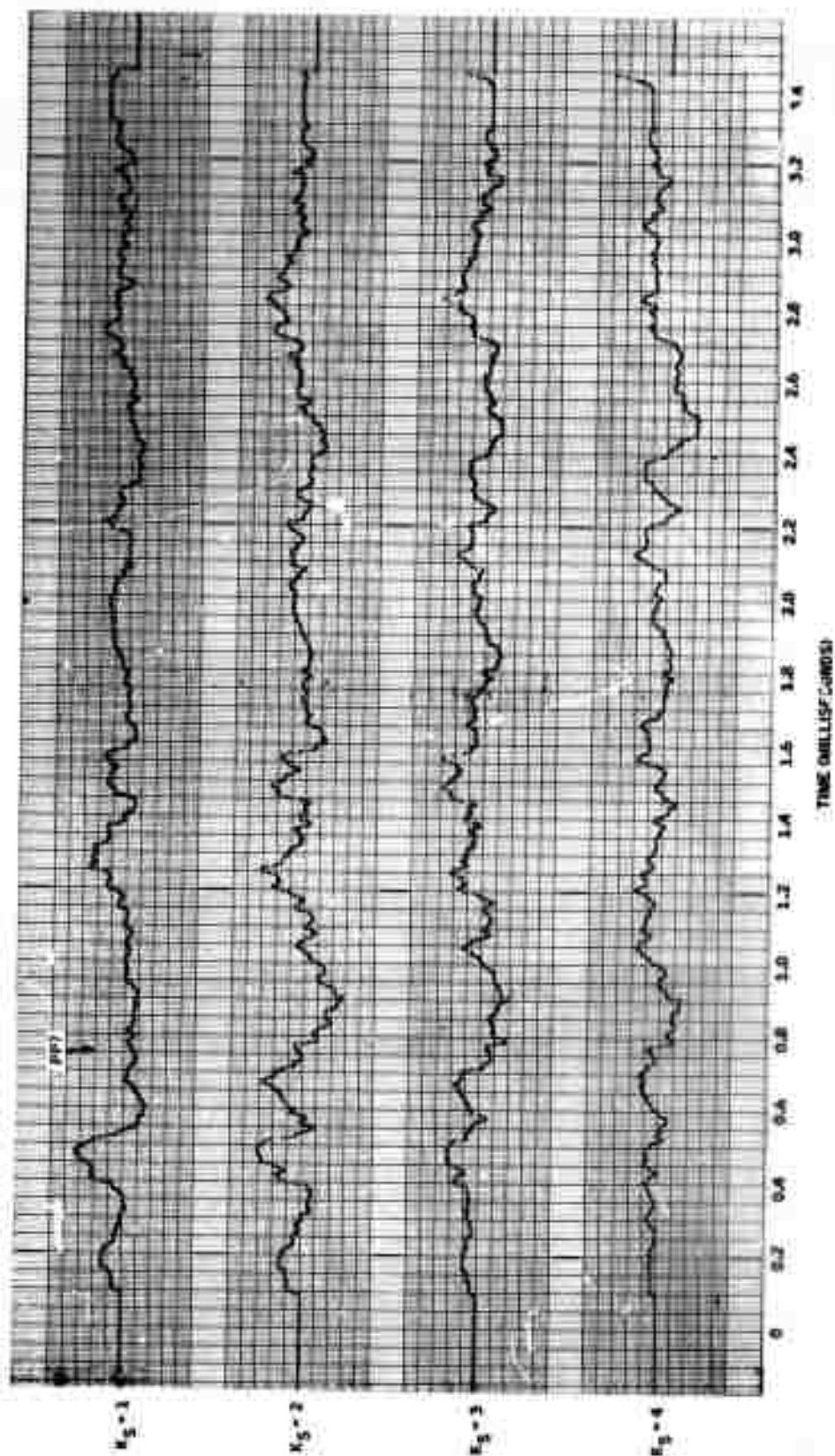
Figure 4·70. Charcoal Quarry, Cross-Correlation (SXE) of Ten-Element DIMUS Beams
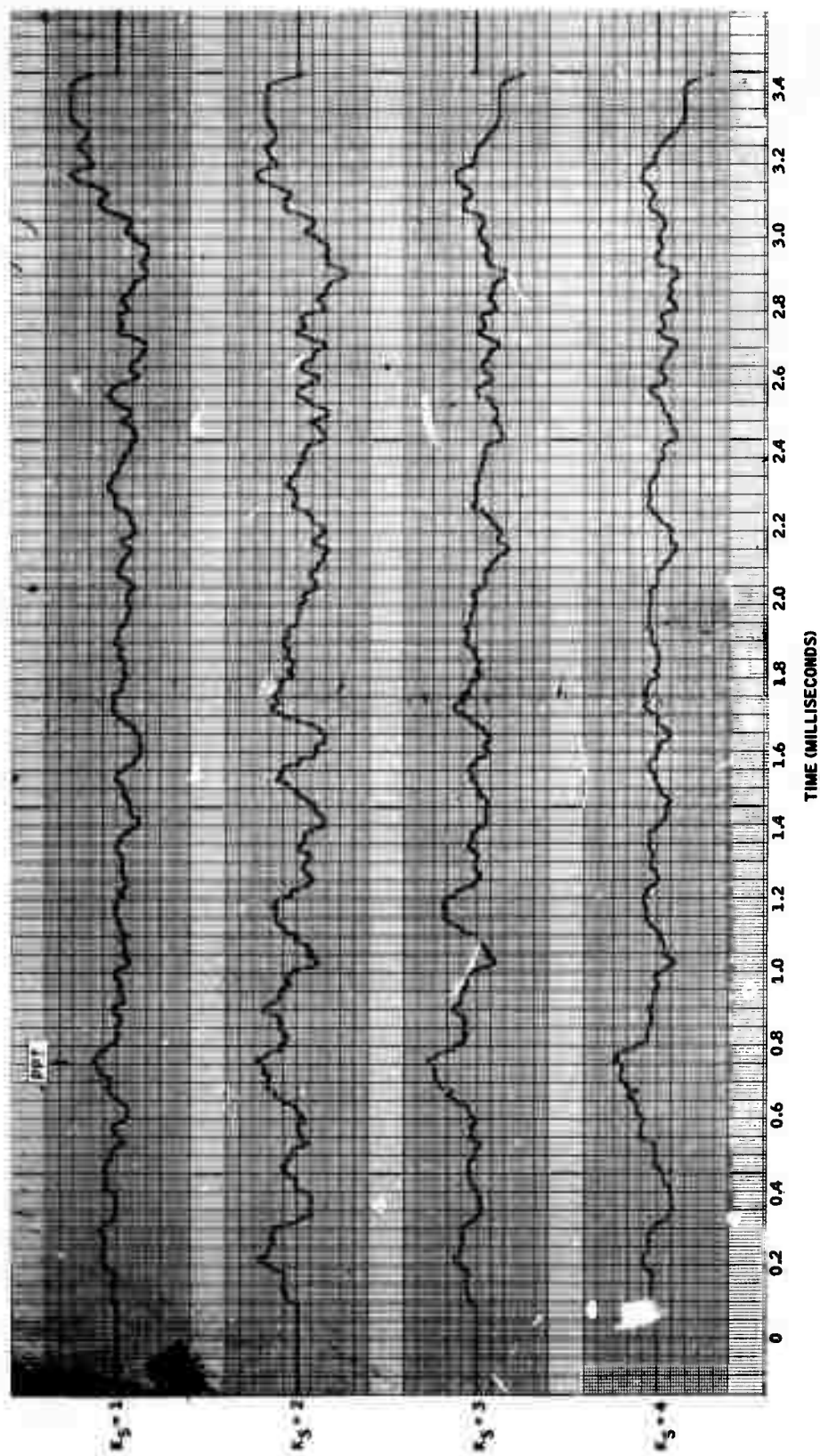
Figure 4-71. Charcoal Quarry, Cross-Correlation (SXW) of Ten-Element DIMUS Beams

TIME (MILLISECONDS)
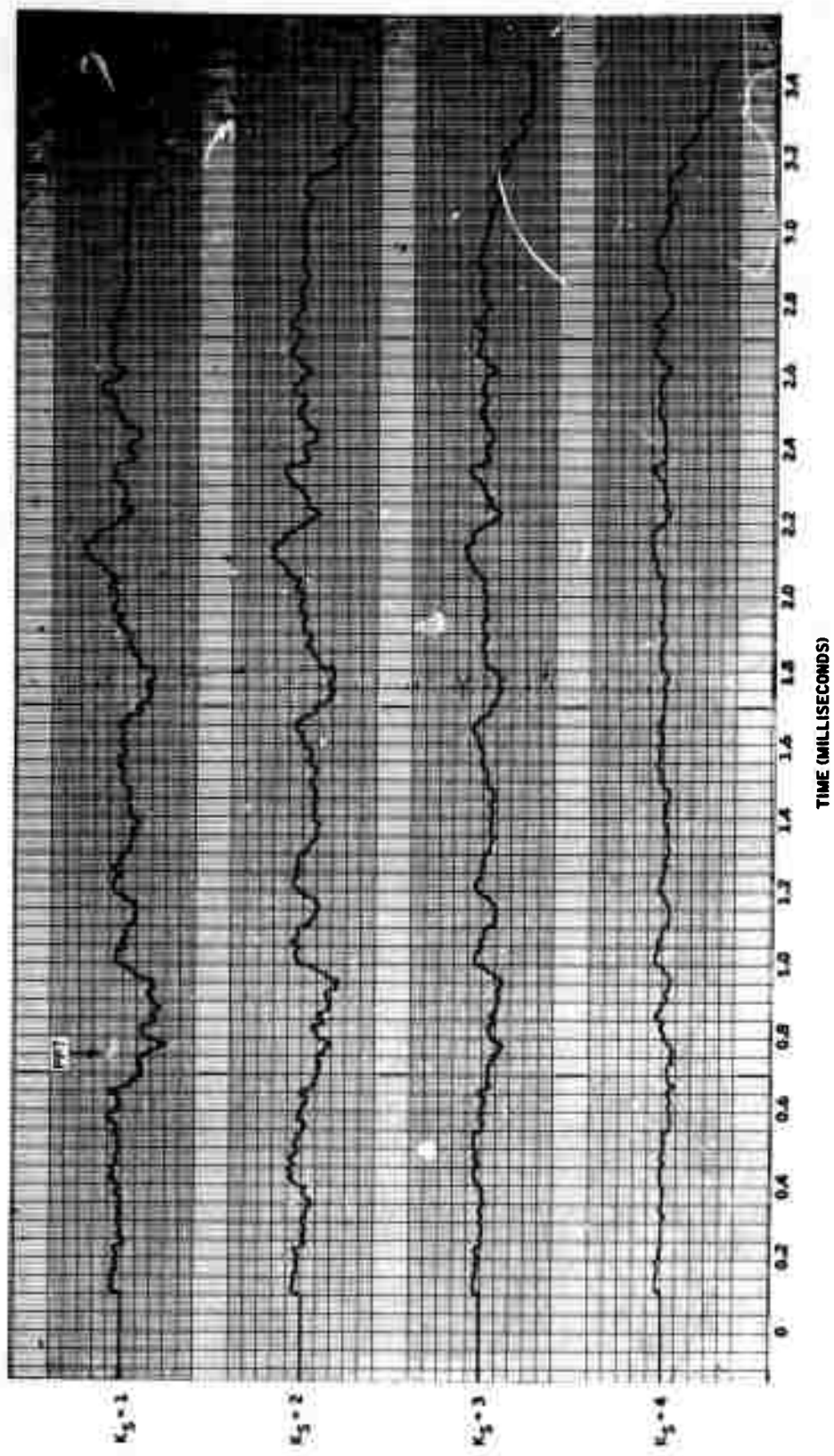
Figure 4-72. Charcoal Quarry, Cross-Correlation (NXW)
of Ten-Element DIMUS Beams
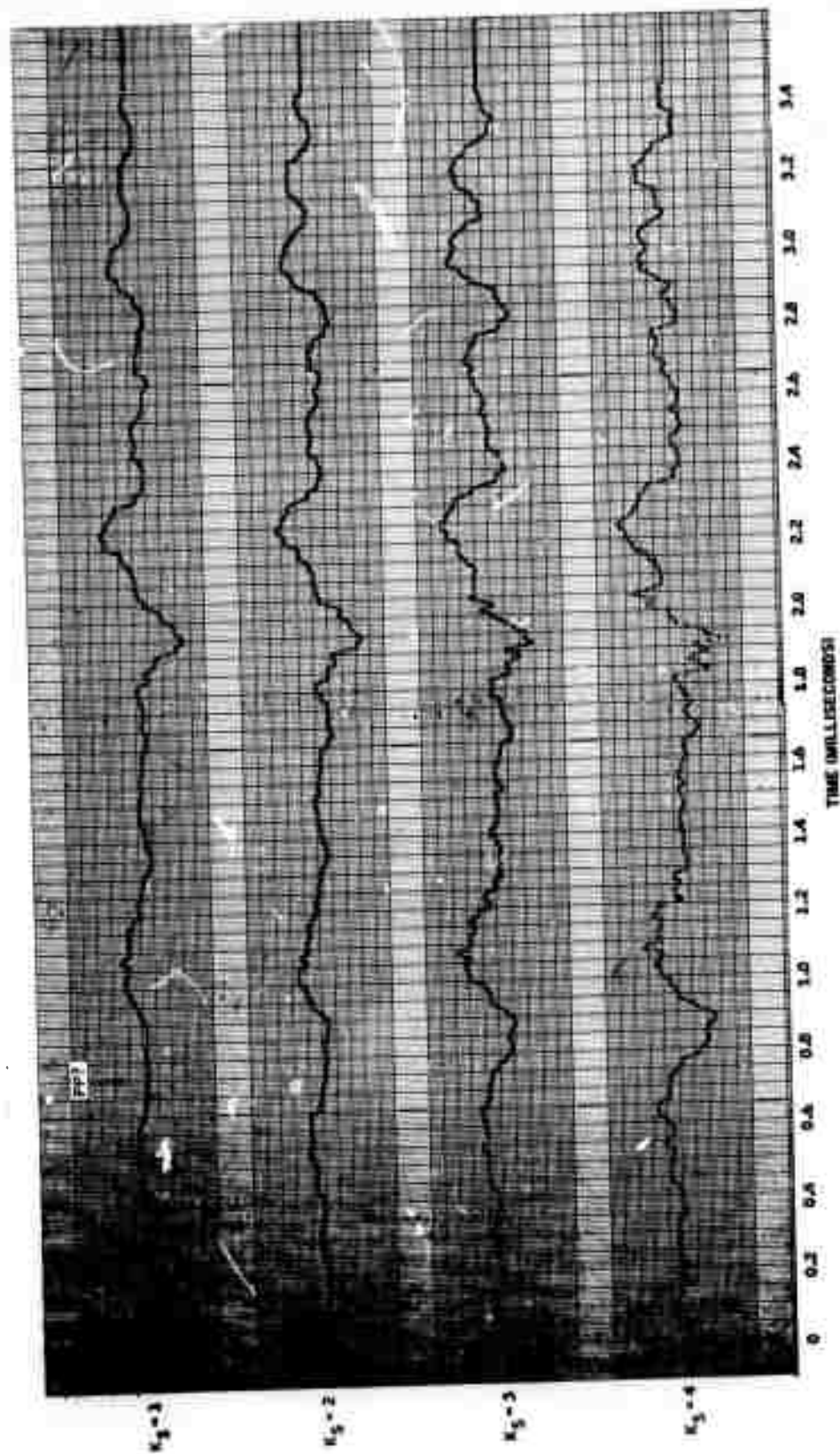
Figure 4-73. Charcoal Quarry, Cross-Correlation (NXE) of Nine-Element DIMUS/AN Beams

4-85
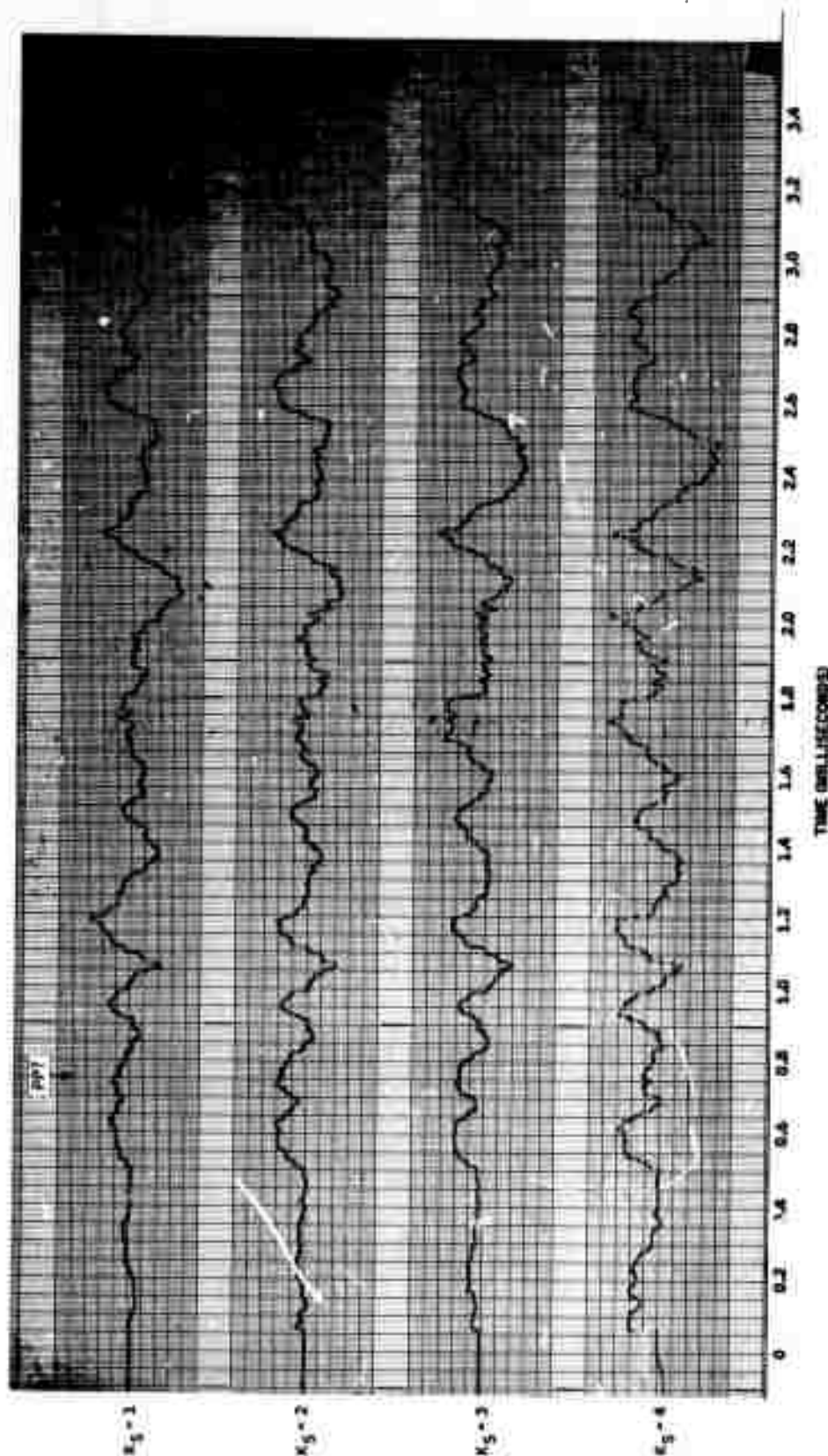
Figure 4-74. Charcoal Quarry, Cross-Correlation (SXE) of Nine-Element DIMUS/AN Beams
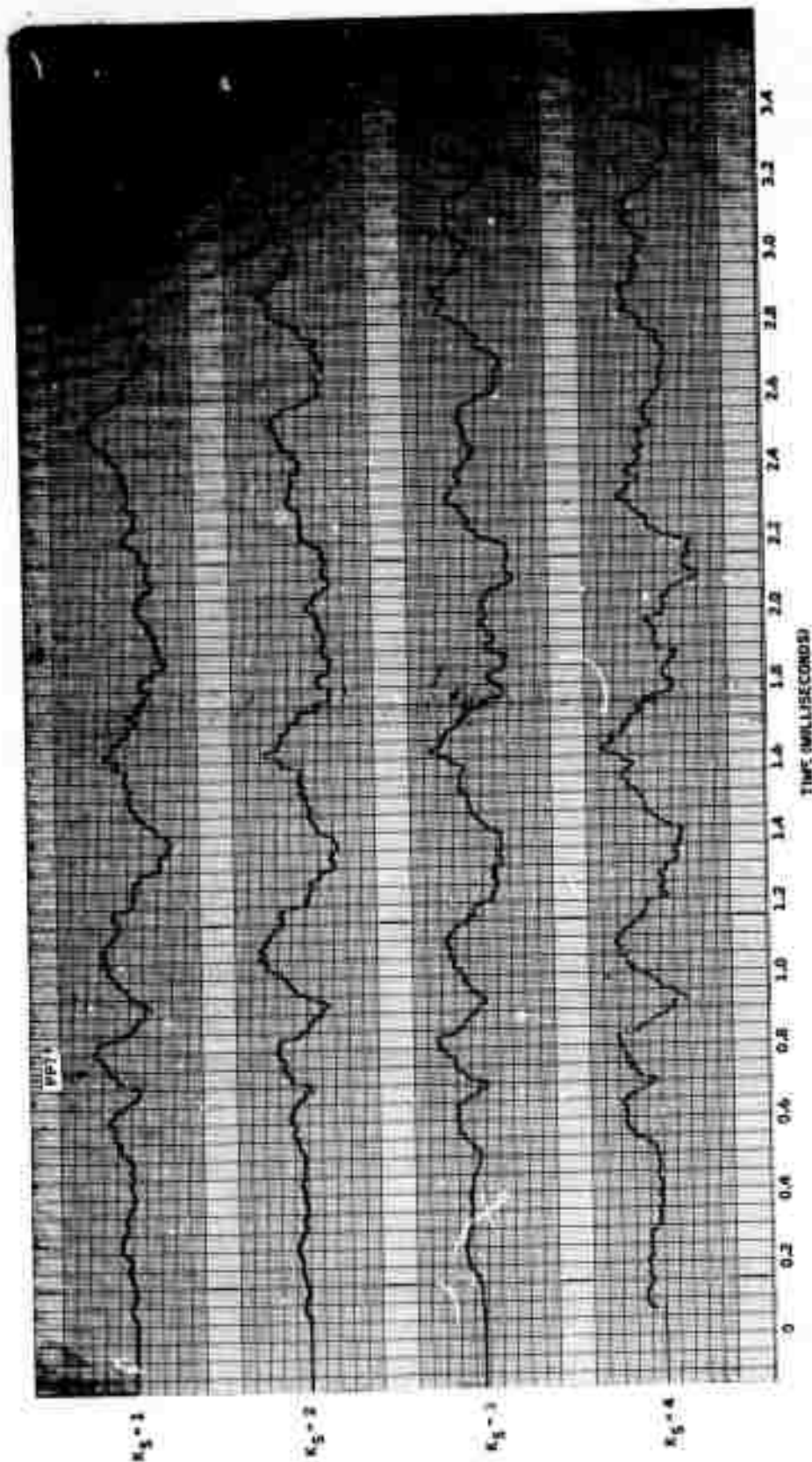
Figure 4-75. Charcoal Quarry, Cross-Correlation (SXW) of Nine-Element DIMUS/AN Beams

4-87

TIME (MILLISECONDS)
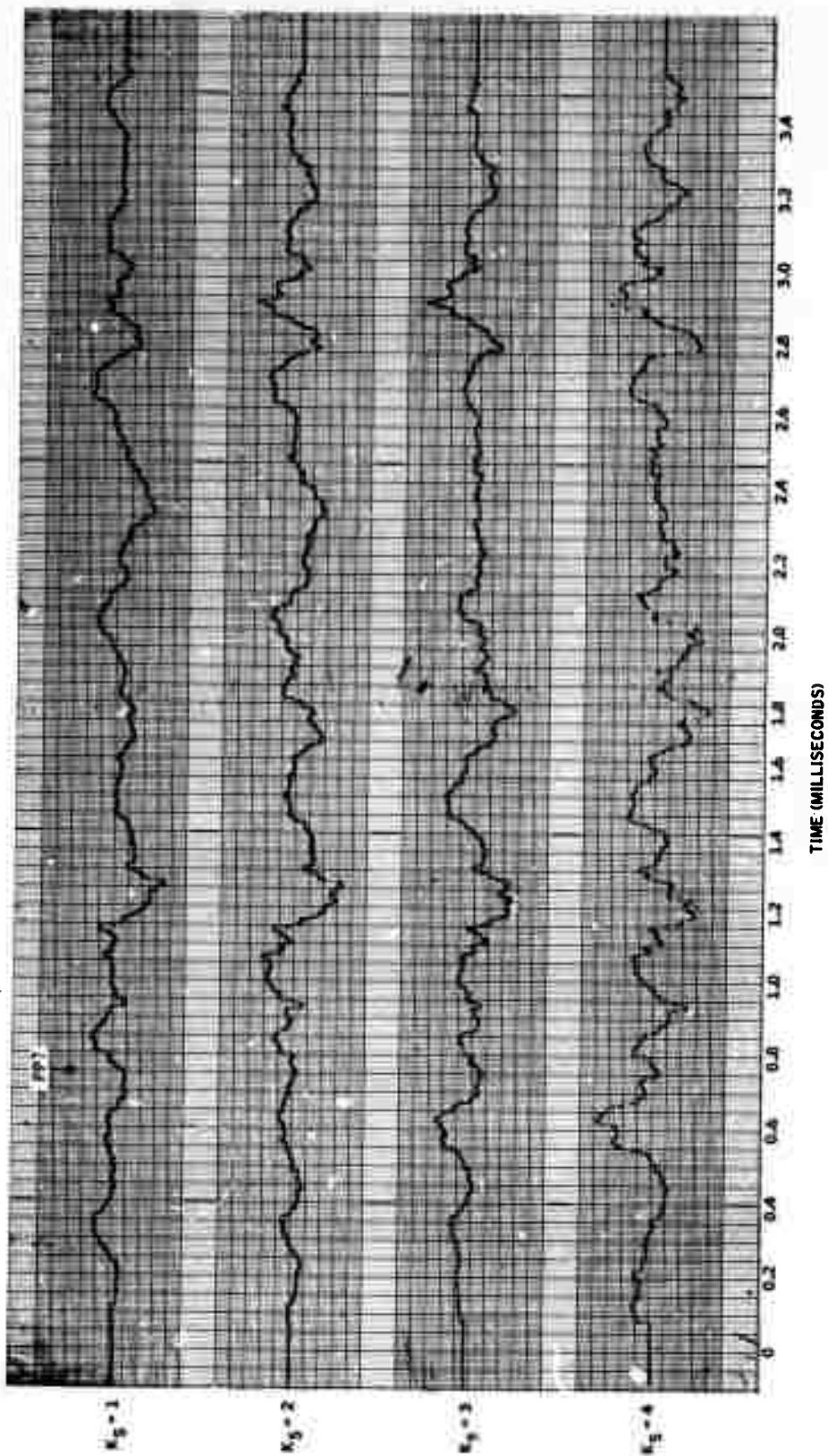
Figure 4-76. Charcoal Quarry, Cross-Correlation NXW)
of Nine-Element DIMUS/AN Beams

SECTION V
PROCESSOR DIGITAL IMPLEMENTATION

The recommended adaptive null processor algorithm has been analyzed, and a number of implementation schemes have been developed. These are presented, and one is recommended. The problems of data input and output are also discussed, and an approach is recommended.

5.1 ASSUMPTIONS

Before discursing the algorithm, the experimental setup is discussed to provide the basis on which the analysis was conducted.

A seismic pulse with a repetition rate of up to 20 Hz is transmitted into hard rock with a duration of approximately 200 μsec at 5 KHz. The pulse propagates at approximately 15,000 to 20,000 ft/sec.

The echo caused by rock anomalies up to 100 feet of the transmitting face is to be sensed by two linear arrays of receivers deployed as in Figure 5-1. The receiver elements are separated by approximately one-third the wavelength of the compressional P wave. The algorithm may be applied over a subset of these elements such as elements 1, 2, ..., K or 3, 4, ..., K, K+1. Up to 2K+2 elements may be used, where K ≤ 10.

The echo is digitized at 25 times the transmitter frequency using sign (+1, -1) digitization.

For 100 feet penetration (200 feet total path length) the input data time duration, T_d, is bounded by

$$\frac{200 \text{ feet}}{20 \times 10^3 \text{ ft/sec}} \leq T_d \leq \frac{200 \text{ feet}}{15 \times 10^3 \text{ ft/sec}}$$

$$10^{-2} \text{ sec} \leq T_d \text{ length} \leq 13.5 \times 10^{-3} \text{ sec}$$

At 125×10^3 samples/sec, corresponding to 5-KHz transmitted frequency, the corresponding number of samples is

$$1250 \text{ samples} \leq N \leq 1688 \text{ samples}$$
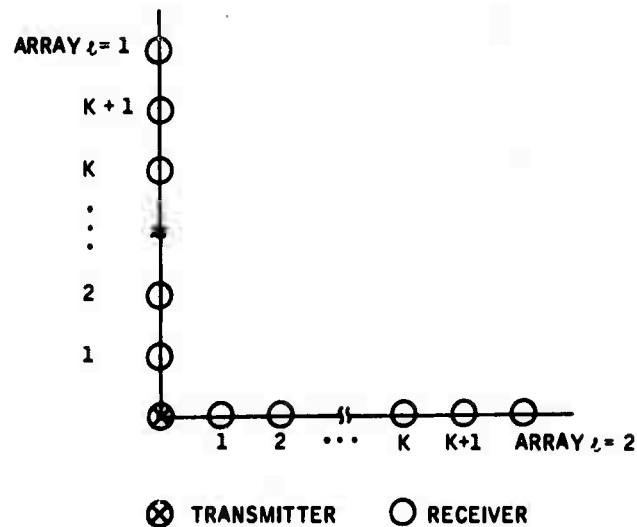
Figure 5-1. Orthogonal Array Geometry

5.2 THE ADAPTIVE NULL ALGORITHM

The recommended algorithm is discussed in the paragraphs which follow.
The algorithm consists of four parts:

- Data accumulation

- Interelement correlation

- Line array beamforming

- Orthogonal array multiplication and time-averaging

5.2.1 Data Accumulation

Let $X_{\ell k q}(n)$ be the nth sample of the echo for the ℓth array, k^{th} element,
for the qth pulse repetition. Accumulate data according to

$$\xi_{\ell k}(n) = \sum_{q=1}^{Q} \text{sgn } X_{\ell kq}(n); \qquad \begin{array}{l} 0 \leq n \leq N \\ \ell = 1, 2 \\ k = K_B, \ldots, K_E \end{array} \qquad (5.1)$$

where

$$\text{sgn } X_{\ell kq}(n) = +1 \text{ or } -1 \text{ according to the polarity of } X_{\ell kq}(n).$$

After generating $\xi_{\ell k}(n)$, store

$$\epsilon_{\ell k}(n) = \text{sgn } \xi_{\ell k}(n), \qquad \begin{array}{l} 0 \leq n \leq N \\ \ell = 1, 2 \\ k = K_B, \ldots, K_E \end{array} \qquad (5.2)$$

The expression $\epsilon_{\ell k}(n)$ is either +1 or -1 and may thus be stored in one bit. This process is repeated for both arrays on the elements K_B, K_B+1, ..., K_E to generate echo records for each element on the arrays. The total number of elements is limited to 22 (2K + 2) where $K = K_E - K_B + 1 \leq 10$.

Each of the $\epsilon_{\ell k}(n)$ requires one bit of storage. For the specified 22 elements, the total store required is 22N bits or 2.75 N bytes.

5.2.2 Element Correlation

Divide each of the 22 stored signals into $D = N/\Delta$ subintervals, where Δ is two carrier periods. In samples, $\Delta = 50$ samples. Number the subintervals 1, 2, ..., D-2, D-1, D and perform D-2 correlations on the 2K pairs [i.e., 2K (D-2) correlations]:

$$\rho_{\ell k}(i, j) = \sum_{n=j\Delta}^{(j+1)\Delta - 1} \epsilon_{\ell k}(n) \epsilon_{\ell, k+1}(n+i), \qquad \begin{array}{l} \ell = 1, 2 \\ k = K_B, \ldots, K_E \\ j = 1, 2, \ldots, D-2 \\ -I \leq i \leq I \end{array} \qquad (5.3)$$

Then find and store the 2K (D-2) critical delays, $\hat{i}_{\ell kj}$, that maximize $\rho_{\ell k}$ in the jth subinterval

$$\rho_{\ell k}(i_{\ell kj}, j) = \max_{i \, \epsilon \, [-I, I]} \rho_{\ell k}(i, j), \qquad \begin{array}{l} \ell = 1, 2 \\ k = K_B, \ldots, K_E \\ j = 1, 2, \ldots, D-2 \end{array} \qquad (5.4)$$

The surface wave propagates at approximately one-half the compressional wave velocity. For the given element separation ($\lambda_p \cong 1/4$ ft)

$$\left(0.25 \text{ ft}\right) \left(\frac{1}{20 \times 10^3 \text{ ft/sec}}\right) \left(\frac{1}{2}\right) \leq \text{interelement surface-wave propagation time}$$

$$\leq \left(0.25 \text{ ft}\right) \left(\frac{1}{15 \times 10^3 \text{ ft/sec}}\right) \left(\frac{1}{2}\right)$$

or

$25 \ \mu\text{sec} \leq$ interelement surface wave propagation time $\leq 33 \ \mu\text{sec}$.

In samples (500K samples/sec),

$13 \leq I \leq 17$.

Thus we correlate for $-I \leq i \leq I$, $I \sim 17$.

5.2.3 Line Array Adaptive Beamforming

The original algorithm calculates delays for beamforming assuming plane wave arrivals. Let $p_{\ell S}$ be the interelement steering delay (in numbers of samples) for the Sth steering order on the ℓth array.

Define the weight

$$W_{\ell p j} = \begin{cases} 0; & |p_{\ell S} - \hat{i}_{\ell k j}| \leq \delta \\ 1; & \text{otherwise} \end{cases} \tag{5.5}$$

Then the ℓS^{th} beam is:

$$y_{\ell S}(n) = \sum_{k=1}^{K} \left[\epsilon_{\ell k}^{(j)}(n + k p_{\ell S}) - W_{\ell p j} \epsilon_{\ell,k+1}^{(j)}(n + k p_{\ell S} + \hat{i}_{\ell k j}) \right] \tag{5.6}$$

The superscript j denotes the subinterval, and resulting $W_{\ell k j}$ and $\hat{i}_{\ell k j}$, appropriate to the sample number $(n + k p_{\ell S})$.

5-4

5.2.4 Recursive Beamforming

An alternate form for Equation (5.6) was derived as follows:

$$y_{\ell S}(n) = e_{\ell 1}^{(j)}(n + p_{\ell S}) - W_{\ell 1 j}\, e_{\ell 2}^{(j)}(n + p_{\ell S} + \hat{i}_{\ell 1 j}) + e_{\ell 2}^{(j)}(n + 2p_{\ell S})$$

$$- W_{\ell 2 j}\, e_{\ell 3}^{(j)}(n + 2p_{\ell S} + \hat{i}_{\ell 2 j}) + \ldots + e_{\ell k}^{(j)}(n + kp_{\ell S})$$

$$- W_{\ell k j}\, e_{\ell,\,k+1}^{(j)}(n + kp_{\ell S} + \hat{i}_{\ell k j})$$

Grouping like terms in e, we have

$$y_{\ell S}(n) = e_{\ell 1}^{(j)}(n + p_{\ell S}) + e_{\ell 2}^{(j)}(n + 2p_{\ell S}) - W_{\ell 1 j}\, e_{\ell 2}^{(j)}(n + p_{\ell S} + \hat{i}_{\ell 1 j}) + \ldots$$

$$+ e_{\ell k}^{(j)}(n + k\,p_{\ell S}) - W_{\ell,\,k-1,\,j}\, e_{\ell k}^{(j)}[n + (K-1) p_{\ell S} + \hat{i}_{\ell,\,k-1,\,j}]$$

$$- W_{\ell k j}\, e_{\ell,\,k+1}^{(j)}(n + k\,p_{\ell S} + \hat{i}_{\ell k j})$$

Recursively, this becomes

$$y_{\ell S}^{v}(n) = e_{\ell 1}^{(j)}(n + p_{\ell S}), \quad v = 1$$

$$y_{\ell S}^{v}(n) = y_{\ell 1}^{v-1}(n) + e_{\ell k}^{(j)}(n + k\,p_{\ell S}) - W_{\ell k j}\, e_{\ell,\,k}[n + (k-1) p_{\ell S} + \hat{i}_{\ell k j}],$$

$$v = 2, \ldots \tag{5.6'}$$

$$y_{\ell S}(n) = y_{\ell S}^{v}(n) - W_{\ell k j}\, e_{\ell,\,k+1}(n + k\,p_{\ell S} + \hat{i}_{\ell k j})$$

5.2.5 Orthogonal Array Multiplication and Averaging

Define

$$Z_S(n) = \sum_{m=-M}^{M} y_{1S}(n + m)\, y_{2S}(n + m), \quad \Delta \leq n \leq N - \Delta \tag{5.7}$$

For improved computational efficiency, a recursive form for $Z_S(n)$ is

$$Z_S(n+1) = Z_S(n) + y_{1S}(n + 1 + m)\, y_{2S}(n + 1 + M) - y_{1S}(n - M)$$

$$y_{2S}(n - M) \tag{5.7'}$$

5.2.6 Computer Sizing

To establish computer memory and speed requirements, a program based on the recommended algorithm was written and is listed in Appendix B. In writing the program, provision was made for performing the algorithm with or without the adaptive-null feature (which allows standard DIMUS beamforming), and for displaying Y_iS as well as Z_S. This analysis provided the following memory requirements, which include programming for display generation, parameter increment/decrement, and all necessary subroutines:

Data	7450 words
Processing	500
Overhead	1100
Total	9050 words

5.3 DATA INPUT

A number of input schemes were considered for this application. The central difficulty in input is twofold. First, Equations (5.1) and (5.2) require the echo to be "averaged" over Q iterations. Thus, an averaging mechanism must be provided for each sample (N) of each receiver (2K + 2) requiring N (2K + 2) "averages". Second, the input sample rate is high.

Several approaches for dealing with the input problems are discussed in the following paragraphs.

5.3.1 Full Parallel Input with Averaging

In this approach, all 2K+2 channels would be sampled simultaneously at up to 500 KHz and the values added to an appropriate store in the computer. This is indicated schematically in Figure 5-2.

The input rate for this scheme is given by

$$(22 \text{ channels}) (1 \text{ bit/sample}) (500 \times 10^3 \text{ sample/sec}) = 11 \times 10^6 \text{ bit/sec}$$

For small computers, a DMA channel will operate at approximately 500K words/sec. Assuming a 16-bit word we have 687K words/sec as input, which is clearly too high. To reduce the rate to 500K words/sec would require a word 22 bits wide. This rules out most machines in the "small" class.
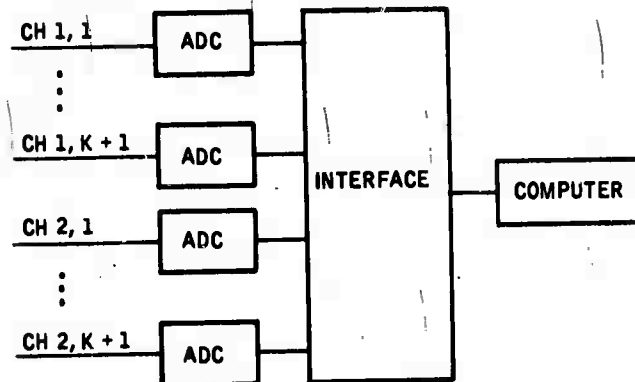
Figure 5-2. Full Parallel Input with Averaging

In addition, this approach requires a data store of 22 N bytes for the averaging.

An add-to-memory scheme will be required since there are 22 adds each 2 μsec.

Because of the high data rate, large memory requirements and necessity for add-to memory, this scheme was rejected.

5.3.2 Full Parallel with Off-Line Averaging

This approach uses full parallel recording, but the data is stored and averaged in a special device. Four schemes were considered.

The first was a rotating drum analog recorder with a track for each signal (22 tracks) and an address track as illustrated in Figure 5-3.

The drum is initially erased. A pulse is transmitted and the echo recorded for each sensor. Subsequently, each echo is summed with the previous echo(s) and recorded.
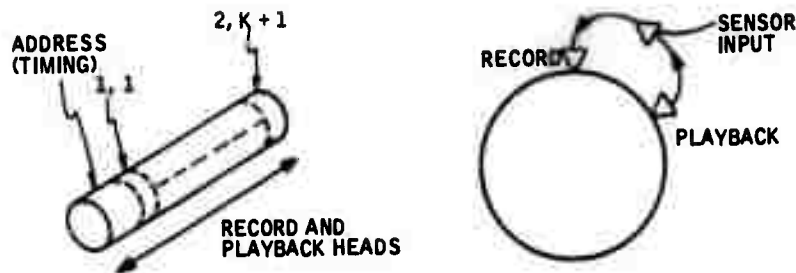
Figure 5-3. Rotating Drum Analog Recorder

The principal advantage of this approach is that it is independent of the digitization accuracy, and all the data can be recorded off-line. Consequently, input problems are minimized. In addition, we may begin the algorithm at Equation (5.2) and process in parallel, thus reducing the storage requirements, since we must only store approximately 2Δ sample points.

The second approach uses a similar drum as a digital store where the summing amplifier is replaced by an adder. It has similar advantages but is less independent of the digitization accuracy.

The third approach uses a circulating shift register in place of the drum. It has a reliability advantage but is costly and cannot hold as much data.

The fourth approach uses a charge storage (bucket brigade) register in place of the analog drum to achieve reliability. Its disadvantages are cost and data capacity.

All of these approaches require hardware development beyond the present scope of this effort. If a special-purpose hardware implementation is attempted, these schemes should be reconsidered.

5.3.3 Word Buffer

In this approach the outputs are multiplexed through a single ADC to a one-word buffer (16 bits). The buffer is cleared and the input stored until the buffer is full. It is read out and cleared. Then another word (16 bits) is collected, and so on, until the entire echo is recorded. Averaging is then done in the computer.

This approach is not recommended for two reasons: first, the buffer must be read and cleared in 2 μsec (one period) requiring very close timing or secondary buffering and extensive control logic. Second, if any changes are made to the input scheme, extensive modifications would be required in the buffer control logic.

5.3.4 Shift Register Buffer

This approach is illustrated in Figure 5-4. To use this interface the computer first clears the counter and FFs. The delay is loaded and the pulse enable set. The computer idles until the done flag is raised, and then the data is shifted into the computer and averaged using the readout.

This approach is recommended because it offers the advantages of fully buffering the input with a simple control and flexibility. In addition, the input enters serially for averaging. Finally, it is relatively insensitive to changes in digitization accuracy, rate or signal length. A signal length of 2048 samples was assumed to limit computer storage requirements.

5.3.5 Parameter Input

Parameter input can be accomplished by initially keying in the parameters from the front panel. Subsequently, they may be changed as follows:

- Use five front panel switches to select the parameter.

- Display its current value on the display screen.

- Set three switches to an increment/decrement rate.

- Increment/decrement as long as a front-panel switch is set, and change the parameter value on the screen. The rate of change increases with time but is reset to "slow" whenever the switch is released.

5.4 CONCLUSIONS

Based on this analysis, a minicomputer with 12K core and a 1-μsec cycle time is recommended.
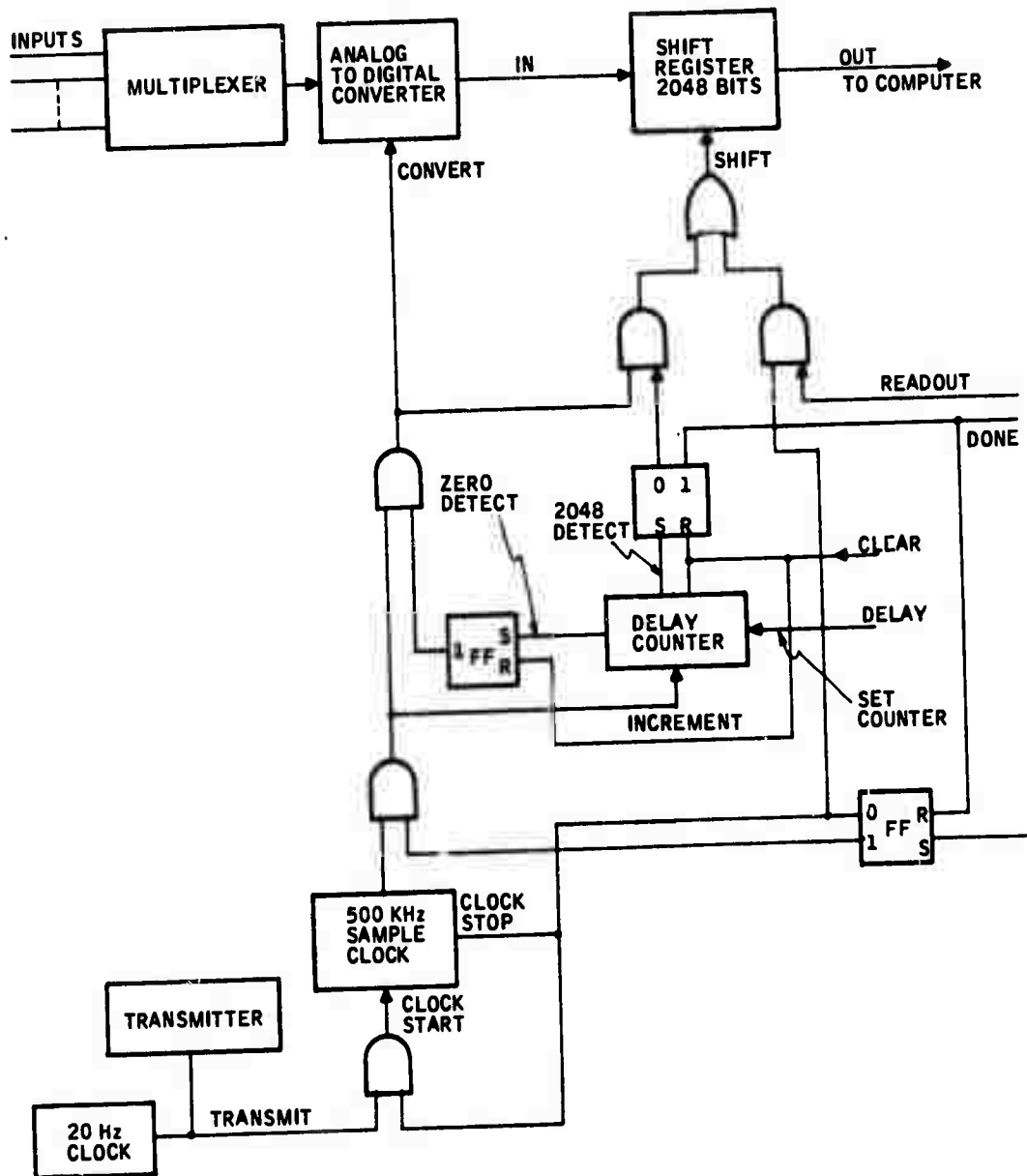
Figure 5-4. Shift Register Input Buffering

Most of the operations in this process are bit- or byte-oriented or memory-referenced through sequential list. Virtually any minicomputer could accomplish this task. However, the PDP-11 or NOVA are particularly suitable because of their bit and byte handling capacity.

The input scheme of 5.3.4 is recommended. The machine should have a paper tape reader for program loading.

The system would be configured as shown in Figure 5-5.
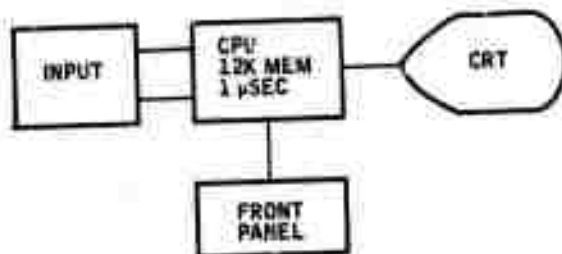
Figure 5-5. Recommended Processor Configuration

The processing time for each beam exclusive of display after data is in memory will be about 6 seconds. The time to get data into memory (100 summations at a 20-pps repetition rate is approximately 5 seconds. Display generation time depends on the display device.

Total processing time per beam is less than 30 seconds.

SECTION VI

REFERENCES

1. J.W. Dunkin and F.K. Levin, "Isochrons for a Three-Dimensional Seismic System," Geophysics, 36, 1099 (1971).

2. J.W. Birtill and F.E. Whiteway, "The Application of Phased Arrays to the Analysis of Seismic Body Waves," Tran. Roy. Soc. A, 258, 421 (1965).

3. M.A. Biot, "Propagation of Elastic Waves in a Cylindrical Bore Containing a Fluid," J. App. Phys., 23, 997 (1952).

4. G.F. Miller and H. Pursey, "On the Partition of Energy Between Elastic Waves in a Semi-infinite Solid," Proc. Roy. Soc., 233, 55 (1955).

5. J.E. White, Seismic Waves, McGraw-Hill, 1965.

6. P. A. Heelan, Radiation from a Cylindrical Source of Finite Length, Geophysics, 18, 685 (1953).

7. G.L. Brown, "Theory and Design of Pressure Pulse Transducers and Transient Detectors for Solid Media," PhD Thesis, UCLA (1956).

8. V.C. Anderson, "Digital Array Phasing," J. Acoust. Soc. Am., 32, 867 (1960).

9. R.J. Urick, Principles of Underwater Sound for Engineers, Chap. 3, McGraw-Hill, New York (1962).

10. M.J. Jacobson, "Analysis of a Multiple Receiver Correlation System," J. Acoust. Soc. Am., 31, 1638 (1959).

11. C.L. Dolph, "A Current Distribution of Broadside Arrays which Optimizes the Relationship between Beam Width and Side-Lobe Level," Proc. Inst. Radio Engrs., 44, 335 (1956).

12. P. Embree, J.P. Burg and M.M. Backus, "Wide Band Velocity Filtering - the Pie Slice Process," Geophysics, 28, 948 (1963).

13. S. Treitel, J.L. Shanks and C.W. Frasier, "Some Aspects of Fan Filtering," Geophysics, 32, 789 (1967).

14. J.F. Claerbout, "A Summary, by Illustrations, of Least-Squares Filters with Constraints," IEEE Trans. Info. Thy., IT-14, 269 (1968).

15. H. Kobayashi, "Iterative Synthesis Methods for a Seismic Array Processor," IEEE Trans. Geosci. Elec., GE-8, 169 (1970).

16. R. H. Duhamel, "Optimum Patterns for Endfire Arrays," Proc. IRE, 652 (May 1953).

17. V. O. Albers, Underwater Acoustics Handbook, Chapt. 11, Penn State Univ. Press, University Park, Pa. (1960).

18. F. C. Schweppe, "Sensor-Array Data Processing for Multiple Signal Sources," IEEE Trans. Info. Thy. IT-14, 294 (1968).

19. V. C. Anderson, "DICANNE, A Realizable Adaptive Process," J. Acoust. Soc. Am., 45, 398 (1969).

20. B. Widrow, P. E. Mantey, L. J. Griffiths and B. B. Goode, "Adaptive Antenna System," Proc. IEEE, 55, 2143 (1967).

21. L. J. Griffiths, "A Simple Adaptive Algorithm for Real-Time Processing of Antenna Arrays," Proc. IEEE, 57, 1696 (1969).

APPENDIX A

MATHEMATICAL DESCRIPTION OF ARRAY
PROCESSING TECHNIQUES

For the sake of completeness, this appendix catalogs the algorithms programmed on the general-purpose computer (DDP-24) to implement the various array processing techniques used in this study.

Consider the pair of uniformly spaced, orthogonal line arrays depicted in Figure 5-1 of Section V. Let $s_{ik}(n)$ be the signal sensed at the kth element on the ith array at the nth sample instant after transmission of a pulse by the source.

Denoting the arrays by their axis designation ($i = x, y$), if $b_i(n)$ is the beamformed output of the ith array, the cross correlation of the orthogonal arrays is computed by

$$ C(n) = \frac{1}{(2M+1)} \sum_{m=-M}^{M} b_x(n+m) \, b_y(n+m) $$

In all cases, the correlation window, (2M+1) samples, was chosen equivalent to a pulse length, which was roughly two signal carrier periods (100 μsec).

In the following discussion, we shall treat only the beamformed outputs. Since the beamforming algorithms were the same on each array for a given type of processing, the subscript i will be dropped for the sake of brevity.

Figure numbers for block diagrams of most processors are noted after the caption heading. The symbol $\langle m \rangle$ in the diagrams denotes an m sample delay.

P-1: DELAY AND SUM (Figure A1, $W_k = 1$, all k)

The beamformer output in this case is simply

$$ b(n) = \sum_{k=K_S}^{K_S+K_A-1} s_k(n - m_k) $$

A1

Here, K_A is the number of elements used in beamforming, K_S is the first element in the array (also denoting the beam number of the stack) and m_k is the sample delay for phasing the kth array element. Again for brevity, we shall omit the limits on k in future same since they are all identical.

P-2: DOLPH-TCHEBYSCHEFF (Figure A1)

In this case, the array element outputs are weighted by the Dolph-Tchebyscheff coefficients, W_k:

$$b(n) = \sum_k W_k s_k (n-m_k)$$

D-T shading weights used in this study are tabulated in Table A1.

P-3: DIMUS (Figure A2)

DIMUS beamforming is achieved by delay and sum on hard-clipped data:

$$b(n) = \sum_k sgn \lceil s_k (n-m_k) \rceil$$

where

$$sgn(z) = \begin{cases} 1, & Z \geq 0 \\ -1, & Z < 0 \end{cases}$$
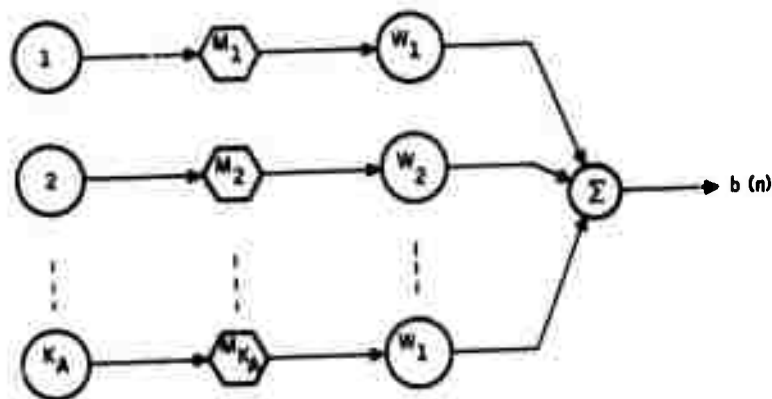
Figure A1.   D&S and D-T Beamformers

Table A1.   Dolph-Tchebyscheff Weights

K_A	Shading
5	D-T/20: (0.518, 0.831, 1.0, 0.831, 0.518)
	D-T/30: (0.319, 0.769, 1.0, 0.769, 0.319)
	D-T/40: (0.241, 0.726, 1.0, 0.726, 0.241)
9	D-T/20: (0.601, 0.615, 0.812, 0.950, 1.0, 0.950, 0.812, 0.615, 0.601)
	D-T/30: (0.253, 0.459, 0.719, 0.923, 1.0, 0.923, 0.719, 0.459, 0.253)
	D-T/40: (0.130, 0.349, 0.643, 0.898, 1.0, 0.898, 0.643, 0.349, 0.130)
13	D-T/20: (0.746, 0.534, 0.678, 0.808, 0.911, 0.977, 1.0, 0.977, 0.911, 0.808, 0.678, 0.534, 0.746)
	D-T/30: (0.267, 0.354, 0.531, 0.708, 0.860, 0.964, 1.0, 0.964, 0.860, 0.708, 0.531, 0.354, 0.267)
	D-T/40: (0.113, 0.234, 0.416, 0.621, 0.813, 0.950, 1.0, 0.950, 0.813, 0.621, 0.416, 0.234, 0.113)
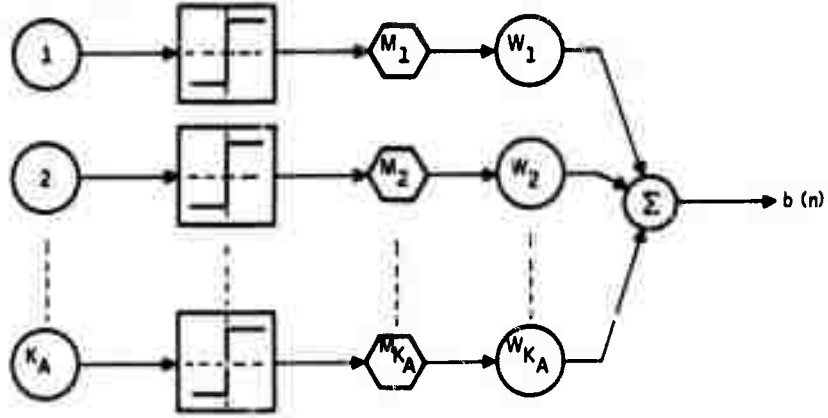
Figure A2.   DIMUS Beamformer

P-4:   FIXED NULL (Figure A3)

Fixed-null beamforming attempts to null the direct surface wave by subtracting a coherent estimate of the surface wave obtained from the (k+1)st element from the kth element output.   The beam output in this case is

$$b(n) = \sum_{k} [s_k (n-m_k) - s_{k+1} (n-m_k + \mu_s)]$$

where μ_s is the sample delay corresponding to the propagation time of the surface wave between adjacent elements.

P-5:   FAN FILTER (Figure A4)

Because of differences in notation with the literature (e.g., Ref. 12, 13) for the convenience of the reader we shall briefly review the derivation of the fan filter.   The fan-pass filter has the two-dimensional transfer function

Figure A3. Fixed-Null Beamformer

$$\eta_k = M_k - \mu_s$$
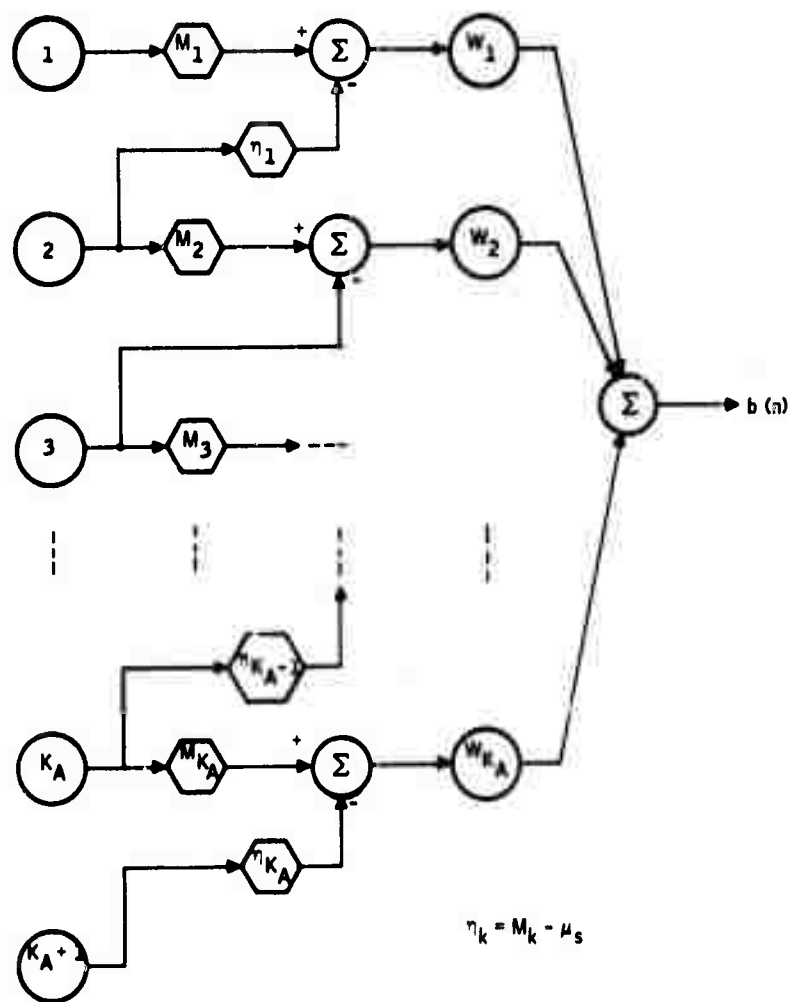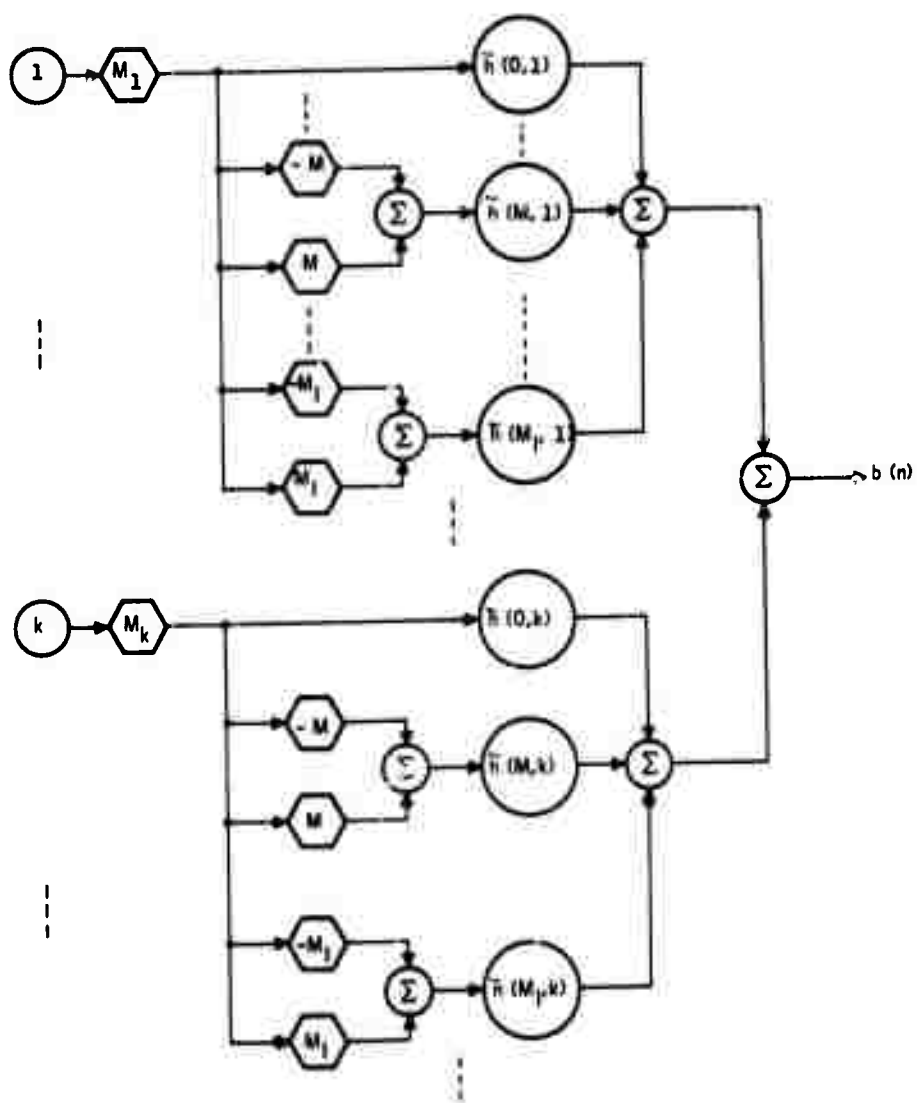
Figure A4. Fan Filter Beamformer

$$H(\omega, \varkappa) = \begin{cases} 1; & |\varkappa| \leq \dfrac{\omega}{V_o}, \quad |\omega| \leq \omega_o \\ \\ 0; & \text{otherwise} \end{cases}$$

in the circular frequency, ω, and wavenumber, $\varkappa$, space. That is to say, it has a lowpass frequency and a highpass trace velocity characteristic, passing signals incident on the array with frequencies $\omega \leq \omega_o$ and trace velocities $V \geq V_o$. The corresponding space-time filter impulse response is given by the two-dimensional inverse Fourier transform

$$h(t, x) = \frac{1}{(2\pi)^2} \int_{-\infty}^{\infty} d\omega \, e^{j\omega t} \int_{-\infty}^{\infty} d\varkappa \, e^{-j\varkappa x} \, H(\omega, \varkappa)$$

$$= \frac{1}{\pi^2 V_o} \left[\frac{\frac{1}{2}}{\frac{x}{V_o}^2 - t^2} \right] - \frac{1}{2\pi^2 x} \left[\frac{\cos \omega_o (t + x/V_o)}{(t + x/V_o)} \right.$$

$$\left. - \frac{\cos \omega_o (t - x/V_o)}{(t - x/V_o)} \right]$$

In the space-time continuum, beamforming can be performed by integrating (summing) over the entire observation space. Thus, the most general fan filter beam can be formed by

$$b(t) = \int_X dx \, b(t, x)$$

where

$$b(t, x) = \int_T d\tau \int_X d\xi \, h(t - \tau, \, x - \xi) \, s \, (\tau - \tau_\xi, \, \xi),$$

T and X define the temporal and spatial observation space, and τ_ξ is the phasing delay for the signal sensed at point ξ in the space X. For space sampled data, this leads to a processor structure of the form shown below in the case of a two-element array:

$$x = \frac{(2\ell+1)}{2} \Delta_x, \quad -L \le \ell \le L - 1$$

$$\omega_o = \frac{\pi}{\Delta_t}$$

(half the Nyquist sample rate)

$$\varkappa_o = \frac{\pi}{\Delta_x}$$

$$V_o = \omega_o/\varkappa_o = \Delta_x/\Delta_t$$

the normalized sampled data impulse response is

$$\tilde{h}(m, \ell) = \frac{\pi^2}{4} h[m\Delta_t, (2\ell+1)\Delta_x/2] = \frac{1}{\Delta_x \Delta_t [(2\ell+1)^2 - 4m^2]}$$

Converting the beamforming integral to its approximating sum (using $\tilde{h}$)

$$b(n) = \sum_{m=-M_I}^{M_I} \sum_{\ell=-L}^{L-1} \frac{s(n - m_\ell - m, -\ell)}{[(2\ell+1)^2 - 4m^2]}$$

Finally, to convert this expression to the geometry of Figure 4-1, let

$$K_A = 2L$$

$$k = \ell + L + K_S$$

$$K_T = K_A + 2K_S - 1$$

Then the fan-filter beamformer output can be expressed as

$$b(n) = \sum_k \left[\frac{s_k(n-m_k)}{(K_T-2k)^2}\right] + \sum_{m=1}^{M_I} \frac{[s_k(n - m_k - m) + s_k(n - m_k + m)]}{[(K_T - 2k)^2 - 4m^2]}$$

A9

A rule of thumb for selecting M_I is to ensure that the maximum value of the denominator of the filter impulse response is of the order of 10 times its minimum value. For $K_A \leq 14$, $M_I = 11$ is adequate.

P-6: ZERO-MEMORY, LEAST-SQUARES FILTER

This processor is a delay, weight and sum beamformer wherein the weights are adaptively selected to minimize the energy output of the beamformer in a given time observation interval, but subject to a desired signal fidelity constraint which permits signals on the beam axis to pass undistorted. Thus, for a beam output

$$b(n) = \sum_{k=K_S}^{K_S+K_A-1} W_{pk} \, s_k \, (n-m_k); \quad p N_o \leq n \leq (p+1) N_o - 1,$$

we seek weights W_{pk} that minimize the energy

$$P_p = \frac{1}{N_o} \sum_{n=p N_o}^{(p+1) N_o - 1} b^2(n)$$

on the pth sample interval of length N_o subject to the fidelity constraint

$$\sum_{k=K_S}^{K_S + K_A - 1} W_{pk} = 1.$$

It is convenient to change subscript notation by letting $i = k-K_S$, with $I = K_A-1$. Inserting the constraint in the expression for $b(n)$, P_p can be written in matrix notation as

$$P_p = S_o^2 + 2 \, \underline{W}' \, \underline{\rho} + \underline{W}' \, \underset{\sim}{R} \, \underline{W}$$

Here, the under bar denotes a vector, the under tilda denotes a matrix, and the prime denotes a transpose. Specifically, in the i subscript notation

$$\overline{s}_0^2 = \frac{1}{N_0} \sum_{n=pN_0}^{(p+1)N_0-1} s_0^2 (n-m_0),$$

W is an (Ix1) column vector with components W_i, $i = 1, \ldots, I$, corresponding to the original weights W_{pk}, $k = K_S + 1, \ldots, K_S + K_A - 1$,

$\underline{\rho}$ is an (Ix1) column vector with components

$$\rho_i = \frac{1}{N_0} \sum_{n=pN_0}^{(p+1)N_0-1} s_0 (n-m_0) [s_i (n-m_i) - s_0 (n-m_0)],$$

and $\underset{\sim}{R}$ is an (IxI) symmetric matrix with components

$$r_{ij} = \frac{1}{N_0} \sum_{n=pN_0}^{(p+1)N_0-1} [s_i (n-m_i) - s_0 (n-m_0)] [s_j (n-m_j) - s_0 (n-m_0)].$$

Minimizing P_p by setting $\partial P_p / \partial \underline{W} = \underline{0}$, the optimal weight vector is given by

$$\hat{\underline{W}} = - \underset{\sim}{R}^{-1} \underline{\rho}$$

with

$$\hat{W}_0 = 1 - \sum_{i=1}^{I} \hat{W}_i .$$

Computation of the inverse of $\underset{\sim}{R}$ was accomplished by a recursive matrix inversion algorithm that utilizes the symmetry of R. In order to demonstrate its derivation, let $\underset{\sim}{R}^{(\ell)}$ be the ($\ell \times \ell$) submatrix of $\underset{\sim}{R}$ with components r_{ij}, $2 \leq i$, $j \leq \ell \leq I$. Write

$$\underset{\sim}{R}^{(\ell)} = \begin{Bmatrix} \underset{\sim}{R}^{(\ell-1)} & \underline{r}^{(\ell)} \\ \underline{r}^{(\ell)'} & r_{\ell\ell} \end{Bmatrix}$$

A11

where $\underline{r}^{(\ell)}$ is the $(\ell-1) \times 1$ correlation vector with components $r_{i\ell}$, $1 \le i \le \ell-1$. Assume that $Q^{(\ell-1)} = [R^{(\ell-1)}]^{-1}$ is known and we wish to compute the inverse, $\underset{\sim}{Q}^{(\ell)}$, of $\underset{\sim}{R}^{(\ell)}$ in the form

$$\underset{\sim}{Q}^{(\ell)} = \left\{ \begin{array}{cc} \underset{\sim}{T}^{(\ell)} & \underline{q}^{(\ell)} \\ \underline{q}^{(\ell)'} & q_{\ell\ell}^{(\ell)} \end{array} \right\}$$

where $\underset{\sim}{T}^{(\ell)}$ has components $q_{ij}^{(\ell)}$, $1 \le i$, $j \le \ell - 1$, and $\underline{q}^{(\ell)}$ has components $q_{i\ell}^{(\ell)}$, $1 \le i \le \ell-1$. The superscript serves to indicate both the dimensions of matrices and vectors, and the iteration number of $\underset{\sim}{Q}$.

Since

$$\underset{\sim}{R}^{(\ell)} \underset{\sim}{Q}^{(\ell)} = \left\{ \begin{array}{cc} \underset{\sim}{I} & \underline{0} \\ \underline{0}' & 1 \end{array} \right\}$$

where I is the identity matrix and $\underline{0}$ is the null vector, the resulting three independent equations

1. $\underset{\sim}{R}^{(\ell-1)} \underset{\sim}{T}^{(\ell)} + \underline{r}^{(\ell)} \underline{q}^{(\ell)'} = \underset{\sim}{I}$

2. $\underset{\sim}{R}^{(\ell-1)} \underline{q}^{(\ell)} + \underline{r}^{(\ell)} q_{\ell\ell}^{(\ell)} = \underline{0}$

3. $\underline{r}^{(\ell)'} \underline{q}^{(\ell)} + r_\ell \, q_{\ell\ell}^{(\ell)} = 1$

can be solved for the components of $\underset{\sim}{Q}^{(\ell)}$ as follows:

1. $\underset{\sim}{T}^{(\ell)} = \underset{\sim}{Q}^{(\ell-1)} - \underline{v}^{(\ell)} \underline{q}^{(\ell)'}$

2. $\underline{q}^{(\ell)} = -Q^{(\ell-1)} \underline{r}^{(\ell)} q_{\ell\ell}^{(\ell)} = -\underline{v}^{(\ell)} q_{\ell\ell}^{(\ell)}$

3. $q^{(\ell)} = [r_{\ell\ell} - \underline{r}^{(\ell)'} \underline{v}^{(\ell)}]^{-1}$

A12

In summary, the recursive algorithm for inversion of $\underset{\sim}{R}$ can be written as follows:

- Initialization:

$$r_{11} = \frac{1}{N_o} \sum_{n=pN_o}^{(p+1)N_o-1} [s_1(n-m_1) - s_0(n-m_0)]^2$$

$$q_{11}^{(1)} = \frac{1}{r_{11}}$$

- ℓ^{th} iteration $(2 \leq \ell \leq I)$:

$$r_{i\ell} = \frac{1}{N_o} \sum_{n=pN_o}^{(p+1)N_o-1} [s_i(n-m_i) - s_0(n-m_o)][s\ell(n-m\ell) - s_0(n-m_o)];$$

$$1 \leq i \leq \ell$$

$$v_i^{(\ell)} = -\sum_{j=1}^{\ell-1} q_{ij}^{(\ell)} r_{j\ell} ; \quad 1 \leq i \leq \ell-1$$

$$q_{\ell\ell}^{(\ell)} = (r_{\ell\ell} - \sum_{i=1}^{\ell-1} v_i^{(\ell)} r_{i\ell})^{-1}$$

$$q_{i\ell}^{(\ell)} = q_{\ell i}^{(\ell)} = -q_{\ell\ell}^{(\ell)} v_i^{(\ell)} ; \quad 1 \leq i \leq \ell-1$$

$$q_{ij}^{(\ell)} = q_{ij}^{(\ell-1)} - v_i^{(\ell)} q_{j\ell}^{(\ell)} ; \quad 1 \leq i, j \leq \ell-1$$

P-7: ADAPTIVE NULL (Figure A5)

The adaptive-null processor is similar to the fixed-null processor, P-4, except that the interference estimate is optimized in a least-square sense. Given a beam output of the form

$$b(n) = \sum_k [s_k (n-m_k) - W_{pk} s_{k+1} (n - m_k - \mu_{pk})]; \quad pN_0 \leq n \leq (p+1) N_0 - 1$$

We now minimize the energy

$$P_p = \frac{1}{N_0} \sum_{n=pN_0}^{(p+1) N_0 - 1} b^2(n)$$

on the pth sample interval with respect to the W_{pk} and the μ_{pk}, subject to the constraint

$$W_{pk} = 0 \text{ if } |\mu_{pk}| \leq \delta_{pk}.$$

This constraint prevents nulling of a desired return within the beam provided δ_{pk} is chosen equivalent to a half beamwidth in interelement sample delay.

The optimum delay μ_{pk} is chosen by maximizing the cross correlations

$$\hat{\delta}_{pk} (\mu_{pk}) = \max_{|i| \leq m_s} \left[\frac{1}{N_0} \sum_{n=pN_0}^{(p+1)N_0} s_k (n-m_k) s_{k+1} (n-m_k-i) \right]$$

scanned over a range encompassing the maximum interelement propagation time for surface-wave interferences, m_s in samples, for every $K_S \leq k \leq K_S + K_A - 1$. It is necessary to perform the search for the cross-correlation maximum on every element pair because the majority of the beamforming is in the near field of the array.

Simple minimization of P_p with respect to W_{pk} yields the optimal weights

$$\hat{W}_{pk} = \begin{cases} 0; & |\mu_{pk}| \leq \delta_{pk} \\ \\ \dfrac{\rho_{pk}(\mu_{pk})}{\sigma^2_{p,k+1}}; & |\mu_{pk}| > \delta_{pk} \end{cases}$$

where

$$\sigma^2_{p,k+1} = \frac{1}{N_o} \sum_{n=pN_o}^{(p+1)N_o-1} s^2_{k+1}(n - m_k - \mu_{pk}) .$$

P-8: ADAPTIVE NULL/CLIPPER CORRELATOR

This processor speeds up search for a correlation maximum in the adaptive-null processor by performing the cross correlation on hard-clipped data. Thus, the processor is identical to that of P-7 except that here the optimum delay is determined by maximizing

$$\hat{c}_{pk}(\mu_{pk}) = \max_{|i| \leq m_s} \left[\sum_{n=pN_o}^{(p+1)N_o-1} \epsilon_k(n-m_k) \epsilon_{k+1}(n-m_k-i) \right]$$

where

$$\epsilon_k(n) = \text{sgn}[s_k(n)] .$$

P-9: DIMUS/ADAPTIVE NULL (Figure A6)

A further simplification of the adaptive-null processor is obtained by exclusive processing of clipped data. Here, the beamformer output is

$$b(n) = \sum_k [\epsilon_k(n-m_k) - W_{pk}\epsilon_{k+1}(n - m_k - \mu_{pk})]; \quad pN_o \leq n \leq (p+1)N_o - 1$$

A15
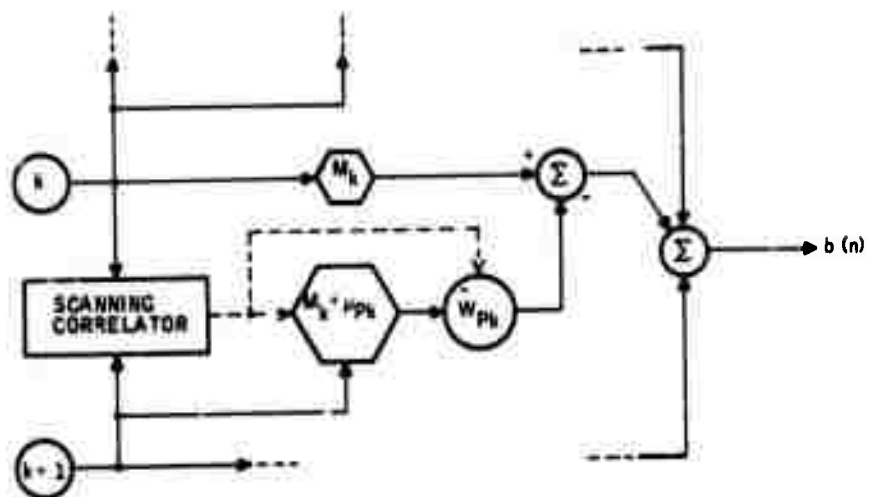
Figure A5.   Adaptive Null Beamformer
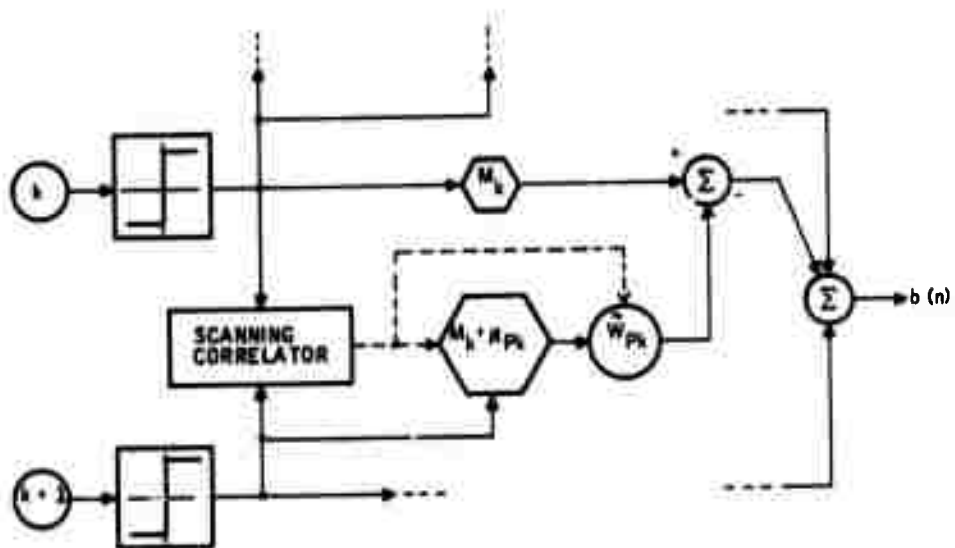
Figure A6.   DIMUS/AN Beamformer

A16

where μ_{pk} is selected as in P-8, while

$$\hat{W}_{pk} = \begin{cases} 0; & |\mu_{pk}| \leq \delta_{pk} \\ \\ 1; & |\mu_{pk}| > \delta_{pk} \end{cases}$$

P-10: DIMUS/ADAPTIVE NULL: SLIDING WINDOW

In this algorithm, advantage is taken of the savings that a recursive computation of the adjacent element cross correlations would have over the stepped interval computation previously described on long data records.

For

$$\zeta_k(n, i) = \sum_{m = n - N_o}^{n + N_o} \epsilon_k (m - m_k) \, \epsilon_{k+1} (m - m_k - i),$$

$$\zeta_k (n+1, i) = \zeta_k (n, i) - \epsilon_k (n - N_o - m_k) \, \epsilon_{k+1} (n - N_o - m_k - i)$$

$$+ \epsilon_i (n + N_o + 1 - m_k) \, \epsilon_{k+1} (n + N_o + 1 - m_k - i).$$

This permits an optimal weight, $\hat{W}_{nk}$, to be selected for each sample $n > N_o$, yielding

$$b(n) = \sum_k \lceil \epsilon_k (n - m_k) - W_{nk} \, \epsilon_{k+1} (n - m_k - \mu_{nk}) \rceil; \, n > N_o$$

with

$$\hat{W}_{nk} = \begin{cases} 0; & |\mu_{nk}| \leq \delta_{nk} \\ \\ 1; & |\mu_{nk}| > \delta_{nk} \end{cases}$$

where

$$\mu_{nk} = \max_{|i| \leq m_s} \zeta_k (n, i).$$

A17

APPENDIX B
COMPUTER PROGRAM REQUIREMENTS

DATA ACCUMULATION

This Data Accumulation routine performs

$$\xi_{\ell k}(n) = \sum_{q=1}^{Q} \text{sgn } X_{\ell kq}(n)$$

$$\epsilon_{\ell k}(n) = \text{sgn } \xi_{\ell k}(n)$$

using the input from the ADC and buffer circuit.

		No of Machine Instructions
	JQ2 = JQ/2	3
	DO5 IL = 1, 2	6
	DO5 IK = 1, JK	6
	DO1 IN = 1, 2048	6
1	IRO (IN) = Ø	4
	WRITE IL, JK	3
	DO2 IQ = 1, JQ	6
	CALL CLEAR	1
	CALL DELAY (NDELAY)	2
	CALL ENABLE	1
	CALL WAIT	2
	DO2 IN = 1, 2048	6
2	IRO(IN) = IRO(IN) + DATA	6
	DO5 IN = 1, 2048	6
	IF[IRO(IN) - JQ2] 3, 3, 4	8
3	IE (IL, IK, IN) = -1	2
	GO TO 5	1
4	IE (IL, IK, IN) = 1	2
5	CONTINUE	1

B1

Subroutines

CLEAR	-	CLEAR INTERFACE LOGIC
DELAY	-	Set INTERFACE Delay
ENABLE	-	Set Interface LNABLE Line
WIAT	-	Wait in a loop until DONE flag is raised
DATA	-	Shift out next bit of buffered data

Parameters

IL	-	Arrays pointer
IK	-	Element pointer
JK	-	Maximum element number
IN	-	Sample number
IRO(IN)	-	Vector of averages (1 byte/sample)
JQ	-	Iteration index
JQ2	-	Test index
IE(IL, IK, IN)	-	Array of stored data (2048 bits/sensor)

Assembly Language

```
IE      .BLOCK    6400 / 2048 bits/echo, 2 arrays, 25 elements
IRO     .BLOCK    1024 / 2048 bytes
IL      ∅
IK      ∅
IN      ∅
JQ      ∅
IQ      ∅
JQ2     ∅
JK      ?
DATA    LAC       (-2
        DAC       IL
        LAC       JQ
        RCR
        CMA
        TAD       (1
        DAC       JQ2
LLL3    LAC       (-JK

        DAC       IK
LL3     LAC       (-2048₁₀
        DAC       IN
        LAC       (IRO
        DAC       PT
L1      DZM*      PT
        ISZ       PT
        ISZ       IN
```

```
          JMP        L1
          JMS        WRITE
          IL
          IK
          LAC        JQ
          DAC        IQ
LL2       LAC        NDELAY
          IOT        DELAY
          IOT        ENABLE
          IOT        WAIT
          JMP        .-1
          LAC        (-2048_{10}
          DAC        IN
          LAC        (IRO
          DAC        PT
L2        LAC*       PT
          IOT        DATA
          LRS        10_8
          IOT        DATA
          LLS        10_8
          DAC*       PT
          ISZ        PT
          ISZ        IN
          JMP        L2
          ISZ        IQ
          JMP        LL2
          LAC        (-2048
          DAC        IN
          LAC        (IRO
          DAC        PT
L3        LAC*       PT
          LRS        10_8
          JMS        TEST
          CLA
          LLS        10_8
          JMS        TEST
          ISZ        PT
          ISZ        IN
          JMP        L3
          ISZ        IK
          JMP        LL3
          ISZ        IL
          JMP        LLL3
          JNP        COR
TEST      $\phi$
          TAD        JQ2
          SPA
          JMP        L4
```

B3

```
            LAC        (1
            SKP

L4          LAC        (∅
            JNS        STORE
            JNP*       TEST
```

*Note: This is code for a typical memory register machine without auto increment.

Storage Requirement

Data	7424
Program	100

ELEMENT CORRELATION, LINE ARRAY BEAMFORMING AND ORTHOGONAL CORRELATION FOR $\Delta \leq t \leq N - \Delta$

$$\rho_{\ell k}^{t}(i) = \sum_{n=t}^{t+\Delta-1} \epsilon_{\ell k}(n) \, \epsilon_{\ell, k+1}(n+i); \quad -I \leq i \leq I$$

$$\hat{\rho}_{\ell k}^{t}(\hat{i}_{\ell k}) = \max_{i \in [-I, I]} \rho_{\ell k}(i)$$

$$W_{\ell k}^{t} = \begin{cases} 0; & |p_{\ell s} - \hat{i}_{\ell k}^{t}| \leq \delta \\ \\ 1; & \text{otherwise} \end{cases}$$

$$y_{\ell S}^{(t)} = \sum_{k=1}^{K} [\epsilon_{\ell k}(t + k \, p_{\ell S}) - W_{\ell k} \, \epsilon(t + k \, p_{\ell S} + \hat{i}_{\ell K})]$$

$$Z_S(t) = \sum_{m=-M}^{M} y_{1S}^t(t+m) \, y_{2S}^t(t+m)$$

$$Z_S(t+1) = Z_S(t) + y_{1S}(t+1+M) \, y_{2S}(t+1+M) - y_{1S}(t-M) \, y_{2S}(t-M)$$

	No. of Machine Instructions
NDEL = N-JDEL	3
IT = JDEL	2
IZ = 0	1
M2 = 2*JM+1	6
M21 = M2-1	2
DO 10 IM = 1, M2	6
ITM = IM + IT	3
CALL YLS (ITM, IY1, IY2)	4
CALL DISPLAY (1, IY1)	3
CALL DISPLAY (2, IY2)	3
IYSV(IN) = IY1*IY2	10
10 IZ = IZ + IYSV (IN)	6
CALL DISPLAY (3, IZ)	3
IDELM1 = JDEL + JM + 1	4
IDELNM = JN - JDEL + JM	4
DO 12 IT = IDELM1, IDELNM	6
IZ = IZ - IYSV(°)	4
DO 11 IM = 1, M21	6
11 IYSU(IM) = IYSV (IM + 1)	8
CALL YLS (IT, KY1, IY2)	4
CALL DISPLAY (1, IY1)	3
CALL DISPLAY (2, IY2)	3
IYSV (M2) = IY1*IY2	4
IZ = IZ + IYSV (M2)	4
12 CALL DISPLAY (3, IZ)	3
TO TO 40	1
END	106
SUBROUTINE YLS (IT, Y1, Y2)	6
DO 23 IL = 1, 2	6
IY = 0	1
DO 22 IK = JKB, JKE	6
IF (NOCOR) GO TO 21	6
ICRIT = - JI	4
ICOMX = ICOR (IL, IK, -I, IT)	8

```
        LJI2  =  2*JI  =  1                              6
        DO 20 LJ  =  1, LJI2                             6
        III  =  II-JI                                    3
        ICON  =  ICOR (IL,  IK, III)                     8
        IF (ICOMX.GT.ICON) TO TO 20                      8
        ICONX  =  ICON                                   2
        ICRIT  =  III                                    2
   20   CONTINUE                                         1
        IW  =  0                                         1
        IF (ABS(P(IL) -  ICRIT).LE.DELI) IW  =  -1      14
        IW  =  IW + 1                                    1
        IP  =  IT  +  IK * IP (IL)  +  ICRIT            10
        IY  =  IY   ·  IW * IE (IL, IK, IP)             14
   21   IP  =  IT  +  ID * IP (IL)                      10
   22   IY  =  IY  +  IE (IL, IK, IP)                   12
        IF (IL.EQ.1) IY1  =  IY                          4
        IF (IL.EQ.2) IY2  =  IY                          4
   23   CONTINUE                                         1
        RETURN                                           1
        END                                             1
                                                       146

        FUNCTION ICOR (IL, IK, II, IT)                  6
        COMMON JDEL, I
        ISUM  =  φ                                       1
        IT1  =  IT  +  JDEL  -  1                        4
        DO 30 IN  =  IT, IT1                             6
        IK1  =  IK+1                                     3
        INI  =  IN+1                                     3
   30   ISUM  =  ISUM  +  IE (IL, IK, IN)*IE (IL, IK1, INI)   14
        ICOR  =  ISUM                                    3
        RETURN                                           1
        END                                             1
                                                        42
```

Note: IE(IL, IR, I) is a function which packs and unpacks data as appropriate.

The code for the segmented interval is analogous except that $\hat{\imath}_{lkj}$ and W_{lkj}
are chosen appropriate to $n + kp_{lS}$.

Subroutine

IE (IL, IK, J) is a function which returns ± 1 from $(0, 1)$ and packs and unpacks
as necessary.   DISPLAY (I, K) is the display routine.

Parameters

IT - sample no.
JDEL - input correlation window
IZ - orthogonal output
M2, M21, IM, ITM, IDELMI, IDELNM - INDICES
IY1 - Array 1 beam
IY2 - Array 2 beam
IYSV(IM) - Array of beam products (2*JN = 1)
IY, IK, IL, LJI2, II, III, IP, ISUM, IT1, INI, IN - index pointer
JI - delay interval
JKB, JKE - Element indices
NOCOR - Logical variable for correlation
ICOMX - max correlation
ICRIT - critical delay
ICON - New correlation
IW - weight
P(IL) - Steering delay
DELI - test parameters

Assembly Language

This code was not generated. The size is estimated from the Fortran 4.

Storage Requirements

Data	57	JM ~ 10
Program	400	

DISPLAY ROUTINE

This routine controls the plotting of the echo on the screen. Based on past experience, storage is allocated as follows:

Plotting	100
Housekeeping	50
Alphanumeric	120
Misc.	80
Total	350

APPENDIX C
DIMUS BEAMFORMING AND ARRAY DESIGN

An important aspect of beamforming in this application is the necessity of near-field beamforming over much, if not most, of the data record when a single source located at the origin of the L-shaped array is used. Referring to Figure C-1, suppose it is desired to steer and hold a beam pointed in the (ϕ_S, θ_S) direction throughout the length of the record. At a penetration depth of r_S, assume a parallel reflecting plane normal to the beam axis. The delays in arrival times at the kth elements on the x and y arrays of a signal emanating from the image source at $(2r_S, \phi_S, \theta_S)$, relative to the signal arrival at the origin, are

$$\tau_{xks} = \frac{2r_s}{v_p} \left\{ 1 - \left[1 + \left(\frac{x_k}{2r_s}\right)^2 + \left(\frac{\xi_{xk}}{2r_s}\right)^2 \right. \right.$$
$$\left. \left. - \frac{1}{r_s}(x_k \sin\phi_s \cos\theta_s + \xi_{yk} \cos\phi_s)\right]^{\frac{1}{2}} \right\}$$

$$\tau_{yks} = \frac{2r_s}{v_p} \left\{ 1 - \left[1 + \left(\frac{y_k}{2r_s}\right)^2 + \left(\frac{\xi_{yk}}{2r_s}\right)^2 \right. \right.$$
$$\left. \left. - \frac{1}{r_s}(y_k \sin\phi_s \sin\theta_s + \xi_{yk} \cos\phi_s)\right]^{\frac{1}{2}} \right\}$$

Here, v_p is the P-wave velocity and ξ_{xk} and ξ_{yk} are deviations in element positions normal to the x-y plane due to irregularities on the surface.

For sampled data, the sample number n is related to the penetration depth by

$$n = \frac{2r_s}{v_p \Delta} = \frac{2r_s}{\lambda_p}\left(\frac{T_c}{\Delta}\right)$$

where Δ is the sample interval, T_c is the pulse carrier period, and λ_p is the P wavelength. The delay in pulse samples for phasing the kth element on the ith array (i = x or y) to steer a product beam in the ϕ_s, θ_s) direction at the nth record sample instant is then
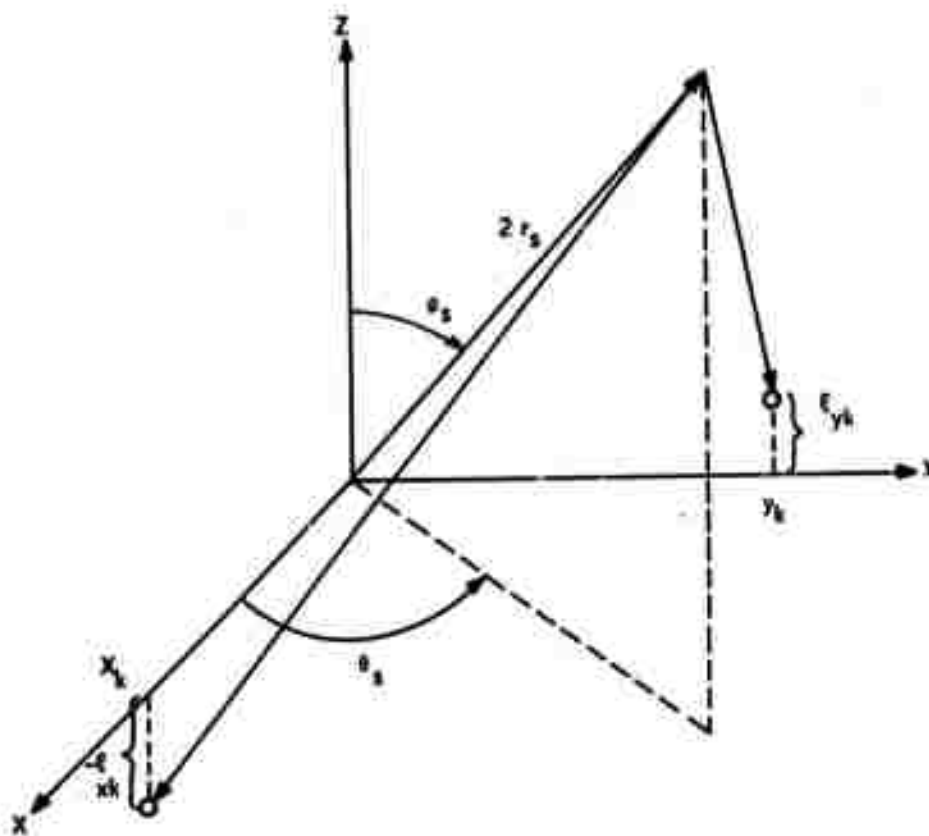
C1

Figure C1. Geometry for Orthogonal Line Arrays Probing
the Half-Space Z>0

$$m_{iks}(n) = \text{Int}\left\{\frac{\tau_{iks}}{\Delta}\right\}$$

$$= \text{Int}\left\{n\left[1 - \sqrt{1 + c_{iks}(n)}\right]\right\}$$

where Int(u) denotes the integer part of u. Here

$$c_{iks} = \frac{1}{n^2}\left(\frac{T_c}{\Delta}\right)^2\left(\frac{d}{\lambda_p}\right)^2(k^2 + x_{ik}^2)$$

$$-\frac{2}{n}\left(\frac{T_c}{\Delta}\right)\left(\frac{d}{\lambda_p}\right)(k\,a_{is} + x_{ik}\,b_s)$$

with

$$x_{ik} = \xi_{ik}/d$$

$$a_{is} = \begin{cases} \sin\phi_s\cos\theta_s; & i = x \\ \sin\phi_s\sin\theta_s; & i = y \end{cases}$$

$$b_s = \cos\phi_s$$

for uniformly spaced ($x_k = y_k = kd$) line arrays.

Computation of the $m_{iks}(n)$ in the above exact form is very costly in time and hardware, and could easily negate the savings that DIMUS processing affords. It is therefore desirable to investigate the conditions under which simplifying approximations can be made for a specific array design.

Selection of an array design to provide coverage over a specified solid angle is reasonably based upon the requirement that a minimum number of beams with acceptable resolution and minimal overlap be formed. In this case of multiplicative DIMUS arrays and sampled data, the design is of necessity a cut-and-try procedure because of the nonlinear beamforming and a discrete set of steering delays.

C3

There are some additional constraints and guides which can be used to aid the array design. Since the minimum interelement steering delays occur in far field beamforming, we select our design on the basis of the far field pattern and require that the steering delays for the far fieldbeams be exact multiples of the sample interval, Δ. Also, a DIMUS array with an odd number of elements can never have a zero in the sidelobe region of its beam pattern. Therefore, we constrain the individual line arrays to an even number of elements.

Finally, the number of beams required to scan the specified solid angle should be reasonable so as not to overtax the processor and display. Fairly broad beams for P waves can be tolerated in this application where the main source of interference is surface waves. Since $\lambda_s \simeq 2\lambda_p$, the beamwidth for surface waves is about half that for P waves.

In the far field, the sample steering delays are

$$m_{iks} = \lim_{n \to \infty} m_{iks}(n) = (\frac{T_c}{\Delta})(\frac{d}{\lambda_p}) k\, a_{is}$$

assuming the array is mounted on a plane surface. Thus, in addition to array size, $K\Delta$, we have the ratios (T_c/Δ) and (d/λ_p) at our disposal to control beamwidth and location of the beam axes. Since the ratio $(T_c/\Delta) = 25$ used in the experimental data seemed appropriate, positioning of the beam axes was achieved through selection of d/λ_p.

The recommended DIMUS array design consists of two orthogonal six-element line arrays with element spacings $d/\lambda_p = 1/3$. Beam contours at the 3-db points for beams in the first quadrant generated by multiplication and averaging of the orthogonal DIMUS arrays are shown in Figure C2. A total of 25 beams will provide coverage over the solid angle $\phi \lesssim 40°$, although four beams at $(\phi_s, \theta_s) = (43°, 45° \mod 90°)$ could be dropped at the expense of a relatively small gap in the vicinity of $(40°, 45° \mod 90°)$.

The beam centers in Figure C2 are classified by a steering order of the form (S_x, S_y). Beams in the remaining quadrants are obtained by taking these orders with the three remaining ± sign combinations. The steering coefficients corresponding to a given steering order are:

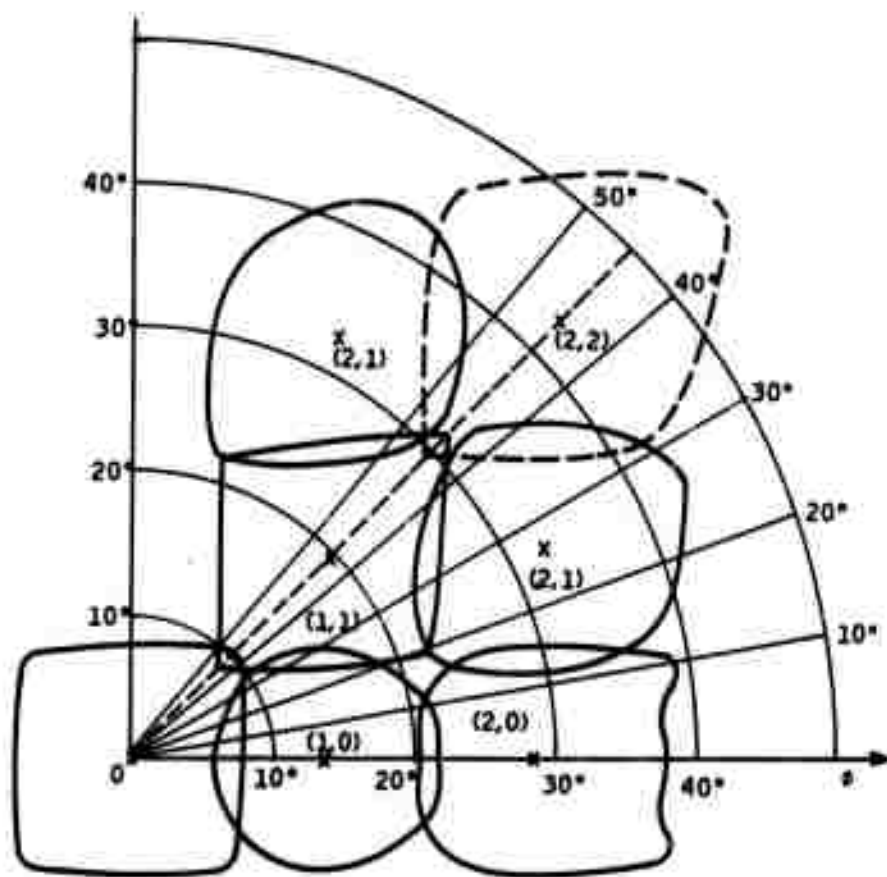| S_i	a_{is}
0	0
±1	±0.24
±2	±0.48

C4

Figure C2. Far-Field DIMUS 3-db Beam Contours for
Orthogonal Correlated Line Arrays - $k_A = 6$,
$d/\lambda_p = 1/3$

Far-field beam patterns for P waves incident on the correlated DIMUS arrays are shown in Figures C3 through C5. The patterns are shown in pairs, the top trace of a pair at fixed θ_s for the beam axis while $-90° \leq \phi \leq 90°$, and the bottom trace of the pair at fixed ϕ_s for the beam axis while $-90° \leq \theta \leq 90°$. The spherical coordinates of the beam axis in the first quadrant are noted in parentheses. Note how the beam broadens in the ϕ direction and narrows in the θ direction as the axis angle ϕ_s increases.

Multiplicative DIMUS beam patterns for incident surface waves are presented in Figures C6 through C8. Again, the traces are in pairs for a given beam, but because there is no ϕ dependence in the surface wave, the top plot in the pair covers the range $-90° \leq \theta \leq 90°$, and the bottom plot of the pair covers $90° \leq \theta \leq 270°$. Here we note the consistently narrow main lobe width for all the beams, and the preponderance of zeros in the sidelobes region of the patterns. The (2, 1) beam (Figure C8) does exhibit a grating lobe centered at 153.4 degrees which is not desirable. However, on the whole, these theoretical far-field patterns for the surface wave are quite acceptable.

The final set of beam patterns in Figures C9 through C11 illustrate the effects of misalignment of transducers with the plane due to surface roughness. Since the ξ_{ik} can be accurately measured, the additional normalized delay

$$\left(\frac{T_c}{\Delta}\right) \left(\frac{d}{\lambda_p}\right) x_{ik} b_s$$

in the far-field sample delay resulting from surface roughness can be corrected to the nearest integer. Uncorrectable misalignments were simulated by drawing a random number in the range (-0.5, 0.5) for each element and including it as a phasing error in the beam forming. Comparison of these results with like beam patterns for the plane array (Figures C3 through C5) show only isolated, narrow, low-amplitude deviations from the plane array beam patterns. It is concluded, therefore, that nonplanar surface for array can be tolerated in multiplicative DIMUS beamforming.

Having defined an array and its geometry and steering orders, let us return to the problem of near-field beamforming. A power series expansion of $m_{iks}(n)$ yields

$$m_{iks}(n) = \text{Int} \left\{ n \left[-\frac{1}{2} C_{iks}(n) + \frac{1}{8} C_{\overline{iks}}^2(n) - \frac{1}{16} C_{\overline{iks}}^3(n) \right. \right.$$
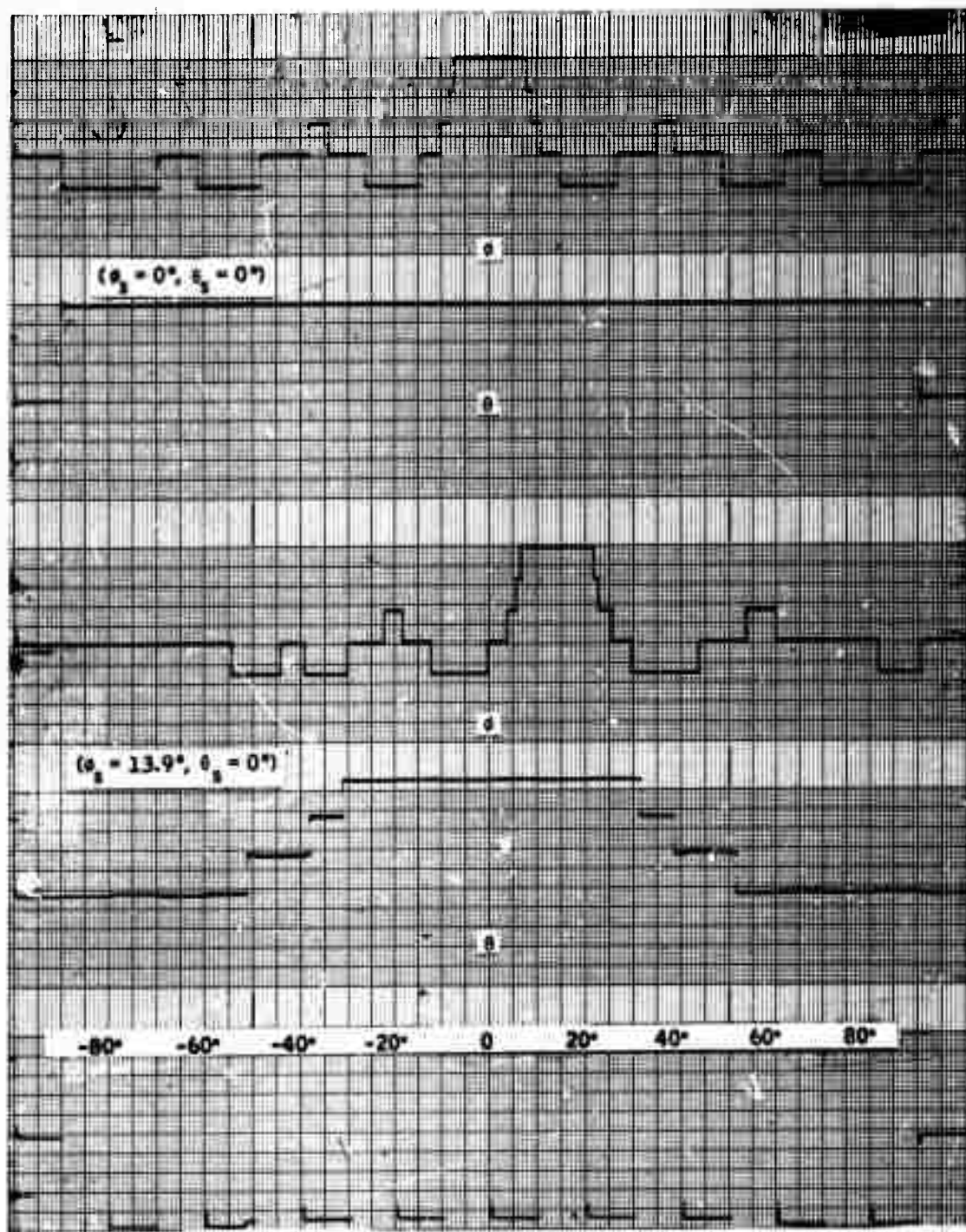$$\left. \left. + \frac{5}{128} C_{iks}^4(n) \ldots \right] \right\}$$

Figure C3.   Multiplicative DIMUS Beam Patterns - P-Wave,
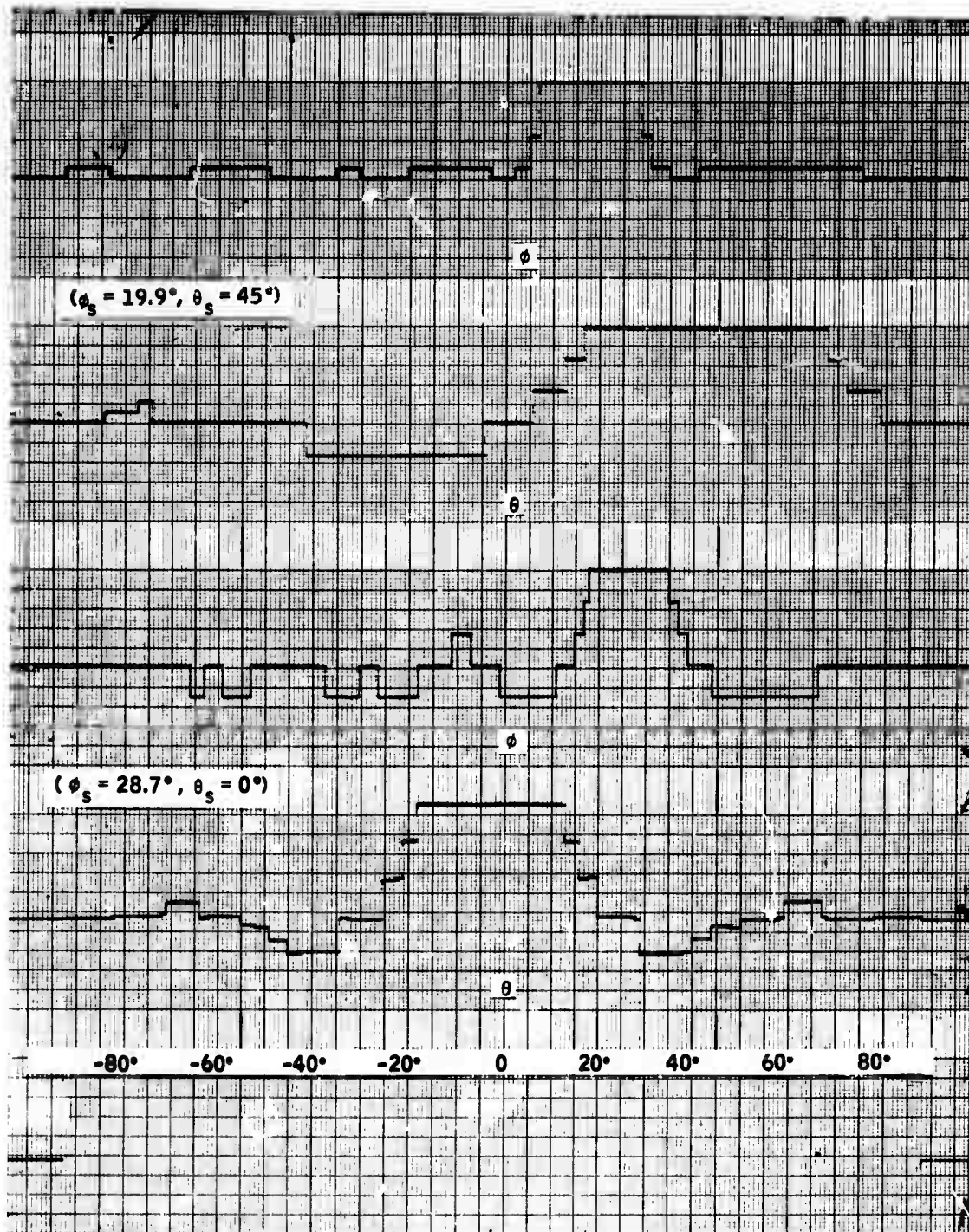(0, 0) and (1, 0) Beams

C7

Figure C4. Multiplicative DIMUS Beam Patterns - P-Wave,
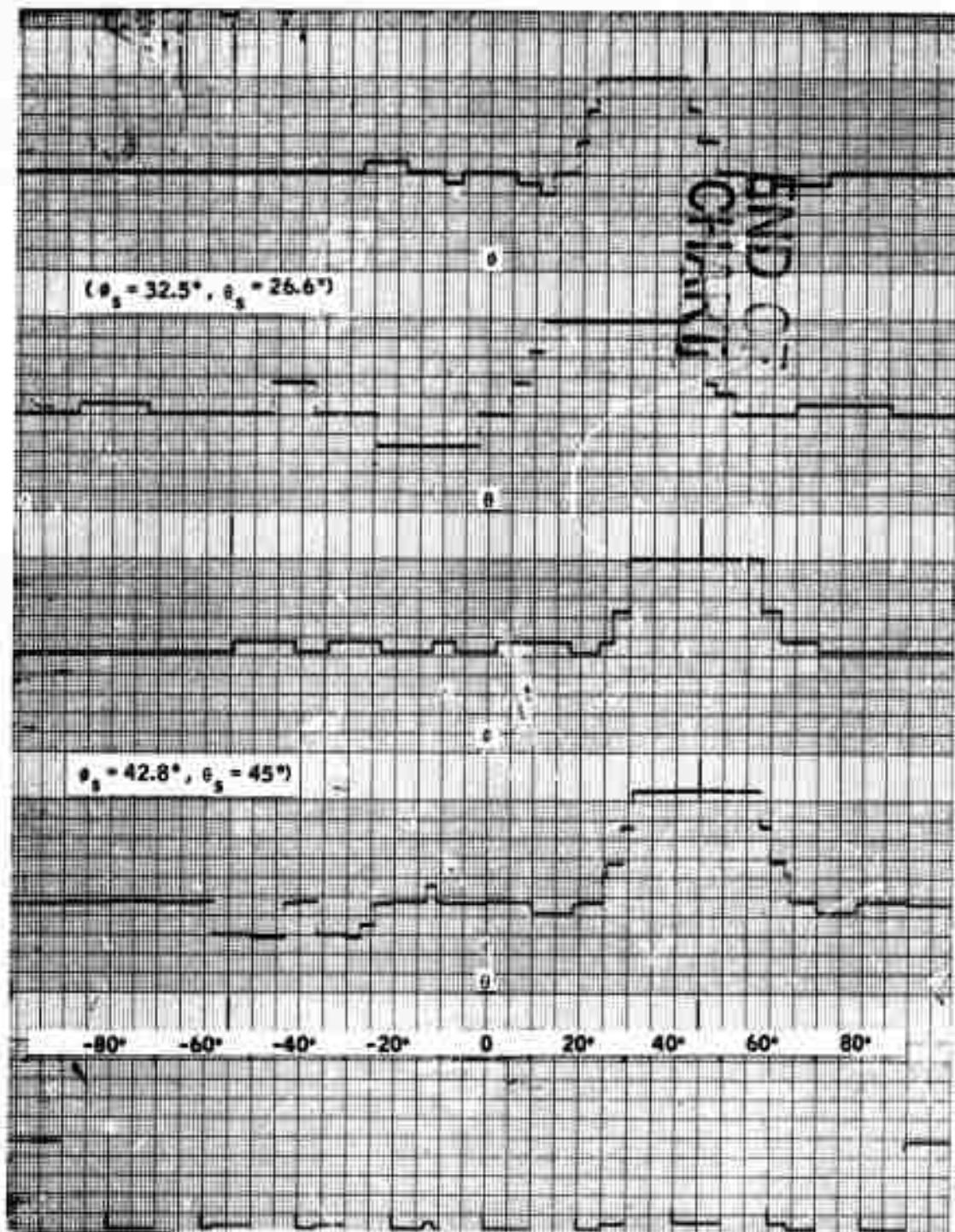(1, 1) and (2, 0) Beams

C8

Figure C5. Multiplicative DIMUS Beam Patterns - P-Wave, (2, 1) and (2, 2) Beams
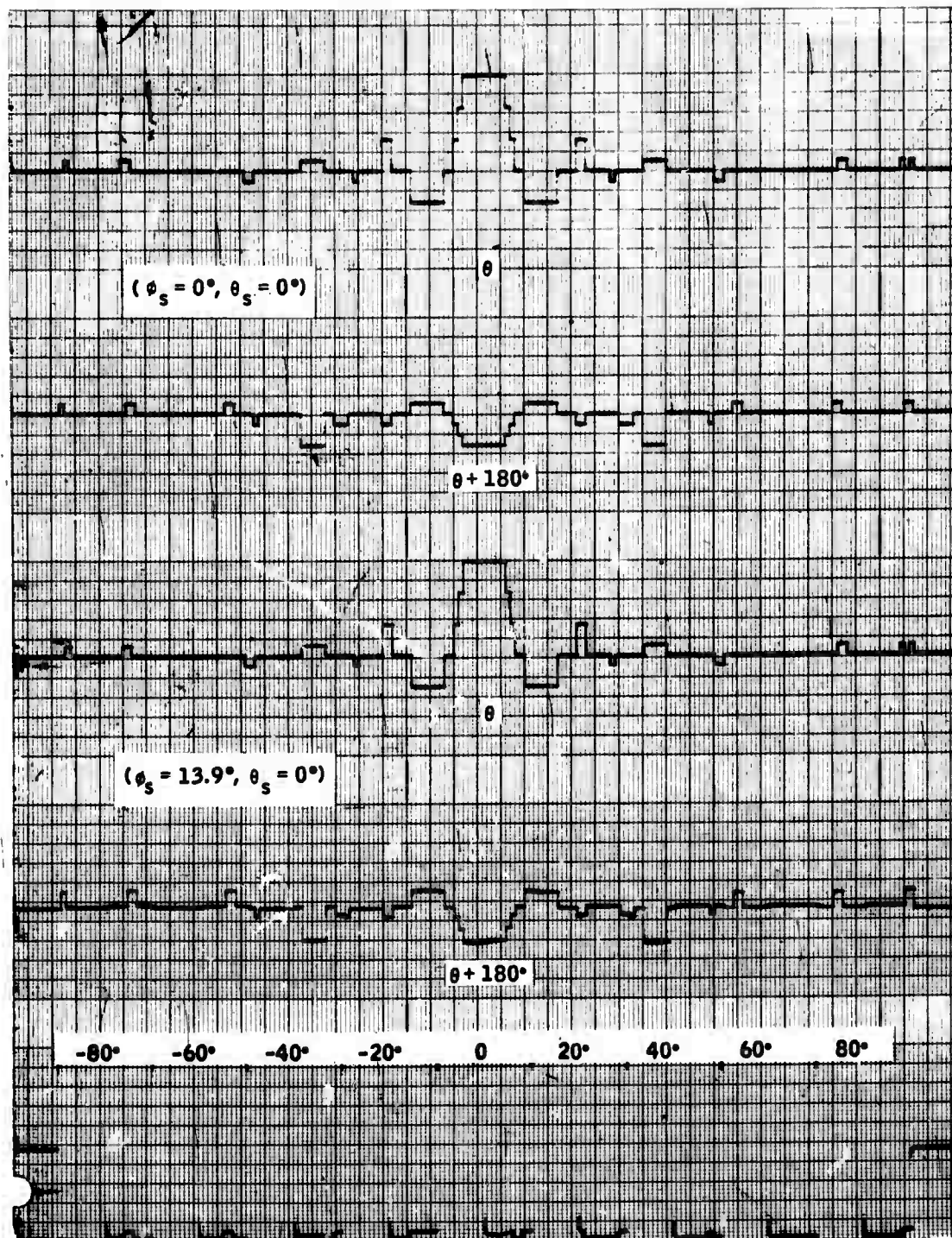
C9

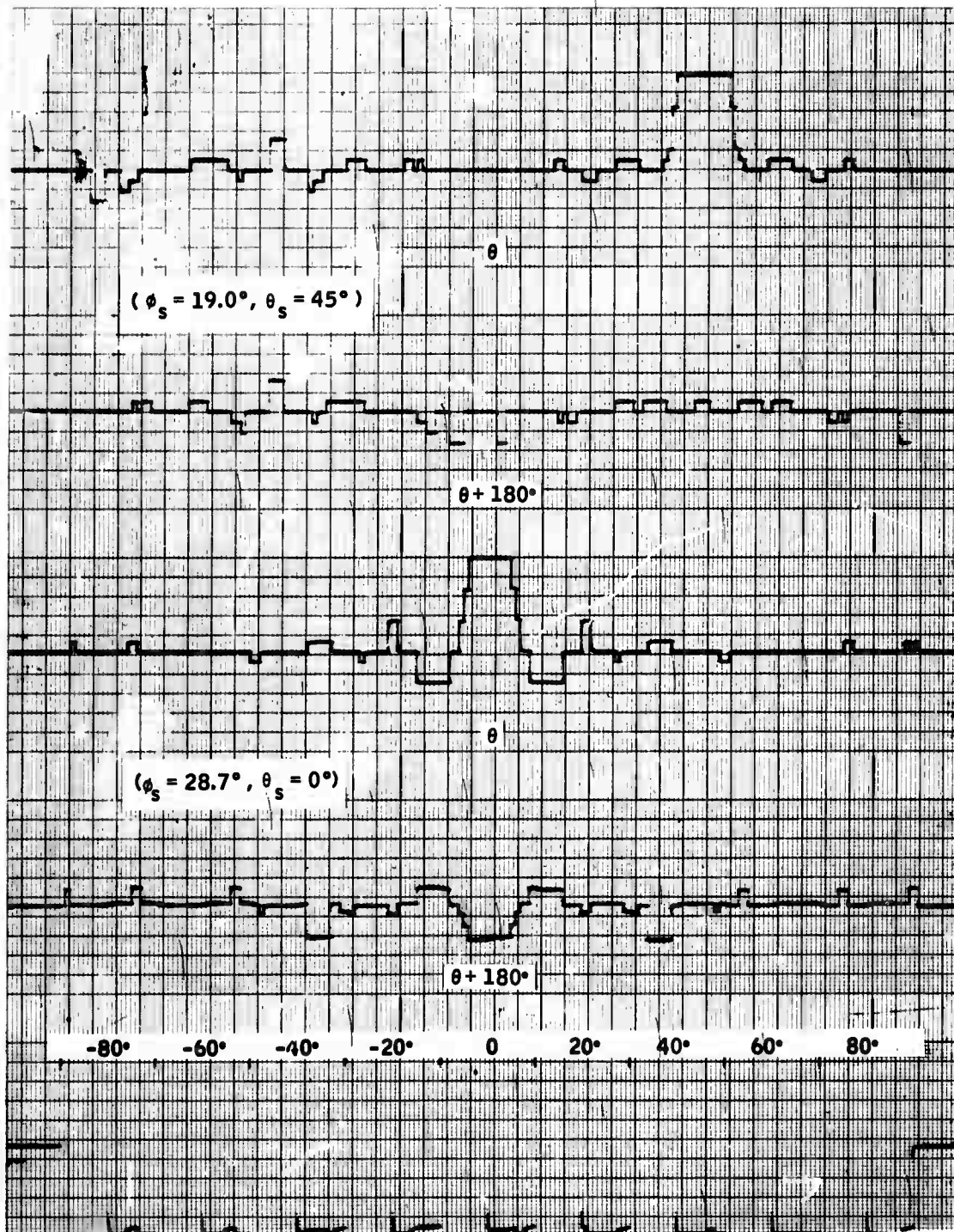Figure C6. Multiplicative DIMUS Beam Patterns - Surface
Wave, (0, 0) and (1, 0) Beams

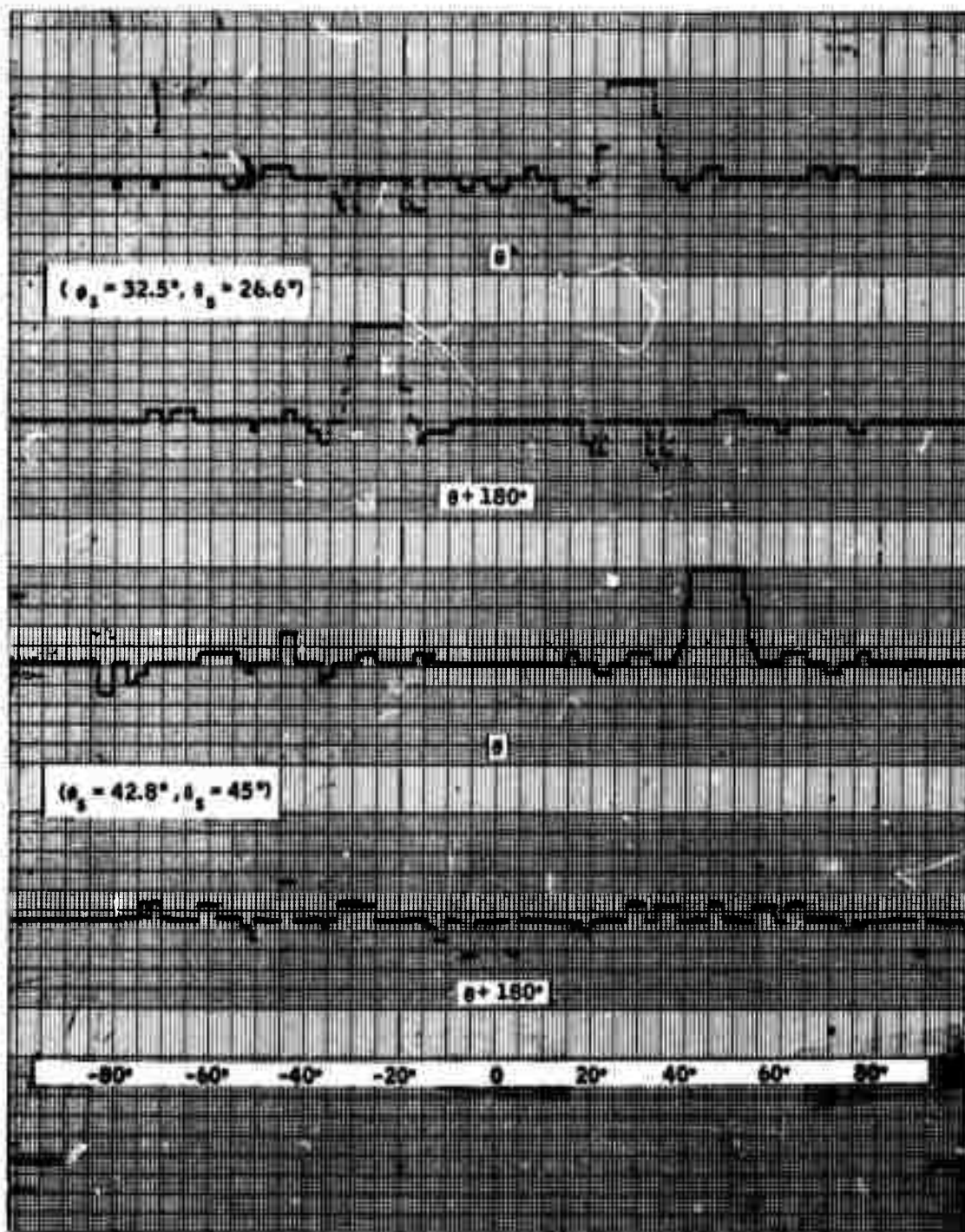Figure C7. Multiplicative DIMUS Beam Patterns - Surface
Wave, (1,1) and (2,0) Beams

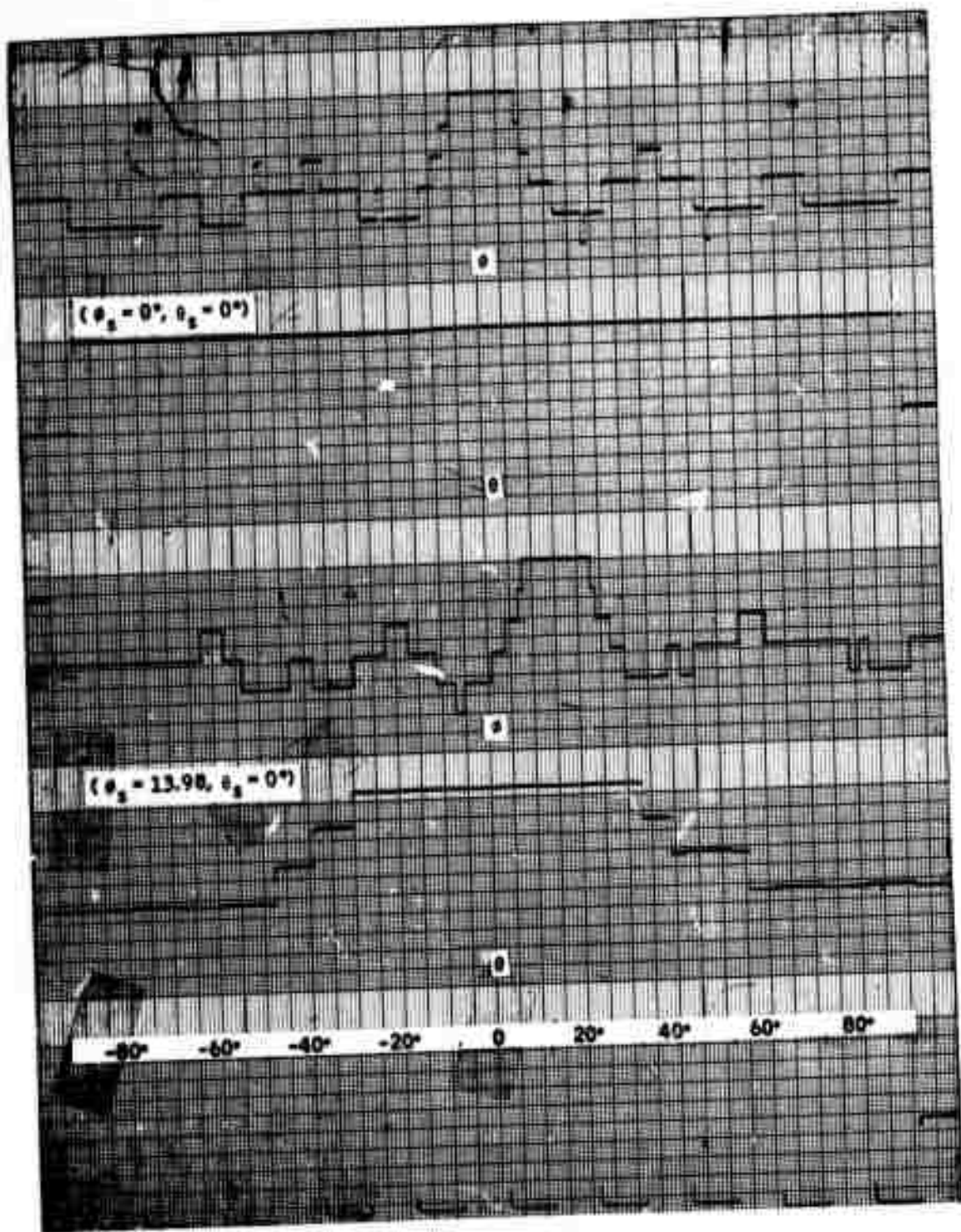Figure C8. Multiplicative DIMUS Beam Patterns - Surface
Wave, (2, 1) and (2, 2) Beams

C12

Figure C9.   Multiplicative DIMUS Beam Patterns - Random
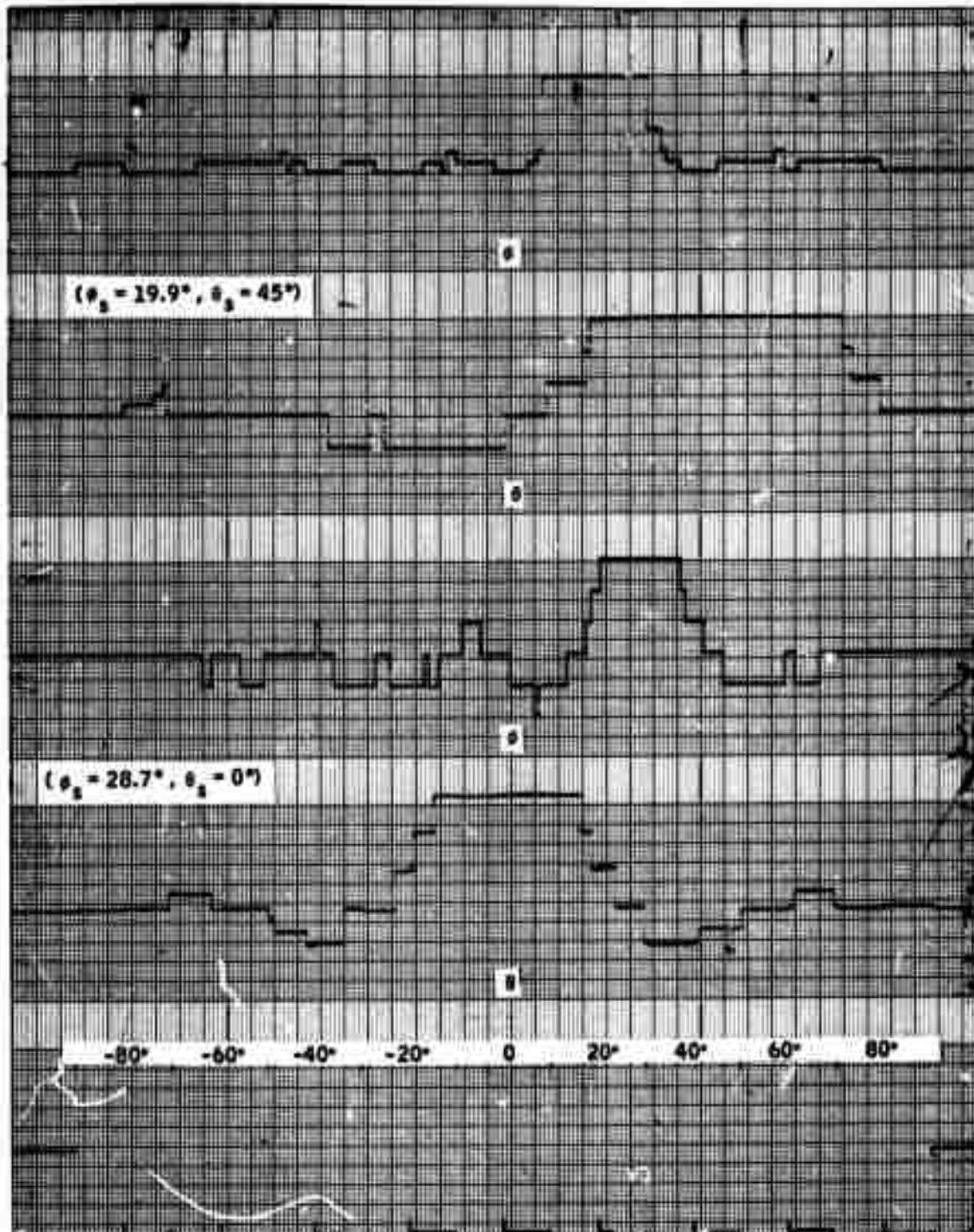Surface, P-Wave, (0, 0) and (1, 0) Beams

C13

Figure C10. Multiplicative DIMUS Beam Patterns - Random
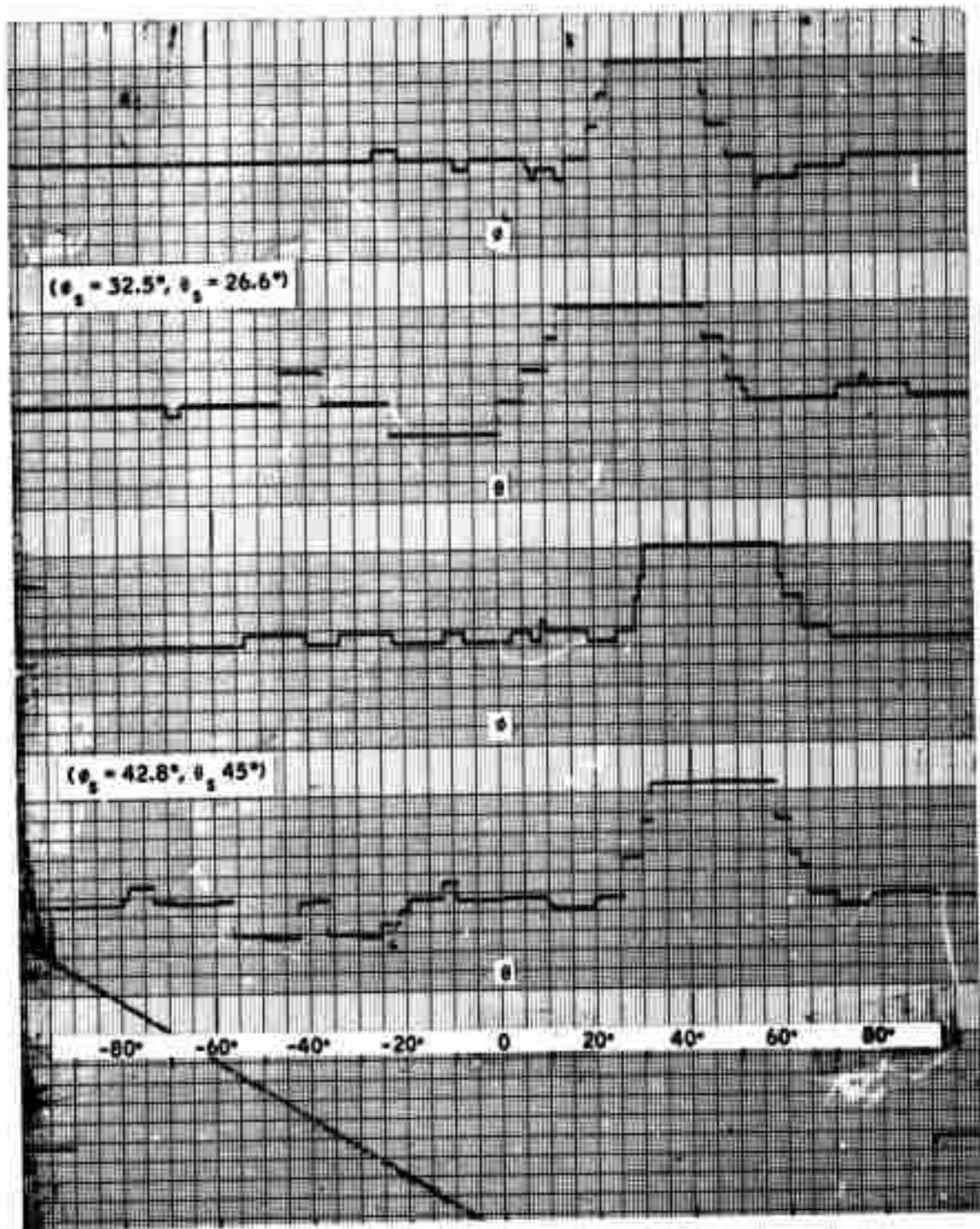Surface, P-Wave (1,1) and (2,0) Beams

Figure C11. Multiplicative DIMUS Beam Patterns - Random Surface, P-Wave (2, 1) and (2, 2) Beams

where for $(T_c/\Delta) = 25$ and $(d/\lambda_p) = 1/3$,

$$C_{iks}(n) = \frac{625}{9n^2}(k^2 + x_{ik}^2) - \frac{50}{3n}(k\,a_{is} + x_{ik}\,b_s)$$

We are interested in the order of approximation that must be carried in the power series expansion as a function of sample number, n, on the record.

If it is assumed that a stack of three records is desired on the display, eight array elements per line array are required to form three sets of six-element beams. To determine the minimum sample number for the jth approximation to be valid at the kth element, we seek the minimum n such that

$$\left| \frac{1}{\Delta}\,\text{iks}(n) - m_{iks}^{(j)}(n) \right| \leq \frac{1}{2}\,.$$

In addition, for far-field beamforming, the first-order approximation is valid. Here we require less than a half-sample error in neglecting the second-order term in $n\,C_{iks}(n)/2$; i.e., we seek the minimum n satisfying

$$n \geq \left(\frac{T_c}{\Delta}\right)^2 \left(\frac{d}{\lambda_p}\right)^2 \lceil k^2 + x_{ik}^2 \rceil\,.$$

For the worst-case steering order ($a_{is} = -0.48$), and assuming $|\, \varepsilon_{ik}\,| \leq \lambda_p/6$, the lower bounds, n_{min}, on the sample number for validity of the jth order approximation at the kth array element are as shown in Table C1.

Since $r_s/\lambda_p = n/50$, the third-order approximation is valid for all elements at penetration depths $r_s/\lambda_p \geq 3.4$.

For maximum penetration depths of the order of 100 feet, there are about 5000 samples per record for the sample interval of 2 μsec used here. Clearly, most of the beamforming will be done in the near field. However, it does appear to be worthwhile to use the lowest-order approximation applicable on each element to conserve computation time in the beamforming.

C16

Table C1. Number of Samples Required for Near-Field Beamforming (j= order of polynomial)

k	n_{min}			
	j = 3	j = 2	j = 1	Far Field
1	---	---	---	80
2	---	---	150	300
3	---	80	270	640
4	---	110	420	1125
5	---	145	600	1750
6	---	185	825	2510
7	150	225	1075	3420
8	170	270	1355	4450